



HAL
open science

Presentation and evaluation of the IPSL-CM6A-LR climate model

Olivier Boucher, Jérôme Servonnat, Anna Lea Albright, Olivier Aumont, Yves Balkanski, Vladislav Bastrikov, Slimane Bekki, Rémy Bonnet, Sandrine Bony, Laurent Bopp, et al.

► To cite this version:

Olivier Boucher, Jérôme Servonnat, Anna Lea Albright, Olivier Aumont, Yves Balkanski, et al.. Presentation and evaluation of the IPSL-CM6A-LR climate model. *Journal of Advances in Modeling Earth Systems*, 2020, 12 (7), pp.e2019MS002010. 10.1029/2019MS002010 . hal-02875593v1

HAL Id: hal-02875593

<https://hal.science/hal-02875593v1>

Submitted on 16 Jul 2020 (v1), last revised 6 Jan 2023 (v2)

HAL is a multi-disciplinary open access archive for the deposit and dissemination of scientific research documents, whether they are published or not. The documents may come from teaching and research institutions in France or abroad, or from public or private research centers.

L'archive ouverte pluridisciplinaire **HAL**, est destinée au dépôt et à la diffusion de documents scientifiques de niveau recherche, publiés ou non, émanant des établissements d'enseignement et de recherche français ou étrangers, des laboratoires publics ou privés.



Presentation and evaluation of the IPSL-CM6A-LR climate model

Olivier Boucher¹, Jérôme Servonnat², Anna Lea Albright³, Olivier Aumont⁴,
Yves Balkanski², Vladislav Bastrikov², Slimane Bekki⁵, Rémy Bonnet¹,
Sandrine Bony³, Laurent Bopp³, Pascale Braconnot², Patrick Brockmann²,
Patricia Cadule¹, Arnaud Caubel², Frédérique Cheruy³, Francis Codron⁴,
Anne Cozic², David Cugnet³, Fabio D'Andrea³, Paolo Davini⁶, Casimir de
Lavergne⁴, Sébastien Denvil¹, Julie Deshayes⁴, Marion Devilliers⁷, Agnès
Ducharne⁸, Jean-Louis Dufresne³, Elliott Dupont¹, Christian Éthé¹, Laurent
Fairhead³, Lola Falletti⁵, Simona Flavoni⁴, Marie-Alice Foujols¹, Sébastien
Gardoll¹, Guillaume Gastineau⁴, Josefine Ghattas¹, Jean-Yves Grandpeix³,
Bertrand Guenet², Lionel Guez³, Éric Guilyardi⁴, Matthieu Guimberteau²,
Didier Hauglustaine², Frédéric Hourdin³, Abderrahmane Idelkadi³, Sylvie
Joussaume², Masa Kageyama², Myriam Khodri⁴, Gerhard Krinner⁹, Nicolas
Lebas⁴, Guillaume Levavasseur¹, Claire Lévy⁴, Laurent Li³, François Lott³,
Thibaut Lurton¹, Sebastiaan Luysaert¹⁰, Gurvan Madec⁴, Jean-Baptiste
Madeleine³, Fabienne Maignan², Marion Marchand⁵, Olivier Marti², Lidia
Mellul³, Yann Meurdesoif², Juliette Mignot⁴, Ionela Musat³, Catherine Ottlé²,
Philippe Peylin², Yann Planton⁴, Jan Polcher³, Catherine Rio¹¹, Nicolas
Rochetin³, Clément Rousset⁴, Pierre Sepulchre², Adriana Sima³, Didier
Swingedouw⁷, Rémi Thiéblemont¹², Abdoul Khadre Traore³, Martin
Vancoppenolle⁴, Jessica Vial³, Jérôme Vialard⁴, Nicolas Viovy², Nicolas
Vuichard²

¹Institut Pierre-Simon Laplace, Sorbonne Université / CNRS, Paris, France

²Laboratoire des Sciences du Climat et de l'Environnement, Institut Pierre-Simon Laplace, CEA / CNRS
/ UVSQ, Gif-sur-Yvette, France

³Laboratoire de Météorologie Dynamique, Institut Pierre-Simon Laplace, Sorbonne Université / CNRS /
École Normale Supérieure – PSL Research University / École Polytechnique – IPP, Paris, France

⁴Laboratoire d'Océanographie et du Climat : Expérimentations et Approches Numériques, Institut
Pierre-Simon Laplace, Sorbonne Université / CNRS / IRD / MNHN, Paris, France

⁵Laboratoire Atmosphères, Milieux, Observations Spatiales, Institut Pierre-Simon Laplace, Sorbonne
Université / CNRS / UVSQ, Paris, France

⁶Istituto di Scienze dell'Atmosfera e del Clima, Consiglio Nazionale delle Ricerche, Torino, Italy

This article has been accepted for publication and undergone full peer review but has not been through the copyediting, typesetting, pagination and proofreading process which may lead to differences between this version and the Version of Record. Please cite this article as doi: 10.1029/2019MS002010

This article is protected by copyright. All rights reserved.

34 ⁷Environnements et Paléoenvironnements Océaniques et Continentaux, Université de Bordeaux / CNRS,
35 Bordeaux, France

36 ⁸Milieux environnementaux, transferts et interactions dans les hydrosystèmes et les sols, Institut
37 Pierre-Simon Laplace, Sorbonne Université / CNRS / EPHE, Paris, France

38 ⁹Institut des géosciences de l'environnement, CNRS / Université de Grenoble, Grenoble, France

39 ¹⁰Department of Ecological Sciences, Vrije Universiteit Amsterdam, Amsterdam, Netherlands

40 ¹¹Centre national des recherches météorologiques, Météo-France / CNRS, Toulouse, France

41 ¹²Bureau de Recherches Géologiques et Minières, Orléans, France

42 **Key Points:**

- 43 • The IPSL-CM6A-LR model climatology is much improved over the previous ver-
44 sion although some systematic biases and shortcomings persist.
- 45 • A long pre-industrial control and a large number of historical and scenario sim-
46 ulations have been performed as part of CMIP6.
- 47 • The effective climate sensitivity of the IPSL model increases from 4.1 to 4.8 K be-
48 tween IPSL-CM5A-LR and IPSL-CM6A-LR.

Corresponding author: Olivier Boucher, olivier.boucher@ipsl.fr

Abstract

This study presents the global climate model IPSL-CM6A-LR developed at IPSL to study natural climate variability and climate response to natural and anthropogenic forcings as part of the 6th phase of the Coupled Model Intercomparison Project (CMIP6). This article describes the different model components, their coupling, and the simulated climate in comparison to previous model versions. We focus here on the representation of the physical climate along with the main characteristics of the global carbon cycle. The model's climatology, as assessed from a range of metrics (related in particular to radiation, temperature, precipitation, wind), is strongly improved in comparison to previous model versions. Although they are reduced, a number of known biases and shortcomings (e.g., double ITCZ, frequency of midlatitude wintertime blockings, and ENSO dynamics) persist. The equilibrium climate sensitivity and transient climate response have both increased from the previous climate model IPSL-CM5A-LR used in CMIP5. A large ensemble of more than 30 members for the historical period (1850-2018) and a smaller ensemble for a range of emissions scenarios (until 2100 and 2300) are also presented and discussed.

Plain Language Summary

Climate models are unique tools to investigate the characteristics and behaviour of the climate system. While climate models and their components are developed gradually over the years, the 6th phase of the Coupled Model Intercomparison Project has been the opportunity for the Institut Pierre-Simon Laplace to develop, test and evaluate a new configuration of its climate model called IPSL-CM6A-LR. The characteristics and emerging properties of this new model are presented in this study. The model climatology, as assessed from a range of metrics, is strongly improved although a number of biases common to many models do persist. The equilibrium climate sensitivity and transient climate response have both increased from the previous climate model IPSL-CM5A-LR used in CMIP5.

1 Introduction

The Institut Pierre-Simon Laplace Climate Modelling Centre (IPSL CMC, see <https://cmc.ipsl.fr>) has set up a new version of its climate model in the runup of phase 6 of the Coupled Model Intercomparison Project (known as CMIP6, see Eyring et al., 2016,

80 for more information). Here we provide a brief description of the coupled model, doc-
81 ument the model climatology and its performance against a range of observations and
82 reanalyses, and present some key emerging properties of the model (internal variability
83 and response to forcings). The implementation of the model boundary conditions (Lurton
84 et al., 2019) and the development process for this new model configuration in prepara-
85 tion to CMIP6 are described in two companion papers.

86 IPSL CMC developed IPSL-CM5A-LR (CM stands for climate model and LR for
87 low resolution) as its main model for phase 5 of CMIP (Dufresne et al., 2013; Szopa et
88 al., 2013). IPSL-CM5A-LR also had two variants: a medium resolution configuration,
89 IPSL-CM5A-MR, and an experimental version, IPSL-CM5B-LR, based on a new ver-
90 sion of the atmospheric physics (Hourdin et al., 2013). The resolution of the atmospheric
91 model was 96×95 points in longitude and latitude in the LR configuration, and 144×143
92 in the MR configuration. Both versions had 39 layers in the vertical. The nominal res-
93 olution of the NEMO oceanic model was 2° for both configurations. Since then, many
94 improvements have been implemented in the various model components: LMDZ (atmo-
95 sphere), NEMO (ocean, sea ice, marine biogeochemistry) and ORCHIDEE (land surface,
96 hydrology, land carbon cycle). In this article we describe only the coupled ocean-atmosphere
97 model and the carbon cycle in the terrestrial and marine model components as the full
98 Earth System version of IPSL-CM6 is still under development. The resolution of the at-
99 mospheric model is now 144×143 points in longitude and latitude, which corresponds
100 to an average resolution of $\sqrt{4\pi R^2/144/142} = 157$ km (R being the Earth's radius),
101 and 79 vertical layers (with a model top at ~ 80 km). The low horizontal resolution (LR)
102 of IPSL-CM6 thus corresponds to the medium horizontal resolution (MR) of IPSL-CM5.
103 The nominal resolution of the ocean model has been increased to 1° and 75 layers in the
104 vertical.

105 This article provides an entry point to the IPSL-CM6A-LR model with a brief sci-
106 entific and technical description of the model, a thorough evaluation of its climatology
107 and some presentation of the DECK (Diagnostic, Evaluation, and Characterization of
108 Klima) and ScenarioMIP simulations that were prepared for CMIP6. Further studies on
109 the IPSL-CM6A-LR model emerging properties and model intercomparison studies are
110 expected to be ongoing for the next few years.

2 Brief overview of the IPSL-CM6A-LR model

2.1 Introduction

IPSL-CM6A-LR is composed of the LMDZ atmospheric model version 6A-LR (Hourdin, Rio, Grandpeix, et al., 2020), the NEMO oceanic model version 3.6 (see references below) and the ORCHIDEE land surface model version 2.0. We briefly describe below each of the three model components and the coupling procedure between them. Further description of the IPSL-CM6A-LR climate model is available on the ES-DOC interface (<https://explore.es-doc.org/cmip6/models/ipsl/ipsl-cm6a-lr>).

2.2 LMDZ6 atmospheric component

The atmospheric general circulation model LMDZ6A-LR is based on a finite-difference formulation of the primitive equations of meteorology (Sadourny & Laval, 1984), on a staggered and stretchable longitude-latitude grid (the Z of LMDZ standing for Zoom). Water vapor, liquid and solid water and atmospheric trace species are advected with a monotonic second order finite volume scheme (Van Leer, 1977; Hourdin & Armengaud, 1999). In the vertical, the model uses a classic so-called hybrid sigma-pressure coordinate. Regarding the physical parameterizations, IPSL participated to CMIP5 with two versions: a “Standard Physics” version (atmospheric component LMDZ5A used in IPSL-CM5A, Hourdin et al., 2013) and a “New Physics” (NP) version (LMDZ5B used in IPSL-CM5B, Hourdin et al., 2013) based on a full rethinking of the parameterizations of turbulence, convection and clouds on which the 6A version is built. This NP package includes in particular a turbulent scheme based on the prognostic equation for the turbulent kinetic energy that follows Yamada (1983), a mass flux representation of the organized structures of the convective boundary layer called “Thermal Plume Model” (Hourdin et al., 2002; Rio & Hourdin, 2008; Rio et al., 2010) and a parameterization of the cold pools or wakes created below cumulonimbus by the evaporation of convective rainfall (Grandpeix & Lafore, 2010; Grandpeix et al., 2010). The “episodic mixing and buoyancy sorting” scheme originally developed by Emanuel (1991) used for deep convection was modified to make the closure and triggering rely on the description of the sub-cloud vertical motions by thermal plumes and wakes (Rio et al., 2009). Regarding convection, two important improvements were made from version 5B to 6A: a modification of the lateral detrainment in the thermal plume model that allows to represent satisfactorily well the tran-

142 sition from stratocumulus to cumulus clouds (Hourdin et al., 2019a) and the introduc-
143 tion of a statistical triggering for deep convection (Rochetin, Couvreur, et al., 2014; Ro-
144 chetin, Grandpeix, et al., 2014). The radiation scheme was inherited from the European
145 Centre for Medium-Range Weather Forecasts. In the LMDZ6A version, it includes the
146 Rapid Radiative Transfer Model (RRTM) code for thermal infrared radiation and an im-
147 proved six-band version of the Fouquart and Bonnel (1980) scheme for solar radiation.
148 Cloud cover and cloud water content are computed using a statistical scheme using a log-
149 normal function for deep convection (Bony & Emanuel, 2001) and a bigaussian function
150 for shallow cumulus (Jam et al., 2013).

151 The 6A-LR version is based on a regular horizontal grid with 144 points regularly
152 spaced in longitude and 142 in latitude, corresponding to a resolution of $2.5^\circ \times 1.3^\circ$. The
153 model has 79 vertical layers and extends up to 80 km, which makes it a “high-top” model.
154 It includes a representation of gravity waves generated by mountains as well as by con-
155 vection (Lott & Guez, 2013) and fronts (de la Cámara & Lott, 2015; de la Cámara et
156 al., 2016). The model shows a self-generated quasi-biennial oscillation (QBO) whose pe-
157 riod has been tuned to the observed one for the present-day climate. The source of wa-
158 ter vapour in the stratosphere due to methane oxidation is not activated.

159 The readers are directed to Hourdin, Rio, Grandpeix, et al. (2020) for more details.

160 **2.3 NEMO oceanic component**

161 The ocean component used for IPSL-CM6A-LR is based on the version 3.6 stable
162 of NEMO (Nucleus for European Models of the Ocean), which includes three major com-
163 ponents: the ocean physics NEMO-OPA (Madec et al., 2017), the sea-ice dynamics and
164 thermodynamics NEMO-LIM3 (Vancoppenolle et al., 2009; Rousset et al., 2015) and the
165 ocean biogeochemistry NEMO-PISCES (Aumont et al., 2015). The configuration used
166 is eORCA1 (with the e standing for extended), the quasi-isotropic global tripolar grid
167 with a 1° nominal resolution, and extended to the south so as to better represent the
168 contribution of Antarctic under-ice shelf seas to the Southern Ocean freshwater cycle (Mathiot
169 et al., 2017). The grid has a latitudinal grid refinement of $1/3^\circ$ in the equatorial region.
170 Vertical discretization uses a partial step formulation (Barnier et al., 2006), which en-
171 sures a better representation of bottom bathymetry, with 75 levels. The initial layer thick-

nesses increase non-uniformly from 1 m at the surface to 10 m at 100 m depth, and reaches
200 m at the bottom; they are subsequently time-dependent (Levier et al., 2007).

174 **2.3.1 Ocean Physics: NEMO-OPA**

175 The eORCA1 configuration used has a non-linear free surface using the variable
176 volume layer formulation, which induces time-variability of all layer thicknesses (Levier
177 et al., 2007). It uses a polynomial representation of the equation of state TEOS-10 (Roquet
178 et al., 2015). The vertical mixing of tracers and momentum uses the turbulent kinetic
179 energy scheme (Gaspar et al., 1990; Blanke & Delecluse, 1993) and an energy-constrained
180 parameterization of mixing due to internal tides (de Lavergne, 2016; de Lavergne et al.,
181 2019). There is no constant background diffusivity other than a floor at molecular lev-
182 els: $1.4 \times 10^{-6} \text{ m}^2 \text{ s}^{-1}$ for momentum and $1.4 \times 10^{-7} \text{ m}^2 \text{ s}^{-1}$ for tracers. The mixing in-
183 duced by submesoscale processes in the mixed layer is also parameterized (Fox-Kemper
184 et al., 2011). A quadratic bottom friction boundary condition is applied together with
185 a parameterization of a diffusive bottom boundary layer for the tracers with a coefficient
186 of $1000 \text{ m}^2 \text{ s}^{-1}$. The model uses an energy-entropy-conserving scheme for momentum
187 advection and a no-slip boundary condition is applied on the momentum equations. Lat-
188 eral diffusion of momentum is performed on geopotential surfaces and uses a Laplacian
189 viscosity with a coefficient of $20,000 \text{ m}^2 \text{ s}^{-1}$. Lateral diffusion of tracers is performed along
190 isoneutral surfaces using Laplacian mixing with a spatially varying coefficient of $1000 \text{ m}^2 \text{ s}^{-1}$
191 at the Equator decreasing with the reduction of the grid spacing with the latitude and
192 reaches a value less than $500 \text{ m}^2 \text{ s}^{-1}$ poleward to 60°N and S . In addition, there is a pa-
193 rameterization of adiabatic eddy mixing (Gent & McWilliams, 1990) varying spatially
194 as a function of Rossby radius and local growth rate of baroclinic instabilities. The con-
195 figuration also includes representation of the interaction between incoming shortwave ra-
196 diation into the ocean and the phytoplankton (Lengaigne et al., 2009). A spatially vary-
197 ing geothermal heat flux is applied at the bottom of the ocean (Goutorbe et al., 2011),
198 with a global mean value of 66 mW m^{-2} .

199 **2.3.2 Sea-ice: NEMO-LIM**

200 IPSL-CM6A-LR utilises v3.6 of the Louvain-la-Neuve Ice Model (LIM), instead of
201 version 2 for IPSL-CM5, hence many of the sea ice model features were revised since CMIP5.
202 LIM3.6 is a multi-category halo-thermodynamic dynamic sea ice model embedded in the

203 NEMO environment (Vancoppenolle et al., 2009; Rousset et al., 2015), based on the Arc-
204 tic Ice Dynamics Joint EXperiment (AIDJEX) framework (Coon et al., 1974). LIM3.6
205 combines the ice thickness distribution approach (Thorndike et al., 1975; Bitz et al., 2001;
206 Lipscomb, 2001), the conservation of horizontal momentum (Hibler, 1979), treating sea
207 ice as a 2D elastic-viscous plastic continuum (Hunke & Dukowicz, 1997; Bouillon et al.,
208 2013), horizontal transport (Prather, 1986), and energy-conserving halo-thermodynamics
209 (Bitz & Lipscomb, 1999; Vancoppenolle et al., 2009). The multiple ice categories allow
210 resolving the enhanced growth of thin ice and solar radiation uptake through thin ice,
211 and the redistribution of thin onto thick ice through ridging and rafting. Sea ice salin-
212 ity is an integral part of the model, evolving dynamically to resolve brine entrapment
213 and drainage; and influencing sea ice thermal properties and ice-ocean exchanges (Vancoppenolle
214 et al., 2009). Five thickness categories are used. Ice temperature and salinity fields are
215 further discretized onto two vertical layers of sea ice and one layer of snow. Horizontally,
216 the ice fields are resolved on the same grid as the ocean component.

217 The large-scale sea ice state was adjusted over atmosphere-forced, first, then at the
218 end of each tuning cycle step of the fully-coupled simulations, adding up to several thou-
219 sands of simulated years. The sea ice tuning parameters include the cloud-sky albedo
220 nodal values (dry snow 0.87, wet snow 0.82, dry ice 0.65, wet ice 0.58) and the snow ther-
221 mal conductivity ($0.31 \text{ W m}^{-1} \text{ K}^{-1}$). The albedo values lie in the high end of the range,
222 to enhance sea ice formation and reduce melting, and compensate for the effects of high
223 air temperatures above sea ice, in particular in the Arctic winter. The albedo nodal val-
224 ues were kept within observational uncertainty range, leaving a low Arctic sea ice bias
225 still. The ice strength parameter was set to $P^* = 20,000 \text{ N m}^{-2}$. A maximum ice con-
226 centration is imposed, which is equivalent to impose a minimum open water fraction, and
227 done specifically for each hemisphere (0.997 in the Northern Hemisphere, and 0.95 in the
228 Southern Hemisphere). This choice is justified by the difficulty of the model to main-
229 tain open water within the pack, in particular in winter, and even more so for Antarc-
230 tic sea ice.

231 ***2.3.3 Ocean biogeochemistry: NEMO-PISCES***

232 The biogeochemical model is based on PISCES-v2 (Aumont et al., 2015) which sim-
233 ulates the lower trophic levels of marine ecosystem (phytoplankton, microzooplankton
234 and mesozooplankton) and the biogeochemical cycles of carbon and of the main nutri-

235 ents (P, N, Fe, and Si). There are twenty-four prognostic variables (tracers) including
236 two phytoplankton compartments (diatoms and nanophytoplankton), two zooplankton
237 size-classes (microzooplankton and mesozooplankton) and a description of the carbon-
238 ate chemistry. Formulations in PISCES-v2 are based on a mixed Monod/Quota formal-
239 ism. On the one hand, stoichiometry of C/N/P is fixed and growth rate of phytoplank-
240 ton is limited by the external availability in N, P and Si. On the other hand, the iron
241 and silicon quotas are variable and growth rate of phytoplankton is limited by the in-
242 ternal availability in Fe. Nutrients and/or carbon are supplied to the ocean from three
243 different sources: atmospheric deposition, rivers, and sediment mobilization. PISCES is
244 used here to compute air-sea fluxes of carbon and also the effect of a biophysical cou-
245 pling: the chlorophyll concentration produced by the biological component feedbacks on
246 the ocean heat budget by modulating the absorption of light as well as the oceanic heat-
247 ing rate (Lengaigne et al., 2009).

248 **2.4 ORCHIDEE land surface component**

249 ORCHIDEE is a global process-based model of the land surface and the terrestrial
250 biosphere, that calculates water, energy, and carbon fluxes between the surface and the
251 atmosphere. The model, initially described in Krinner et al. (2005) for the version used
252 in the IPSL-CM5 model, has been significantly improved in version 2.0 used in IPSL-
253 CM6A-LR. We only summarize below the main characteristics of ORCHIDEE and key
254 improvements from the CMIP5 version.

255 The vegetation heterogeneity is described using fractions of 15 different Plant Func-
256 tional Types (PFTs, Prentice et al., 1992) for each grid cell. All PFTs share the same
257 equations but with different parameters, except for the leaf phenology. The annual evo-
258 lution of the PFT maps (including a wood harvest product) is derived from the LUHv2
259 database (Lurton et al., 2019). In each grid cell, the PFTs are grouped into three soil
260 tiles according to their physiological behavior: high vegetation (forests) with eight PFTs,
261 low vegetation (grasses and crops) with 6 PFTs, and bare soil with one PFT. An inde-
262 pendent hydrological budget is calculated for each soil tile, to prevent forests from ex-
263 hausting all soil moisture. In contrast, only one energy budget (and snow budget) is cal-
264 culated for the whole grid cell. Note that the energy budget is solved with an implicit
265 numerical scheme that couples the lower atmosphere to the surface, in order to increase
266 numerical stability. All components of the surface energy and water budgets, as well as

267 plant/soil carbon fluxes, are computed at the same time step as the atmospheric physics
268 (i.e. 15 min., Hourdin, Rio, Grandpeix, et al., 2020) using a standard "big leaf" approach,
269 but the "slow" processes (carbon allocation in the different plant reservoir and litter and
270 soil carbon dynamic) are computed on a daily time step. The routing scheme to trans-
271 form runoff into river discharge to the ocean (Ngo-Duc et al., 2007) also proceeds at the
272 daily time step, and has not changed since IPSL-CM5.

273 A physically-based 11-layer soil hydrology scheme has replaced the 2-layer bucket
274 model used in IPSL-CM5. Vertical water fluxes are described using the Richard equa-
275 tion discretized with 11 layers for a 2 m soil depth and a free drainage condition is im-
276 posed at the bottom of the soil column (de Rosnay et al., 2002; d'Orgeval et al., 2008).
277 As detailed in F. Wang et al. (2016), the vertical discretization for heat diffusion is now
278 identical to that adopted for water up to 2 m. Furthermore the soil depth for heat dif-
279 fusion is extended to 90 m, with a zero flux condition at the bottom and 18 calculation
280 nodes, extrapolating the moisture content of the deepest hydrological layer to the en-
281 tire profile between 2 and 90 m. The soil thermal properties (heat capacity and conduc-
282 tivity) of each layer now depend on soil moisture and soil texture, like the soil hydro-
283 logical properties (hydraulic conductivity and diffusivity). Each model grid cell is char-
284 acterized by the dominant soil texture, as derived from the map of Zobler (1986) (but
285 reduced to three classes: coarse / sandy loam, medium / loam, and fine / clay loam),
286 and controlling the constant soil parameters (porosity, Van Genuchten parameters, field
287 capacity and wilting point, dry and saturated thermal properties). All these changes have
288 a significant impact on the surface temperature and its high frequency variability in most
289 regions (Cheruy et al., 2017).

290 In contrast to IPSL-CM5, soil freezing is allowed and diagnosed in each soil layer
291 following a scheme proposed by Gouttevin et al. (2012), but the latent heat release/consumption
292 associated with water freezing/thawing is not accounted for. The freezing state of the
293 soil mainly impacts the computation of soil thermal and hydraulic properties, reducing
294 for instance the water infiltration capacity at soil surface. Finally, the 1-layer snow scheme
295 of IPSL-CM5 was replaced by a 3-layer scheme of intermediate complexity described in
296 T. Wang et al. (2013) and inspired by the scheme proposed in Boone and Etchevers (2001).
297 A revised parameterization of the vegetation and snow albedo has been also introduced
298 with optimized parameters based on remote sensing albedo data from MODIS sensor.

299 For the carbon cycle, photosynthesis depends on light availability, CO₂ concentra-
300 tion, soil moisture and surface air temperature. It is parameterized based on Farquhar
301 et al. (1980) and Collatz et al. (1992) for C3 and C4 plants, respectively. We used the
302 implementation proposed by X. Yin and Struik (2009) that derives an analytical solu-
303 tion of the three equations linking the net assimilation rate, the stomatal conductance,
304 and the intercellular CO₂ partial pressure. In addition, the new version of ORCHIDEE
305 used in IPSL-CM6A-LR includes a “downregulation” capability which accounts for a re-
306 duction of the maximum photosynthesis rates as the CO₂ concentration increases in or-
307 der to account for nutrient limitations. This downregulation mechanism is modelled as
308 a logarithmic function of the CO₂ concentration relative to 380 ppm following Sellers et
309 al. (1996). Once the carbon is fixed by photosynthesis, we compute the autotrophic res-
310 piration (growth and maintenance) and then allocate the remaining carbon into 8 plant
311 compartments (below and above ground sapwood and heartwood; leaves; fruit; roots; re-
312 serves). Each compartment has a specific turnover depending on environmental stresses
313 and the living biomass is turned into a litter pool that is distributed in four compart-
314 ments (metabolic or structural, both above or below ground). The litter is decomposed
315 following first order kinetics equations, modulated by upper soil moisture and temper-
316 ature, with a fraction that is respired and a fraction that is distributed into 3 soil organic
317 carbon pools (active, slow and passive), following the CENTURY model (Parton et al.,
318 1987). Each soil organic carbon pool is also decomposed following first order kinetic equa-
319 tions modulated by soil moisture and temperature. Overall, the carbon respired from
320 the litter and soil carbon pools defines the heterotrophic respiration.

321 **2.5 Coupling between the components**

322 The LMDZ and ORCHIDEE models are coupled at every time step of the physics
323 of the atmospheric model (i.e., 15 minutes) with the exception of the biogeochemical pro-
324 cesses and the vegetation dynamics for which the coupling frequency is one day.

325 The coupling between LMDZ and NEMO in IPSL-CM5 is described in Marti et
326 al. (2010). It is now performed with the OASIS3-MCT coupler. IPSL-CM6A-LR intro-
327 duces some modifications and new features: models are coupled with a frequency of 90
328 minutes, which is both the timestep of the sea-ice model and of the radiation compu-
329 tation in the atmosphere. Atmospheric variables passed to the ocean model (heat, wa-
330 ter and momentum fluxes) are averaged temporally over the six 15-minute timesteps of

331 the LMDZ physics. The flux of freshwater from rivers is passed to the ocean model at
332 river mouth locations with a frequency of one day, which is also the timestep of the river
333 routing in ORCHIDEE. On the ocean grid, the water coming from a river is smoothed
334 over about 200 km to avoid strong haloclines that may occasionally cause the ocean model
335 to crash. To ensure water conservation, the water flux into endorheic basins is globally
336 integrated and homogeneously redistributed over the ocean. Oceanic model variables sent
337 to the atmosphere every 90 minutes are sea surface temperature, sea-ice fraction, sea-
338 ice surface temperature and albedo, averaged on two ocean dynamics time-steps. Albedo
339 for the open surface ocean is computed at every timestep in LMDZ following S  f  rian
340 et al. (2018), which represents a significant improvement over the parameterization used
341 in IPSL-CM5 models. Ocean albedo is a function of solar zenith angle, waveband and
342 surface wind speed; the optional dependence on chlorophyll content of the surface ocean
343 has not been activated. Separate albedoes are provided to the radiative transfer scheme
344 for direct and diffuse radiation.

345 The model includes a very simple scheme to represent the water budget of ice sheets.
346 Snow can accumulate on the land ice fraction of a gridbox, while water vapour can de-
347 posit or sublimate depending on the surface relative humidity. The snowpack is capped
348 to a value of 3000 kg m^{-2} and any excess is sent to a buffer reservoir before returning
349 to the ocean. This buffering is achieved through a temporal smoothing of the freshwa-
350 ter flux (with a 10 year e-folding time) to avoid any spurious low-frequency variability
351 in the freshwater input to the ocean. The flux is then integrated in three latitudinal bands
352 (90°N – 40°N , 40°N – 40°S and 40°S – 90°S) and passed to the ocean. In the north and in
353 the tropical/subtropical bands, the flux is equally distributed over the ocean on the same
354 latitudinal bands. In the south band, it is split in two contributions of 50% each corre-
355 sponding to ice shelf melting and iceberg melting. The ice shelf melting is geographically
356 and vertically distributed along Antarctica so as to mimic the observed distribution from
357 Depoorter et al. (2013) as described in Mathiot et al. (2017). The iceberg melting is spread
358 offshore following the observed geographical distribution of icebergs of Merino et al. (2016)
359 and distributed vertically over the top 150 m, similarly to river runoffs.

360 Insufficient information is available from the atmospheric and land surface mod-
361 els on the temperatures of freshwater inputs to the ocean so a number of simplifying as-
362 sumptions are made: the temperatures of rain and snow reaching the ocean are assumed
363 to be that of the SST or the ice surface temperature in the ice-covered areas, the tem-

364 perature of the riverflow is assumed to be that of the SST at the river mouth (except
365 if the latter is negative, in which case riverflow is assumed to be at 0°C). The freshwa-
366 ter flux from iceberg melting is treated as runoff hence the latent heat required to melt
367 the ice is ignored and its temperature is set to the SST. In contrast the freshwater flux
368 from iceshelf melting is treated as ice at 0°C and the latent heat required to melt it is
369 accounted for.

370 The lack of representation of the energy content of precipitation, riverflow and ice-
371 bergs results in energy not being conserved exactly in the model. It should be noted that
372 these are not the only non-energy-conserving processes in the model. A number of subgrid-
373 scale parameterizations in both the ocean (e.g., eddy-induced velocity, convection, hor-
374 izontal momentum mixing, turbulent kinetic energy dissipation), in the atmosphere (e.g.,
375 convection scheme) and at the ocean-atmosphere interface (e.g., wind stress interpola-
376 tion) are not conserving energy exactly. A small lack of energy conservation is not a ma-
377 jor issue as small energy sources and sinks do not prevent the model from equilibrating,
378 at least if the non-conserving terms are stationary. Achieving a more exact energy con-
379 servation is an objective for the next version of our climate model.

380 **2.6 Optional model components**

381 Other model components can be activated in IPSL-CM6A-LR but are neither fur-
382 ther described in this article nor used in the model experiments presented below. These
383 include atmospheric chemistry / aerosol microphysics models such as the INteractions
384 with Chemistry and Aerosols (INCA, Hauglustaine et al., 2014), the REactive Processes
385 Ruling the Ozone BUdget in the Stratosphere (REPROBUS, Marchand et al., 2012), and
386 the Sectional Stratospheric Sulfur Aerosol (S3A, Kleinschmitt et al., 2017) models. Ac-
387 tivation of one of these model components (instead of specifying atmospheric chemical
388 composition and aerosol climatologies) requires a small re-tuning of either the LMDZ6A
389 model or, in the case of S3A, the background stratospheric sulfur budget in order to en-
390 sure a similar baseline climate than in IPSL-CM6A-LR. The coupling of these chemistry
391 and aerosol models with the other model components will be described in forthcoming
392 publications.

2.7 Testing, tuning and evaluation procedure

The model was largely developed and tested under present-day climate using a setup we refer to as a *pdControl* setup, which corresponds to present-day climate forcings with an artificial sink of shortwave radiative energy reaching the ocean surface in order to compensate for the ongoing oceanic heat uptake of the current unequilibrated climate. A number of model features were tuned towards observations (see Hourdin et al. (2017) for the rationale).

The parameters considered during the tuning of the atmospheric model are given in Table 3 of Hourdin, Rio, Grandpeix, et al. (2020). They concern in particular the control of the deep convection scheme, the control of the conversion of clouds condensed water to rainfall, and the control of the vertical dependency of the width of the subgrid-scale water distribution for non convective clouds. A parameter was introduced as well in the “thermal plume” model to control the representation of the transition from cumulus to stratocumulus clouds (Hourdin et al., 2019b; Hourdin, Rio, Jam, et al., 2020). The threshold value for the conversion from liquid cloud water to rainfall as well as a parameter that controls the indirect effect of clouds were used for the final tuning of the global radiative balance because they affect specifically the optical thickness of liquid (low) clouds, thus modifying the total shortwave radiation much more than the longwave.

At some point during the development process, the main development stream switched from a *pdControl* to a *piControl* setup, which corresponds to pre-industrial climate forcings. The spin up lasts several hundreds years but with some evolution of the model physics as the tuning was being finalized. The final tuning process involved changes in parameters associated with the sea ice physical properties (albedo and conductivity), subgrid-scale orography parametrization, and penetration of energy in the upper ocean with and without sea-ice cover. Various options were envisaged as well concerning the control of atmospheric deep convection and its competition with shallow convection. One important choice of the final configuration was to consider boundary-layer convective transport by the “thermal plume model” outside cold pools only. With this choice, thermal plumes see a more unstable environment (since the thermal plume is more stable than the mean column). Thermal plumes are therefore more active, which in turns favors shallow convection compared to deep. The atmospheric deep convection activity over the ocean was modified as well by using a different (larger) value of the horizontal density of cold

425 pools: 1 cold pool per $(33 \text{ km})^2$ over ocean versus 1 per $(350 \text{ km})^2$ over land (note that
426 the parameterization of this cold pool density is currently further tested in more recent
427 versions). The surface drag over the ocean was also modified by introducing a gustiness
428 term computed as a function of the vertical velocity associated with air lifting by the ther-
429 mal plumes and by the gust fronts of cold pools.

430 The model code was then frozen (version 6.1.0) and subsequently altered only for
431 correcting diagnostics or allowing further options and configurations. Versions 6.1.0 to
432 6.1.11 (the current version) are therefore bit-reproducible for a given domain decompo-
433 sition, compiling options and supercomputer.

434 A multi-centennial pre-industrial control was then simulated: 100 years (1750–1850)
435 as the *piControl-spinup* experiment and 2000 years (1850–3849) as the *piControl* exper-
436 iment. It should be noted that the *piControl* experiment suffers from a small cooling drift
437 of $\sim 0.2 \text{ K}$ in 2000 years. A shorter *piControl* experiment of 250 years labelled `r1i2p1f1`
438 was run on the Joliot-Curie supercomputer to check the consistency. A large ensemble
439 (32 members) of *historical* (1850–2014) simulations were performed following the CMIP6
440 protocol. Initial conditions for the *historical* simulations were sampled every 20 or 40
441 years of the *piControl* starting with year 1870 of the *piControl*. The `r1i1p1f1` simula-
442 tion was selected qualitatively among the first ~ 12 available members at the time of se-
443 lection on the basis of a few key observables of the historical period such as the evolu-
444 tion of the global-mean surface air temperature, summer sea ice extent in the Arctic ocean,
445 and annual sea ice volume in the Arctic ocean. The rationale for highlighting a partic-
446 ular member is that we expect many users to only consider `r1i1p1f1` rather than the
447 whole ensemble. A more thorough ongoing analysis of our historical large ensemble shows
448 that other members appear to be closer to the observed record in many respects. Most
449 of the *historical* simulations were prolonged (outside the CMIP6 protocol) to 2059 us-
450 ing SSP245 atmospheric, land use and solar forcings (except for the wood harvest and
451 ozone forcings, not available at the time, which have been kept constant to their 2014
452 values). An ensemble of scenario simulations for 2015–2100 with a few extensions to the
453 year 2300 were also performed following ScenarioMIP guidelines (O’Neill et al., 2016).

2.8 Infrastructure improvements

The IPSL-CM6A-LR model can be extracted, installed and compiled on a specific machine using a suite of scripts called modipsl. Simulations are executed within the bigCM running environment, which can be used to set up and run a simulation on a specific machine through a chain of computing and post-processing jobs. Metadata from the simulations are sent to the Hermes supervising tool which can be used to monitor progress in the simulations and key variables from different simulations can be intercompared using an intermonitoring tool on a dedicated web server (closed access).

The CMIP6 simulations were performed at the Très Grand Centre de Calcul (TGCC) on the Curie supercomputer with a switch during the CMIP6 production in October 2018 to the Joliot-Curie supercomputer. Both a *piControl* and a *historical* simulations initially performed on Curie were repeated on the Joliot-Curie supercomputer to ensure the climate statistics were comparable on both supercomputers. The throughput is about 13 and 16 simulated years per day on Curie and Joliot-Curie, respectively, on 960 processors with the full CMIP6 output.

Outputs from the IPSL-CM6A-LR model are managed by the XML Input/Output Server (XIOS Meurdesoif et al., 2016). For the CMIP6 production, model output variables in native format were kept to the minimum. Instead, and in sharp contrast to CMIP5, the CMIP6-compliant model output has been produced on the fly using XIOS methods from the code. XIOS is driven by XML files describing the whole netCDF file structure (dimensions, attributes, etc.). Such XML files were produced using the *dr2XML* (<https://github.com/rigoudyg/dr2xml>) python library developed by our CNRM-CERFACS collaborators, which translates the CMIP6 Data Request and Controlled Vocabulary (https://github.com/WCRP-CMIP/CMIP6_CVs) into XML files for XIOS. We use *dr2XML* to generate XML files for each simulated year of a given CMIP6 experiment and member. The netCDF time series are created and filled by XIOS all along the simulation to avoid concatenation during post-processing.

A quality assurance is applied at the end of each CMIP6 model simulation. The simulation is validated from a scientific point of view to make sure there is no critical issue or inconsistencies in the diagnostics (e.g., incorrect application of a forcing term, wrong sign, recurring patterns, etc). Each file then undergoes several checks against the CMIP6 controlled vocabulary to ensure its conformance with the CMIP6 Data Refer-

486 ence Syntax (<http://pcmdi.llnl.gov/CMIP6>) in terms of time axis and coverage, vari-
 487 able and global required metadata, filename syntax, etc.

488 The data are then published on the Earth System Grid Federation (ESGF), which
 489 guarantees a strong and effective data management. The *esgprep* toolbox ([http://esgf](http://esgf.github.io/esgf-prepare)
 490 [.github.io/esgf-prepare](http://esgf.github.io/esgf-prepare)) is a piece of software that eases data preparation accord-
 491 ing to CMIP6 conformance. Once a model simulation is validated and checked, the netCDF
 492 files are migrated in the proper CMIP6 directory structure with the *esgprep* commands
 493 in a shared space of the file system. The IPSL hosts an ESGF index with all datasets
 494 from the French climate simulations and a data node to disseminate datasets from the
 495 IPSL climate simulations. The IPSL CMIP6 data sets are published on the ESGF data
 496 node using the usual *esgpublish* command-line provided by the node stack. During the
 497 publication process, the Persistent IDentifier (PID) included in each netCDF file, is per-
 498 manently stored in a dedicated database at the German Climate Computing Centre (DKRZ)
 499 allowing further data citation.

500 **3 Evaluation of present-day climatology**

501 In this section we evaluate the present-day climate of IPSL-CM6A-LR against our
 502 CMIP5 flagship configurations, IPSL-CM5A-LR and IPSL-CM5A-MR, by considering
 503 recent periods (i.e., the 1980–2005 period, when not mentioned otherwise) of our *histor-*
 504 *ical* simulations. The references (i.e., observations and/or reanalyses) used to evaluate
 505 the models generally cover the same period, but may sometimes include some years af-
 506 ter (like ERA-Interim) or before (like WOA13-v2). We argue that not considering the
 507 exact same periods for the simulations and the observations only has a minor impact on
 508 the results given that i) the model internal variability is not synchronized with that of
 509 the observations and ii) large volcanic eruptions are included in the periods considered.
 510 The list of evaluated model variables and datasets against which they are evaluated are
 511 presented in Table 1.

512 Thirty-two members have been performed for the *historical* period. Most of the
 513 diagnostics are not qualitatively sensitive to the choice of the member (when looking es-
 514 sentially at the mean state). We thus use only the first member (**r1i1p1f1**) in the di-
 515 agnostics and illustrate the spread within the ensemble for some of the diagnostics. We
 516 present the most common variables used in climatology (like sea surface temperature,

517 surface air temperature, precipitation etc.) and concentrate on variables that are affected
518 by the coupling between LMDZ, NEMO and ORCHIDEE. Thus we do not repeat the
519 evaluation of variables that are close to those presented in LMDZ6A AMIP paper (Hourdin,
520 Rio, Grandpeix, et al., 2020). There have been numerous developments in the different
521 components of the model; tracing back the evolution of the biases to particular devel-
522 opments requires a well-defined experimental framework (Bodas-Salcedo et al., 2019) and
523 additional simulations which we have not performed. For this reason we focus this study
524 on the evolution of the biases between the IPSL-CM5 and IPSL-CM6 models. The eval-
525 uation starts with surface temperatures (Sea Surface Temperature and Surface Air Tem-
526 perature) and follows with results for the atmosphere, the ocean and the sea ice.

527 **3.1 Sea Surface Temperatures and Surface Air Temperatures**

528 We first evaluate sea surface temperatures (SST) simulated by the model keeping
529 in mind that the average SST between 50°S and 50°N was tuned to fit the observations
530 in the *pdControl* experiment. In this respect it should be noted that, towards the end
531 of the development process, a slightly negative bias in the model SST was deliberately
532 introduced, along with a tuning of some sea ice parameters, to partly compensate for a
533 negative bias in summertime sea ice volume. The overall biases in the SST (Figure 1)
534 have been significantly reduced between the IPSL-CM5A models and IPSL-CM6A-LR.
535 Part of the improvement is due to the fact that IPSL-CM5A-LR was inadvertently tuned
536 too cold. Nevertheless, the improvements are also clear when the mean bias is subtracted
537 (figures not shown). The North Atlantic negative anomaly around 45°N associated with
538 the position of the North Atlantic drift is slightly reduced with a value of -4.3°C in IPSL-
539 CM6A-LR, compared to -6.8°C in IPSL-CM5A-LR (with the value taken as the min-
540 imum temperature from the 60°W–15°W, 40°N–55°N box). For comparison this index
541 ranges from -6.8 to $+2.0^{\circ}\text{C}$ (90% interval) with a median around -3.8°C in CMIP5
542 models, and ranges from -7.1 to $+1.1^{\circ}\text{C}$ (90% interval) with a median around -3.7°C
543 in CMIP6 models. We hypothesize that the increase in horizontal resolution (and the
544 better representation of the ocean topography that comes with it) together with the im-
545 proved atmospheric circulation in LMDZ (notably the influence of the orography) have
546 contributed to improve the oceanic circulation and the resulting SST in the area. The
547 East Boundary warm biases have also been reduced in both extent and amplitude in IPSL-
548 CM6A-LR subsequent to the improvements in the boundary layer humidity and stra-

549 tocumulus clouds in those areas (Hourdin, Rio, Grandpeix, et al., 2020) and to a care-
550 ful tuning of radiative fluxes. Yet this improvement is less clear in the tropical south At-
551 lantic. In addition to global mean and latitudinal variation, the contrast between east-
552 ern tropical basins and the rest of the tropical oceans was used as a target, considering
553 East Tropical Ocean Anomalies (ETOA) defined by Hourdin et al. (2015). A similar at-
554 tention was given to the reduction of the classic latitudinal SST biases, which counter-
555 acts a tendency of the model to produce too cold midlatitude SSTs and a warm bias close
556 to Antarctica (e.g., C. Wang et al., 2014). In the North Pacific, a warm bias (mostly dur-
557 ing summer time) persists over the ocean in IPSL-CM6A-LR. This bias is much less vis-
558 ible in Figure 1 (top and middle panels) because as indicated above, the CMIP5 versions
559 were globally too cold. Relative anomalies show that the North Pacific bias was already
560 present, although slightly weaker. This bias, robust to many tests which were conducted
561 during the tuning phase of the coupled model is also present in other CMIP5 and CMIP6
562 climate models (not shown). Its origin is still to be investigated. The cold bias over the
563 Equatorial Pacific, another classic deficiency of coupled models, is reinforced in IPSL-
564 CM6A-LR.

565 Nevertheless, the SST biases against observations are altogether significantly re-
566 duced, even when comparing to IPSL-CM5A-MR which uses the same atmospheric hor-
567 izontal grid as IPSL-CM6A-LR, with a reduction of the root mean square error (RMSE)
568 from 1.4 to 0.975 and an increase of the correlation coefficient from 0.986 to 0.988. It
569 is difficult to assess the statistical significance of such subtle changes. However it can be
570 noted that the correlation for IPSL-CM5A-MR falls outside of the range from the IPSL-
571 CM6A-LR ensemble members (0.9875 to 0.9885).

572 Consistent with the discussion above, there is a general reduction of the bias in sur-
573 face air temperature (notably over the ocean) from IPSL-CM5A-LR to IPSL-CM6A-LR
574 (see Figure 2). Globally the increase in resolution has surely played a role as can be seen
575 by comparing IPSL-CM5A-LR and IPSL-CM6A-LR. However the difference between IPSL-
576 CM5A-MR and IPSL-CM6A-LR is largely attributable to improvements in the model
577 physics and subsequent improvements in the radiative budget in LMDZ (Hourdin, Rio,
578 Grandpeix, et al., 2020) and a much more systematic and better tuning of the model key
579 parameters in IPSL-CM6A-LR in order to adjust the radiative fluxes.

580 Compared with IPSL-CM5A-MR, the warm bias over the Amazon basin and trop-
581 ical Africa is reduced in IPSL-CM6A-LR. Cheruy et al. (2019) attribute the improve-
582 ment to the reduction of the overestimation of the SW downward radiation at the sur-
583 face. The cold bias over Asia (especially in winter) is stronger in IPSL-CM6A-LR than
584 in IPSL-CM5 models. The changes in the snow albedo in ORCHIDEE are likely to be
585 the cause of this amplification of the bias in comparison to IPSL-CM5A-MR. The new
586 snow scheme improves the realism of the physical properties of the snowpack (albedo,
587 density) in IPSL-CM6A-LR relative to IPSL-CM5A-MR. However, due to strong surface-
588 atmosphere couplings, the larger value of the snow albedo appears to cancel out a pre-
589 vious error compensation (Cheruy et al., 2019) and favours a too strong snow cover in
590 these continental areas. Part of this deficiency in summertime may be explained by the
591 fact that the parameterization of snow albedo does not account for shading effects in moun-
592 tainous regions, a process which is thought to reduce the surface albedo on the scale of
593 a model gridbox. A strong negative bias is indeed observed over the Tibet including dur-
594 ing summertime. A model development to account for the impact of orography on sur-
595 face albedo is planned for a future model version.

596 In the Northern high latitudes the biases have also largely changed, due primar-
597 ily to the revision of the boundary layer scheme which allows more decoupling in sta-
598 ble situations. Modifications in the subgrid-scale orography parameters affecting the at-
599 mospheric circulation, the sea ice model and the land surface scheme also contribute to
600 the change. The warm bias over the Northern part of Canada has been reduced in the
601 annual mean. There is actually some compensation of a warm bias in summer and a cold
602 bias in winter in IPSL-CM6A-LR that replaces a warm bias all year long in IPSL-CM5A-
603 MR (Figure 2). The biases over the Arctic are linked to the position of the sea ice edge
604 and depend to some extent on the member being considered. However, a large warm bias
605 is consistently simulated in winter over the Arctic.

606 Over inland Antarctica, a cold bias can be seen in IPSL-CM6A-LR surface air tem-
607 perature in all seasons. This cold bias is likely to correspond to a warm bias diagnosed
608 in the reanalysis surface temperature from a comparison with weather station data (Fréville
609 et al., 2014; Jones & Lister, 2015) but the magnitude of this cold bias (up to 8 °C) ex-
610 ceeds the warm bias in ERA (up to 5 °C). In LMDZ6, the boundary layer scheme was
611 indeed improved to match the temperatures observed at Dome C (Vignon et al., 2018).
612 LMDZ5 tended to prevent the decoupling of the surface from the atmosphere in very sta-

613 ble conditions (Cheruy et al., 2019). To reach a good agreement with the observations,
 614 the ice sheet albedo was also changed in IPSL-CM6A-LR following Grenfell et al. (1994).

615 Consistent with the reduction in SW radiation bias, the strong warm summer bias
 616 in midlatitudes that was shared by many models participating in CMIP5 (Cheruy et al.,
 617 2014) is reduced in the CMIP6 version. However, it remains present in smaller areas, par-
 618 ticularly on the Southern Great Plains. In these regions the bias results from complex
 619 interactions between the land surface and the atmosphere, especially through convec-
 620 tion (Koster et al., 2004). It is also likely that the lack of parameterization of propagat-
 621 ing mesoscale convective systems that are known to occur frequently in the region, con-
 622 tributes to this bias (Moncrieff, 2019).

623 **3.2 Atmospheric variables**

624 In this section we present the evaluation of a set of common atmospheric variables
 625 –namely surface precipitation and wind, temperature and atmospheric water on zonal
 626 mean diagnostics– and conclude with a set of evaluation metrics obtained with the PCMDI
 627 Metrics Package (PMP, Gleckler et al., 2016).

628 *3.2.1 Atmospheric structure*

629 The zonal mean temperature and zonal wind (Figure 3) show a decrease in the warm
 630 bias over the Antarctic and of the cold bias at 200 mb in the polar vortex at both poles.
 631 The cold bias at midlatitudes between 850 and 400 mb was present in IPSL-CM5A-LR,
 632 vanished in IPSL-CM5A-MR but reappears in IPSL-CM6A-LR. The most striking im-
 633 provement is for the zonal atmospheric circulation (Figure 3, bottom row). The subtrop-
 634 ical jets used to be too close to the Equator in the two CMIP5 IPSL models. The dif-
 635 ference in resolution between IPSL-CM5A-LR and IPSL-CM5A-MR led to only slight
 636 improvements. Despite the same horizontal resolution than IPSL-CM5A-MR, IPSL-CM6A-
 637 LR has a much better zonal circulation with jets moving polewards. This improvement
 638 is mainly due to the changes in the physics of the atmospheric model and the increase
 639 in vertical resolution from 39 to 79 layers.

640 The atmosphere is more humid than in previous models (Figure 4): the specific hu-
 641 midity in IPSL-CM5A (both LR and MR) used to be too low (i.e., corresponding to a
 642 dry bias) in the lower troposphere in the Tropics, and it is now slightly larger (i.e., cor-

643 responding to a wet bias) than in ERA Interim. In terms of relative humidity (RH), IPSL-
 644 CM6A-LR appears to be too saturated compared with ERA Interim between 30° and
 645 60° in latitude (in both hemispheres). The wet RH bias in the free troposphere of the
 646 midlatitudes was already present to some extent in the previous versions. This bias is
 647 known to partly reduce with increasing horizontal resolution as illustrated by the com-
 648 parison of the IPSL-CM5A-LR and IPSL-CM5A-MR versions, as well as the compar-
 649 ison between the LR and HighResMIP horizontal grid in stand-alone atmospheric sim-
 650 ulations with the LMDZ6A version (Hourdin, Rio, Grandpeix, et al., 2020). The main
 651 difference of the IPSL-CM6A-LR version compared to IPSL-CM5A-LR/MR is the much
 652 wetter lower troposphere, at around 800 hPa. This change is related to the parametriza-
 653 tion of the boundary layer transport to the boundary layer top of the air evaporated at
 654 the surface which is much more efficient with the thermal plume model in the IPSL-CM6A-
 655 LR version than with the old eddy diffusion scheme. This contributed to dry the near
 656 surface air over the ocean, in better agreement with observation, but also resulted in a
 657 moist bias in the lower troposphere when compared to ERA Interim. The subgrid-scale
 658 distribution of total (vapour and condensed) water within a grid-box as a function of height
 659 may also play a role in this. This wet bias should be put in relation with the increase
 660 in equilibrium climate sensitivity (ECS) in IPSL-CM6A-LR relative to IPSL-CM5A-LR
 661 and the diagnosed increased contribution of the water vapor feedback to the ECS (see
 662 Section 6).

663 *3.2.2 Surface precipitation*

664 In terms of precipitation, biases are generally consistent between the three model
 665 versions (see Figure 5 for global maps), with the main changes concerning the Tropics
 666 (see Figure 6).

667 The Equatorial Pacific is dryer in IPSL-CM6A-LR, reinforcing a classic bias of cou-
 668 pled model, associated with the above-mentioned negative SST bias. This dry bias, par-
 669 ticularly strong over the Warm Pool, is probably one of the most negative aspect of this
 670 new model version. Preliminary analysis indicates that it may be associated with reduced
 671 surface evaporation as a consequence of the modification of boundary-layer mixing by
 672 the thermal plume model in this region. In contrast, rainfall over the Maritime Conti-
 673 nent is strongly overestimated. This strong overestimation, also present in stand-alone
 674 atmospheric simulations, seems to be related to parameters of the deep convection schemes,

675 in particular those taking different values over ocean and over land, such as the verti-
676 cal velocity at the basis of convective clouds and the density of cold pools. Preliminary
677 analysis suggests that the improvement of the SPCZ seems to be related to the activa-
678 tion of the thermal plume model, and a better representation of the shallow versus the
679 deep convective regimes. Meanwhile, the so-called double ITCZ issue, with overestimated
680 rainfall South of the Equator over the East Pacific, is less pronounced in the new ver-
681 sion. The double ITCZ issue is sometimes associated to entrainment in convective clouds
682 (Oueslati & Bellon, 2013, 2015). The rainfall is altogether reduced over the eastern part
683 of tropical oceans due to the modification of the parameterization of stratocumulus clouds
684 and a careful tuning of the parameters that control precipitation in these clouds.

685 Rainfall is generally increased over semi arid regions like North India, Sahel, Aus-
686 tralia, or around the Mediterranean Sea, in better general agreement with observations.
687 Another major improvement of the new version is the reduction of the strong dry biases
688 over the Amazon basin (as stated above).

689 The global precipitation rate is overestimated in the last version of the model, more
690 than in the previous versions. For CMIP5, the global rainfall was considered as a tar-
691 get of tuning, and a strong effort was done to reduce the mean rainfall, which otherwise
692 was generally overestimated by the IPSL model, as is the case in most global climate mod-
693 els. This target was intentionally abandoned for the tuning of IPSL-CM6A-LR, which
694 explains for a large part the overestimation by 0.3 mm day^{-1} of the global precipitation
695 rate (about 10% of the observed value). This positive bias in the global mean precipi-
696 tation is common to many other models. It cannot be excluded that this overestima-
697 tion is partly due to an underestimation of the observed precipitation rate attributable
698 to an underestimation of light rain over the tropical oceans (Berg et al., 2010; Stephens
699 et al., 2012; Hourdin, Rio, Grandpeix, et al., 2020).

700 ***3.2.3 PMP large-scale summary statistics***

701 This section provides a general synthetic view of the evolution of the climatology
702 of the atmosphere of the IPSL models between CMIP5 and CMIP6. We have used the
703 PCMDI Metrics Package (PMP) to calculate a set of large-scale performance metrics (Gleckler
704 et al., 2008), also called summary statistics, to summarize the agreement between the
705 climate simulated by the model over the recent period and a set of references (observa-

706 tions and reanalysis, as listed in Table 1). Figure 7 shows the results for the most com-
 707 mon atmospheric variables: 2-meter air temperature (tas), surface precipitation (pr), pre-
 708 cipitable water (prw), pressure at sea level (psl), upwelling shortwave (rsut) and long-
 709 wave (rlut) radiation at the top of the atmosphere, cloud radiative effect at top of at-
 710 mosphere on longwave (rltcre) and shortwave (rstcre) radiation, temperature, zonal and
 711 meridional wind at 850 mb (ta850, ua850, va850) and at 200 mb (ta200, ua200, va200),
 712 and geopotential height at 500 mb (zg500).

713 We display the results of the metrics using parallel coordinates plots, which has the
 714 advantage to display raw results and avoid the necessary normalization of the portrait
 715 plot (Gleckler et al., 2008). For the sake of readability, the variables are sorted to dis-
 716 play the results by increasing order of performance for the IPSL-CM5A-MR model. The
 717 individual members of IPSL-CM6A-LR (blue lines) are grouped together, with no sin-
 718 gle ensemble member coming out of the pack. For the large majority of the metrics, the
 719 results for IPSL-CM5A-LR (red line) and IPSL-CM5A-MR (green line) are out of the
 720 spread of the IPSL-CM6A-LR ensemble, demonstrating a difference in climatology that
 721 cannot be explained by internal variability. The Root Mean Squared Error computed
 722 over the globe over the 12 months of the climatological annual cycle (Figure 7, top panel)
 723 has decreased for all variables except for ta_850 and zg_500. For many variables (va_200,
 724 ua_200, psl, va_850, ua_850, rsut, rlut, rstcre and rltcre), the error has considerably de-
 725 creased compared to IPSL-CM5A-MR and is within or at the bottom of the CMIP5 model
 726 range. The global bias has not necessarily decreased for all the variables. The colder at-
 727 mosphere of IPSL-CM6A-LR compared with IPSL-CM5A-MR shown in Figure 3 explains
 728 the higher negative biases for ta_850 and ta_200. For tas, IPSL-CM6A-LR is a little colder
 729 than IPSL-CM5A-MR but still shows the benefits of a better tuning compared with IPSL-
 730 CM5A-LR (which was much colder). The global bias for the meridional wind at 200 mb
 731 (va_200) has also increased (it is more positive), when it is only slightly more negative
 732 at 850 mb (va_850), and much closer to zero for the surface meridional wind (vas). For
 733 zg_500 the bias has increased (it is more negative) due to a general reduction of the al-
 734 titude of the geopotential at this standard level, over the whole globe except the Antarc-
 735 tic (not shown). The global bias for the upwelling shortwave and longwave radiation at
 736 the top of the atmosphere has slightly increased in absolute value (actually close to IPSL-
 737 CM5A-LR). It has not really changed for prw, uas and va_850. The increase in the bi-
 738 ases for ta_850 and zg_500 partly explains the relatively larger RMSE for these variables.

739 The improvement is also striking when looking at the correlation coefficients (Figure 7,
740 bottom panel) with all the variables experiencing higher correlations in terms of their
741 annual mean patterns.

742 **3.3 Oceanic variables**

743 This section evaluates the model in terms of Sea Surface Salinity (SSS), the global
744 vertical temperature profile, the structure of the Atlantic Meridional Overturning Cir-
745 culation (AMOC) and Mixed Layer Depth (MLD), the meridional heat transport and
746 a set of mass transports through key transects (Figures 8–15).

747 **3.3.1 *Sea Surface Salinity***

748 The climatology of SSS shows many evolutions since IPSL-CM5A-LR (see Figure 8).
749 Overall, the SSS is globally reduced. This corresponds to a relative increase of the pre-
750 cipitation in subtropical basins. In the Atlantic Ocean, this translates into a reduction
751 of the positive bias in the subtropics and an increase of the fresh bias in the subpolar
752 latitudes. A SSS decrease is also visible in the South Pacific Ocean and Southern Ocean.
753 The negative bias around Indonesia is corrected in IPSL-CM6A-LR in spite of an over-
754 estimation of precipitation locally. This may be due to enhanced exchanges between the
755 Pacific and the Indian Oceans (see transport in Indonesian Throughflow in Table 2). The
756 North and tropical parts of the Pacific Ocean are a little saltier in IPSL-CM6A-LR com-
757 pared with IPSL-CM5A-MR, which is consistent with the reduction in precipitation in
758 the area.

759 **3.3.2 *Vertical profile of temperature***

760 The vertical profile of temperature as a function of latitude has strongly evolved
761 between IPSL-CM5A and IPSL-CM6A-LR (Figure 9). Overall, biases are larger in IPSL-
762 CM6A-LR as compared to IPSL-CM5A, except to the north of 60°N, where warm anoma-
763 lies are present in all versions. IPSL-CM6A-LR exhibit negative temperature anomalies
764 in the Southern Ocean and globally below 1500 m and positive ones above, except near
765 the surface (see the discussion on SST in Section 3.1). Changes in the Southern Ocean
766 are presumably associated with an increase in the ocean ventilation around Antarctica
767 (Figure 11) and local negative surface air temperature anomalies in winter (Figure 2i).

768 The cold ventilated water masses penetrate the deep ocean globally down to a depth of
 769 2000 m. Above, temperature anomalies are positive, reflecting the fact that the model
 770 is globally warmer in IPSL-CM6A-LR compared to IPSL-CM5A. Furthermore, the model
 771 presumably forms too much mode water, as found in many other climate models (Stouffer
 772 et al., 2017). A cold bias is also visible in the subtropical surface waters, reflecting the
 773 relatively cold SST (see Figure 1). Altogether, this can be interpreted as a stronger (weaker)
 774 thermocline (surface) stratification in midlatitudes in IPSL-CM6A-LR. To what extent
 775 this stronger stratification is an outcome of the tuning of the eORCA1 configuration used
 776 here, or a robust characteristic of the mean state in IPSL-CM6A-LR given the other com-
 777 ponents of the climate model, remains to be clarified.

778 ***3.3.3 Structure of the Atlantic Meridional Overturning Circulation and*** 779 ***Mixed Layer Depth***

780 We now turn to the oceanic general circulation and to the AMOC in particular.
 781 The above-mentioned excessive thermocline stratification at midlatitudes translates into
 782 a pinching of the upper limb of the AMOC in the Atlantic Ocean (Figure 12). Indeed,
 783 at 26°N, the RAPID-WATCH observations suggest a maximum overturning around 1000 m
 784 depth, while it is reached at 700 m depth in IPSL-CM6A-LR. In this respect, the ver-
 785 tical profile was more realistic in IPSL-CM5A configurations, but with a lower magni-
 786 tude. Note that all versions of IPSL-CM exhibit an underestimation of the AMOC max-
 787 imum at 26°N (by about 25% in IPSL-CM6A-LR), a bias that is common to many coarse
 788 resolution climate models in the absence of overflow parametrization (Danabasoglu et
 789 al., 2014). This may in part be explained by the difference in time period used in this
 790 comparison (2004–2017 for the observations as compared to 1980–2005 for the models).
 791 However it is more likely to be due to biases in precipitation in the North Atlantic and/or
 792 the representation of overflows and western boundary currents, which remains a chal-
 793 lenge in climate modelling.

794 The AMOC profile at 26°N also illustrates the excessive volume of cold deep wa-
 795 ter masses that is apparent in Figure 9: the streamfunction changes sign at a depth of
 796 around 2800 m in IPSL-CM6A-LR versus 4500 m in observations. Notwithstanding, the
 797 strength of the deep overturning cell is realistic, and the latitudinal extent of that cell
 798 compares well with previous versions of the model (Figure 13). In particular, the 0-contour
 799 of the AMOC around 2500 m depth, is very horizontal at all latitudes, a characteristic

800 of all three model configurations. Above that contour, the positive AMOC cell, is max-
801 imum around 40°N in IPSL-CM6A-LR, as in previous versions of the model. This max-
802 imum reaches roughly 14 Sv in IPSL-CM6A-LR, which is notably larger than before. This
803 may be related to the fact that dense water production in IPSL-CM6A-LR is different
804 than in previous versions (Figure 10). In IPSL-CM5A, deep mixed layers are found south
805 of Iceland and south of Greenland, which was unrealistic. This bias in IPSL-CM5A is
806 associated to an over extended winter sea ice in the Labrador and Nordic Seas. In IPSL-
807 CM6A-LR, deep mixed layers are confined to the Labrador Sea and the Nordic Seas, which
808 is close to observed locations. Still, when looking at other members of the historical en-
809 semble, it appears clearly that there is substantial variability in the North Atlantic deep
810 convection in this model (Figure 10, the three panels of the bottom row).

811 Deep convection in the Nordic Seas may be directly related to the strengthening
812 of the upper limb of the AMOC in IPSL-CM6A-LR north of 60°N (Figure 13, although
813 the streamfunction at these latitudes were integrated along distorted model grid lines).
814 The northward transport through the Barents opening is also more intense in IPSL-CM6A-
815 LR compared to previous versions, and so is the return flow through the Fram Strait (Ta-
816 ble 2). This can be interpreted as more intense exchanges between the North Atlantic
817 and the Arctic, which is likely to affect sea ice there (see below).

818 In IPSL-CM6A-LR, deep convection in the Southern Hemisphere is also very in-
819 tense, much more than in IPSL-CM5A models. There are important observational un-
820 certainties related to the mixed layer depth estimations (Pellichero et al., 2017). How-
821 ever, this convection is possibly overestimated in IPSL-CM6A-LR (Figure 11). This pro-
822 vides cold water masses that invade the deep ocean and strengthens the meridional den-
823 sity gradients in the Southern ocean, inducing a very strong Antarctic Circumpolar Cur-
824 rent (Table 2, Drake Passage). This constitutes a major difference in barotropic stream-
825 function –and in the overall horizontal circulation– between IPSL-CM5A and IPSL-CM6A-
826 LR (Figure 14).

827 One of the major influence of the ocean to the global climate is through the merid-
828 ional heat transport. This quantity is closer to observations in IPSL-CM6A-LR compared
829 to previous versions (Figure 15a), which is a substantial improvement. However a strong
830 convergence of heat at 40°S remains, a feature which was already present in IPSL-CM5A
831 model versions but is likely to be unrealistic. Direct observations at that latitude are not

832 available, but the common view is that the global meridional heat transport is south-
833 ward in the whole Southern Hemisphere (Trenberth & Caron, 2001), which is not the
834 case in our models. This seems to be related to the strong meridional gradient in den-
835 sity at that latitude, in particular in the Atlantic Ocean, a consequence of excessive mode
836 water formation to the north, as described above. We also see an anomalous northward
837 heat transport at 50°S in IPSL-CM6A-LR, presumably linked to the excessive dense wa-
838 ter formation to the south.

839 In the Northern Hemisphere, the northward heat transport in IPSL-CM6A-LR is
840 larger than in IPSL-CM5A versions. Notwithstanding, the simulated value remains slightly
841 underestimated at the latitude where direct observations are available (24°N). Further
842 north, it is very similar with observations, but this is due to an overestimated contribu-
843 tion from the Pacific Ocean (not shown). This might be partly responsible for the posi-
844 tive SST anomalies found in the north Pacific (Figure 1).

845 In the Atlantic Ocean, the meridional heat transport remains underestimated at
846 all latitudes, particularly at tropical latitudes (Figure 15b). Still, this bias is much re-
847 duced in IPSL-CM6A-LR compared to IPSL-CM5A versions, which presumably contributes
848 to reducing SAT biases over Europe and northern Africa (Figure 2).

849 3.4 Sea ice

850 Arctic sea ice was one of the targets considered during the tuning process (Hourdin,
851 Rio, Grandpeix, et al., 2020). We targeted around 20,000 km³ of pre-industrial annual
852 mean Arctic sea ice volume and ultimately obtained slightly more, typically within a range
853 20,000-25,000 km³, much less than for IPSL-CM5A-LR, but a bit more than in IPSL-
854 CM5A-MR. We also aimed for a seasonal cycle of ice coverage in our *pdControl* exper-
855 iment that was broadly consistent with observations in both hemispheres. The Antarc-
856 tic sea ice volume was not specifically considered during the tuning stage. Overall we
857 obtain a reasonably realistic simulation of sea ice, significantly improved, as compared
858 with IPSL-CM5A-LR.

859 In the Northern Hemisphere, there is less sea ice in IPSL-CM6A-LR than in both
860 IPSL-CM5A models, which typically results in a better agreement with satellite data (Fig-
861 ure 16). The possible causes are a better tuning (Massonnet et al., 2018), higher model
862 resolution, and more elaborated ice-ocean physics (Vancoppenolle et al., 2009; Uotila et

863 al., 2017). Wintertime sea ice extent and area in IPSL-CM6A-LR slightly underestimate
864 satellite retrievals, but is still within observational uncertainty. Regionally, there is a lack
865 of winter sea ice in Okhotsk sea, associated with warm air temperatures, and less ice than
866 observed in Barents Sea. Summertime area and extent are generally lower than observed,
867 but are still within observational uncertainty. Excess summer ice decay occurs on the
868 Siberian Shelf.

869 Looking at both sea ice area and extent, the amplitude of the seasonal cycle ap-
870 pears to be on the high range. The annual mean volume and its seasonal cycle are within
871 the rather wide observational range (Massonnet et al., 2018). There are noticeable sim-
872 ulated decadal fluctuations in sea ice volume.

873 In the Southern Hemisphere, IPSL-CM6A-LR overall improves over both previous
874 CMIP5 models, in particular in summer (Figure 17). Wintertime sea ice extent is over-
875 estimated by 1-2 million square kilometers, sea ice area even more so. This points to the
876 classic high concentration bias of current sea ice models. Summertime extent and area
877 are within uncertainty range. As a result, the amplitude of the seasonal cycle of areal
878 sea ice coverage appears to be somewhat over-estimated. Sea ice volume varies between
879 5,000 to 25,000 km³ with the season in the pre-industrial climate, which is much higher
880 than in our CMIP5 models. It is mostly wintertime sea ice that decreases in the 21st cen-
881 tury. Summertime sea ice also decreases, but less clearly.

882 **3.5 Model evaluation from a CMIP5 point of view**

883 To complement the above evaluation of the model climatology, we now revisit the
884 recommendations for CMIP6 made by Stouffer et al. (2017) based on the results of a sur-
885 vey made after the CMIP5 exercise. One of the main scientific challenges facing the cli-
886 mate modelling community (first reported in Meehl et al. (2014)) is indeed to understand
887 “[...] the origins and consequences of systematic model biases”. Stouffer et al. (2017) listed
888 six main long-lasting (across the various CMIP exercises) model biases from the survey
889 as major points for improvement: 1) the double ITCZ, 2) the Walker circulation, the dry
890 Amazon basin bias and tropical variability, 3) tropical and subtropical low clouds and
891 the East Boundary warm bias, 4) a too deep tropical thermocline, 5) too warm and too
892 dry continental surfaces during summertime, and 6) the position of the Southern Hemi-
893 sphere subtropical jet. In this final subsection of the evaluation of the present-day cli-

894 matology of the model we illustrate how some of these biases evolved between IPSL-CM5A
895 and IPSL-CM6A-LR in order to focus the evaluation of the model on identified prob-
896 lems for the CMIP community.

897 We make use of the diagnostics described in the previous sections along with a set
898 of large-scale evaluation metrics (Figures 18–21) presented in the context of other CMIP5
899 and CMIP6 climate models. Note that only CMIP6 models available on the ESGF at
900 the time of writing this study have been considered. All model outputs were regridded
901 to the same regular $3^\circ \times 2^\circ$ resolution longitude-latitude grid before assessing global
902 mean biases and RMSE against observations. The model ranking shows a consistent but
903 varying improvement of IPSL-CM6A-LR over IPSL-CM5 for the metrics presented on
904 the Figures and discussed below. Some of these metrics have been considered during the
905 tuning process of the model, hence their improvement is expected. This is the case of
906 the radiative metrics (OLR, OSR, Figure 18, and the SW and LW cloud radiative effects,
907 Figure 19) even though the metrics used for the tuning are not exactly the same as those
908 presented here. Indeed it was not the RMSE on the seasonal cycle (considered as met-
909 rics in the multi-model plots) which was used for tuning but rather its latitudinal de-
910 pendency as well as the contrasts between East tropical oceans and the rest of the trop-
911 ics (Hourdin, Rio, Grandpeix, et al., 2020). Most of the tuning procedure aimed at re-
912 ducing the main regional SST biases. Thus the reduced RMSE on the SST is clearly an
913 outcome of the tuning process.

914 The rainfall and position of the jets were not directly considered as tuning targets
915 because the results were seen as reasonable enough from the beginning, but, if it would
916 not have been the case, some additional work or tuning would probably have been done
917 in this direction. Concerning the mean rainfall bias in version IPSL-CM6A-LR, we al-
918 ready mentioned that it was abandoned as a target for tuning, explaining the increased
919 bias compared to IPSL-CM5A and IPSL-CM5B. However, the bias of IPSL-CM6A-LR
920 is only slightly larger than the averaged bias of CMIP6 models. The RMSE has slightly
921 decreased as a result of the combination of regional decreases and increases in the er-
922 rors, as discussed above.

923 Coming back to the six points listed by Stouffer et al. (2017), the following com-
924 ments can be made:

- 925 • Progress made on the double ITCZ, although not a target for tuning, is illustrated
 926 on the maps of annual mean precipitation climatologies on Figure 6 and on the
 927 scores shown on Figure 20. It can be seen that the southern branch of the dou-
 928 ble ITCZ in the eastern part of the Tropical Pacific basin (as well as in the Trop-
 929 ical Atlantic) has weakened in IPSL-CM6A-LR compared to the IPSL-CM5A mod-
 930 els. The scores on Figure 20 (left panel) show the improvement of the Double ITCZ
 931 Pacific Index, with IPSL-CM6A-LR (in red) getting closer to the observed value.
 932 It must be noticed however that this improvement is accompanied by a reinforce-
 933 ment of another classic bias over the Pacific Ocean, consisting in a cold and dry
 934 tongue over the Equator that extends too far west toward the Maritime Continent.
- 935 • Concerning the Walker circulation, the dry Amazon basin bias and tropical vari-
 936 ability, we provide evidence for a reduction of the dry Amazon basin bias in Sec-
 937 tion 3.2.2 and Figure 20. We speculate that the improvement comes from a mix
 938 of better parameterizations of relevant local processes and a more realistic rep-
 939 resentation of the regional patterns of the radiative budget as teleconnections are
 940 known to influence precipitation in tropical South America (L. Yin et al., 2013).
- 941 • The East Boundary warm bias together with subtropical low cloud biases have also
 942 been reduced and are clearly one of the major improvements in IPSL-CM6A-LR
 943 (as noted in section 3.1). This reduction is linked for a large part to the improve-
 944 ment of the representation of cumulus and stratocumulus clouds in LMDZ (Hourdin
 945 et al., 2019b) and to a careful tuning of radiative and latent heat fluxes at the sur-
 946 face over tropical oceans.
- 947 • Concerning the summertime warm bias over continents, IPSL-CM6A-LR shows
 948 almost no improvement against IPSL-CM5A-LR but a pronounced improvement
 949 against IPSL-CM5B-LR (see Figure 2, bottom row). More importantly the warm
 950 bias is much reduced in IPSL-CM6A-LR *amip* simulations for the two regions shown
 951 on Figure 21. It is thus clear that the lack of improvement between IPSL-CM5A-
 952 LR and IPSL-CM6A-LR is due to the general cold bias introduced by the tuning
 953 in the former version. The warm bias is reduced because of an improved –but still
 954 not perfect– shortwave radiative flux at the surface (Cheruy et al., 2014, 2019).
- 955 Over the Southern Great Plains the complexity of land-atmosphere interactions
 956 together with the difficulty to represent the convective activity (Van Weverberg

957 et al., 2018) in relation with the absence of representation of the propagating con-
 958 vection in the present model (Klein et al., 2006) can explain the remaining bias.

- 959 • The improvement to the position of the Southern Hemisphere subtropical jet is
 960 illustrated on Figure 21, with IPSL-CM6A-LR performing better than previous
 961 IPSL-CM5 model versions. The jets, which are located too close to the Equator
 962 in most CMIP models, are known to generally move polewards when the horizon-
 963 tal resolution is increased (Hourdin et al., 2013). This was clearly the case between
 964 the IPSL-CM5A-LR and IPSL-CM5A-MR model versions. However, IPSL-CM6A-
 965 LR –which has the same horizontal grid as IPSL-CM5A-MR– shows a much bet-
 966 ter location of those jets as seen in Figure 3 and, for the Southern Hemisphere,
 967 in Figure 21. We do not have a definite explanation so far, but it may be related
 968 to the much better tuning of the latitudinal dependency of radiative fluxes in IPSL-
 969 CM6A-LR, which in turn controls the thermal structure, itself tightly related to
 970 the zonal wind through the thermal wind balance.

971 4 Modes of variability

972 We now turn to the main modes of variability of the model. We first present the
 973 El Niño Southern Oscillation (ENSO) as it is the dominant coupled ocean-atmosphere
 974 mode of variability, the new behaviour of the ocean multidecadal variability in IPSL-CM6A-
 975 LR and wintertime midlatitude variability and atmospheric blocking. We do not present
 976 the atmospheric modes of variability defined with the leading Empirical Orthogonal Func-
 977 tions of dynamical variables like the North Atlantic Oscillation or the Pacific North Amer-
 978 ica pattern because they are presented in a separate study together with the role of orog-
 979 raphy parameterizations on those modes.

980 4.1 ENSO

981 The El Niño Southern Oscillation (ENSO) is the leading mode of interannual cli-
 982 mate variability, emerging from air-sea interactions in the tropical Pacific, but with cli-
 983 mate impacts worldwide due to atmospheric teleconnections (e.g., Timmermann et al.,
 984 2018). In particular, decadal modulation of ENSO results in decadal fluctuations of the
 985 global-mean surface temperature (GMST), a natural phenomenon that modulates an-
 986 thropogenic climate change (e.g., Kosaka & Xie, 2013). It is thus a very important phe-

987 nomenon to represent in a global climate model. Previous studies have underlined char-
 988 acteristic biases in the representation of the tropical Pacific climate, that translate into
 989 a misrepresentation of some key ENSO processes (e.g., Bayr et al., 2018). Such typical
 990 biases include a too strong equatorial upwelling (“the cold tongue bias”), excessively dry
 991 western equatorial Pacific, and the tendency to form a “double ITCZ”. The cold tongue
 992 and dry western Pacific biases have increased between IPSL-CM5A-LR and IPSL-CM6A-
 993 LR (Figure 1, top and bottom panels, Figure 5a top and bottom panels, Figure 22) but
 994 the “double ITCZ” bias has been reduced, with a South Pacific Convergence Zone that
 995 extends less into the eastern Pacific (Figure 6bd)

996 IPSL-CM5A-LR and IPSL-CM6A-LR reveal relatively similar ENSO pattern evo-
 997 lutions (Figure 22ef), with events that tend to start too early in spring and display west-
 998 ward phase propagation unlike in observations, and end too late the following year (Fig-
 999 ure 22def). The cold and dry equatorial biases in the mean climate result in SST, wind
 1000 and rainfall anomalies that are shifted west relative to those in observations, and too weak
 1001 precipitation anomalies (e.g., Bayr et al., 2018). The amplitude of ENSO has increased
 1002 by $\sim 40\%$ between IPSL-CM5A-LR and IPSL-CM6A-LR (Figure 23), now being slightly
 1003 above the observed value. One of the major issues of ENSO in IPSL-CM5A-LR was its
 1004 seasonality (Bellenger et al., 2014). ENSO events indeed peak in boreal winter in obser-
 1005 vations, but IPSL-CM5A-LR tended to produce a maximum of equatorial Pacific SST
 1006 variability in boreal spring (Figure 23a), due to its tendency to produce events peaking
 1007 in spring in addition to those captured on Figure 22ef. This out of phase behavior has
 1008 disappeared in IPSL-CM6A-LR, but the gap in amplitude between spring and winter
 1009 ENSO signals remains too weak (Figure 23) and below the CMIP5 median.

1010 Overall, some mean-state biases thought to strongly influence ENSO representa-
 1011 tion have diminished (double ITCZ), while others have strengthened (cold tongue and
 1012 dry equatorial biases). The major improvement in ENSO representation between IPSL-
 1013 CM5A-LR and IPSL-CM6A-LR is a better representation of the ENSO seasonality, with
 1014 other aspects of ENSO being quite similar in the two models.

1015 **4.2 Multidecadal variability**

1016 The climate variability at decadal to multidecadal timescales has strongly evolved
 1017 in the latest version of the model (Figure 24 showing 500 years of the *piControl* simu-

1018 lation of each of the model). The Atlantic Multidecadal Variability (AMV) index, de-
1019 fined as the time evolution of the SST anomaly averaged between 0 and 65°N in the North
1020 Atlantic, seems to be dominated by a longer timescale in IPSL-CM6A-LR compared to
1021 both IPSL-CM5A versions (Figure 24, top panel). IPSL-CM5A-LR is indeed character-
1022 ized by a marked bidecadal variability (Escudier et al., 2013; Ortega et al., 2015), also
1023 present, yet with weaker intensity, in IPSL-CM5A-MR (Wen et al., 2016). In the new
1024 model, the typical AMV timescale is much longer: successive peaks in the AMV index
1025 are separated by about 200 years. This bicentennial variability is very robust to small
1026 modifications in the oceanic code (not shown) but weakens towards the end of our 1200
1027 year-long *piControl* simulation. It should be noted that a similar feature is found in at
1028 least another CMIP6 model (CNRM-CM6, Voltaire et al., 2019) that shares the same
1029 ocean model as IPSL-CM6A-LR. Exact origin of this behavior is still under investiga-
1030 tion. The spatial pattern of the AMV (Figure 25) exhibits a strong subpolar center of
1031 action and a relatively weaker tropical one as compared to observations. Note however
1032 that the AMV pattern in HadISST (Figure 25) was computed from the 1920–2016 pe-
1033 riod and the global SST averaged between 60°S and 60°N was removed from all grid points
1034 before computing the North Atlantic average (0°N–60°N, 80°W–0°W) following (Trenberth
1035 & Shea, 2006). Hence this represents variability over a shorter and different period than
1036 the 500 years of the pre-industrial control and possibly still polluted by external forc-
1037 ings in spite of the detrending. The AMV pattern in IPSL-CM6A-LR is also marked by
1038 a relatively clear teleconnection in the Pacific, with a pattern resembling a negative phase
1039 of the Interdecadal Pacific Oscillation (IPO) associated with a positive AMV phase, as
1040 in observations. Both IPSL-CM5A models failed to reproduce this teleconnection.

1041 The difference in the main timescale of variability is also found in the evolution of
1042 the AMOC maximum (Figure 24, middle panel). In IPSL-CM6A-LR, the AMOC has
1043 a predominant variability at centennial timescales, with peak-to-peak amplitude of al-
1044 most 4 Sv. The same index has weaker variability, and predominantly over a shorter timescale,
1045 in IPSL-CM5A versions. The intensity of the Antarctic Circumpolar Current (ACC) mea-
1046 sured at the Drake Passage is also different between IPSL-CM6A-LR and IPSL-CM5A
1047 versions (Figure 24, bottom panel). In IPSL-CM6A-LR, there is a marked periodicity
1048 with an 80-year timescale, with peak-to-peak amplitude of up to 15 Sv. Such a period-
1049 icity is not visible in IPSL-CM5A models, although there seems to be a predominant vari-
1050 ability at a similar timescale. The mechanisms leading to this variability are not yet fully

1051 understood. The AMOC centennial variability seems to be related to freshwater anoma-
 1052 lies building up at very slow timescales in the Arctic Ocean and flushing into the North
 1053 Atlantic Ocean. The links between AMV, AMOC, and ACC variability in IPSL-CM6A-
 1054 LR remain to be investigated.

1055 **4.3 Wintertime midlatitude variability and atmospheric blocking**

1056 Figure 26a shows the frequency of wintertime blocked days in the IPSL models against
 1057 observations. The envelope of blocking frequency from an ensemble of CMIP5 and CMIP6
 1058 models is also reported. Blocking is defined estimating the reversal of the daily geopo-
 1059 tential height gradient at 500 hPa following D’Andrea et al. (1998). With respect to D’Andrea
 1060 et al. (1998) here data is interpolated on a regular $2.5^\circ \times 2.5^\circ$ grid, so that $\Delta = 0^\circ, \pm 2.5^\circ, \pm 5^\circ$
 1061 and $\Phi_n = 80^\circ\text{N}$, $\Phi_0 = 60^\circ\text{N}$, $\Phi_s = 40^\circ\text{N}$. For a comprehensive review on blocking physics and
 1062 climatology, the reader is referred to Woollings et al. (2018). It is particularly pertinent
 1063 to analyse blocking frequency, because it has been a challenging phenomenon to repro-
 1064 duce for Numerical Weather Prediction (NWP) and global climate models alike for a long
 1065 time. Davini and D’Andrea (2016) showed that there has been some improvement over
 1066 generations of models, especially in the Pacific sector. In Europe, on the contrary, only
 1067 a small number of models have blocking frequencies close to observed levels. This gen-
 1068 eral tendency of climate models is by and large confirmed for the CMIP6 generation (see
 1069 the light orange and light blue bands of Figure 26a). IPSL-CM6A-LR simulates more
 1070 blocked days than the two IPSL-CM5 models over Europe ($0\text{--}30^\circ\text{E}$) in better agreement
 1071 with observations, although the frequency of blocked days is still underestimated. In this
 1072 region, IPSL-CM6A-LR remains in line with the average behavior of the other CMIP6
 1073 models. There is a second maximum of blocking frequency at about 70°E , correspond-
 1074 ing to Ural blocking, that is largely overestimated with respect to observations and other
 1075 CMIP5 and CMIP6 models. The Pacific sector is also slightly overestimated.

1076 In order to have a consistent understanding of the model behavior, Figure 26b–g
 1077 gives an overview of the wintertime midlatitude variability of IPSL-CM6A-LR. Differ-
 1078 ence maps with IPSL-CM5A-LR are also shown Figure 26h–l. In the Atlantic sector, the
 1079 midlatitude atmospheric jet is overestimated and too zonal, penetrating deeply into the
 1080 European continent (Figure 26b and e) and carrying the Atlantic stormtrack along (Fig-
 1081 ure 26d and f). This brings about the underestimation of European blocking, and the
 1082 overestimation of the Ural one. Over the Ural, excess low-frequency variability is con-

1083 sistently found (Figure 26d and g). The tendency towards excessively zonal midlatitude
 1084 jets is linked to an underestimation of orographic drag (Pithan et al., 2016). In the Pa-
 1085 cific sector the slight excess of blocking frequency is in agreement with a southward dis-
 1086 placement of the jet (Figure 26b–c) and an excess cyclonic wave breaking (Rivière, 2009)
 1087 at high latitudes, as visible in the variability maps (Figure 26d–g).

1088 Improvements with respect to IPSL-CM5A-LR are clearly visible. The overestima-
 1089 tion of the jet is much reduced in the new model (Figure 26h), which is consistent with
 1090 the increase of blocking frequency in the Euro Atlantic sector. In IPSL-CM5 the jet is
 1091 stronger and penetrates in the Eurasian continent slightly to the south with respect to
 1092 IPSL-CM6A-LR. This causes larger low frequency variability in IPSL-CM5 (Figure 26j)
 1093 in a region spanning the eastern Mediterranean to the low latitudes of the the Siberian
 1094 region. At the same time the southward displacement of the jet explains the absence of
 1095 an overestimation Ural blocking frequency.

1096 **5 Simulations of the historical period**

1097 **5.1 Simulation of global-mean surface temperature**

1098 As a reminder, the members of our ensemble of *historical* simulations have the same
 1099 natural and anthropogenic forcings and differ only in their initial conditions which were
 1100 sampled every 20 to 40 years in the *piControl* simulation. All *historical* simulations have
 1101 been prolonged to 2030 using SSP245 forcings. Because of the large uncertainties in the
 1102 observations before the 1880s, the analysis here is limited to the 1880–2018 period.

1103 Figure 27 shows the time evolution of GMST (here computed from the surface air
 1104 temperature), both in absolute terms and as an anomaly relative to the 1880–2018 pe-
 1105 riod. A large spread is present in both panels, with differences up to 0.75 K for a given
 1106 year. The ensemble mean of the anomaly (Figure 27b) can be interpreted as the forced
 1107 component of climate change (due to natural and anthropogenic forcings) with varia-
 1108 tions around it due to internal natural variability. We compare this anomaly to both the
 1109 Cowtan and Way (2014) and Rohde, Muller, Jacobsen, Muller, et al. (2013); Rohde, Muller,
 1110 Jacobsen, Perlmutter, et al. (2013) observational datasets. The observed GMST time
 1111 series is within the spread of the ensemble simulations but the model ensemble mean qual-
 1112 itatively departs from observed changes around 1935–1945 and since 2005 (Figure 27b).
 1113 The departure from observations for the recent period is slightly enhanced if the anomaly

1114 is computed from the 1850–1899 reference period (not shown). This large range of pos-
1115 sibilities in the GMST evolution of the *historical* members is induced by their different
1116 initial conditions. It is not restricted to interannual variability as the long-term warm-
1117 ing trends also depends on the *historical* member. The observed GMST response to the
1118 Pinatubo volcanic eruption is well represented by the model ensemble mean but there
1119 are large differences in the GMST evolution in the period around the Pinatubo eruption
1120 (i.e., 1990–1994) depending on the phasing of natural modes of variability in the sim-
1121 ulations.

1122 Figure 28 shows the observed and simulated recent warming trends over the 1978–
1123 2018 period. Some members compares better to observations, e.g., with some degree of
1124 “warming hole” in the North Atlantic Ocean. There are however some discrepancies; in
1125 particular there is no member that reproduces the observed cooling trends in the South-
1126 eastern Pacific and the Southern Ocean to their full extent. The model generally repro-
1127 duces the land/sea contrast in warming, with an average ratio of 1.61 (ranging from 1.52
1128 to 1.79) between the global temperature over land and ocean over the 1978–2018 period
1129 compared to the observed ratio of 1.67 from the HadCRUT4 dataset (Morice et al., 2012)
1130 (the model data, SST over ocean and TAS over land, are regridded onto the observations
1131 temporally masked prior to the analysis). The Arctic amplification tends to be overes-
1132 timated by the model, with an average trend of 0.88 K per decade over the 70–90°N re-
1133 gion (ranging from 0.22 to 1.58 K per decade) relative to the global-mean trend of 0.26 K
1134 per decade (ranging from 0.16 to 0.36 K per decade), whereas the trend is about 0.79 K
1135 per decade over the 70–90°N region and about 0.19 K per decade for the global mean
1136 in the Cowtan and Way (2014) dataset. Further work is going on to assess the diversity
1137 of *historical* members of the IPSL-CM6A-LR model and their relevance against obser-
1138 vations.

1139 5.2 Carbon fluxes

The *historical* simulations have prescribed CO₂ atmospheric mixing ratio as per observations (Meinshausen et al., 2017). Global fluxes to the ocean and land can be estimated from the spatially resolved flux calculations of the NEMO-PISCES and ORCHIDEE models in response of atmospheric CO₂ concentration and simulated climate (Figure 29 and Table 3). Compatible emissions are defined as the anthropogenic emissions that would be required to simulate the prescribed CO₂ concentration if the carbon cycle were to be

fully interactive in the model. These compatible emissions can be diagnosed from the following equation:

$$E_{\text{ff}} = E_{\text{tot}} - E_{\text{lcc}} = G_{\text{atm}} + S_{\text{ocean}} + S_{\text{land}} - E_{\text{lcc}} \quad (1)$$

1140 where E_{ff} is the CO₂ emission flux from fossil fuel combustion and cement production,
 1141 E_{tot} is the total anthropogenic CO₂ emission flux, E_{lcc} the CO₂ emission flux due to land
 1142 cover changes (which is also estimated in the model), G_{atm} the growth rate of atmospheric
 1143 CO₂ concentration, S_{ocean} the oceanic sink, and S_{land} the terrestrial sink (not account-
 1144 ing for changes in land cover).

1145 The ocean is a net sink of CO₂ and that sink increases from near-zero in 1850 to
 1146 $\sim 2.9 \text{ PgC yr}^{-1}$ in 2018 with very little variability among the 32 *historical* members (stan-
 1147 dard deviation of $\pm 0.07 \text{ PgC yr}^{-1}$). This simulated oceanic sink is consistent with the
 1148 $2.5 \pm 0.6 \text{ PgC yr}^{-1}$ estimate from the Global Carbon Project for the 2009–2018 decade
 1149 (Friedlingstein et al., 2019). Similarly, the simulated oceanic sink over the 1990–1999 decade
 1150 ($2.1 \pm 0.04 \text{ PgC yr}^{-1}$) is very similar to the 2.2 PgC yr^{-1} flux diagnosed in IPSL-CM5A-
 1151 LR.

1152 The net terrestrial flux remains broadly negative (i.e., a source to the atmosphere)
 1153 until approximately 1970 due to land cover change effects. The flux then increases and
 1154 the land becomes a sink due primarily to the increasing CO₂ fertilisation effect that dom-
 1155 inates the land cover change effect. The net sink reaches 1.5 PgC yr^{-1} in the last decade
 1156 of the *historical* period. It should be noted that, over the 1990–1999 decade, the simu-
 1157 lated sink is very close to that of the IPSL-CM5A-LR model ($1.3 \pm 0.13 \text{ PgC yr}^{-1}$ com-
 1158 pared to $1.28 \pm 0.1 \text{ PgC yr}^{-1}$). The simulated net terrestrial sink is however less than the
 1159 net flux of $2.1 \pm 0.7 \text{ PgC yr}^{-1}$ estimated by (Friedlingstein et al., 2019) for the 2009–2018
 1160 decade. There is also a fairly large year-to-year variability due to climate variability at
 1161 the regional scale (e.g., Schaefer et al., 2002), and a correspondingly large variability
 1162 between the 32 ensemble members. The net terrestrial carbon fluxes, $S_{\text{land}} - E_{\text{lcc}}$, are
 1163 consistent with the Global Carbon Project (Friedlingstein et al., 2019) estimates even
 1164 though the E_{lcc} emissions are underestimated. This leads to simulated compatible emis-
 1165 sions within the range of estimated fossil fuel emissions and cement production, E_{ff} , of
 1166 the Global Carbon Project (Friedlingstein et al., 2019).

1167 6 Transient climate response and equilibrium climate sensitivity

1168 6.1 Estimates

1169 Transient climate response (TCR) and equilibrium climate sensitivity (ECS) are
 1170 two important quantities that characterize the model response to the CO₂ radiative forc-
 1171 ing. There is increasing awareness however that these quantities are not intrinsic prop-
 1172 erties to the climate system (or to a given climate model) but may depend on the cli-
 1173 mate state (Mauritsen et al., 2019; Rugenstein et al., 2020). Furthermore estimates of
 1174 these quantities depend on the details of how they are estimated in a particular model.

1175 The equilibrium climate sensitivity (ECS) is traditionally defined as the equilib-
 1176 rium global-mean surface temperature change for a CO₂ doubling. We follow Gregory
 1177 (2004) to estimate an effective ECS by assuming a linear –or quasi-linear– forcing-feedback
 1178 relationship between the anomalies of the net downward radiative flux at the top of the
 1179 atmosphere ΔR and the global mean surface air temperature ΔT to a giving forcing F ,
 1180 and extrapolating ΔT to its value for $\Delta R = F + \lambda\Delta T = 0$, where λ is the feedback
 1181 parameter.

1182 To calculate these radiative and temperature anomalies, we subtract the pre-industrial
 1183 global-mean value of the net downward radiative imbalance and near-surface air tem-
 1184 perature ('rtmt' and 'tas', respectively, from the first 500 years of the pre-industrial con-
 1185 trol run, 1850-2350) from the respective radiative and temperature values from the *abrupt2xCO2*
 1186 and *abrupt-4xCO2 r1i1p1f1* experiments. Results are sensitive to the length of the sim-
 1187 ulation because of the spatial and temporal dependence of the feedback parameters (Andrews
 1188 et al., 2012, 2015; Knutti et al., 2017; Rugenstein et al., 2020). An ordinary least squares
 1189 regression of the radiative imbalance on temperature anomalies results in equilibrium
 1190 ΔT for CO₂ quadrupling of 9.05, 9.49 and 10.02 K depending on whether 150, 300 or
 1191 900 years of simulation are considered (Table 4). This translates into an ECS of 4.75 K
 1192 (95% confidence interval: [4.32, 5.20]) when the fit is performed on 300 years and a fac-
 1193 tor two is used to scale a quadrupling to a doubling CO₂ as per the usual assumption
 1194 of a logarithmic dependence of the CO₂ radiative forcing on its atmospheric mixing ra-
 1195 tio. This corresponds to a 17% increase from the value of 4.06 K in IPSL-CM5A-LR (95%
 1196 confidence interval: [3.73, 4.41]), estimated by the same method (Table 4).

1197 The factor two scaling from $4\times\text{CO}_2$ to $2\times\text{CO}_2$ can be questioned because: i) the
 1198 CO_2 forcing is supra-logarithmic in the atmospheric CO_2 concentration as shown by Zhong
 1199 and Haigh (2013) and Etminan et al. (2016) for detailed radiative transfer models and
 1200 Lurton et al. (2019) for our climate model; and ii) feedback parameters may depend on
 1201 the forcing magnitude. In our model the effective radiative forcings (ERF) for CO_2 dou-
 1202 bling and quadrupling are 3.46 and 7.53 W m^{-2} , respectively (Lurton et al., 2019). Renor-
 1203 malizing the surface temperature change extrapolated in the CO_2 quadrupling with the
 1204 estimated ERF values leads to a reduced ECS for a CO_2 doubling of 4.35 K . This is to
 1205 be compared to an ECS of 3.83 K if the regression is performed directly on the 300-year
 1206 *abrupt2xCO2* experiment. This last value may correspond better to the original defini-
 1207 tion of the ECS.

1208 The transient climate response (TCR) is defined as the temperature change at the
 1209 time of CO_2 doubling in an experiment where the CO_2 atmospheric concentration in-
 1210 creases by 1% per year. More specifically it is computed as the twenty-year global av-
 1211 erage in the 2-meter surface temperature around the time of CO_2 doubling (years 61 to
 1212 80) in the *1pctCO2* experiment relative to the same quantity in the corresponding pe-
 1213 riod of the *piControl*. TCR amounts to 2.45 K in IPSL-CM6A-LR against published val-
 1214 ues of 2.09 , 2.05 and 1.52 K in IPSL-CM5A-LR, IPSL-CM5B-LR and IPSL-CM5B-MR,
 1215 respectively (Dufresne et al., 2013). Thus the larger ECS in IPSL-CM6A-LR also trans-
 1216 lates into a larger TCR in comparison to our previous generation of models.

1217 **6.2 Differences in ECS between IPSL-CM5A-LR and IPSL-CM6A-LR**

1218 As discussed above, the effective ECS increases from 4.1 to 4.8 K between IPSL-
 1219 CM5A-LR and IPSL-CM6A-LR. The relative contributions to ECS are calculated fol-
 1220 lowing Dufresne and Bony (2008) and Vial et al. (2013) and illustrated in the bar plots.
 1221 This method decomposes the contributions to ECS into i) rapid tropospheric and strato-
 1222 spheric adjustments to carbon dioxide and ii) temperature-mediated feedbacks operat-
 1223 ing on longer timescales. More specifically the rapid tropospheric adjustment includes
 1224 the climate response associated with all tropospheric adjustments (temperature, water
 1225 vapor, and clouds), surface albedo change, and the small land surface warming due to
 1226 the CO_2 forcing (Vial et al., 2013). The method also quantifies the relative contributions
 1227 of the water vapor and temperature lapse rate, surface albedo, and cloud feedbacks. In-
 1228 dividual feedbacks are calculated by the radiative kernel method (Bony et al., 2006; So-

den et al., 2008; Shell et al., 2008). A radiative kernel acts as a partial derivative, representing the sensitivity of the radiative flux to changes in a climate variable, such as water vapor, temperature, and surface albedo. The radiative kernel is multiplied by the change in the climate variable of interest (i.e., water vapor) diagnosed from a model simulation and then normalized by the GMST change to produce the feedback value. We employ the same kernels as in Shell et al. (2008) for water vapor, temperature, and surface albedo. The cloud feedback is calculated as a corrected residual term, correcting for a cloud-masking term (Vial et al., 2013), which adds a consistent offset to net cloud feedback value estimated from the cloud radiative effect method (Andrews et al., 2012). A small residual term reflects nonlinearities in the relationship between radiative perturbation and the temperature response.

The main drivers of this larger ECS in IPSL-CM6A-LR are more positive rapid tropospheric adjustment to CO₂, and a stronger combined lapse rate and water vapor feedback (Figure 30a). We diagnose the strong tropospheric adjustment from *aqua-4xCO2* and *amip-4xCO2* simulations, as well as the *abrupt-4xCO2* simulations, and find that the stronger adjustments come from clear-sky regimes (not shown). The stronger water vapor feedback primarily results from strong moistening tendencies in weak ascent regimes around 500 hPa (Figure 30c). We diagnose this moistening tendency in weak ascent regimes by projecting the relative humidity anomalies, defined as the difference between relative humidity after 150 years of the *abrupt-4xCO2* simulation and the *pi-Control*, into a circulation regime basis, wherein ω_{500} , the vertical pressure velocity at 500 hPa, acts as a proxy for the large-scale tropical circulation (Bony et al., 2004). This framework introduced by Bony et al. (2004) allows for attribution of changes in a climate variable to a given tropical circulation regime, ranging from strong ascent to strong subsidence regimes with increasing ω_{500} values. Relative humidity anomalies reach up to 15% in these weak ascent regimes. However, it has also been shown that the IPSL-CM6A-LR model is too moist in the tropical atmosphere compared with ERA-Interim data (see Figure 4) which suggests this moistening might be exaggerated as well.

The net cloud feedback, in contrast, is less positive in IPSL-CM6A-LR than in the previous model version. Compensating positive and negative feedbacks in the tropics give rise to a less positive tropical cloud feedback. Plotted in Figure 30b is the spatial distribution of the net global cloud feedback, calculated from the kernel method, in W m⁻² per K of GMST. A positive, warming feedback is in red, while a negative, stabilizing feed-

back is in blue. This feedback map demonstrates that the cloud response in IPSL-CM6A-LR is spatially heterogeneous, with large swathes of the tropical ocean covered in positive or negative cloud feedbacks. To interpret the spatial discontinuity between the regions of positive and negative cloud feedbacks, we project the net cloud feedback in the Tropics onto the ω_{500} basis, analogous to what was done for relative humidity anomalies. Based on the decomposition, the regions of positive cloud feedback can be linked to weak ascent regimes $[-20, 0 \text{ hPa day}^{-1}]$ and moderate to strong subsidence regimes $[25, 100 \text{ hPa day}^{-1}]$ (Figure 30d). By contrast, negative net cloud feedbacks arise in deep convective regimes and a portion of weak subsidence regimes. Moreover, we divide the net cloud feedback into SW and LW components to see whether the SW or LW component drives the net cloud feedback in particular regimes. In convecting regimes, the net cloud feedback more closely tracks the negative, LW cloud feedback, while in subsiding regimes, the net cloud feedback more closely follows the positive, SW cloud feedback (Figure 30d). The cloud feedback map shows that, geographically, positive values are found in regions of large-scale subsidence, which cover large parts of the tropical ocean and are associated with marine boundary-layer cloud such as stratocumulus and shallow cumulus (Bony & Dufresne, 2005). By contrast, negative cloud feedback values occur in regions of deep convection, such as the Western Pacific Warm Pool. A negative feedback also occurs over the Southern Ocean, which could result from phase changes or thermodynamic changes with warming (Ceppi et al., 2016).

1282 **7 Future scenarios**

1283 **7.1 Change in surface temperature**

1284 We now briefly present and discuss some results from the scenario simulations. The
 1285 time evolution of the global-mean surface air temperatures are shown on Figure 31. The
 1286 temperature change in 2100 relative to 1850-1900 is larger than 2°C in all scenarios ex-
 1287 cept the SSP119 where it overshoots 2°C before returning to below 2°C . It should be
 1288 noted that the temperature change trajectory is very similar for all scenarios until circa
 1289 2040 when it starts to diverge according to the emission trajectory. This highlights the
 1290 long timescales associated with the carbon cycle and the climate system (Collins et al.,
 1291 2013). We also compare on Figure 31 the IPSL-CM5A-LR and IPSL-CM6A-LR mod-
 1292 els recognizing that the RCP and SSP scenarios are not fully equivalent as the repar-
 1293 titution of the total net radiative forcing between the different terms has changed (Lurton

1294 et al., 2019). IPSL-CM6A-LR shows more warming than IPSL-CM5A-LR for the high-
 1295 end scenarios (RCP245 / SSP245, RCP6.0 / SSP460, RCP8.5 / SSP585). This is expected
 1296 from the larger TCR and ECS in IPSL-CM6A-LR. More surprising is the larger warm-
 1297 ing in IPSL-CM5A-LR for the historical period, which we attribute to a number of small
 1298 differences in ERF. More specifically, the CO₂ ERF is smaller (1.59 vs 1.83 W m⁻² in
 1299 2015), and on the contrary the ERF of the non-CO₂ greenhouse gases (CH₄, CFCs, N₂O,
 1300 O₃) is larger (1.58 vs 1.03 W m⁻² in 2015) in IPSL-CM5A-LR compared to IPSL-CM6A-
 1301 LR. The ERF for the anthropogenic aerosols is approximately the same for the two model
 1302 (≈ -0.6 W m⁻²). Assuming that the climate feedback parameter and the ocean heat up-
 1303 take efficiency are the same in the *historical* and *1pctCO2* experiments, we can indeed
 1304 expect more warming in IPSL-CM5A-LR for the historical period compared to IPSL-
 1305 CM6A-LR (1.61 vs 1.43 K) despite a smaller TCR (2.09 vs 2.45 K).

1306 **7.2 Distribution of temperature and precipitation changes**

1307 Figure 32 shows the distributions of changes in surface air temperature normalised
 1308 by the GMST change, for the SSP126 and SSP585 *scenario* experiments, both for the
 1309 end of the 21st century (2070–2100 period), and at the end of the 23rd century (2270–
 1310 2300, extended scenario runs). The normalised changes are defined relative to a 100-year
 1311 pre-industrial average. The patterns of change are quite similar for SSP126 and SSP585
 1312 at the end of the 21st century. In contrast, at the end of the 23rd century, patterns dif-
 1313 fer more between the two scenarios: SSP126 shows an Arctic warming pattern quite sim-
 1314 ilar to that of 2100, whereas the relative warming for this region in the SSP585 scenario
 1315 is less severe. However, SSP585 in 2300 shows an overall stronger warming in the South-
 1316 ern Hemisphere (if we average values on both hemispheres, we have a Northern Hemi-
 1317 sphere to Southern Hemisphere ratio of 1.13:0.87 for SSP585, versus 1.24:0.76 for SSP126),
 1318 and its global patterns are more homogeneous than for the SSP126 scenario. The for-
 1319 mer shows more warming over the Southern Ocean while the latter exhibits a noticeable
 1320 cold spot in the Southern Pacific Ocean.

1321 For precipitation, the patterns at the end of the 21st century are similar in both
 1322 SSP126 and SSP585 scenarios, but they tend to differ more at the end of the 23rd cen-
 1323 tury, with a somewhat smoother precipitation signature on some of the equatorial re-
 1324 gion for the SSP585 experiment (Figure 33).

1325 7.3 Changes in sea ice

1326 We observe a rather large response of sea ice to the 21st century anthropogenic forc-
 1327 ings, much larger than in IPSL-CM5A-LR. Summertime Arctic sea ice extent (Figure 16)
 1328 responds more to changes in global mean temperature (Notz et al., 2020). The simulated
 1329 loss rate per °C of global mean temperature change in IPSL-CM6A-LR (-3.39 ± 0.87
 1330 $\times 10^6 \text{ km}^2 \text{ K}^{-1}$) has largely increased in comparison to IPSL-CM5A-LR (-1.48 ± 0.43
 1331 $\times 10^6 \text{ km}^2 \text{ K}^{-1}$) and IPSL-CM5A- MR ($-1.67 \pm 0.87 \times 10^6 \text{ km}^2 \text{ K}^{-1}$). This is consis-
 1332 tent with the near-zero summer Arctic sea ice extent for all scenarios in IPSL-CM6A-
 1333 LR – a feature that is shared with the majority of CMIP6 models. It is also remarkable
 1334 that winter sea ice almost disappears by 2100 in the fossil-fuel intensive scenario (SSP585),
 1335 which some of the other CMIP6 models also predict. Possible causes for this greater sen-
 1336 sitivity, which should be further investigated, include the warm winter Arctic atmosphere,
 1337 an ocean heat supply, changes in aerosol forcing, and ice drift. The ice volume loss starts
 1338 in the early 20th century and accelerates in its last three decades of the century. This
 1339 is followed by a steady decrease over the 21st century. In the Southern Ocean (Figure 17),
 1340 it is mostly winter sea ice that decreases in the 21st century. Summer sea ice also decreases,
 1341 but less clearly so.

1342 7.4 Changes in carbon fluxes

1343 The land and oceanic net carbon fluxes for the scenarios are shown on Figure 29.
 1344 The oceanic carbon uptake is projected to increase or decrease according to the scenario
 1345 being considered, with a clear saturation occurring at large CO₂ concentrations (e.g., SSP585
 1346 and SSP460) and a decrease in the sink when the atmospheric CO₂ levels off or decreases.
 1347 The net land carbon uptake peaks at about 3 PgC yr⁻¹ between 2020 and 2060 in all
 1348 scenarios before returning to near-zero, or even negative, values. The downregulation of
 1349 the maximum photosynthetic capacity that was implemented to account for the impact
 1350 of nutrient limitation on the CO₂ fertilization effect (see section 4.2) may overestimate
 1351 the limitation effect when atmospheric CO₂ concentration goes over 700 ppm (mainly
 1352 after 2050) and thus may explain this extreme behavior at the end of the century. The
 1353 formulation was chosen to broadly reproduce the change in gross primary production ob-
 1354 served at Free Air Enrichment experiment when CO₂ is doubled (FACE, Norby & Zak,
 1355 2011) but we overlooked the responses at very high CO₂ concentrations. A new parametriza-
 1356 tion is being designed and implemented as an option in the model.

1357 8 Conclusions

1358 We have described the main features of the IPSL-CM6A-LR climate model which
 1359 has been developed at IPSL for CMIP6. We discuss the implementation of climate forc-
 1360 ings in the model in Lurton et al. (2019) and will discuss the development philosophy
 1361 and methodology in a future paper. In comparison to the previous generation of IPSL
 1362 model several improvements have been introduced to the model: more physically-based
 1363 parameterizations (e.g., Hourdin, Rio, Grandpeix, et al., 2020), more realistic implemen-
 1364 tation of some forcings (e.g., stratospheric aerosols), and more systematic tuning of ad-
 1365 justable parameters with a view to simulate key aspects of the model’s climatology (SST,
 1366 AMOC, and Arctic sea ice). The IPSL-CM6A-LR model performance is significantly im-
 1367 proved over IPSL-CM5A-LR and IPSL-CM5A-MR and compares well to other published
 1368 CMIP6 models for a number of metrics. However some systematic regional biases and
 1369 shortcomings persist (e.g., double ITCZ, frequency of midlatitude wintertime blockings,
 1370 and ENSO dynamics).

1371 The effective ECS (computed from a 300-year regression on *abrupt-4xCO2* and di-
 1372 vided by a factor 2) increases from 4.1 to 4.8 K between IPSL-CM5A-LR and IPSL-CM6A-
 1373 LR. The TCR correspondingly increases from 2.1 to 2.4 K. The increased ECS is due
 1374 to increased contributions from tropospheric rapid adjustments and the combined lapse
 1375 rate and water vapour feedback, which are only partly compensated by less positive cloud
 1376 feedbacks.

1377 A grand ensemble of 32 *historical* members has been performed with IPSL-CM6A-
 1378 LR. The global mean surface air temperature increase simulated by the model is in the
 1379 range 1.1 to 1.6 K in 2014 relative to 1850–1899 (across the ensemble members). While
 1380 the ensemble mean warms more than the observations, some members are more consis-
 1381 tent with observations. The IPSL-CM6A-LR shows a 1.6 to 6.8 K warming in 2100 across
 1382 the scenarios relative to the same 1850-1899 period. The IPSL-CM6A-LR model exhibits
 1383 a sea-ice response to 21st century climate forcings on the high range in comparison to
 1384 other CMIP5 and CMIP6 models.

1385 A range of other papers in the Special collection further evaluate particular aspects
 1386 of the IPSL-CM6A-LR model. A comprehensive assessment of the model will require a
 1387 lot more work in the coming years. We expect this to take place in the context of the

1388 CMIP6 multi-model ensemble on the basis of the vast amount of data we have published
1389 on the Earth System Grid Federation.

1390 **Author contribution**

1391 Both JS and OB coordinated the writing of this article. JD, CE and GM wrote the
1392 NEMO description section. FH wrote the LMDZ description section. PP, PC, AD, NVu
1393 and FC wrote the ORCHIDEE description section. OB, JD and OM wrote the model
1394 coupling description section. GL, ArC and JG wrote the infrastructure description sec-
1395 tion. JS and FH performed the evaluation of the model climatology for atmospheric vari-
1396 ables and wrote the corresponding sections. FC, JS and FH performed the evaluation
1397 of the model climatology for land surface variables and wrote the corresponding sections.
1398 JM, JS, JD and GG performed the evaluation of the model climatology for the oceanic
1399 variables and wrote the corresponding sections. MV performed the evaluation and wrote
1400 the sea ice section. JerV performed the evaluation and wrote the ENSO section. FDA
1401 and PD performed the analysis of atmospheric blockings. FH performed the performance
1402 analysis across the CMIP5/CMIP6 models. TL performed the CO₂ radiative forcing cal-
1403 culations. ANA conducted the ECS and feedback analysis, with tools developed by JesV
1404 and SaB. RB performed the analysis of the historical ensemble. PC performed the anal-
1405 ysis of the carbon fluxes and PC, OB and NVu wrote the corresponding section. TL per-
1406 formed the analysis and wrote the section on future scenarios. OB coordinated the IPSL-
1407 CM6A-LR model development. All other authors contributed to the model development,
1408 the modelling infrastructure, the CMIP6 experiments, data processing and/or data dis-
1409 tribution.

1410 **Competing interests**

1411 The authors do not declare any competing interests.

1412 **Acknowledgments**

1413 The authors are grateful to the developers of the OASIS software and the Earth System
1414 model components not in the author list. This work was undertaken in the framework
1415 of the L-IPSL LABEX and the IPSL Climate Graduate School EUR. As such it bene-
1416 fitted from the French state aid managed by the ANR under the “Investissements d’avenir”
1417 programme with the reference ANR-11-IDEX-0004 - 17-EURE-0006. It also benefited

1418 from Belmont project GOTHAM, under grant ANR-15-JCLI-0004-01, the ANR project
 1419 ARISE under grant ANR-18-CE01-0012, and MOPGA/Investissements d’Avenir project
 1420 Archange, under grant ANR-18-MPGA-0001. The CMIP6 project at IPSL used the HPC
 1421 resources of TGCC under the allocations 2016-A0030107732, 2017-R0040110492 and 2018-
 1422 R0040110492 (project gencmip6) provided by GENCI (Grand Équipement National de
 1423 Calcul Intensif). This study benefited from the ESPRI (Ensemble de Services Pour la
 1424 Recherche l’IPSL) computing and data centre (<https://mesocentre.ipsl.fr>) which
 1425 is supported by CNRS, Sorbonne Université, École Polytechnique and CNES and through
 1426 national and international grants. Support from the European Commission’s Horizon
 1427 2020 Framework Programme is acknowledged, under Grant Agreement number 641816
 1428 for the “Coordinated Research in Earth Systems and Climate: Experiments, kNowledge,
 1429 Dissemination and Outreach (CRESCENDO)” project (11/2015-10/2020) and under Grant
 1430 Agreement number 820829 for the “Constraining uncertainty of multi-decadal climate
 1431 projections (CONSTRAIN)” project. Peter Gleckler and colleagues from the Program
 1432 for Climate Model Diagnosis and Intercomparison (PCMDI) are acknowledged for their
 1433 contribution to the performance metrics package.

1434 **References**

- 1435 Adler, R. F., Sapiano, M. R. P., Huffman, G. J., Wang, J.-J., Gu, G., Bolvin, D., ...
 1436 Shin, D.-B. (2018). The Global Precipitation Climatology Project (GPCP)
 1437 monthly analysis (new version 2.3) and a review of 2017 global precipitation.
 1438 *Atmosphere*, *9*(4), 138. doi: 10.3390/atmos9040138
- 1439 Andrews, T., Gregory, J. M., & Webb, M. J. (2015). The dependence of radiative
 1440 forcing and feedback on evolving patterns of surface temperature change in
 1441 climate models. *J. Clim.*, *28*(4), 1630–1648. doi: 10.1175/JCLI-D-14-00545.1
- 1442 Andrews, T., Gregory, J. M., Webb, M. J., & Taylor, K. E. (2012). Forcing, feed-
 1443 backs and climate sensitivity in CMIP5 coupled atmosphere-ocean climate
 1444 models. *Geophys. Res. Lett.*, *39*(9), L09712. doi: 10.1029/2012GL051607
- 1445 Aumont, O., Ethé, C., Tagliabue, A., Bopp, L., & Gehlen, M. (2015). PISCES-v2:
 1446 an ocean biogeochemical model for carbon and ecosystem studies. *Geophys.*
 1447 *Mod. Dev.*, *8*, 2465–2513. doi: 10.5194/gmd-8-2465-2015
- 1448 Barnier, B., Madec, G., Penduff, T., Molines, J.-M., Treguier, A.-M., Le Sommer, J.,
 1449 ... De Cuevas, B. (2006). Impact of partial steps and momentum advection

- 1450 schemes in a global ocean circulation model at eddy-permitting resolution.
1451 *Ocean Dynamics*, *56*, 543–567. doi: 10.1007/s10236-006-0082-1
- 1452 Bayr, T., Latif, M., Dommenges, D., Wengel, C., Harlaß, J., & Park, W. (2018).
1453 Mean-state dependence of ENSO atmospheric feedbacks in climate models.
1454 *Clim. Dyn.*, *50*, 3171–3194. doi: 10.1007/s00382-017-3799-2
- 1455 Bellenger, H., Guilyardi, E., Leloup, J., Lengaigne, M., & Vialard, J. (2014). ENSO
1456 representation in climate models: from CMIP3 to CMIP5. *Clim. Dyn.*, *42*,
1457 1999–2018. doi: 10.1007/s00382-013-1783-z
- 1458 Berg, W., L'Ecuyer, T., & Haynes, J. M. (2010). The distribution of rainfall over
1459 oceans from spaceborne radars. *J. Appl. Meteorol. Climatol.*, *49*(3), 535–543.
1460 doi: 10.1175/2009JAMC2330.1
- 1461 Bitz, C. M., Holland, M. M., Weaver, A. J., & Eby, M. (2001). Simulating the
1462 ice-thickness distribution in a coupled climate model. *J. Geophys. Res.*, *106*,
1463 2441–2463. doi: 10.1029/1999JC000113
- 1464 Bitz, C. M., & Lipscomb, W. H. (1999). An energy-conserving thermo-
1465 dynamic model of sea ice. *J. Geophys. Res.*, *104*, 15669–15677. doi:
1466 10.1029/1999JC900100
- 1467 Blanke, B., & Delecluse, P. (1993). Low frequency variability of the tropical at-
1468 lantic ocean simulated by a general circulation model with mixed layer physics.
1469 *J. Phys. Ocean.*, *23*, 1363–1388. doi: 10.1175/1520-0485(1993)023<1363:
1470 VOTTAO>2.0.CO;2
- 1471 Bodas-Salcedo, A., Mulcahy, J. P., Andrews, T., Williams, K. D., Ringer, M. A.,
1472 Field, P. R., & Elsaesser, G. S. (2019). Strong dependence of atmospheric
1473 feedbacks on mixed-phase microphysics and aerosol-cloud interactions in
1474 HadGEM3. *J. Adv. Modeling Earth Systems*, *11*(6), 1735–1758. doi:
1475 10.1029/2019MS001688
- 1476 Bony, S., Colman, R., Kattsov, V. M., Allan, R. P., Bretherton, C. S., Dufresne,
1477 J.-L., ... Webb, M. J. (2006). How well do we understand and evalu-
1478 ate climate change feedback processes? *J. Clim.*, *19*, 3445–3482. doi:
1479 10.1175/JCLI3819.1
- 1480 Bony, S., & Dufresne, J.-L. (2005). Marine boundary layer clouds at the heart of
1481 tropical cloud feedback uncertainties in climate models. *Geophys. Res. Lett.*,
1482 *32*, L20806. doi: 10.1029/2005GL023851

- 1483 Bony, S., Dufresne, J.-L., Le Treut, H., Morcrette, J.-J., & Senior, C. (2004). On dy-
1484 namic and thermodynamic components of cloud changes. *Clim. Dyn.*, *22*, 71–
1485 86. doi: 10.1007/s00382-003-0369-6
- 1486 Bony, S., & Emanuel, K. A. (2001). A parameterization of the cloudiness associ-
1487 ated with cumulus convection: Evaluation using TOGA COARE data. *J. At-
1488 mos. Sci.*, *58*, 3158–3183. doi: 10.1175/1520-0469(2001)058<3158:APOTCA>2.0
1489 .CO;2
- 1490 Boone, A., & Etchevers, P. (2001). An inter-comparison of three snow schemes
1491 of varying complexity coupled to the same land-surface model: local
1492 scale evaluation at an Alpine site. *J. Hydrometeorol.*, *2*, 374–394. doi:
1493 10.1175/1525-7541(2001)002<0374:AIOTSS>2.0.CO;2
- 1494 Bouillon, S., Fichefet, T., Legat, V., & Madec, G. (2013). The elastic-viscous-plastic
1495 method revisited. *Ocean Modelling*, *71*, 2–12. doi: 10.1016/j.ocemod.2013.05
1496 .013
- 1497 Cavalieri, D. J., Parkinson, C. L., Gloersen, P., & Zwally, H. J. (1996). *Sea ice
1498 concentrations from Nimbus-7 SMMR and DMSP SSM/I-SSMIS passive mi-
1499 crowave data, version 1* (Tech. Rep.). NASA National Snow and Ice Data
1500 Center Distributed Active Archive Center, Boulder, Colorado, USA. doi:
1501 10.5067/8GQ8LZQVL0VL
- 1502 Ceppi, P., Hartmann, D. L., & Webb, M. J. (2016). Mechanisms of the negative
1503 shortwave cloud feedback in middle to high latitudes. *J. Clim.*, *29*, 139–157.
1504 doi: 10.1175/JCLI-D-15-0327.1
- 1505 Cheruy, F., Ducharne, A., Hourdin, F., Musat, I., Vignon, E., Gastineau, G., . . .
1506 Zhao, Y. (2019). Improved near surface continental climate in ipsl-cm6 by
1507 combined evolutions of atmospheric and land surface physics. *J. Adv. Modeling
1508 Earth Systems*, 2019MS002005, submitted.
- 1509 Cheruy, F., Dufresne, J.-L., At Mesbah, S., Grandpeix, J.-Y., & Wang, F. (2017).
1510 Role of soil thermal inertia in surface temperature and soil moisture-
1511 temperature feedback. *J. Adv. Modeling Earth Systems*, *9*(8), 2906–2919.
1512 doi: 10.1002/2017MS001036
- 1513 Cheruy, F., Dufresne, J.-L., Hourdin, F., & Ducharne, A. (2014). Role of clouds
1514 and land-atmosphere coupling in midlatitude continental summer warm biases
1515 and climate change amplification in CMIP5 simulations. *Geophys. Res. Lett.*,

- 1516 41(18), 6493–6500. doi: 10.1002/2014GL061145
- 1517 Collatz, G. J., Ribas-Carbo, M., & Berry, J. A. (1992). Coupled photosynthesis-
1518 stomatal conductance model for leaves of C4 plants. *Aust. J. Plant Physiol.*,
1519 19, 519–539. doi: 10.1071/PP9920519
- 1520 Collins, M., Knutti, R., Arblaster, J., Dufresne, J.-L., Fichet, T., Friedlingstein, P.,
1521 ... Wehner, M. F. (2013). Long-term climate change: Projections, commit-
1522 ments and irreversibility. In T. F. Stocker et al. (Eds.), *Climate Change 2013*
1523 - *The Physical Science Basis* (pp. 1029–1136). United Kingdom: Cambridge
1524 University Press.
- 1525 Comiso, J. C. (1996). *Bootstrap sea ice concentrations from Nimbus-7 SMMR and*
1526 *DMSP SSM/I-SSMIS, version 3* (Tech. Rep.). NASA National Snow and Ice
1527 Data Center Distributed Active Archive Center, Boulder, Colorado, USA. doi:
1528 10.5067/7Q8HCCWS4I0R
- 1529 Coon, M. D., Maykut, G. A., Pritchard, R. S., Rothrock, D. A., & Thorndike, A. S.
1530 (1974). Modeling the pack ice as an elastic-plastic material. *AIDJEX Bulletin*,
1531 24, 1–105.
- 1532 Cowtan, K., & Way, R. (2014). Coverage bias in the HadCRUT4 temperature se-
1533 ries and its impact on recent temperature trends. *Q. J. R. Meteorol. Soc.*, 140,
1534 1935–1944. doi: 10.1002/qj.2297
- 1535 Danabasoglu, G., Yeager, S. G., Bailey, D., Behrens, E., Bentsen, M., Bi, D., ...
1536 Wang, Q. (2014). North Atlantic simulations in Coordinated Ocean-ice Refer-
1537 ence Experiments phase II (CORE-II). Part I: Mean states. *Ocean Modelling*,
1538 73, 76–107. doi: 10.1016/j.ocemod.2013.10.005
- 1539 D’Andrea, F., Tibaldi, S., Blackburn, M., Boer, G., Déqué, M., Dix, M. R., ...
1540 Williamson, D. (1998). Northern hemisphere atmospheric blocking as simu-
1541 lated by 15 atmospheric general circulation models in the period 1979–1988.
1542 *Clim. Dyn.*, 14(6), 385–407. doi: 10.1007/s003820050230
- 1543 Davini, P., & D’Andrea, F. (2016). Northern hemisphere atmospheric blocking rep-
1544 resentation in global climate models: Twenty years of improvements? *J. Clim.*,
1545 29(24), 8823–8840. doi: 10.1175/JCLI-D-16-0242.1
- 1546 de Boyer Montégut, C., Madec, G., Fischer, A. S., Lazar, A., & Iudicone, D. (2004).
1547 Mixed layer depth over the global ocean: An examination of profile data and
1548 a profile-based climatology. *J. Geophys. Res. Ocean*, 109(C12), C12003. doi:

1549 10.1029/2004JC002378

1550 Dee, D. P., Uppala, S. M., Simmons, A. J., Berrisford, P., Poli, P., Kobayashi, S., ...
 1551 Vitart, F. (2011). The ERA-Interim reanalysis: configuration and performance
 1552 of the data assimilation system. *Q. J. R. Meteorol. Soc.*, *137*(656), 553–597.
 1553 doi: 10.1002/qj.828

1554 de la Cámara, A., & Lott, F. (2015). A stochastic parameterization of the gravity
 1555 waves emitted by fronts and jets. *Geophys. Res. Lett.*, *42*, 2071–2078. doi: 10
 1556 .1002/GL063298

1557 de la Cámara, A., Lott, F., & Abalos, M. (2016). Climatology of the middle
 1558 atmosphere in LMDz: Impact of source-related parameterizations of grav-
 1559 ity wave drag. *J. Adv. Modeling Earth Systems*, *8*(4), 1507–1525. doi:
 1560 10.1002/2016MS000753

1561 de Lavergne, C. (2016). On the lifecycle of Antarctic Bottom Water.

1562 de Lavergne, C., Falahat, S., Madec, G., Roquet, F., Nycander, J., & Vic, C. (2019).
 1563 Toward global maps of internal tide energy sinks. *Ocean Modelling*, *137*, 52–
 1564 75. doi: 10.1016/j.ocemod.2019.03.010

1565 Depoorter, M. A., Bamber, J. L., Griggs, J. A., Lenaerts, J. T. M., Ligtenberg,
 1566 S. R. M., van den Broeke, M. R., & Moholdt, G. (2013). Calving fluxes
 1567 and basal melt rates of antarctic ice shelves. *Nature*, *502*, 89–92. doi:
 1568 10.1038/nature12567

1569 de Rosnay, P., Polcher, J., Bruen, M., & Laval, K. (2002). Impact of a physically
 1570 based soil water flow and soil-plant interaction representation for modeling
 1571 large-scale land surface processes. *J. Geophys. Res.*, *107*(D11), ACL 3-1–ACL
 1572 3-19. doi: 10.1029/2001JD000634

1573 d’Orgeval, T., Polcher, J., & de Rosnay, P. (2008). Sensitivity of the west African
 1574 hydrological cycle in ORCHIDEE to infiltration processes. *Hydrol. Earth Sys-
 1575 tem Sci.*, *12*(6), 1387–1401. doi: 10.5194/hess-12-1387-2008

1576 Dufresne, J.-L., & Bony, S. (2008). An assessment of the primary sources of spread
 1577 of global warming estimates from coupled atmosphere-ocean models. *J. Clim.*,
 1578 *21*, 5135–5144. doi: 10.1175/2008JCLI2239.1

1579 Dufresne, J.-L., Foujols, M.-A., Denvil, S., Caubel, A., Marti, O., Aumont, O., ...
 1580 Vuichard, N. (2013). Climate change projections using the IPSL-CM5 earth
 1581 system model: from CMIP3 to CMIP5. *Clim. Dyn.*, *40*(9), 2123–2165. doi:

1582 10.1007/s00382-012-1636-1

1583 Emanuel, K. A. (1991). A scheme for representing cumulus convection in large-
1584 scale models. *J. Atmos. Sci.*, *48*(21), 2313–2329. doi: 10.1175/1520-0469(1991)
1585 048(2313:ASFRCC)2.0.CO;2

1586 Escudier, R., Mignot, J., & Swingedouw, D. (2013). A 20-year coupled ocean-sea ice-
1587 atmosphere variability mode in the North Atlantic in an AOGCM. *Clim. Dyn.*,
1588 *40*, 619–636. doi: 10.1007/s00382-012-1402-4

1589 Etminan, M., Myhre, G., Highwood, E. J., & Shine, K. P. (2016). Radiative forcing
1590 of carbon dioxide, methane, and nitrous oxide: A significant revision of the
1591 methane radiative forcing. *Geophys. Res. Lett.*, *43*(24), 12614–12623. doi:
1592 10.1002/2016GL071930

1593 Eyring, V., Bony, S., Meehl, G. A., Senior, C. A., Stevens, B., Stouffer, R. J., &
1594 Taylor, K. E. (2016). Overview of the Coupled Model Intercomparison Project
1595 Phase 6 (CMIP6) experimental design and organization. *Geophys. Mod. Dev.*,
1596 *9*, 1937–1958. doi: 10.5194/gmd-9-1937-2016

1597 Farquhar, G. D., Von Caemmerer, S., & Berry, J. A. (1980). A biochemical model
1598 of photosynthetic CO₂ assimilation in leaves of C3 species. *Planta*, *149*, 78–90.
1599 doi: 10.1007/BF00386231

1600 Fouquart, Y., & Bonnel, B. (1980). Computations of solar heating of the Earth's at-
1601 mosphere: a new parametrization. *Contrib. Atmos. Phys.*, *53*, 35–62.

1602 Fox-Kemper, B., Danabasoglu, G., Ferrari, R., Griffies, S. M., Hallberg, W. R., Hol-
1603 land, M. M., ... Samuels, L. B. (2011). Parameterization of mixed layer
1604 eddies. III: Implementation and impact in global ocean climate simulations.
1605 *Ocean Modelling*, *39*, 61–78. doi: 10.1016/j.ocemod.2010.09.002

1606 Fréville, H., Brun, E., Picard, G., Tatarinova, N., Arnaud, L., Lanconelli, C., ...
1607 van den Broeke, M. (2014). Using MODIS land surface temperatures and
1608 the Crocus snow model to understand the warm bias of ERA-Interim reanal-
1609 yses at the surface in Antarctica. *The Cryosphere*, *8*(4), 1361–1373. doi:
1610 10.5194/tc-8-1361-2014

1611 Friedlingstein, P., Jones, M. W., O'Sullivan, M., Andrew, R. M., Hauck, J., Peters,
1612 G. P., ... Zaehele, S. (2019). Global Carbon Budget 2019. *Earth Sys. Sci.*
1613 *Data*, *11*(4), 1783–1838. doi: 10.5194/essd-11-1783-2019

1614 Ganachaud, A., & Wunsch, C. (2003). Large-scale ocean heat and freshwater trans-

- 1615 ports during the World Ocean Circulation Experiment. *J. Clim.*, *16*, 696–705.
 1616 doi: 10.1175/1520-0442(2003)016<0696:LSOHAF>2.0.CO;2
- 1617 Gaspar, P., Grégoris, Y., & Lefevre, J.-M. (1990). A simple eddy kinetic energy
 1618 model for simulations of the oceanic vertical mixing: Tests at Station Papa
 1619 and long-term upper ocean study site. *J. Geophys. Res.*, *95*, 16179–16193.
- 1620 Gent, P. R., & McWilliams, J. C. (1990). Isopycnal mixing in ocean circulation mod-
 1621 els. *J. Phys. Ocean.*, *20*, 150–155. doi: 10.1175/1520-0485(1990)020<0150:
 1622 IMIOCM>2.0.CO;2
- 1623 Gleckler, P., Doutriaux, C., Durack, P., Taylor, K., Zhang, Y., Williams, D., ...
 1624 Servonnat, J. (2016). A more powerful reality test for climate models. *Eos*,
 1625 *97*(12), 20–24. doi: 10.1029/2016eo051663
- 1626 Gleckler, P., Taylor, K., & Doutriaux, C. (2008). Performance metrics for climate
 1627 models. *J. Geophys. Res. Atmos.*, *113*(D6). doi: 10.1029/2007JD008972
- 1628 Goutorbe, B., Poort, J., Lucazeau, F., & Raillard, S. (2011, 12). Global
 1629 heat flow trends resolved from multiple geological and geophysical prox-
 1630 ies. *Geophysical Journal International*, *187*(3), 1405–1419. doi: 10.1111/
 1631 j.1365-246X.2011.05228.x
- 1632 Gouttevin, I., Menegoz, M., Dominé, F., Krinner, G., Koven, C., Ciais, P., ... Boike,
 1633 J. (2012). How the insulating properties of snow affect soil carbon distribution
 1634 in the continental pan-Arctic area. *J. Geophys. Res.*, *117*(G2), G02020. doi:
 1635 10.1029/2011JG001916
- 1636 Grandpeix, J., & Lafore, J. (2010). A density current parameterization coupled
 1637 with Emanuel’s convection scheme. Part I: The models. *J. Atmos. Sci.*, *67*,
 1638 881–897. doi: 10.1175/2009JAS3044.1
- 1639 Grandpeix, J., Lafore, J., & Cheruy, F. (2010). A density current parameterization
 1640 coupled with Emanuel’s convection scheme. Part II: 1D simulations. *J. Atmos.*
 1641 *Sci.*, *67*, 898–922. doi: 10.1175/2009JAS3045.1
- 1642 Gregory, J. M. (2004). A new method for diagnosing radiative forcing and climate
 1643 sensitivity. *Geophys. Res. Lett.*, *31*, L03205. doi: 10.1029/2003GL018747
- 1644 Grenfell, T. C., Warren, S. G., & Mullen, P. C. (1994). Reflection of solar radi-
 1645 ation by the Antarctic snow surface at ultraviolet, visible, and near-infrared
 1646 wavelengths. *J. Geophys. Res.*, *99*, 18669–18684. doi: 10.1029/94JD01484
- 1647 Griffies, S. M., Danabasoglu, G., Durack, P. J., Adcroft, A. J., Balaji, V., Böning,

- 1648 C. W., ... Yeager, S. G. (2016). OMIP contribution to CMIP6: exper-
1649 imental and diagnostic protocol for the physical component of the Ocean
1650 Model Intercomparison Project. *Geophys. Mod. Dev.*, 9(9), 3231–3296. doi:
1651 10.5194/gmd-9-3231-2016
- 1652 Hauglustaine, D. A., Balkanski, Y., & Schulz, M. (2014). Simulation of present
1653 and future nitrate aerosols and their direct radiative forcing of climate. *Atmos.*
1654 *Chem. Phys.*, 14, 11031–11063. doi: 10.5194/acp-14-11031-2014
- 1655 Hibler, W. D. (1979). A dynamic thermodynamic sea ice model. *J. Phys. Ocean.*, 9,
1656 815–846. doi: 10.1175/1520-0485(1979)009<0815:ADTSIM>2.0.CO;2
- 1657 Hourdin, F., & Armengaud, A. (1999). The use of finite-volume methods for
1658 atmospheric advection of trace species. Part I: Test of various formula-
1659 tions in a general circulation model. *Mon. Wea. Rev.*, 127, 822–837. doi:
1660 10.1175/1520-0493(1999)127<0822:TUOFVM>2.0.CO;2
- 1661 Hourdin, F., Couvreur, F., & Menut, L. (2002). Parameterisation of the dry convec-
1662 tive boundary layer based on a mass flux representation of thermals. *J. Atmos.*
1663 *Sci.*, 59, 1105–1123. doi: 10.1175/1520-0469(2002)059<1105:POTDCB>2.0.CO;
1664 2
- 1665 Hourdin, F., Foujols, M.-A., Codron, F., Guemas, V., Dufresne, J.-L., Bony, S., ...
1666 Bopp, L. (2013). Impact of the LMDZ atmospheric grid configuration on the
1667 climate and sensitivity of the IPSL-CM5A coupled model. *Clim. Dyn.*, 40,
1668 2167–2192. doi: 10.1007/s00382-012-1411-3
- 1669 Hourdin, F., Găinuşă-Bogdan, A., Braconnot, P., Dufresne, J.-L., Traore, A.-K., &
1670 Rio, C. (2015). Air moisture control on ocean surface temperature, hidden
1671 key to the warm bias enigma. *Geophys. Res. Lett.*, 42(24), 10,885–10,893. doi:
1672 10.1002/2015GL066764
- 1673 Hourdin, F., Grandpeix, J.-Y., Rio, C., Bony, S., Jam, A., Cheruy, F., ... Roehrig,
1674 R. (2013). LMDZ5B: the atmospheric component of the IPSL climate model
1675 with revisited parameterizations for clouds and convection. *Clim. Dyn.*, 40(9),
1676 2193–2222. doi: 10.1007/s00382-012-1343-y
- 1677 Hourdin, F., Grandpeix, J.-Y., Rio, C., Bony, S., Jam, A., Cheruy, F., ... Roehrig,
1678 R. (2013). LMDZ5B: the atmospheric component of the IPSL climate model
1679 with revisited parameterizations for clouds and convection. *Clim. Dyn.*, 40,
1680 2193–2222. doi: 10.1007/s00382-012-1343-y

- 1681 Hourdin, F., Jam, A., Rio, C., Couvreux, F., Sandu, I., Lefebvre, M.-P., ... Idelkadi,
 1682 A. (2019a). Unified parameterization of convective boundary layer transport
 1683 and clouds with the thermal plume model. *J. Adv. Modeling Earth Systems*,
 1684 *11*(9), 2910–2933. doi: 10.1029/2019MS001666
- 1685 Hourdin, F., Jam, A., Rio, C., Couvreux, F., Sandu, I., Lefebvre, M.-P., ... Idelkadi,
 1686 A. (2019b). Unified parameterization of convective boundary layer transport
 1687 and clouds with the thermal plume model. *J. Adv. Modeling Earth Systems*,
 1688 *11*, 2910–2933. doi: 10.1029/2019MS001666
- 1689 Hourdin, F., Mauritsen, T., Gettelman, A., Golaz, J.-C., Balaji, V., Duan, Q., ...
 1690 Williamson, D. (2017). The art and science of climate model tuning. *Bull. Am.*
 1691 *Meteorol. Soc.*, *98*(3), 589–602. doi: 10.1175/BAMS-D-15-00135.1
- 1692 Hourdin, F., Rio, C., Grandpeix, J.-Y., Madeleine, J.-B., Cheruy, F., Rochetin, N.,
 1693 ... Ghattas, J. (2020). LMDZ6: the improved atmospheric component of
 1694 the IPSL coupled model. *J. Adv. Modeling Earth Systems*, *12*, in press. doi:
 1695 10.1029/2019MS001892
- 1696 Hourdin, F., Rio, C., Jam, A., Traore, A.-K., & Musat, I. (2020). Convective bound-
 1697 ary layer control of the sea surface temperature in the tropics. *J. Adv. Model-*
 1698 *ing Earth Systems*, *12*, in press. doi: 10.1029/2019MS001988
- 1699 Hunke, E. C., & Dukowicz, J. K. (1997). An elastic-viscous-plastic model for sea
 1700 ice dynamics. *J. Phys. Ocean.*, *27*, 1849–1867. doi: 10.1175/1520-0485(1997)
 1701 027(1849:AEVPMF)2.0.CO;2
- 1702 Jam, A., Hourdin, F., Rio, C., & Couvreux, F. (2013). Resolved versus
 1703 parametrized boundary-layer plumes. Part III: Derivation of a statistical
 1704 scheme for cumulus clouds. *Boundary-Layer Meteorol.*, *147*, 421–441. doi:
 1705 10.1007/s10546-012-9789-3
- 1706 Jones, P. D., & Lister, D. H. (2015). Antarctic near-surface air temperatures
 1707 compared with era-interim values since 1979. *Int. J. Climatology*, *35*(7), 1354–
 1708 1366. doi: 10.1002/joc.4061
- 1709 Klein, S. A., Jiang, X., Boyle, J., Malyshev, S., & Xie, S. (2006). Diagnosis of the
 1710 summertime warm and dry bias over the U.S. Southern Great Plains in the
 1711 GFDL climate model using a weather forecasting approach. *Geophys. Res.*
 1712 *Lett.*, *33*(18), L18805. doi: 10.1029/2006GL027567
- 1713 Kleinschmitt, C., Boucher, O., Bekki, S., Lott, F., & Platt, U. (2017). The Sec-

- 1714 tional Stratospheric Sulfate Aerosol module (S3A-v1) within the LMDZ
 1715 general circulation model: description and evaluation against strato-
 1716 spheric aerosol observations. *Geophys. Mod. Dev.*, *10*(9), 3359–3378. doi:
 1717 10.5194/gmd-10-3359-2017
- 1718 Knutti, R., Rugenstein, M. A. A., & Hegerl, G. C. (2017). Beyond equilibrium cli-
 1719 mate sensitivity. *Nature Geoscience*, *10*, 727–736. doi: 10.1038/ngeo3017
- 1720 Kosaka, Y., & Xie, S.-P. (2013). Recent global-warming hiatus tied to equatorial pa-
 1721 cific surface cooling. *Nature*, *501*, 403–407. doi: 10.1038/nature12534
- 1722 Koster, R. D., Dirmeyer, P. A., Guo, Z., Bonan, G., Chan, E., Cox, P., ... Yamada,
 1723 T. (2004). Regions of strong coupling between soil moisture and precipitation.
 1724 *Science*, *305*, 1138–1140. doi: 10.1126/science.1100217
- 1725 Krinner, G., Viovy, N., de Noblet-Ducoudré, N., Ogée, J., Polcher, J., Friedlingstein,
 1726 P., ... Prentice, I. C. (2005). A dynamic global vegetation model for studies
 1727 of the coupled atmosphere-biosphere system. *Global Biogeo. Cycles*, *19*(1),
 1728 GB1015. doi: 10.1029/2003GB002199
- 1729 Lengaigne, M., Madec, G., Bopp, L., Menkes, C., Aumont, O., & Cadule, P. (2009).
 1730 Bio-physical feedbacks in the Arctic Ocean using an Earth System model. *Geo-*
 1731 *phys. Res. Lett.*, *36*, L21602. doi: 10.1029/2009GL040145
- 1732 Levier, B., Tréguier, A.-M., Madec, G., & Garnier, V. (2007, may). *Free surface and*
 1733 *variable volume in the NEMO code* (Tech. Rep.). European Union: Marine En-
 1734 vironment and Security for the European Area (MERSEA) Integrated Project.
 1735 doi: 10.5281/zenodo.3244182
- 1736 Lipscomb, W. H. (2001). Remapping the thickness distribution in sea ice models. *J.*
 1737 *Geophys. Res.*, *106*, 13989–14000. doi: 10.1029/2000JC000518
- 1738 Locarnini, R., Mishonov, A., Antonov, J., Boyer, T., Garcia, H., Baranova, O., ...
 1739 Seidov, D. (2013). *World ocean atlas 2013, volume 1: Temperature* (Tech.
 1740 Rep.). NOAA Atlas NESDIS 73.
- 1741 Loeb, N., Doelling, D., Wang, H., Su, W., Nguyen, C., Corbett, J., ... S., K. (2018).
 1742 Clouds and the Earths Radiant Energy System (CERES) Energy Balanced and
 1743 Filled (EBAF) top-of-atmosphere (TOA) edition-4.0 data product. *J. Clim.*,
 1744 *31*, 895–918. doi: 10.1175/JCLI-D-17-0208.1
- 1745 Lott, F., & Guez, L. (2013). A stochastic parameterization of the gravity waves due
 1746 to convection and its impact on the Equatorial stratosphere. *J. Geophys. Res.*,

- 1747 118, 8897–8909. doi: 10.1002/jgrd.50705
- 1748 Lurton, T., Balkanski, Y., Bastrikov, V., Bekki, S., Bopp, L., Brockmann, P., ...
 1749 Boucher, O. (2019). Implementation of the CMIP6 forcing data in the
 1750 IPSL-CM6A-LR model. *J. Adv. Modeling Earth Systems, submitted*. doi:
 1751 2019MS001940
- 1752 Madec, G., Bourdallé-Badie, R., Bouttier, P., Bricaud, C., Bruciaferri, D., Calvert,
 1753 D., & Vancoppenolle, M. (2017). NEMO ocean engine (version v3.6). *Notes*
 1754 *du Pôle de modélisation de l'Institut Pierre-simon Laplace (IPSL)*. doi:
 1755 10.5281/zenodo.1472492
- 1756 Marchand, M., Keckhut, P., Lefebvre, S., Claud, C., Cugnet, D., Hauchecorne, A.,
 1757 ... Bekki, S. (2012). Dynamical amplification of the stratospheric solar re-
 1758 sponse simulated with the Chemistry-Climate Model LMDz-Reprobus. *J.*
 1759 *Atmos. Solar-Terr. Phys., 75–76*, 147–160. doi: 10.1016/j.jastp.2011.11.008
- 1760 Marti, O., Braconnot, P., Dufresne, J.-L., Bellier, J., Benschila, R., Bony, S., ...
 1761 Talandier, C. (2010). Key features of the IPSL ocean atmosphere model
 1762 and its sensitivity to atmospheric resolution. *Clim. Dyn.*, *34*, 1–26. doi:
 1763 10.1007/s00382-009-0640-6
- 1764 Massonnet, F., Vancoppenolle, M., Goosse, H., Docquier, D., Fichet, T., &
 1765 Blanchard-Wrigglesworth, E. (2018). Arctic sea-ice change tied to its mean
 1766 state through thermodynamic processes. *Nature Clim. Change*, *8*(7), 599–603.
 1767 doi: 10.1038/s41558-018-0204-z
- 1768 Mathiot, P., Jenkins, A., Harris, C., & Madec, G. (2017). Explicit representa-
 1769 tion and parametrised impacts of under ice shelf seas in the z^* coordinate
 1770 ocean model NEMO 3.6. *Geophys. Mod. Dev.*, *10*(7), 2849–2874. doi:
 1771 10.5194/gmd-10-2849-2017
- 1772 Mauritsen, T., Bader, J., Becker, T., Behrens, J., Bittner, M., Brokopf, R., ...
 1773 Roeckner, E. (2019). Developments in the MPI-M Earth System Model version
 1774 1.2 (MPI-ESM1.2) and its response to increasing CO₂. *J. Adv. Modeling Earth*
 1775 *Systems*, *11*(4), 998–1038. doi: 10.1029/2018MS001400
- 1776 Mears, C. A., Smith, D. K., Ricciardulli, L., Wang, J., Huelsing, H., & Wentz, F. J.
 1777 (2018). Construction and uncertainty estimation of a satellite-derived total
 1778 precipitable water data record over the World's oceans. *Earth and Space*
 1779 *Science*, *5*, 197–210. doi: 10.1002/2018EA000363

- 1780 Meehl, G. A., Moss, R., Taylor, K. E., Eyring, V., Stouffer, R. J., Bony, S., &
1781 Stevens, B. (2014). Climate model intercomparisons: Preparing for the next
1782 phase. *Eos, Transactions American Geophysical Union*, *95*(9), 77–78. doi:
1783 10.1002/2014EO090001
- 1784 Meinshausen, M., Vogel, E., Nauels, A., Lorbacher, K., Meinshausen, N., Etheridge,
1785 D. M., ... Weiss, R. (2017). Historical greenhouse gas concentrations for
1786 climate modelling (CMIP6). *Geophys. Mod. Dev.*, *10*, 2057–2116. doi:
1787 10.5194/gmd-10-2057-2017
- 1788 Merino, N., Le Sommer, J., Durand, G., Jourdain, N. C., Madec, G., Mathiot, P.,
1789 & Tournadre, J. (2016). Antarctic icebergs melt over the Southern Ocean:
1790 Climatology and impact on sea ice. *Ocean Modelling*, *104*, 99–110. doi:
1791 10.1016/j.ocemod.2016.05.001
- 1792 Meurdesoif, Y., Caubel, A., Lacroix, R., Dérouillat, J., & Nguyen, M. H. (2016).
1793 *Xios tutorial* (Tech. Rep.). Retrieved from [http://forge.ipsl.jussieu.fr/](http://forge.ipsl.jussieu.fr/ioserver/raw-attachment/wiki/WikiStart/XIOS-tutorial.pdf)
1794 [ioserver/raw-attachment/wiki/WikiStart/XIOS-tutorial.pdf](http://forge.ipsl.jussieu.fr/ioserver/raw-attachment/wiki/WikiStart/XIOS-tutorial.pdf)
- 1795 Moncrieff, M. W. (2019). Toward a dynamical foundation for organized convection
1796 parameterization in GCMs. *Geophys. Res. Lett.*, *46*(23), 14103–14108. doi: 10
1797 .1029/2019GL085316
- 1798 Morice, C. P., Kennedy, J. J., Rayner, N. A., & Jones, P. D. (2012). Quantifying
1799 uncertainties in global and regional temperature change using an ensemble of
1800 observational estimates: The HadCRUT4 data set. *J. Geophys. Res. Atmos.*,
1801 *117*(D8). doi: 10.1029/2011JD017187
- 1802 Ngo-Duc, T., Laval, K., Ramillien, G., Polcher, J., & Cazenave, A. (2007). Val-
1803 idation of the land water storage simulated by Organising Carbon and Hy-
1804 drology in Dynamic Ecosystems (ORCHIDEE) with Gravity Recovery and
1805 Climate Experiment (GRACE) data. *Water Resour. Res.*, *43*, W04427. doi:
1806 10.1029/2006WR004941
- 1807 Norby, R. J., & Zak, D. R. (2011). Ecological lessons from Free-Air CO₂ Enrichment
1808 (FACE) experiments. *Annual Review of Ecology, Evolution, and Systematics*,
1809 *42*(1), 181–203. doi: 10.1146/annurev-ecolsys-102209-144647
- 1810 Notz, D., Drr, J., Bailey, D. A., Blockley, E., Bushuk, M., Debernard, J. B., ...
1811 Vancoppenolle, M. (2020). Arctic sea ice in CMIP6. *Geophys. Res. Lett.*,
1812 *n/a*(n/a), e2019GL086749. doi: 10.1029/2019GL086749

- 1813 O'Neill, B. C., Tebaldi, C., van Vuuren, D. P., Eyring, V., Friedlingstein, P., Hurtt,
1814 G., . . . Sanderson, B. M. (2016). The Scenario Model Intercomparison
1815 Project (ScenarioMIP) for CMIP6. *Geophys. Mod. Dev.*, *9*(9), 3461–3482.
1816 doi: 10.5194/gmd-9-3461-2016
- 1817 Ortega, P., Mignot, J., Swingedouw, D., Sévellec, F., & Guilyardi, E. (2015).
1818 Reconciling two alternative mechanisms behind bi-decadal variability
1819 in the North Atlantic. *Progress in Oceanography*, *137*, 237–249. doi:
1820 10.1016/j.pocean.2015.06.009
- 1821 OSI-SAF, E. (1996). *Global sea ice concentration climate data record 1979–2015*
1822 (*v2.0, 2017*) (Tech. Rep.). Norwegian and Danish Meteorological Institutes.
1823 doi: 10.15770/EUM.SAF.OSI0008
- 1824 Oueslati, B., & Bellon, G. (2013). Convective entrainment and large-scale organ-
1825 ization of tropical precipitation: Sensitivity of the CNRM-CM5 hierarchy of
1826 models. *J. Clim.*, *26*, 2931–2946. doi: 10.1175/JCLI-D-12-00314.1
- 1827 Oueslati, B., & Bellon, G. (2015). The double ITCZ bias in CMIP5 models: Inter-
1828 action between SST, large-scale circulation and precipitation. *Clim. Dyn.*, *44*,
1829 585–607. doi: 10.1007/s00382-015-2468-6
- 1830 Parton, W. J., Schimel, D. S., Cole, C. V., & Ojima, D. S. (1987). Analysis of fac-
1831 tors controlling soil organic-matter levels in Great-Plains grasslands. *Soil Sci.*
1832 *Soc. Am. J.*, *51*, 1173–1179.
- 1833 Pellichero, V., Sallée, J.-B., Schmidtke, S., Roquet, F., & Charrassin, J.-B. (2017).
1834 The ocean mixed layer under Southern Ocean sea-ice: Seasonal cycle and forc-
1835 ing. *J. Geophys. Res. Ocean*, *122*(2), 1608–1633. doi: 10.1002/2016JC011970
- 1836 Pithan, F., Shepherd, T. G., Zappa, G., & Sandu, I. (2016). Climate model biases in
1837 jet streams, blocking and storm tracks resulting from missing orographic drag.
1838 *Geophys. Res. Lett.*, *43*(13), 7231–7240. doi: 10.1002/2016GL069551
- 1839 Prather, M. J. (1986). Numerical advection by conservation of second-order
1840 moments. *J. Geophys. Res. Atmos.*, *91*(D6), 6671–6681. doi: 10.1029/
1841 JD091iD06p06671
- 1842 Praveen Kumar, B., Vialard, J., Lengaigne, M., Murty, V. S. N., & McPhaden, M. J.
1843 (2012). TropFlux: air-sea fluxes for the global tropical oceans—description and
1844 evaluation. *Clim. Dyn.*, *38*(7-8), 1521–1543. doi: 10.1007/s00382-011-1115-0
- 1845 Praveen Kumar, B., Vialard, J., Lengaigne, M., Murty, V. S. N., McPhaden, M. J.,

- 1846 Cronin, M. F., ... Gopala Reddy, K. (2013). TropFlux wind stresses over the
 1847 tropical oceans: evaluation and comparison with other products. *Clim. Dyn.*,
 1848 *40*(7-8), 2049–2071. doi: 10.1007/s00382-012-1455-4
- 1849 Prentice, I., Cramer, W., Harrison, S., Leemans, R., Monserud, R., & Solomon, A.
 1850 (1992). A global biome model based on plant physiology and dominance: Soil
 1851 properties and climate. *J. Biogeogr.*, *19*, 117–134. doi: 10.2307/2845499
- 1852 Rio, C., & Hourdin, F. (2008). A thermal plume model for the convective boundary
 1853 layer: Representation of cumulus clouds. *J. Atmos. Sci.*, *65*, 407–425. doi: 10
 1854 .1175/2007JAS2256.1
- 1855 Rio, C., Hourdin, F., Couvreux, F., & Jam, A. (2010). Resolved versus parametrized
 1856 boundary-layer plumes. Part II: Continuous formulations of mixing rates
 1857 for mass-flux schemes. *Boundary-Layer Meteorol.*, *135*, 469–483. doi:
 1858 10.1007/s10546-010-9478-z
- 1859 Rio, C., Hourdin, F., Grandpeix, J.-Y., & Lafore, J.-P. (2009). Shifting the diur-
 1860 nal cycle of parameterized deep convection over land. *Geophys. Res. Lett.*, *36*,
 1861 L07809. doi: 10.1029/2008GL036779
- 1862 Rivière, G. (2009). Effect of latitudinal variations in low-level baroclinicity on eddy
 1863 life cycles and upper-tropospheric wave-breaking processes. *J. Atmos. Sci.*,
 1864 *66*(6), 1569–1592. doi: 10.1175/2008JAS2919.1
- 1865 Rochetin, N., Couvreux, F., Grandpeix, J.-Y., & Rio, C. (2014). Deep con-
 1866 vection triggering by boundary layer thermals. Part I: LES analysis and
 1867 stochastic triggering formulation. *J. Atmos. Sci.*, *71*, 496–514. doi:
 1868 10.1175/JAS-D-12-0336.1
- 1869 Rochetin, N., Grandpeix, J.-Y., Rio, C., & Couvreux, F. (2014). Deep convec-
 1870 tion triggering by boundary layer thermals. Part II: Stochastic triggering
 1871 parameterization for the LMDZ GCM. *J. Atmos. Sci.*, *71*, 515–538. doi:
 1872 10.1175/JAS-D-12-0337.1
- 1873 Rohde, R., Muller, R., Jacobsen, R., Muller, E., Perlmutter, S., Rosenfeld, A., ...
 1874 Wickham, C. (2013). A new estimate of the average Earth surface land tem-
 1875 perature spanning 1753 to 2011. *Geoinfor. Geostat.: An Overview*, *1*, 1. doi:
 1876 10.4172/2327-4581.1000101
- 1877 Rohde, R., Muller, R., Jacobsen, R., Perlmutter, S., Rosenfeld, A., Wurtele, J., ...
 1878 Mosheet, S. (2013). Berkeley Earth temperature averaging process. *Geoinfor.*

- 1879 *Geostat.: An Overview, 1, 2.* doi: 10.4172/gigs.1000103
- 1880 Roquet, F., Madec, G., McDougall, T. J., & Barker, P. M. (2015). Accu-
 1881 rate polynomial expressions for the density and specific volume of sea-
 1882 water using the TEOS-10 standard. *Ocean Modelling, 90*, 29–43. doi:
 1883 10.1016/j.ocemod.2015.04.002
- 1884 Rousset, C., Vancoppenolle, M., Madec, G., Fichet, T., Flavoni, S., Barthélemy,
 1885 A., ... Vivier, F. (2015). The Louvain-La-Neuve sea ice model LIM3.6:
 1886 global and regional capabilities. *Geophys. Mod. Dev., 28*, 2991–3005. doi:
 1887 10.5194/gmd-8-2991-2015
- 1888 Rugenstein, M., Bloch-Johnson, J., Gregory, J., Andrews, T., Mauritsen, T., Li, C.,
 1889 ... Knutti, R. (2020). Equilibrium climate sensitivity estimated by equili-
 1890 brating climate models. *Geophys. Res. Lett., 47*(4), e2019GL083898. doi:
 1891 10.1029/2019GL083898
- 1892 Sadourny, R., & Laval, K. (1984). January and July performance of the LMD gen-
 1893 eral circulation model. In A. Berger & C. Nicolis (Eds.), *New perspectives in*
 1894 *climate modeling* (pp. 173–197). Amsterdam: Elsevier.
- 1895 Schaefer, K., Denning, A. S., Suits, N., Kaduk, J., Baker, I., Los, S., & Prihodko, L.
 1896 (2002). Effect of climate on interannual variability of terrestrial CO₂ fluxes.
 1897 *Global Biogeo. Cycles, 16*(4), 49–1–49-12. doi: 10.1029/2002GB001928
- 1898 Séférian, R., Baek, S., Boucher, O., Dufresne, J.-L., Decharme, B., Saint-Martin, D.,
 1899 & Roehrig, R. (2018). An interactive ocean surface albedo scheme: Formu-
 1900 lation and evaluation in two atmospheric models. *Geophys. Mod. Dev., 11*,
 1901 321–338. doi: 10.5194/gmd-11-321-2018
- 1902 Sellers, P. J., Bounoua, L., Collatz, G. J., Randall, D. A., Dazlich, D. A., Los, S. O.,
 1903 ... Jensen, T. G. (1996). Comparison of radiative and physiological ef-
 1904 fects of doubled atmospheric CO₂ on climate. *Science, 271*, 1402–1406. doi:
 1905 10.1126/science.271.5254.1402
- 1906 Shell, K. M., Kiehl, J. T., & Shields, C. A. (2008). Using the radiative kernel tech-
 1907 nique to calculate climate feedbacks in ncars community atmospheric model. *J.*
 1908 *Clim., 21*, 2269–2282. doi: 10.1175/2007JCLI2044.1
- 1909 Smeed, D., McCarthy, G., Rayner, D., Moat, B. I., Johns, W. E., Baringer, M. O., &
 1910 Meinen, C. S. (2017). *Atlantic meridional overturning circulation observed by*
 1911 *the RAPID-MOCHA-WBTS (RAPID-Meridional Overturning Circulation and*

- 1912 *Heatflux Array-Western Boundary Time Series) array at 26°N from 2004 to*
 1913 *2017* (Tech. Rep.). British Oceanographic Data Centre - Natural Environment
 1914 Research Council, UK. doi: 10.5285/5acfd143-1104-7b58-e053-6c86abc0d94b
- 1915 Soden, B. J., Held, I. M., Colman, R., Shell, K. M., Kiehl, J. T., & Shields, C. A.
 1916 (2008). Quantifying climate feedbacks using radiative kernels. *J. Clim.*, *21*,
 1917 3504–3520. doi: 10.1175/2007JCLI2110.1
- 1918 Stephens, G., Li, J., Wild, M., Clayson, C. A., Loeb, N., Kato, S., ... Andrews,
 1919 T. (2012). An update on Earth's energy balance in light of the latest global
 1920 observations. *Nature Geoscience*, *5*, 691–696. doi: 10.1038/ngeo1580
- 1921 Stouffer, R. J., Eyring, V., Meehl, G. A., Bony, S., Senior, C., Stevens, B., & Taylor,
 1922 K. E. (2017). CMIP5 scientific gaps and recommendations for CMIP6. *Bull.*
 1923 *Am. Meteorol. Soc.*, *98*(1), 95–105. doi: 10.1175/BAMS-D-15-00013.1
- 1924 Szopa, S., Balkanski, Y., Schulz, M., Bekki, S., Cugnet, D., Fortems-Cheiney, A.,
 1925 ... Dufresne, J.-L. (2013). Aerosol and ozone changes as forcing for cli-
 1926 mate evolution between 1850 and 2000. *Clim. Dyn.*, *40*, 2223–2250. doi:
 1927 10.1007/s00382-012-1408-y
- 1928 Thorndike, A. S., Rothrock, D. A., Maykut, G. A., & Colony, R. (1975). The thick-
 1929 ness distribution of sea ice. *J. Geophys. Res.*, *80*, 4501–4513. doi: 10.1029/
 1930 JC080i033p04501
- 1931 Timmermann, A., An, S.-I., Kug, J.-S., Jin, F.-F., Cai, W., Capotondi, A., ...
 1932 Zhang, X. (2018). El Niño-Southern Oscillation complexity. *Nature*, *559*,
 1933 535–545. doi: 10.1038/s41586-018-0252-6
- 1934 Trenberth, K. E., & Caron, J. M. (2001). Estimates of meridional atmosphere and
 1935 ocean heat transports. *J. Clim.*, *14*, 3433–3443. doi: 10.1175/1520-0442(2001)
 1936 014(3433:EOMAAO)2.0.CO;2
- 1937 Trenberth, K. E., & Shea, D. J. (2006). Atlantic hurricanes and natural variability
 1938 in 2005. *Geophys. Res. Lett.*, *33*(12), L12704. doi: 10.1029/2006GL026894
- 1939 Uotila, P., Iovino, D., Vancoppenolle, M., Lensu, M., & Rousset, C. (2017). Compar-
 1940 ing sea ice, hydrography and circulation between NEMO3.6 LIM3 and LIM2.
 1941 *Geophys. Mod. Dev.*, *10*, 1009–1031. doi: 10.5194/gmd-10-1009-2017
- 1942 Vancoppenolle, M., Fichefet, T., Goosse, H., Bouillon, S., Madec, G., &
 1943 Morales Maqueda, M. A. (2009). Simulating the mass balance and salinity
 1944 of Arctic and Antarctic sea ice. 1. Model description and validation. *Ocean*

- 1945 *Modelling*, 27, 54–69. doi: 10.1016/j.ocemod.2008.11.003
- 1946 Van Leer, B. (1977). Towards the ultimate conservative difference scheme: IV. A
 1947 new approach to numerical convection. *J. Computational Phys.*, 23, 276–299.
 1948 doi: 10.1016/0021-9991(77)90095-X
- 1949 Van Weverberg, K., Morcrette, C. J., Petch, J., Klein, S. A., Ma, H.-Y., Zhang, C.,
 1950 ... Thieman, M. M. (2018). CAUSES: Attribution of surface radiation biases
 1951 in NWP and climate models near the U.S. Southern Great Plains. *J. Geophys.*
 1952 *Res. Atmos.*, 2017JD027188. doi: 10.1002/2017JD027188
- 1953 Vial, J., Dufresne, J.-L., & Bony, S. (2013). On the interpretation of inter-model
 1954 spread in CMIP5 climate sensitivity estimates. *Clim. Dyn.*, 41, 3339–3362. doi:
 1955 10.1007/s00382-013-1725-9
- 1956 Vignon, E., Hourdin, F., Genthon, C., Van de Wiel, B. J. H., Gallée, H., Madeleine,
 1957 J.-B., & Beaumet, J. (2018). Modeling the dynamics of the atmospheric
 1958 boundary layer over the Antarctic plateau with a general circulation model. *J.*
 1959 *Adv. Modeling Earth Systems*, 10, 98–125. doi: 10.1002/2017MS001184
- 1960 Voldoire, A., Saint-Martin, D., Sénési, S., Decharme, B., Alias, A., Chevallier, M.,
 1961 ... Waldman, R. (2019). Evaluation of CMIP6 DECK experiments with
 1962 CNRM-CM6-1. *J. Adv. Modeling Earth Systems*, 11(7), 2177–2213. doi:
 1963 10.1029/2019MS001683
- 1964 Wang, C., Zhang, L., Lee, S.-K., Wu, L., & Mechoso, C. R. (2014). A global per-
 1965 spective on CMIP5 climate model biases. *Nature Clim. Change*, 4, 201–205.
 1966 doi: 10.1038/nclimate2118
- 1967 Wang, F., Cheruy, F., & Dufresne, J.-L. (2016). The improvement of soil thermody-
 1968 namics and its effects on land surface meteorology in the IPSL climate model.
 1969 *Geophys. Mod. Dev.*, 9(1), 363–381. doi: 10.5194/gmd-9-363-2016
- 1970 Wang, T., Ottlé, C., Boone, A., Ciais, P., Brun, E., Morin, S., ... Peng, S. (2013).
 1971 Evaluation of an improved intermediate complexity snow scheme in the OR-
 1972 CHIDEE land surface model. *J. Geophys. Res. Atmos.*, 118, 6064–6079. doi:
 1973 10.1002/jgrd.50395
- 1974 Wen, N., Frankignoul, C., & Gastineau, G. (2016). Active AMOC-NAO coupling in
 1975 the IPSL-CM5A-MR climate model. *Clim. Dyn.*, 47(7), 2105–2119. doi: 10
 1976 .1007/s00382-015-2953-y
- 1977 Woollings, T., Barriopedro, D., Methven, J., Son, S.-W., Martius, O., Harvey, B., ...

- 1978 Seneviratne, S. (2018). Blocking and its response to climate change. *Current*
1979 *Climate Change Reports*, 4(3), 287–300. doi: 10.1007/s40641-018-0108-z
- 1980 Yamada, T. (1983). Simulations of nocturnal drainage flows by a q^2l turbulence clo-
1981 sure model. *J. Atmos. Sci.*, 40, 91–106. doi: 10.1175/1520-0469(1983)040<0091:
1982 SONDFB>2.0.CO;2
- 1983 Yin, L., Fu, R., Shevliakova, E., & Dickinson, R. E. (2013). How well can CMIP5
1984 simulate precipitation and its controlling processes over tropical South Amer-
1985 ica? *Clim. Dyn.*, 41, 3127–3143. doi: 10.1007/s00382-012-1582-y
- 1986 Yin, X., & Struik, P. (2009). C3 and C4 photosynthesis models: An overview
1987 from the perspective of crop modelling. *NJAS - Wageningen Journal of Life*
1988 *Sciences*, 57(1), 27–38. doi: 10.1016/j.njas.2009.07.001
- 1989 Zhong, W., & Haigh, J. D. (2013). The greenhouse effect and carbon dioxide.
1990 *Weather*, 68(4), 100–105. doi: 10.1002/wea.2072
- 1991 Zobler, L. (1986). *A world soil file for global climate modeling* (Tech. Rep.). Na-
1992 tional Aeronautics and Space Administration, Goddard Space Flight Center,
1993 Institute for Space Studies.

Variable full name	CMIP6 variable short name	Product	Period covered	Reference publication
2-meter air temperature	tas	ERA Interim	1980–2009	Dee et al. (2011)
3D temperature	ta	–	–	–
3D zonal wind	ua	–	–	–
3D specific humidity	hus	–	–	–
3D relative humidity	hur	–	–	–
Sea level pressure	slp or psl	–	–	–
10-meter zonal and meridional wind component	uas, vas	–	–	–
Air temperature at 850 and 200 hPa	ta_850, ta_200	–	–	–
Zonal wind component at 850 and 200 hPa	ua_850, ua_200	–	–	–
Meridional wind component at 850 and 200 hPa	va_850, va_200	–	–	–
Geopotential Height at 500 hPa	zg_500	–	–	–
Precipitation	pr	GPCP	1979–2009	Adler et al. (2018)
Precipitable water	prw	REMSS-PRW- v07r01	01/1988– 01/2019	Mears et al. (2018)
Longwave cloud radiative effect	rltcre	CERES-EBAF	2000–2012	Loeb et al. (2018)
Shortwave cloud radiative effect	rstcre	–	–	–
Upwelling shortwave at the top-of- atmosphere	rsut	–	–	–
Upwelling longwave at the top-of- atmosphere	rlut	–	–	–
Sea Surface Salinity	sos	WOA13-v2	1975–2004	Locarnini et al. (2013)
Atlantic Meridional overturning streamfunction	msfyz	Smeed et al. (2017)	2004–2017	Smeed et al. (2017)
Northward oceanic heat transport	hfbasin	Ganachaud and Wunsch (2003)	1985–1996	Ganachaud and Wunsch (2003)

Table 1. List of evaluated model variables and datasets against which they are evaluated.

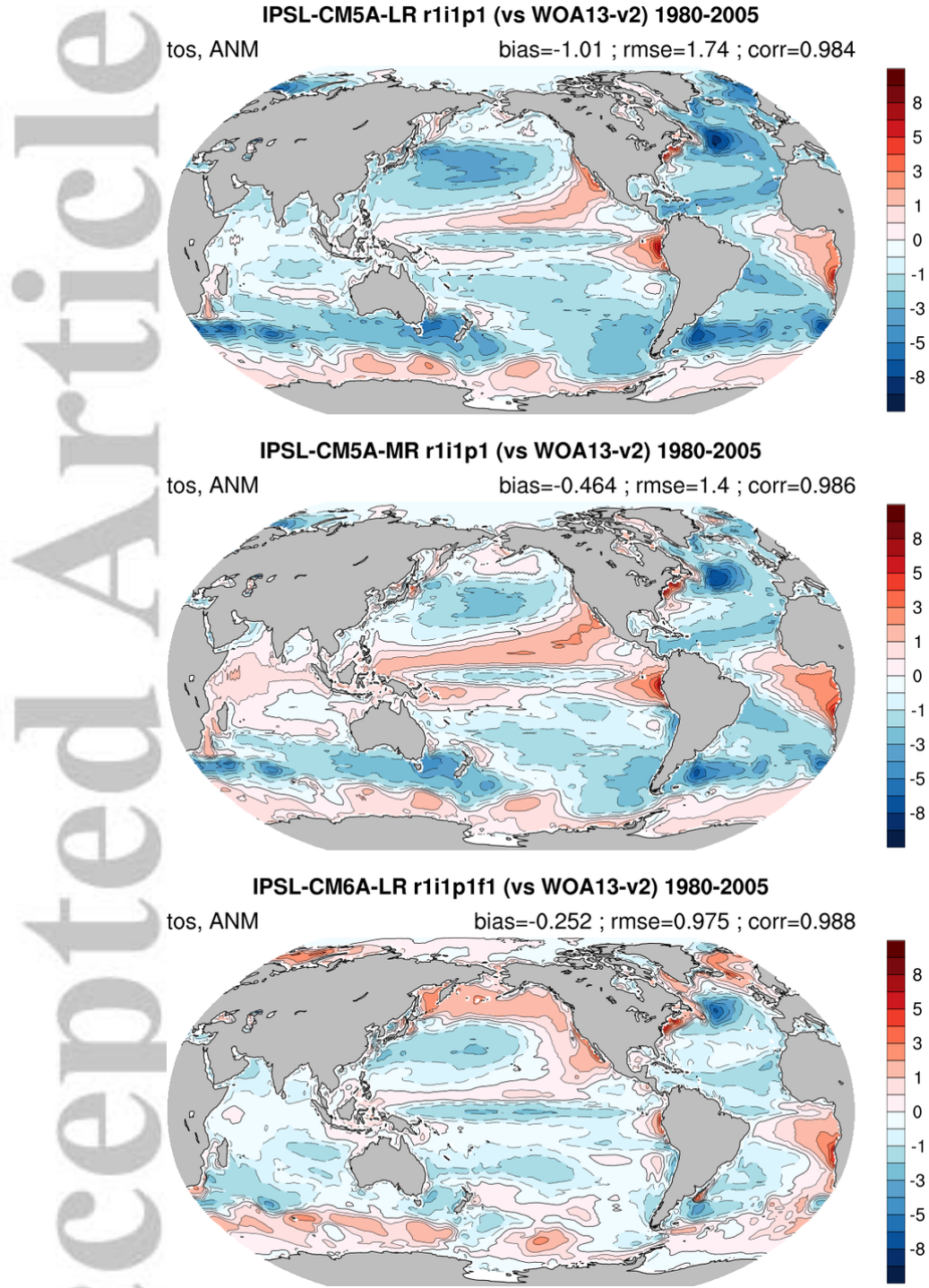


Figure 1. Global distribution of the annually-averaged sea surface temperature (SST) bias (in °C) for IPSL-CM5A-LR (upper row), IPSL-CM5A-MR (middle row) and IPSL-CM6A-LR (bottom row). Biases are computed against data from the World Ocean Atlas (WOA13-v2, Locarnini et al., 2013). Global-mean biases, root mean square errors (RMSE) and correlation coefficients are provided for each model.

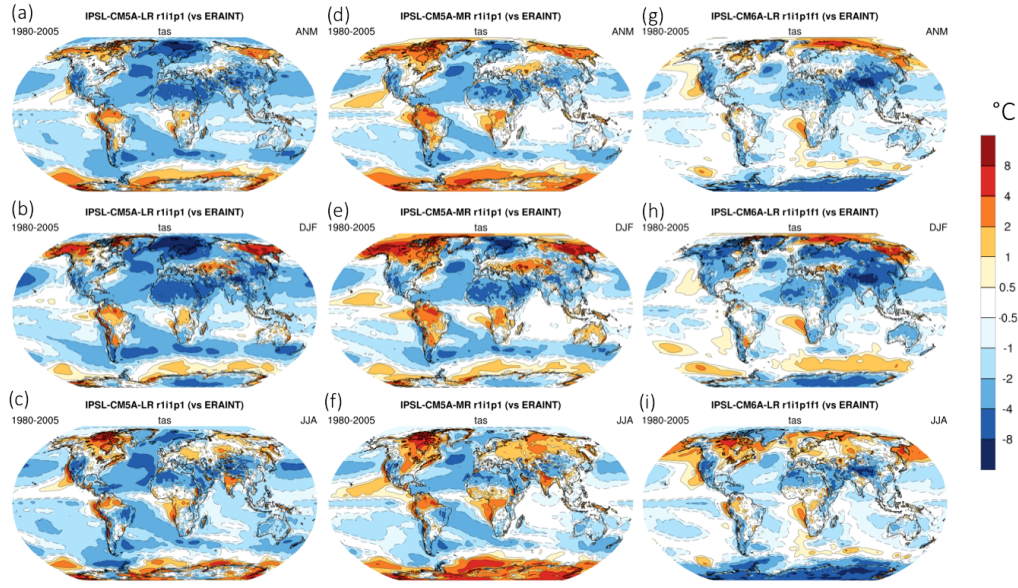


Figure 2. Distributions of biases in the surface (2-meter) air temperature (in °C) for the annual mean (ANM, top row), December-January-February (DJF, middle row) and June-July-August (JJA, bottom row) for IPSL-CM5A-LR (left column), IPSL-CM5A-MR (middle column) and IPSL-CM6A-LR (right column). The bias maps are computed against ERA Interim reanalysis (Dee et al., 2011).

Transect	IPSL-CM5A-LR	IPSL-CM5A-MR	IPSL-CM6A-LR	Observations
Barents opening	-0.89	-0.059	4.06	2.0
Bering Strait	1.09	1.13	1.17	0.8
Denmark Strait	-5.47	-5.73	-5.26	-3.4±1.4
Drake Passage	101.46	109.2	150.87	136.7±6.9
Fram Strait	0.009	-0.86	-3.59	-2±2.7
Indonesian Throughflow	-10.72	-11.17	-13.60	-15
Mozambique Channel	-27.96	-27.21	-23.22	-16.7±8.9

Table 2. Mass transports (in Sv) through a selection of key transects of the global ocean as defined in Griffies et al. (2016). In the three model configurations, the transports are computed as time averages over the period 1980–2005 of the historical simulations (r1i1p1f1 member). Mass transports are counted positively eastwards and northwards. Observations are from Griffies et al. (2016) and references therein.

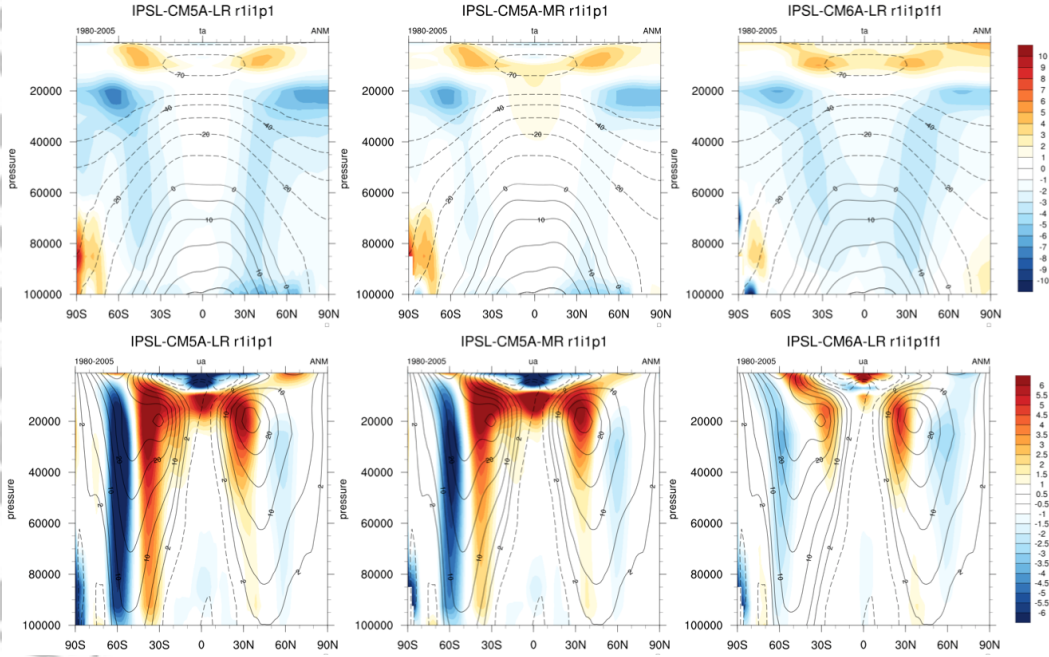


Figure 3. Zonally- and annually-averaged air temperature (top row, in $^{\circ}\text{C}$) and zonal wind component (bottom row, in m s^{-1}) for IPSL-CM5A-LR (left column), IPSL-CM5A-MR (middle column) and IPSL-CM6A-LR (right column). The black contours show the ERA Interim reanalysis (Dee et al., 2011) climatology and the model bias against ERA Interim is depicted by the color scale. The pressure on the vertical axis is expressed in Pa.

	Mean fluxes (PgC yr^{-1})			
	1990–1999		2009–2018	
	IPSL-CM6A-LR	GCP 2019	IPSL-CM6A-LR	GCP 2019
Emissions				
Fossil fuel (E_{ff})	6.5 ± 0.15	6.4 ± 0.3	9.1 ± 0.13	9.5 ± 0.5
Land cover change (E_{lcc})	0.4 ± 0.0	1.3 ± 0.7	0.7 ± 0.0	1.5 ± 0.7
Total emissions ($E_{\text{ff}} + E_{\text{lcc}}$)	7.0 ± 0.15	7.7 ± 0.8	10.0 ± 0.13	11.0 ± 0.8
Partitioning				
Atmospheric growth rate (G_{atm})	3.2	3.1 ± 0.02	5.2	4.9 ± 0.02
Oceanic Sink (S_{ocean})	2.1 ± 0.04	2.0 ± 0.6	2.7 ± 0.04	2.5 ± 0.6
Terrestrial Sink (S_{land})	1.7 ± 0.13	2.6 ± 0.9	2.2 ± 0.14	3.6 ± 1.0
Total land fluxes ($S_{\text{land}} - E_{\text{lcc}}$)	1.3 ± 0.13	1.0 ± 0.8	1.5 ± 0.14	1.7 ± 0.9

Table 3. Decadal mean components of the global CO_2 budget for the 1990–1999 and 2009–2018 periods for IPSL-CM6A-LR and from the Global Carbon Project (Friedlingstein et al., 2019). The GCP carbon budget shows an imbalance of 0.3 to 0.4 PgC yr^{-1} . The error bars represent uncertainties for the GCP estimates and standard deviation across the 32 ensemble members for IPSL-CM6A-LR.

Accepted Article

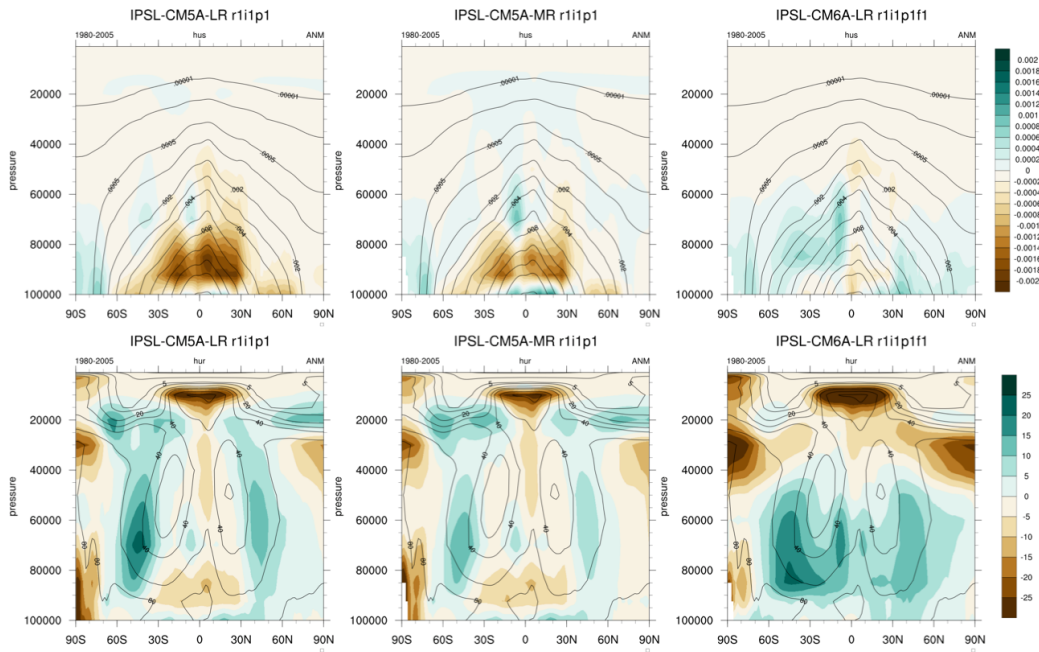


Figure 4. Zonally- and annually-averaged specific humidity (top row, in kg kg^{-1}) and relative humidity (bottom row, in %) for the IPSL-CM5A-LR (left column), IPSL-CM5A-MR (middle column) and IPSL-CM6A-LR (right column). The black contours show the ERA Interim reanalysis (Dee et al., 2011) climatology and the model bias against ERA Interim is depicted by the color scale. The pressure on the vertical axis is expressed in Pa.

Accepted Article

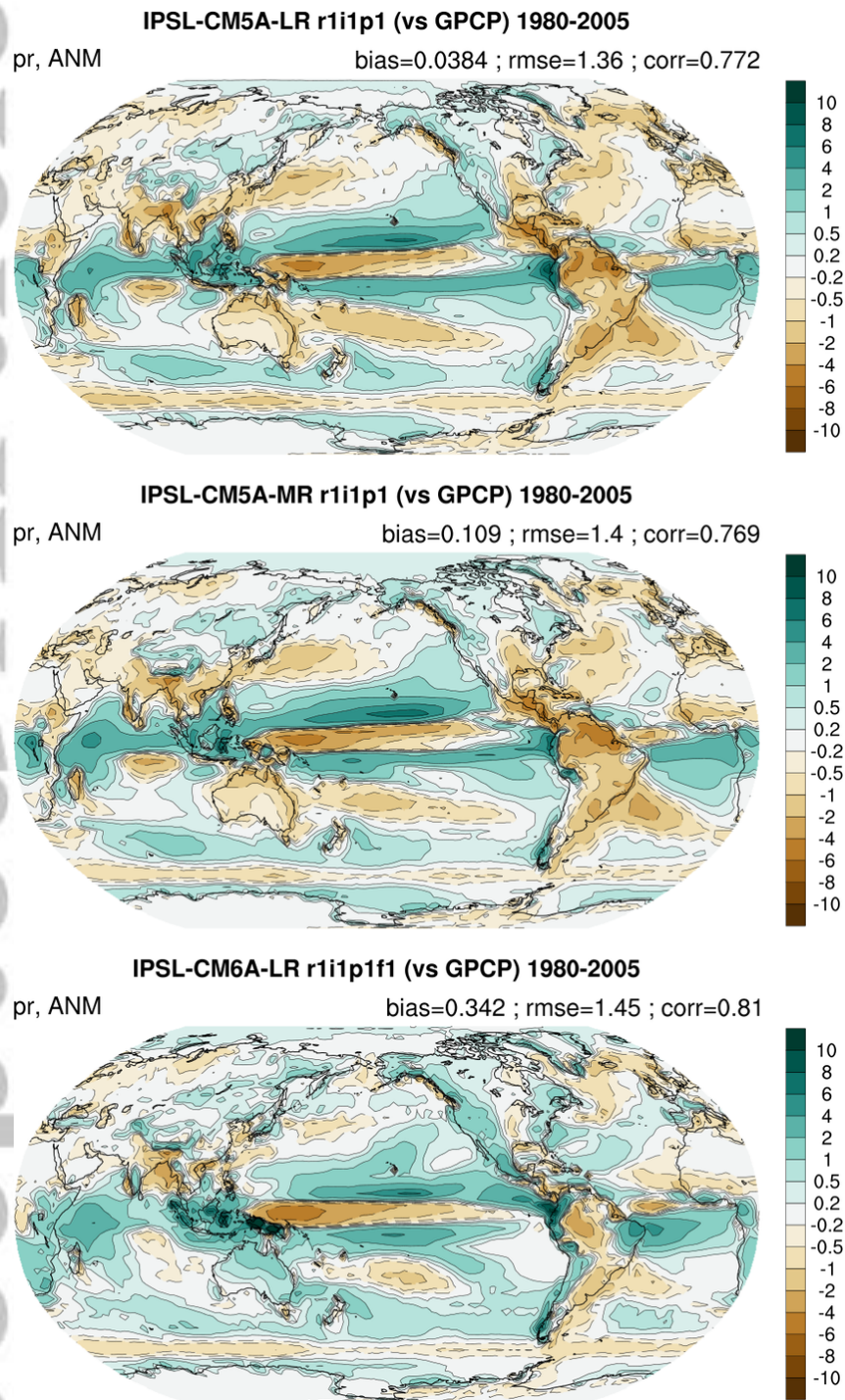


Figure 5. Global distribution of the annual mean precipitation biases (in mm day^{-1}) for the IPSL-CM5A-LR (upper row), IPSL-CM5A-MR (middle row) and IPSL-CM6A-LR (bottom row) models. The bias maps are computed against the Global Precipitation Climatology Project (GPCP, Adler et al., 2018).

Accepted Article

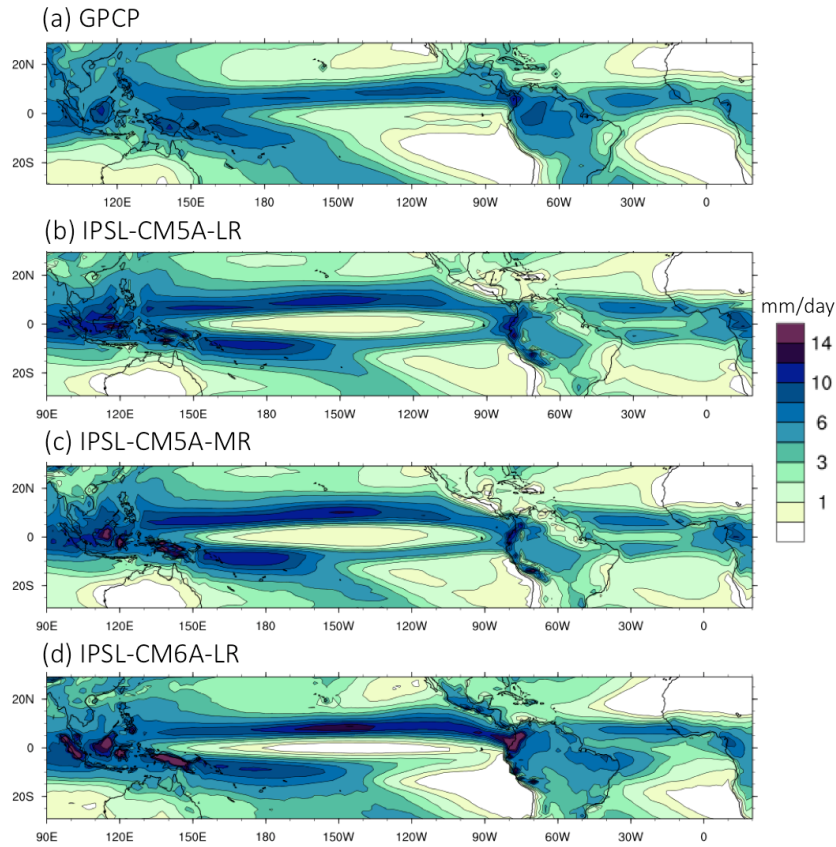


Figure 6. Annual mean precipitation rate (in mm day^{-1}) for a) GPCP, b) IPSL-CM5A-LR, c) IPSL-CM5A-MR and d) IPSL-CM6A-LR in the tropical region. The climatology is computed over the 1980–2005 period for the models and 1980–2009 for GPCP (Adler et al., 2018).

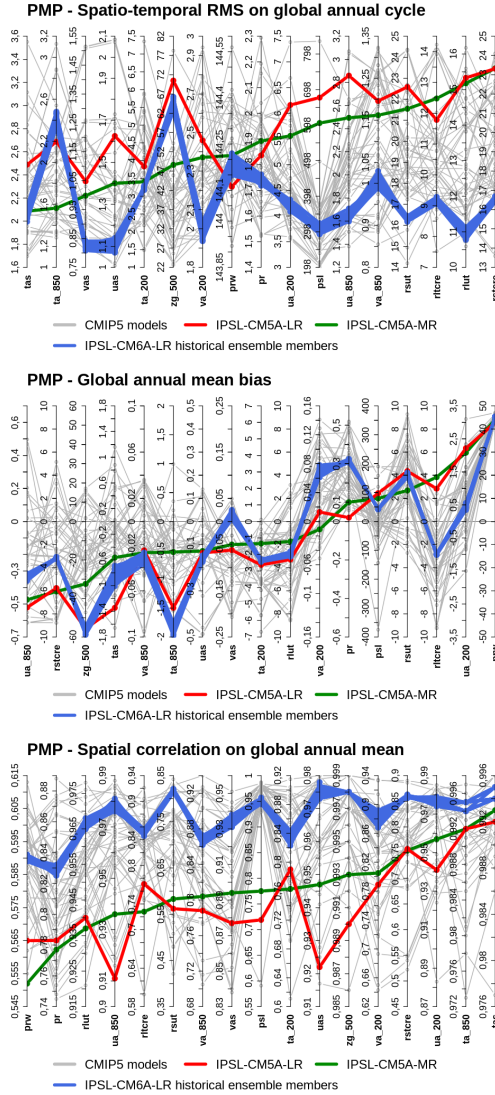


Figure 7. Global metrics summarizing the performance of the IPSL-CM6A-LR members of the historical ensemble (blue lines) against IPSL-CM5A-LR (red line) and IPSL-CM5A-MR (green line) and the CMIP5 multi-model ensemble (grey lines). The metrics are for the global monthly spatio-temporal root mean square error (upper panel), global annual mean bias (middle panel) and spatial correlation on the annual mean field (bottom panel) for 17 atmospheric variables (see full name of the variables in Table 1). The statistics are computed for the models on the 1980–2005 climatology against the reference datasets listed in Table 1. Note that the reference period for the observational datasets can be different from the period listed in Table 1, e.g. 1989–2009 for ERA Interim, 01/1979–04/2018 for GPCP, and 2000–2018 for CERES-EBAF. Each model is represented by a line that connects the values of the metric obtained for the different model variables (vertical axes). For readability the columns are sorted so that the line connecting the IPSL-CM5A-MR results goes up from the left to the right. The metrics were computed with the PCMDI Metrics Package (PMP, Gleckler et al., 2016).

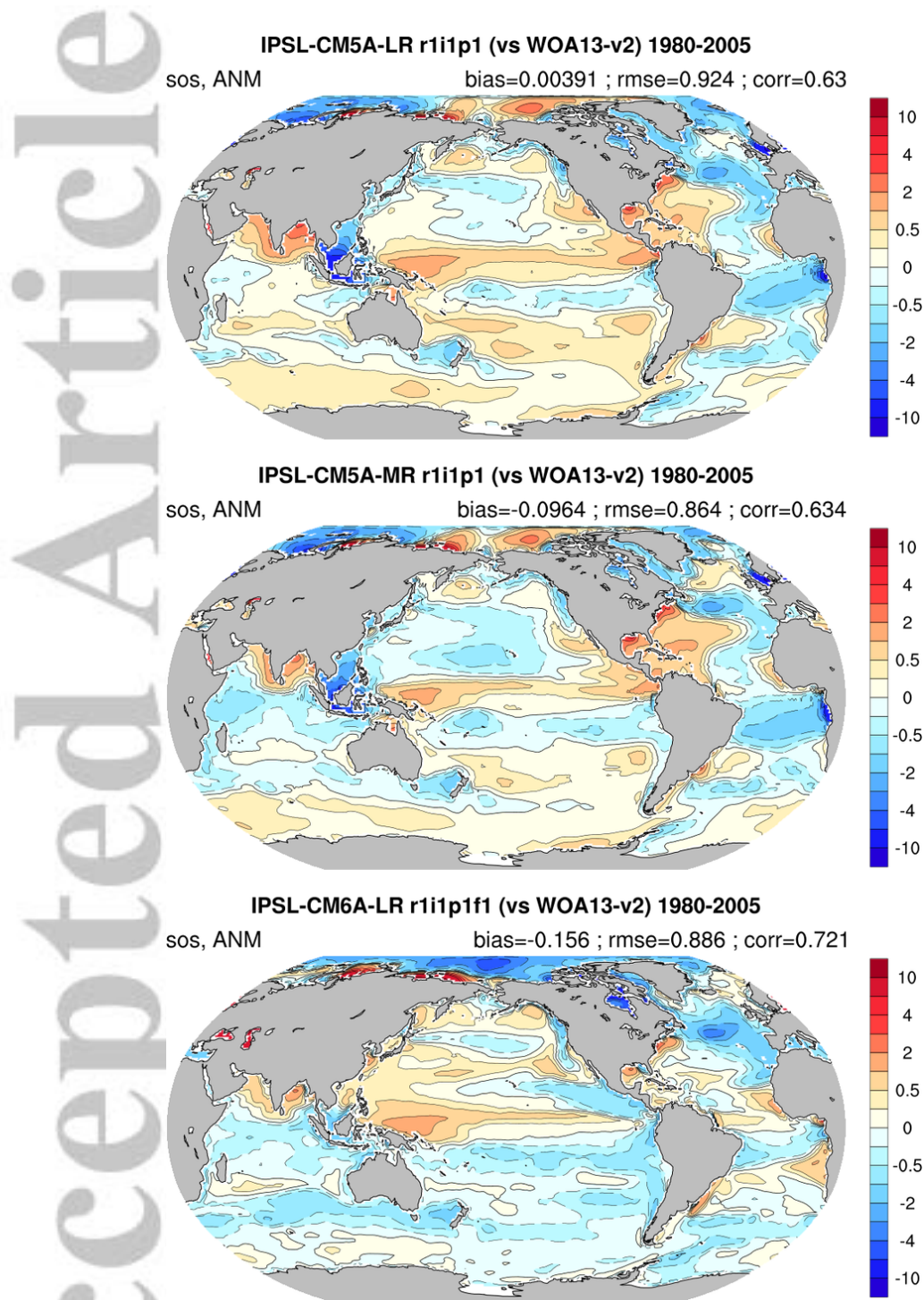


Figure 8. Global distribution of the sea surface salinity (SSS, in ‰) biases in annual mean for IPSL-CM5A-LR (upper row), IPSL-CM5A-MR (middle row) and IPSL-CM6A-LR (bottom row). Biases are computed against data from the World Ocean Atlas (WOA13-v2, Locarnini et al., 2013).

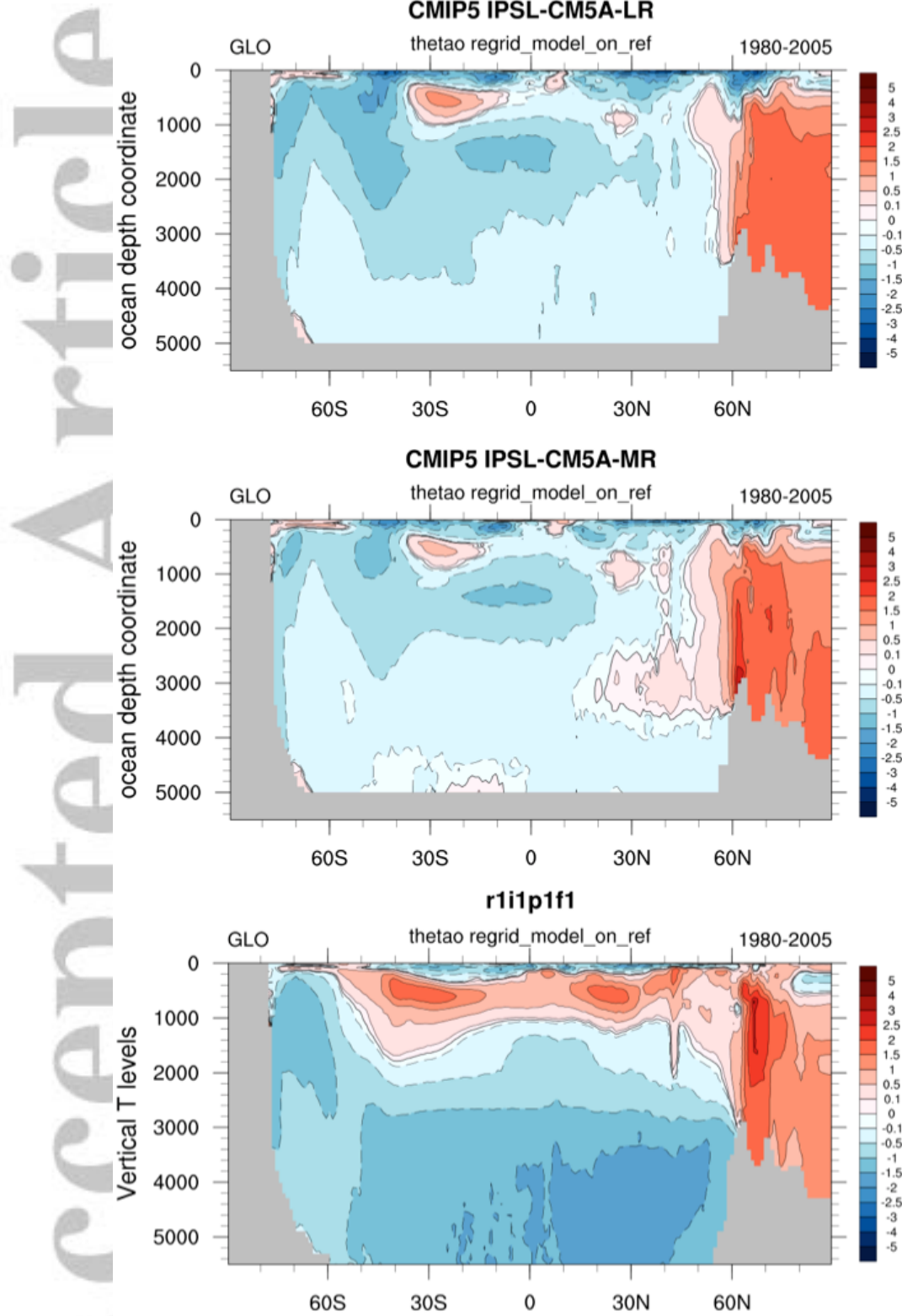


Figure 9. Latitude-depth distribution of the global zonal mean ocean temperature bias ($^{\circ}\text{C}$) for IPSL-CM5A-LR (upper row), IPSL-CM5A-MR (middle row) and IPSL-CM6A-LR (bottom row). Biases are computed against data from the World Ocean Atlas (WOA13-v2, Locarnini et al., 2013) over the 1955-2015 period.

Accepted Article

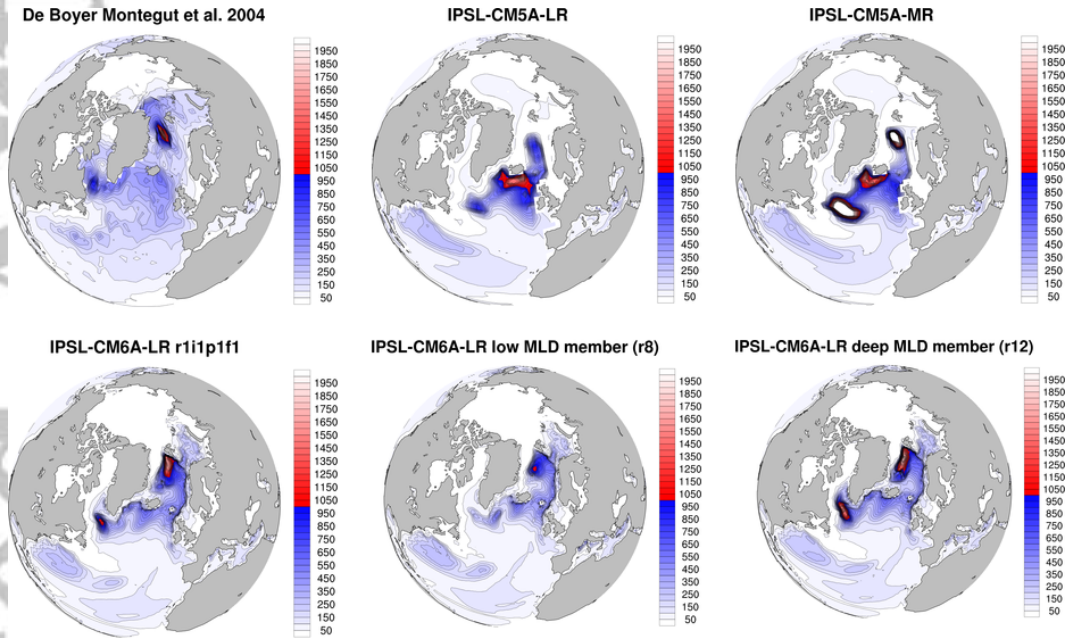


Figure 10. Annual monthly maximum of the Mixed Layer Depth (MLD, in m) in the North Atlantic for the reconstruction of de Boyer Montégut et al. (2004, upper left panel), IPSL-CM5A-LR and IPSL-CM5A-MR (upper middle and right panels), and for three IPSL-CM6A-LR historical members: the first member (r1i1p1f1, lower left panel), a member visually identified with a shallow mixed layer (r8i1p1f1, lower middle panel) and a member visually identified with a deep mixed layer (r12i1p1f1, lower right panel).

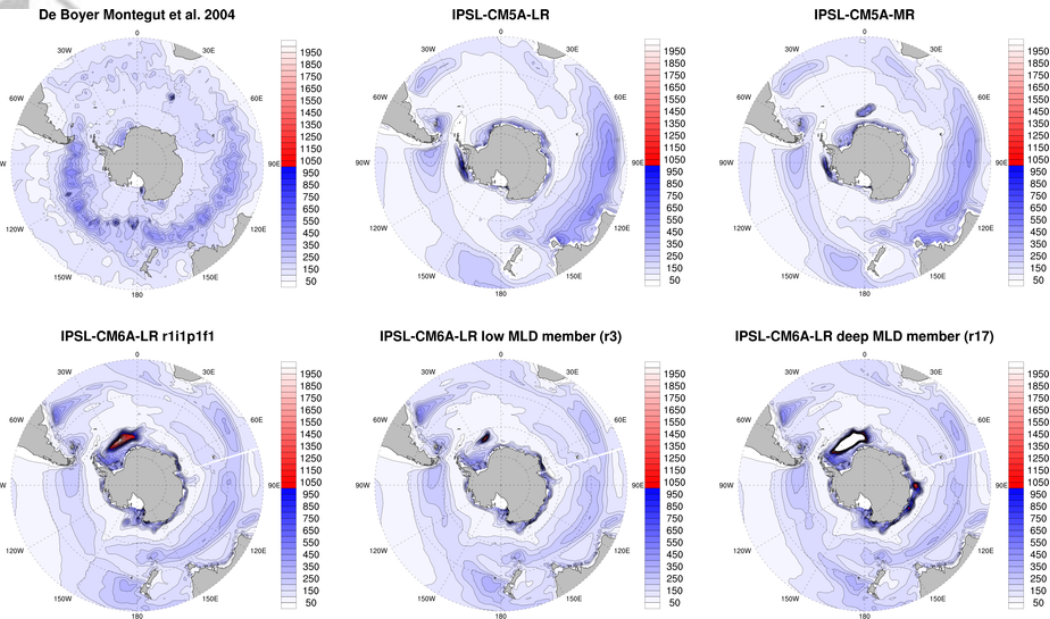


Figure 11. Same as Figure 10 but for the Southern Ocean. For IPSL-CM6A-LR, the lower left panel is also `r1i1p1f1`, the lower middle panel is the member visually identified with a shallow mixed layer (`r3i1p1f1`) and the lower right corner is the member visually identified with a deep mixed layer (`r17i1p1f1`).

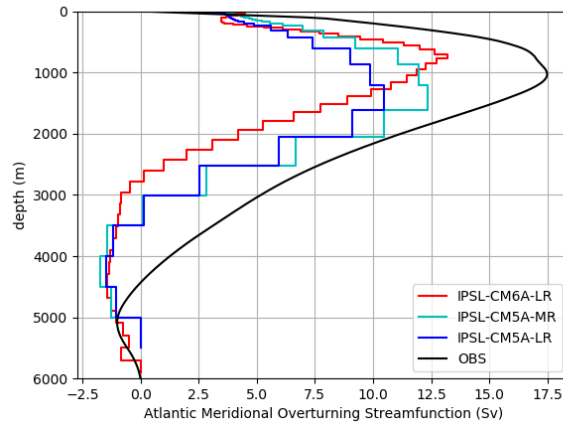


Figure 12. Vertical profile of the meridional overturning streamfunction (in Sv) at 26°N in the Atlantic Ocean for IPSL-CM6A-LR (red line), IPSL-CM5A-LR (dark blue line), IPSL-CM5A-MR (light blue line) and the RAPID-WATCH observations (black line, Smeed et al., 2017).

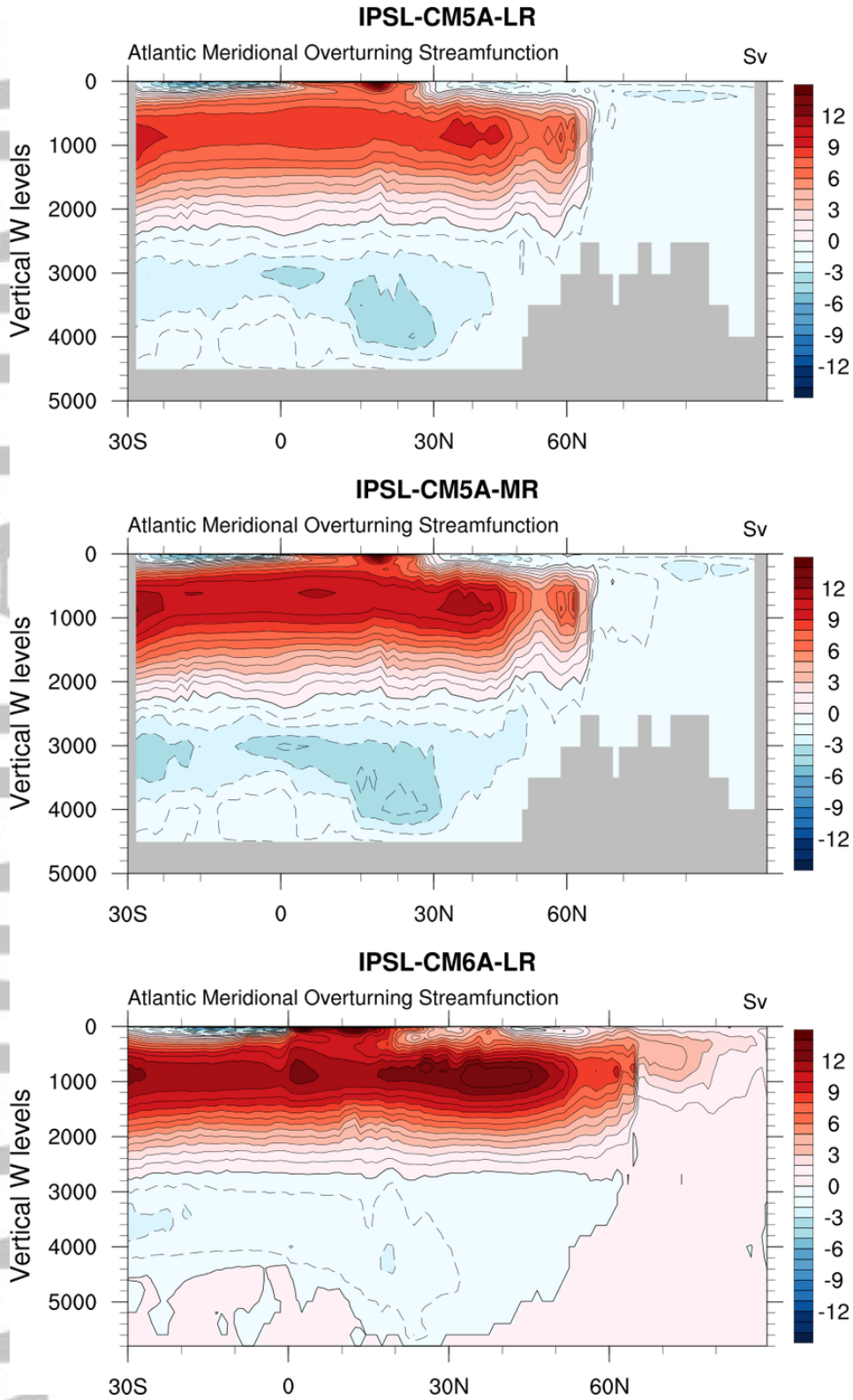


Figure 13. Atlantic meridional overturning streamfunction (in Sv) for IPSL-CM5A-LR (top panel), IPSL-CM5A-MR (middle panel) and IPSL-CM6A-LR (bottom panel) as a function of depth and latitude, on average over the 1980–2005 period.

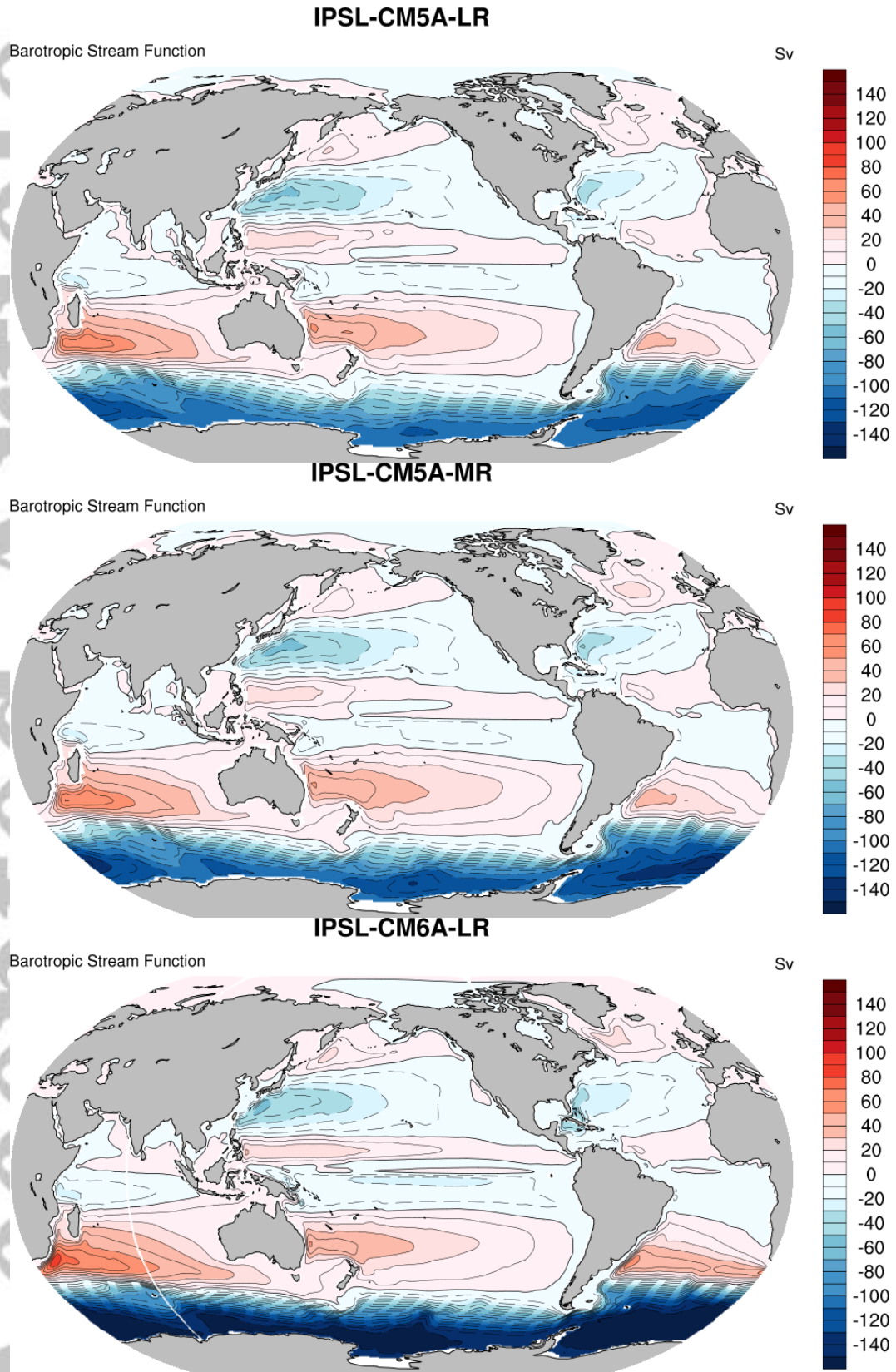


Figure 14. Barotropic streamfunction (in Sv) for IPSL-CM5A-LR (top panel), IPSL-CM5A-MR (middle panel) and IPSL-CM6A-LR (bottom panel).

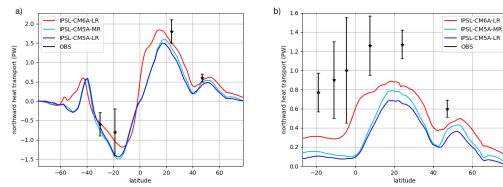


Figure 15. (a) Global and (b) Atlantic Ocean meridional heat transport (in PW) for IPSL-CM5A-LR (dark blue line), IPSL-CM5A-MR (light blue line), and IPSL-CM6A-LR (red line) over the 1980–2005 period and corresponding direct observations (black stars with error bars) from Ganachaud and Wunsch (2003).

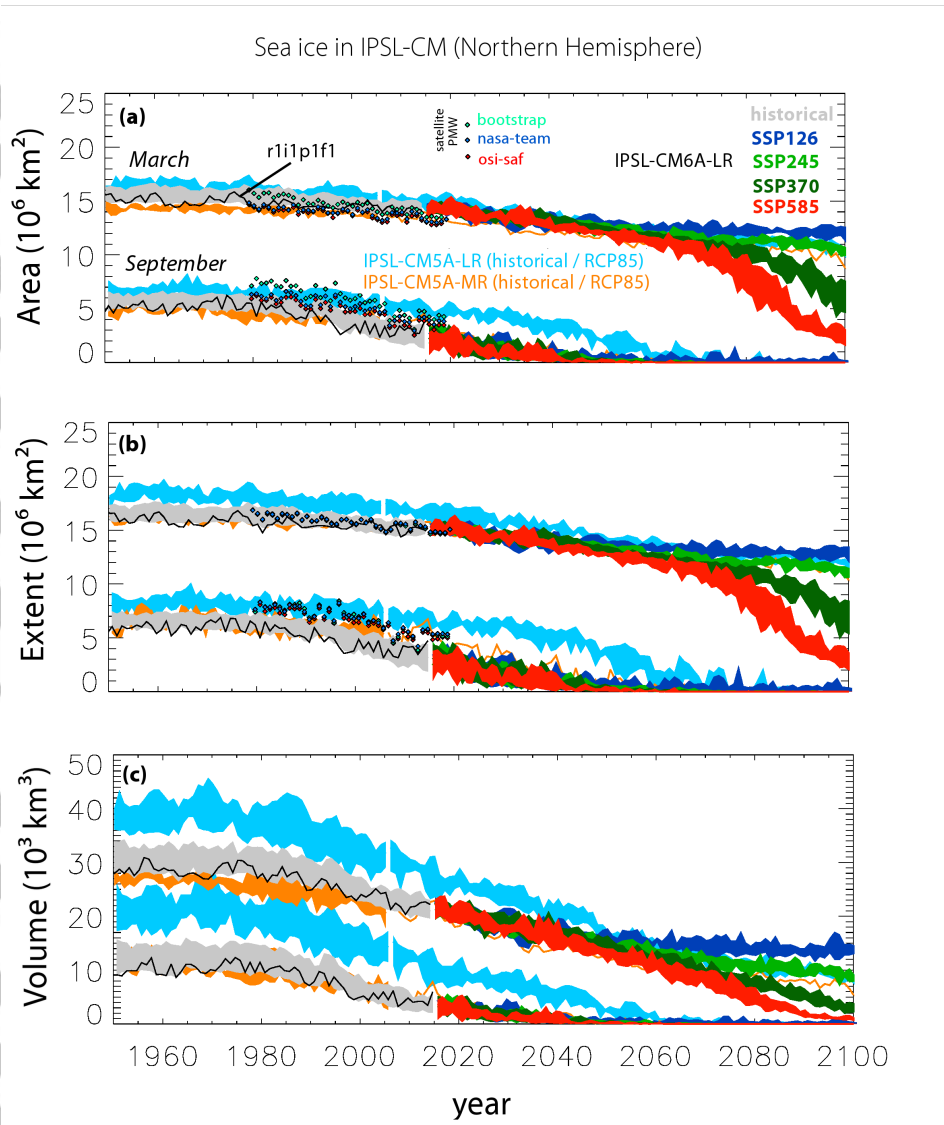


Figure 16. Time series of integrated sea ice diagnostics (area, extent –both in 10^6 km^2 – and volume –in 10^3 km^3) over the Northern Hemisphere. Sea ice area is the integral of ice fraction within a given region – here the Northern Hemisphere. Ice extent is the area total area enclosed within the 15% sea ice fraction contour. Ice volume is the integral of ice fraction times thickness. IPSL-CM6A-LR simulations feature the *historical* *r1i1p1f1* member in black, other *historical* ensemble members in grey (16-85% confidence interval), and selected scenario runs in color. The 16-85% confidence range is also shown for IPSL-CM5A-LR (blue) and IPSL-CM5A-MR (orange), for historical and RCP8.5 runs. Symbols depict passive microwave satellite-based retrievals from three different algorithms: Nasa Team (Cavalieri et al., 1996), Bootstrap (Comiso, 1996), and OSI-SAF (OSI-SAF, 1996). The upper and lower curves correspond to March and September, respectively.

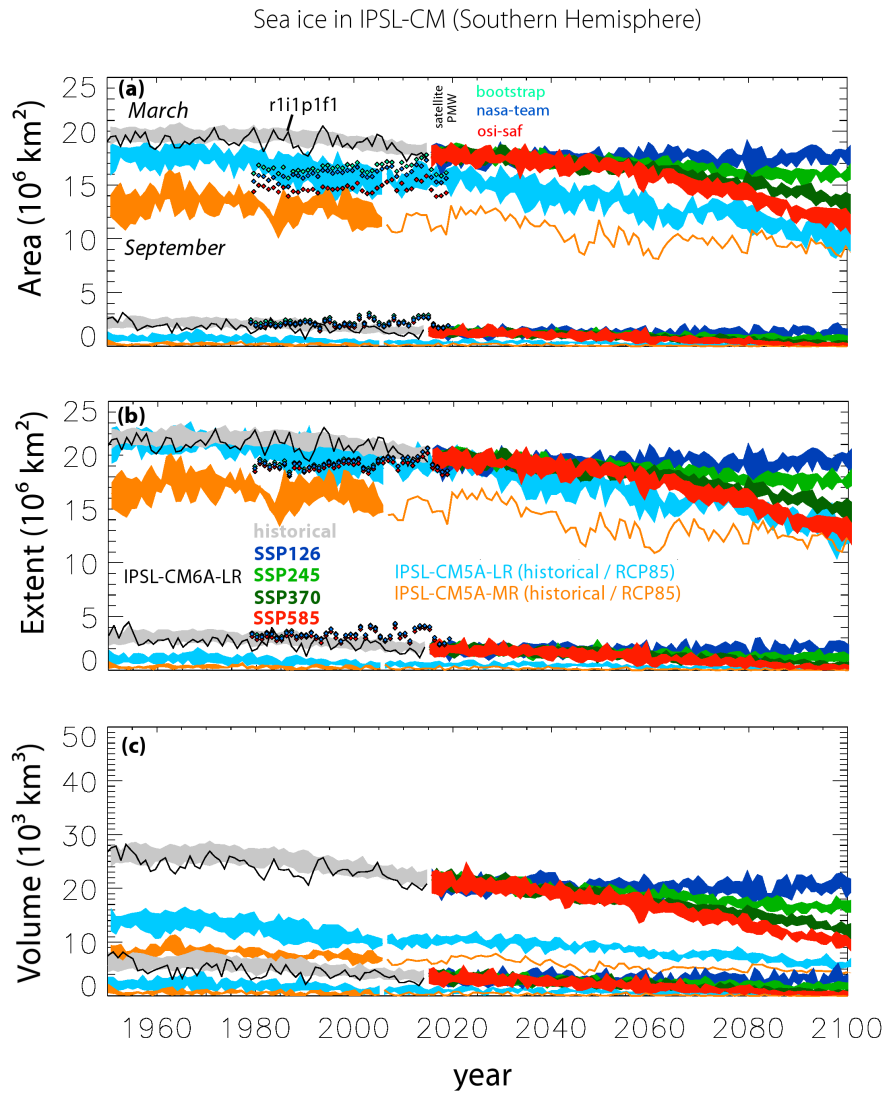


Figure 17. Same as Figure 16 but for the Southern Hemisphere. The upper and lower curves correspond to the September and February months, respectively.

Accepted Article

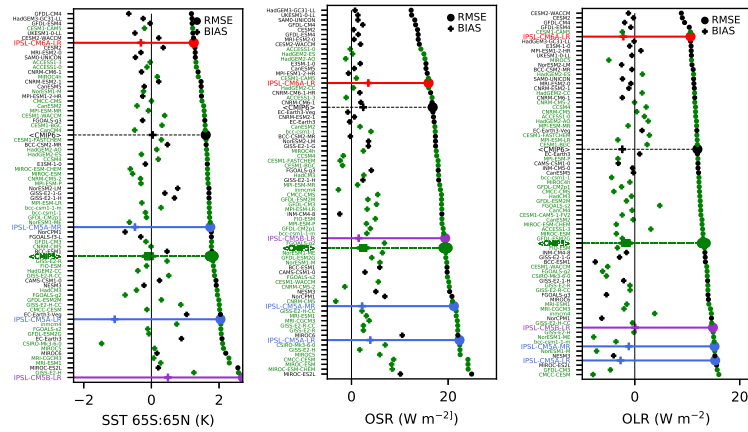


Figure 18. Biases (crosses) and root mean square errors (RMSE, closed circles) against observations of SST averaged over the 65°S–65°N latitudinal region (in °C), outgoing shortwave radiation (OSR, in W m^{-2}) and outgoing longwave radiation (OLR, in W m^{-2}) for CMIP5 models (in green) including IPSL-CM5A-LR and IPSL-CM5A-MR (in blue) and IPSL-CM5B-LR (in purple) and CMIP6 models (in black) including IPSL-CM6A-LR (in red). The averages of the scores for CMIP5 and CMIP6 models are shown as $\langle \text{CMIP5} \rangle$ and $\langle \text{CMIP6} \rangle$, respectively.

The models are ranked according to their RMSE. $\langle \text{CMIP5} \rangle$ is shown as a range through random sampling of an equivalent number of CMIP5 models. The RMSE is computed on the mean

seasonal cycle for the period 1979–2005 against SST from the input4MIPs dataset and radia-

Accepted Article

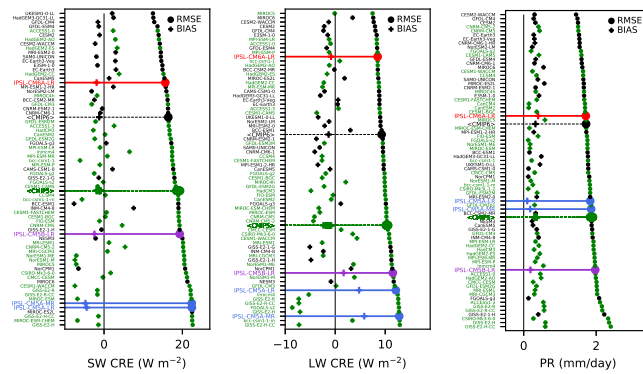


Figure 19. Same as Figure 18 but for the shortwave cloud radiative effect (SW CRE, in W m^{-2}), longwave cloud radiative effect (LW CRE, in W m^{-2}) and precipitation (PR, in mm day^{-1}). The RMSE and biases are computed against the radiative fluxes from CERES-EBAF and precipitation from GPCP.

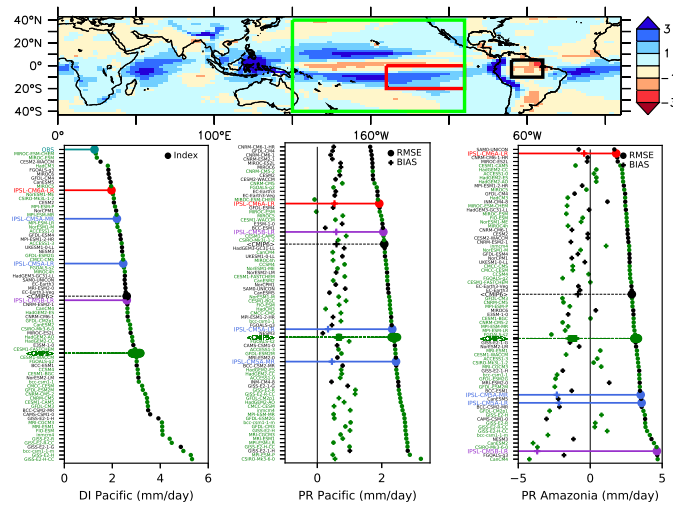


Figure 20. Same as Figure 18 but for the double ITCZ index (DI Pacific, in mm day^{-1}), Pacific precipitation (in mm day^{-1}), and the Amazonian precipitation (in mm day^{-1}). The DI Pacific index is the annually averaged precipitation over the Southeastern Pacific Ocean in the $[150^\circ\text{W}-100^\circ\text{W}, 20^\circ\text{S}-0^\circ\text{S}]$ region (this diagnostics is performed on the native grid). The Pacific precipitation is annually averaged over the $[150^\circ\text{E}-100^\circ\text{W}, 40^\circ\text{S}-40^\circ\text{N}]$ region. The Amazonian precipitation is annually averaged over the $[65^\circ\text{W}, 50^\circ\text{W}, 15^\circ\text{S}, 0^\circ\text{S}]$ region. The map shows the multi-model averaged CMIP6 precipitation bias, which guided the choice of the regions to compute the indices.

Accepted Article

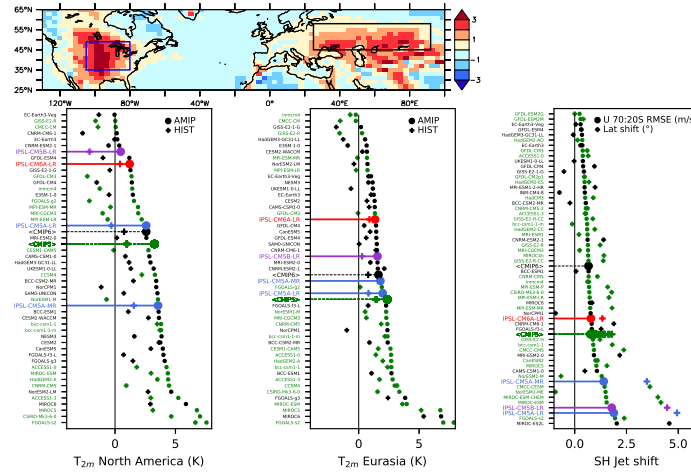


Figure 21. Left and middle panels: mean June-July-August (JJA) near-surface temperature biases (in $^{\circ}\text{C}$) for *amip* (circles) and *historical* (plus signs) CMIP simulations averaged over a North American [105°W – 80°W , 35°N – 50°N] region and an Eurasian [23°E – 92°E , 45°N – 58°N] region. The map shows the multi-model averaged CMIP6 JJA near-surface temperature bias, which guided the choice of the regions to compute the indices. Right panel: same as Figure 18 but for the SH jet latitude. The bias is computed from the annually- and zonally-averaged near-surface wind $\overline{u_{10m}}$ as a weighted average of the latitude ϕ over the [70°S , 10°S] latitudinal band:

$$\int_{70^{\circ}\text{S}}^{10^{\circ}\text{S}} \max(\overline{u_{10m}} - 1, 0) \phi d\phi / \int_{70^{\circ}\text{S}}^{10^{\circ}\text{S}} \max(\overline{u_{10m}} - 1, 0) d\phi.$$

The RMSE on this graph is computed directly from $\overline{u_{10m}}$. The reference near-surface wind climatology is taken from the ERA-Interim

Accepted Article

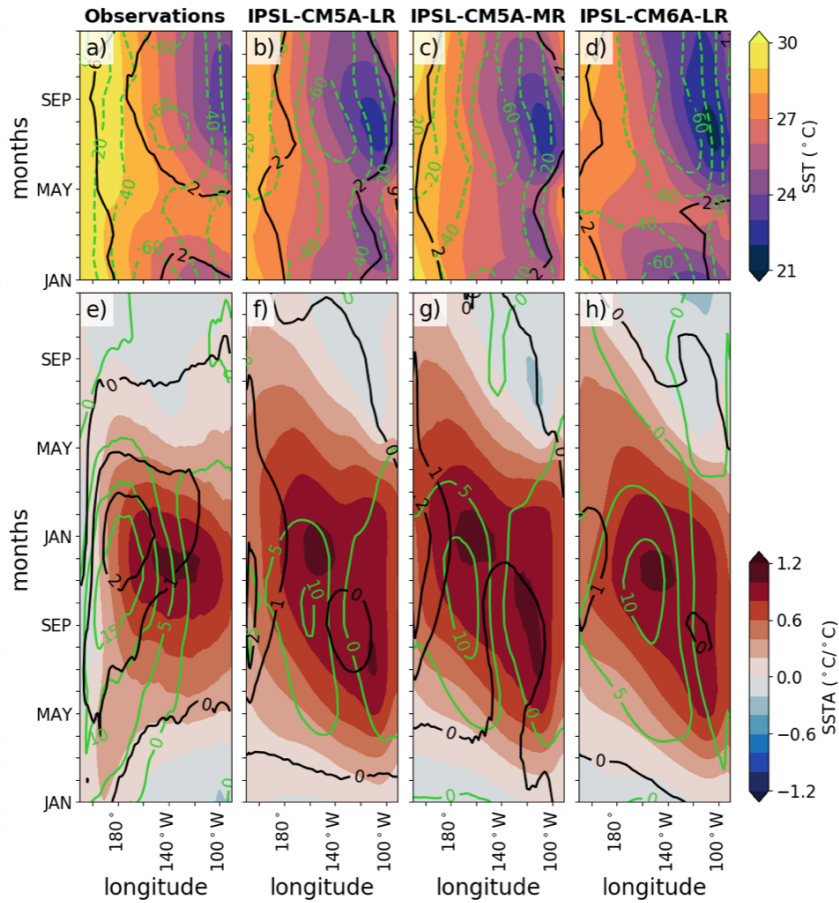


Figure 22. Longitude-time section of the Pacific Ocean 5°S – 5°N average mean seasonal cycle of SST (colors, $^{\circ}\text{C}$), zonal wind stress $\times 1000$ (green contours, N m^{-2}) and rainfall (black contours, mm day^{-1}) for a) observations, b) IPSL-CM5A-LR, c) IPSL-CM5A-MR and d) IPSL-CM6A-LR. Longitude-time section of the 5°S – 5°N typical anomalies during an ENSO event: SST (colors, $^{\circ}\text{C } ^{\circ}\text{C}^{-1}$), zonal wind stress $\times 1000$ (green contours, $\text{N m}^{-2} ^{\circ}\text{C}^{-1}$) and rainfall (black contours, $\text{mm day}^{-1} ^{\circ}\text{C}^{-1}$) for e) observations, f) IPSL-CM5A-LR, g) IPSL-CM5A-MR and h) IPSL-CM6A-LR. The typical ENSO anomalies are obtained as a lead/lag regression to the November-January averaged Niño3.4 SST anomalies. The average of the 6 available IPSL-CM5A-LR, 3 available IPSL-CM5A-MR and 32 available IPSL-CM6A-LR *historical* members is used. Observations (1980–2018) are from GPCPv2.3 (Adler et al., 2018) for rainfall and TropFlux (Praveen Kumar et al., 2012, 2013) for SST and zonal wind stress.

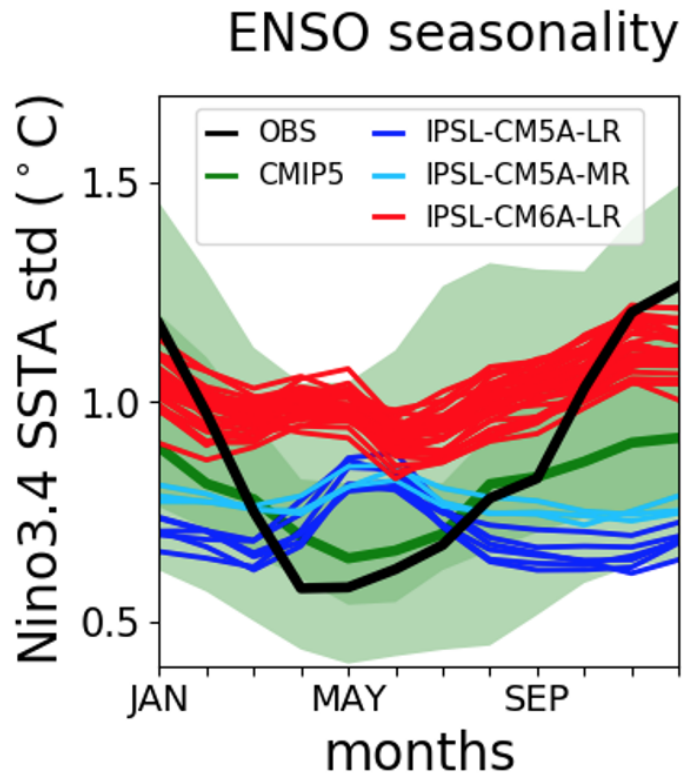


Figure 23. Seasonally-stratified standard deviation of the average Niño3.4 SST anomalies for observations (black), the 6 IPSL-CM5A-LR (dark blue), 3 IPSL-CM5A-MR (light blue) and 32 IPSL-CM6A-LR (red) members. The green shading indicates the range of values from the CMIP5 multi-model database (green curve = median, dark green = 25th to 75th percentiles, light green = 5th to 95th percentile). Observations are from GPCP v2.3 (Adler et al., 2018) for rainfall and TropFlux (Praveen Kumar et al., 2012) for SST over the period 1980–2018.

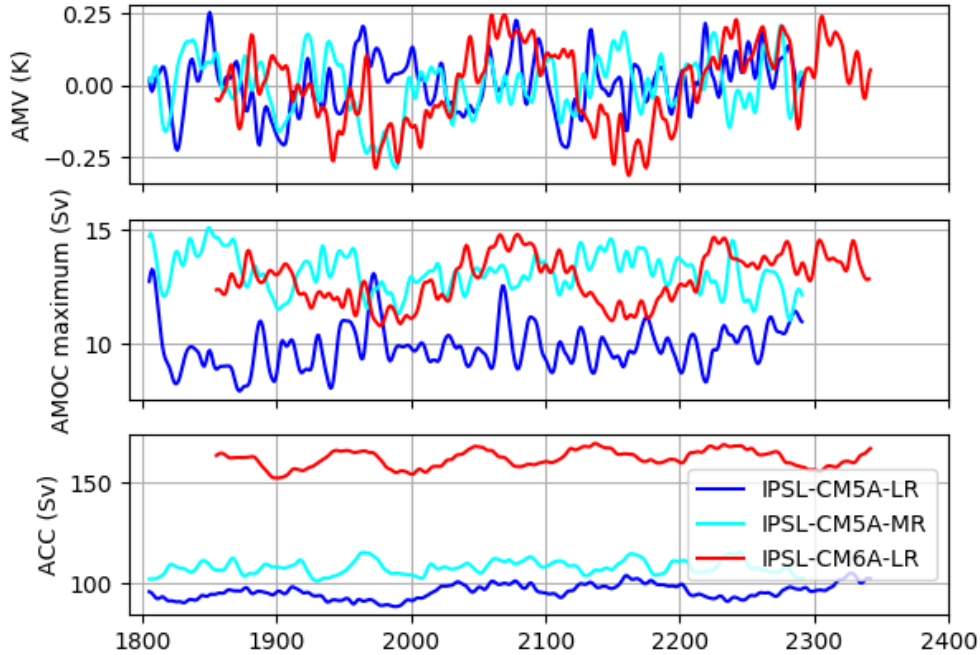


Figure 24. Time evolution of the AMV index (top panel, in K), AMOC maximum (middle panel, in Sv) and Antarctic Circumpolar Current (ACC) measured as the mass transport through the Drake Passage (bottom panel, in Sv) in the IPSL-CM5A-LR, IPSL-CM5A-MR, and IPSL-CM6A-LR model versions. The AMV index is defined as the detrended 10-year low-pass filtered annual mean area-averaged SST anomalies over the North Atlantic basin (0°N – 65°N , 80°W – 0°E). The AMOC maximum is taken from the meridional streamfunction between 10°N and 60°N and below 500 m. The mass transport at the Drake Passage is integrated from the surface to depth between the Cape Horn and the western Antarctic Peninsula.

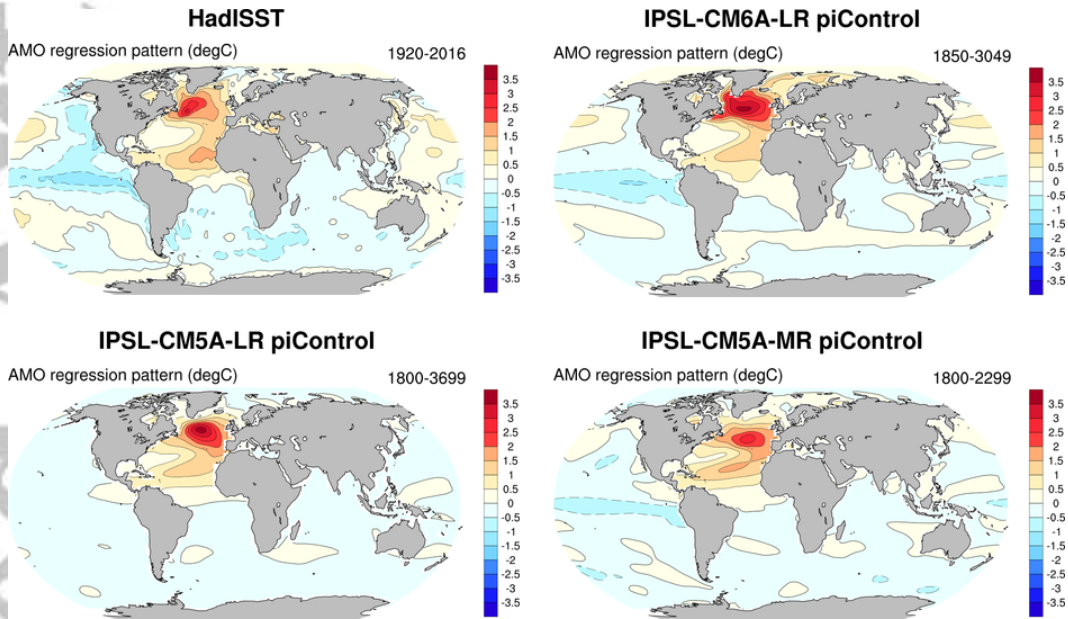


Figure 25. Pattern of the Atlantic Multidecadal Variability (AMV) defined as the regression (in $^{\circ}\text{C}^{\circ}\text{C}^{-1}$) of the global SST on the AMV index defined as the 10-year low-pass filtered annual mean area-averaged SST anomalies over the North Atlantic basin (0°N – 60°N , 80°W – 0°E) for the HadISST observations (1920–2016 period), and the IPSL-CM5A-LR, IPSL-CM5A-MR and IPSL-CM6A-LR models. The SST weighted average between 60°N and 60°S was subtracted from each grid point prior to any calculation, in order to account for the global warming trend following Trenberth and Shea (2006).

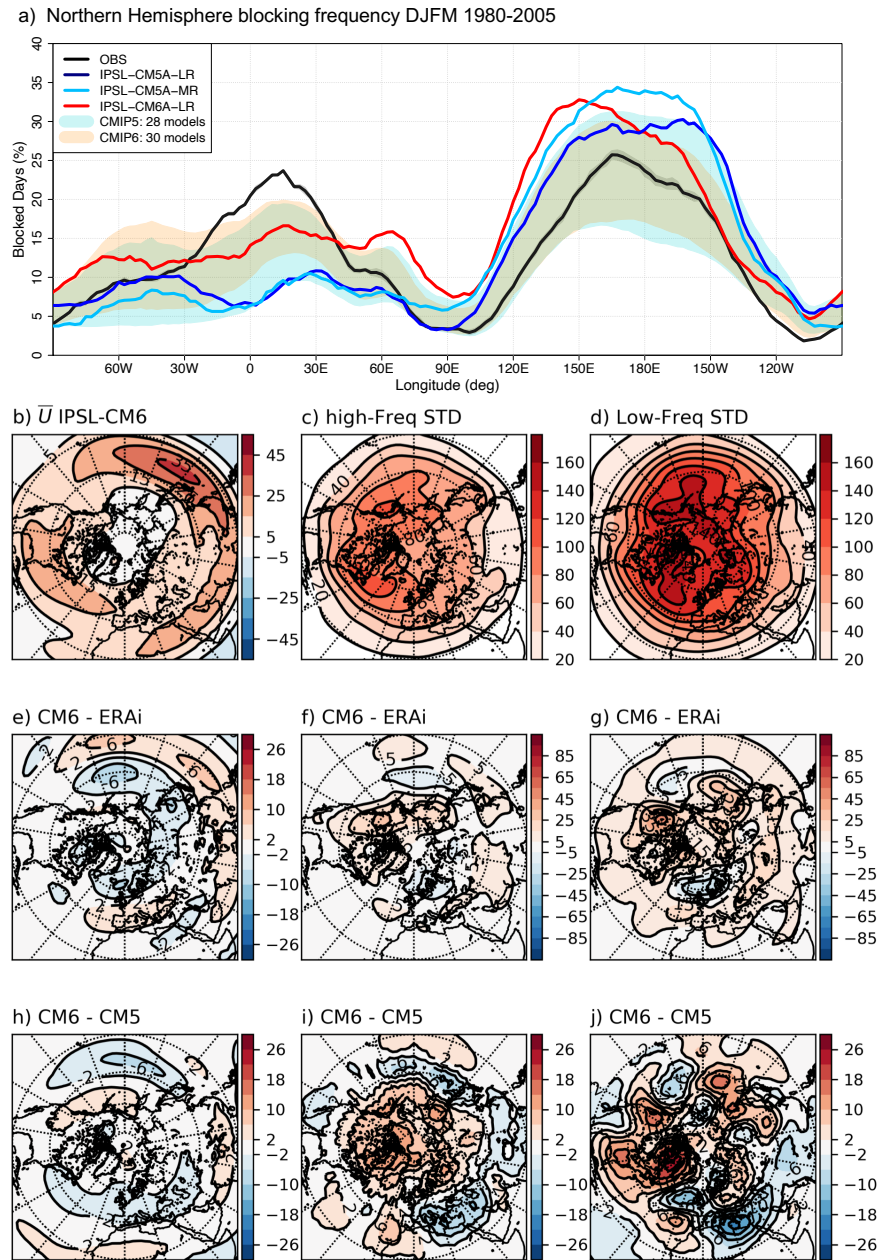


Figure 26. Diagnostics of wintertime (DJFM) Northern Hemisphere midlatitude dynamics: a) 1980–2005 frequency (in %) of blocked days as a function of longitude in observations (black line: average between JRA-55 Reanalysis, NCEP/NCAR Reanalysis and ECMWF ERA-Interim Reanalysis), IPSL-CM5A-LR (dark blue line), IPSL-CM5A-MR (light blue line) and IPSL-CM6A-LR (red line). CMIP5 (shaded blue) and CMIP6 (shaded orange) multi-model ensemble spread is also shown as the ± 1 standard deviation from the ensemble mean; b) 1980–2005 mean zonal

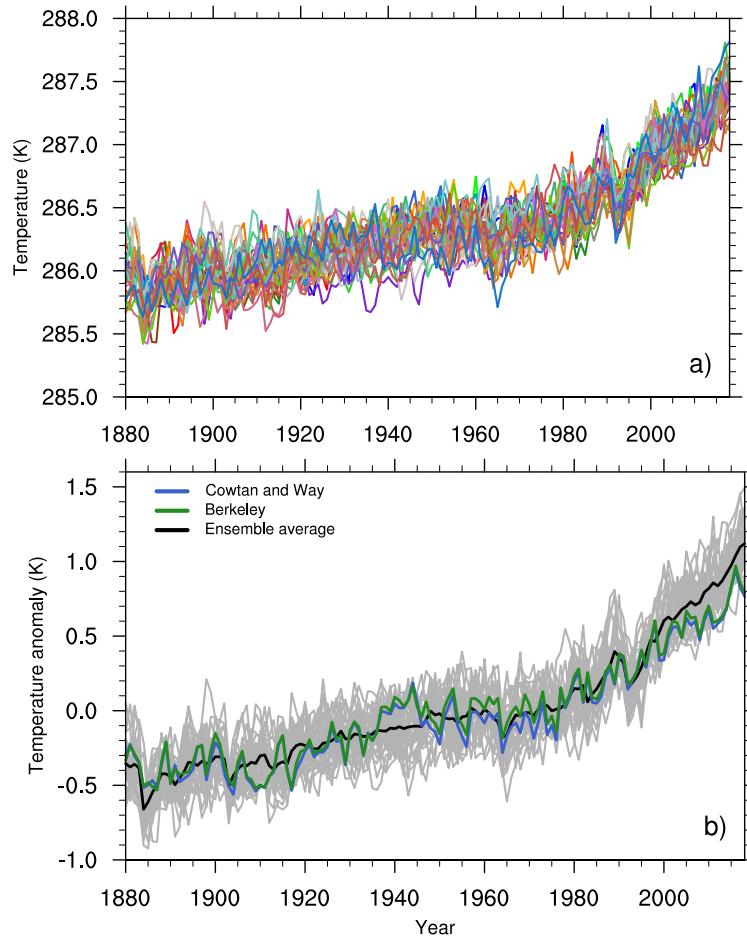


Figure 27. Time evolution of a) the annual global mean near-surface air temperature (GMST, in K) from the 31 *historical* members, prolonged using SSP245 forcings, of the IPSL-CM6A-LR model and b) the anomalies of GMST relative to the 1880-2018 average for the Cowtan and Way (2014, in blue) and the Berkeley (Rohde, Muller, Jacobsen, Muller, et al., 2013; Rohde, Muller, Jacobsen, Perlmutter, et al., 2013, in green) datasets, and for the model ensemble average (in black) of the individual *historical* members (in grey).

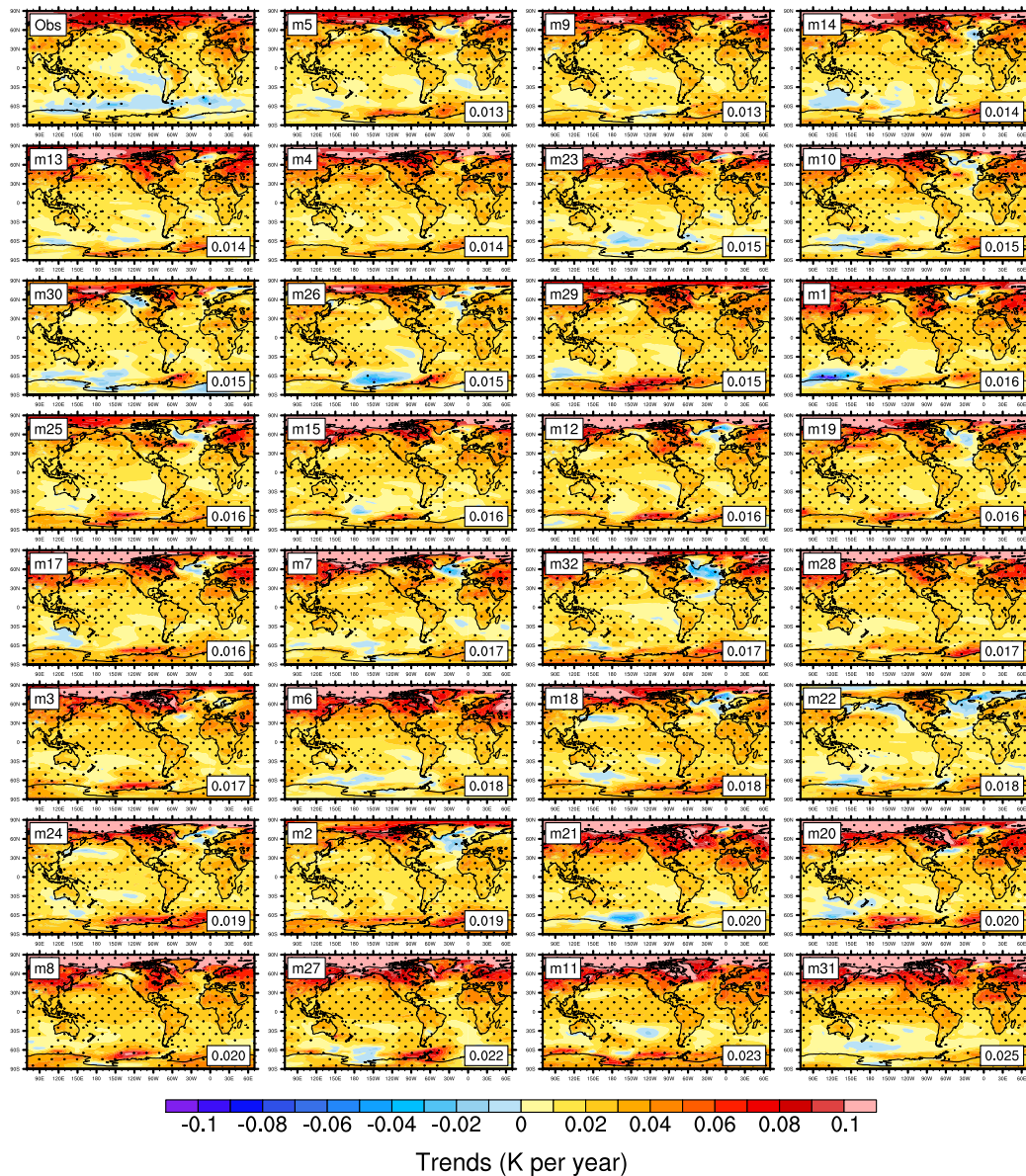


Figure 28. Trends in near-surface air temperature (K yr^{-1}) from the Cowtan and Way (2014) dataset (upper left panel) and from the *historical* members of the IPSL-CM6A-LR model for the 1978–2018 period. Members are classified (from left to right, and top to bottom) by increasing spatial root-mean-square error (RMSE) relative to the observations. The member number and the RMSE values are indicated on the top-left and bottom-right corners of each panel, respectively. Dotted hatching indicates grid boxes where trends are significant (Mann-Kendall test, $p < 0.1$).

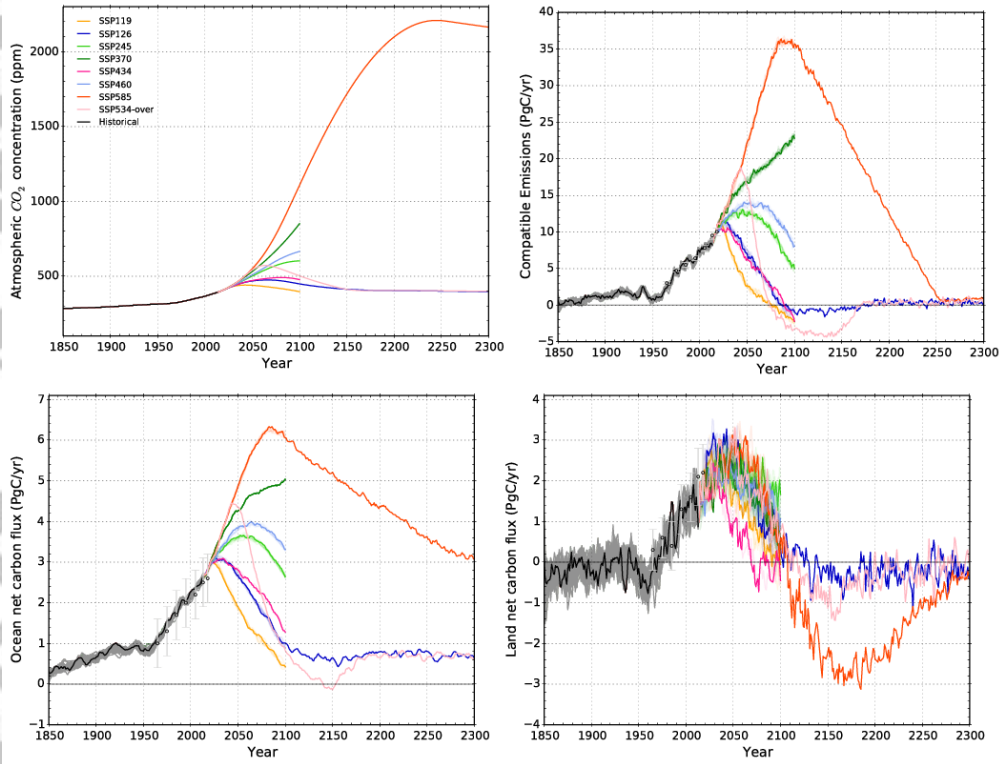


Figure 29. Prescribed atmospheric CO₂ mixing ratio (ppmv, upper left), and inferred “compatible” emissions (upper right), oceanic (lower left) and terrestrial (lower right) net CO₂ fluxes (in Pg C yr⁻¹) in IPSL-CM6A-LR for the historical period (*historical r1i1p1f1* in black and other ensemble members in grey) and the future scenario experiments (colored lines). A five-year running average is applied for the fluxes. Estimates from the Global Carbon Project (Friedlingstein et al., 2019) and their uncertainties are indicated with black circles and grey error bars.

Quantity / Model	IPSL-CM5A-LR	IPSL-CM6A-LR
ERF $2\times\text{CO}_2$ (W m^{-2})	–	3.50 ± 0.27
ERF $4\times\text{CO}_2$ (W m^{-2})	6.65 ± 0.18	7.64 ± 0.22
ΔT $4\times\text{CO}_2$ (900 years, K)	–	10.02 (9.56, 10.62)
ΔT $4\times\text{CO}_2$ (300 years, K)	8.12 (7.55, 8.74)	9.49 (8.65, 10.40)
ΔT $4\times\text{CO}_2$ (150 years, K)	8.08 (7.36, 9.90)	9.05 (8.05, 10.20)
ECS from $4\times\text{CO}_2$ (900 years, factor 2, K)	–	5.01 (4.76, 5.28)
ECS from $4\times\text{CO}_2$ (300 years, factor 2, K)	4.06 (3.78, 4.37)	4.75 (4.33, 5.21)
ECS from $4\times\text{CO}_2$ (150 years, factor 2, K)	4.04 (3.68, 4.45)	4.53 (4.02, 5.10)
ECS from $4\times\text{CO}_2$ (300 years, scaled by ERF, K)	–	4.35
ECS from $4\times\text{CO}_2$ (150 years, scaled by ERF, K)	–	4.15
ECS from $2\times\text{CO}_2$ (300 years, K)	–	3.83 (3.03, 4.88)
TCR (K)	1.96 (2.09)	2.45

Table 4. Effective radiative forcing (ERF, in W m^{-2}), equilibrium global mean surface temperature change (ΔT , in K), different estimates of the equilibrium climate sensitivity (ECS, in K) as derived from *abrupt2xCO2* and *abrupt4xCO2* simulations using variants of the Gregory (2004) method, and transient climate response (TCR) for the IPSL-CM5A-LR and IPSL-CM6A-LR. ERF is calculated as in Lurton et al. (2019) by regressing the anomaly of the net radiative flux at the top-of-atmosphere against the anomaly in global-mean surface temperature using the 20 first years of the experiment. The anomalies are computed after subtracting the *piControl* values year-by-year. The confidence intervals correspond to $\pm 2\sigma$. For IPSL-CM5A-LR, we also provide for reference in parenthesis the TCR value published by (Dufresne et al., 2013).

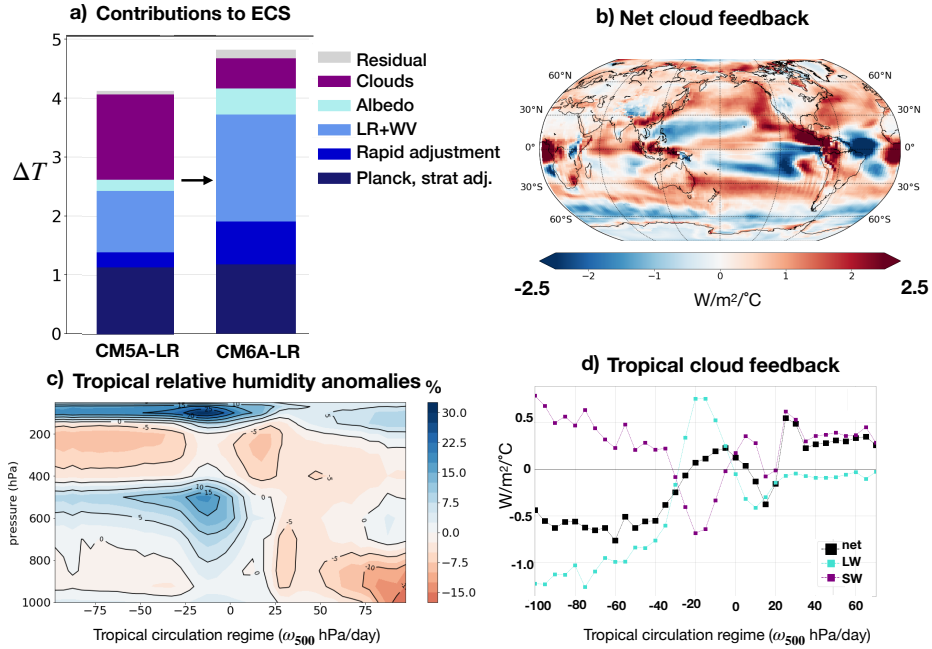


Figure 30. Diagrams supporting our analysis of the model's equilibrium climate sensitivity (ECS). a) Bar plot showing the relative contributions (in K) to the ECS of the stratospheric adjustment, tropospheric rapid adjustments, combined lapse-rate and water vapour (LR+WV), surface albedo and cloud feedbacks for the IPSL-CM5A-LR and IPSL-CM6A-LR models. The residual term is due to nonlinearities in the feedback terms. b) Anomalies in the tropical relative humidity (%) as a function of atmospheric pressure (hPa) and circulation regime as diagnosed by the vertical pressure velocity, ω_{500} in $hPa\ day^{-1}$. c) Distribution of the net cloud feedback (in $W\ m^{-2}\ K^{-1}$) for IPSL-CM6A-LR. d) Tropical net cloud feedback (in $W\ m^{-2}\ K^{-1}$) as a function of the circulation regime as diagnosed by the vertical pressure velocity, ω_{500} in $hPa\ day^{-1}$. The last two diagnostics are computed over the tropical ocean ($30^{\circ}S-30^{\circ}S$)

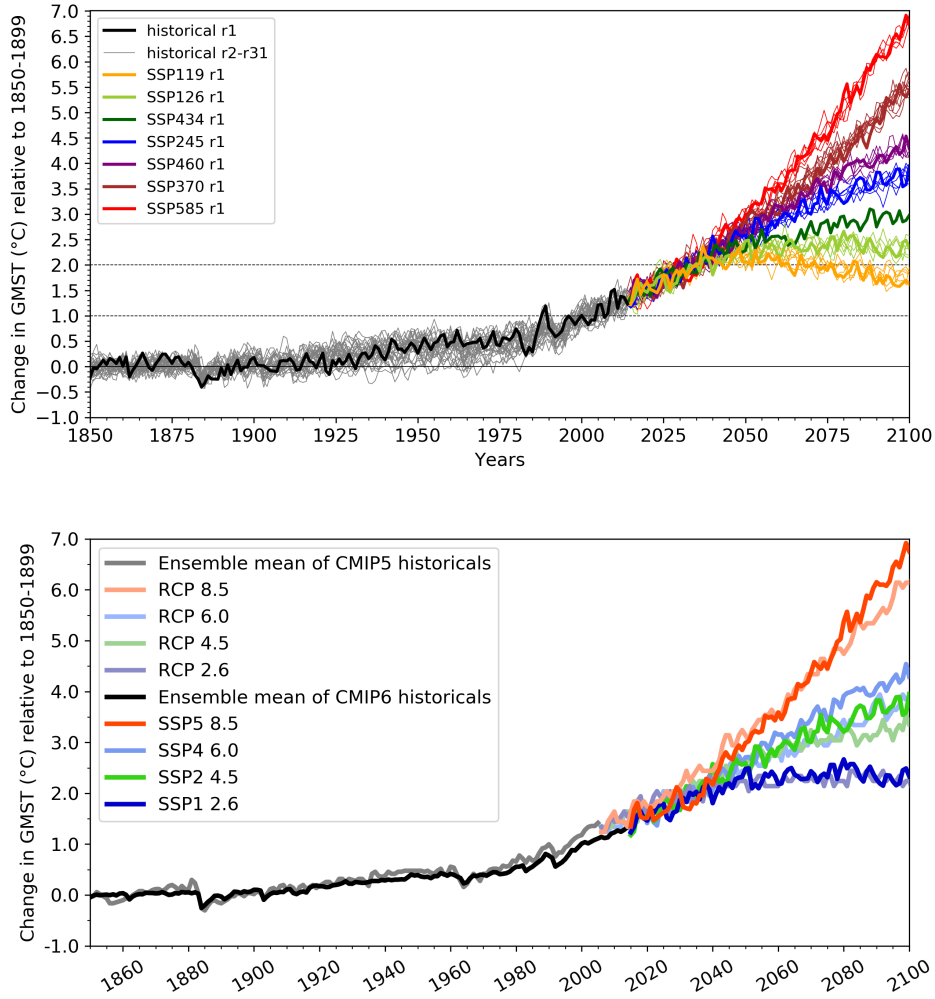


Figure 31. Upper panel: change in global-mean surface air temperature (GMST, in °C) relative to the 1850-1899 period in the *historical r1i1p1f1* member (thick black line) and the other members (thin grey lines) and scenario experiments for the *r1i1p1f1* member (thick colored lines) and other members (thin colored lines). Anomalies for 0, 1, and 2 °C are indicated for reference. Lower panel: change in GMST relative to the 1850-1899 period for the IPSL-CM5A-LR and IPSL-CM6A-LR models for the historical period and the 21st century.

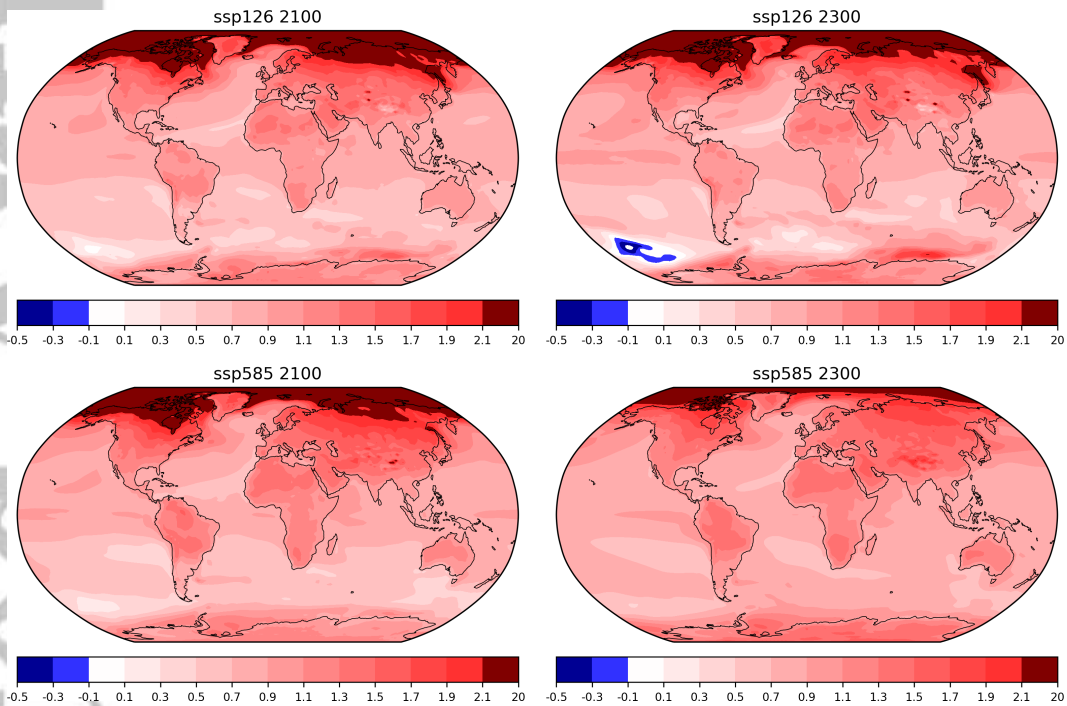


Figure 32. Geographical distributions of the normalised change in near-surface air temperature (in $^{\circ}\text{C } ^{\circ}\text{C}^{-1}$) for the CMIP6 SSP126 (upper panels) and SSP585 (lower panels) *scenario* experiments, at the end of the 21st century (2070–2100 period, left panels) and at the end of the 23rd century (2270–2300, right panels) as simulated by the IPSL-CM6A-LR model. The temperature change is defined relative to the pre-industrial value (averaged over 100 years), and the normalisation consists in dividing the local temperature change by the global-mean surface air temperature change.

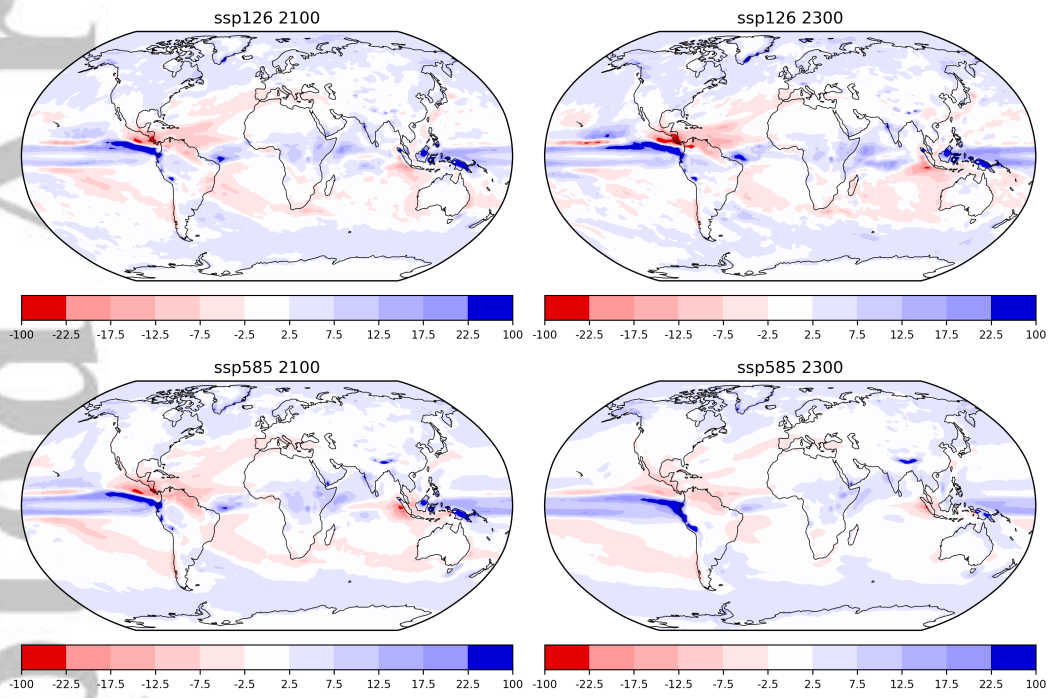


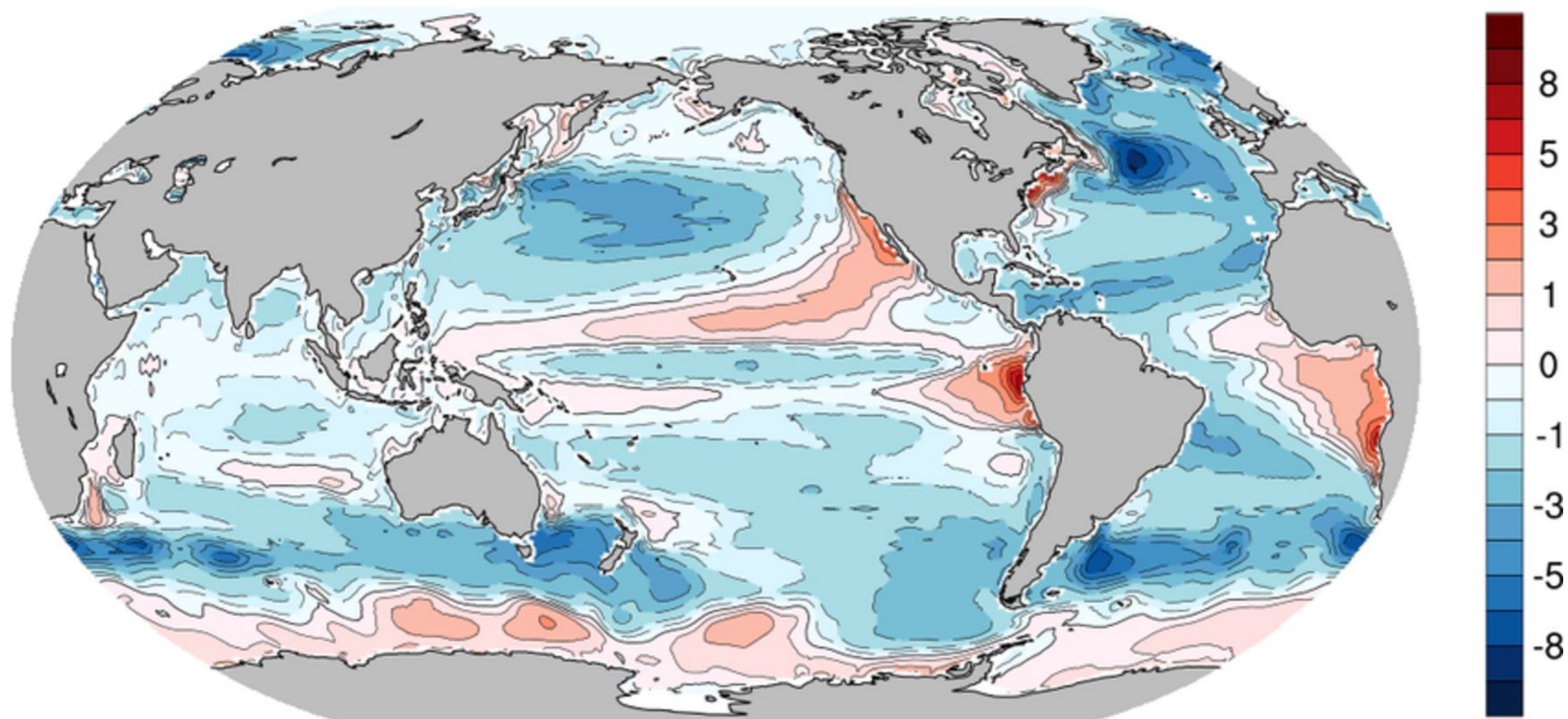
Figure 33. Same as Figure 32 but for the relative change in surface precipitation normalised by the global-mean surface temperature change (in $\% \text{ } ^\circ\text{C}^{-1}$).

Accepted Article

IPSL-CM5A-LR r1i1p1 (vs WOA13-v2) 1980-2005

tos, ANM

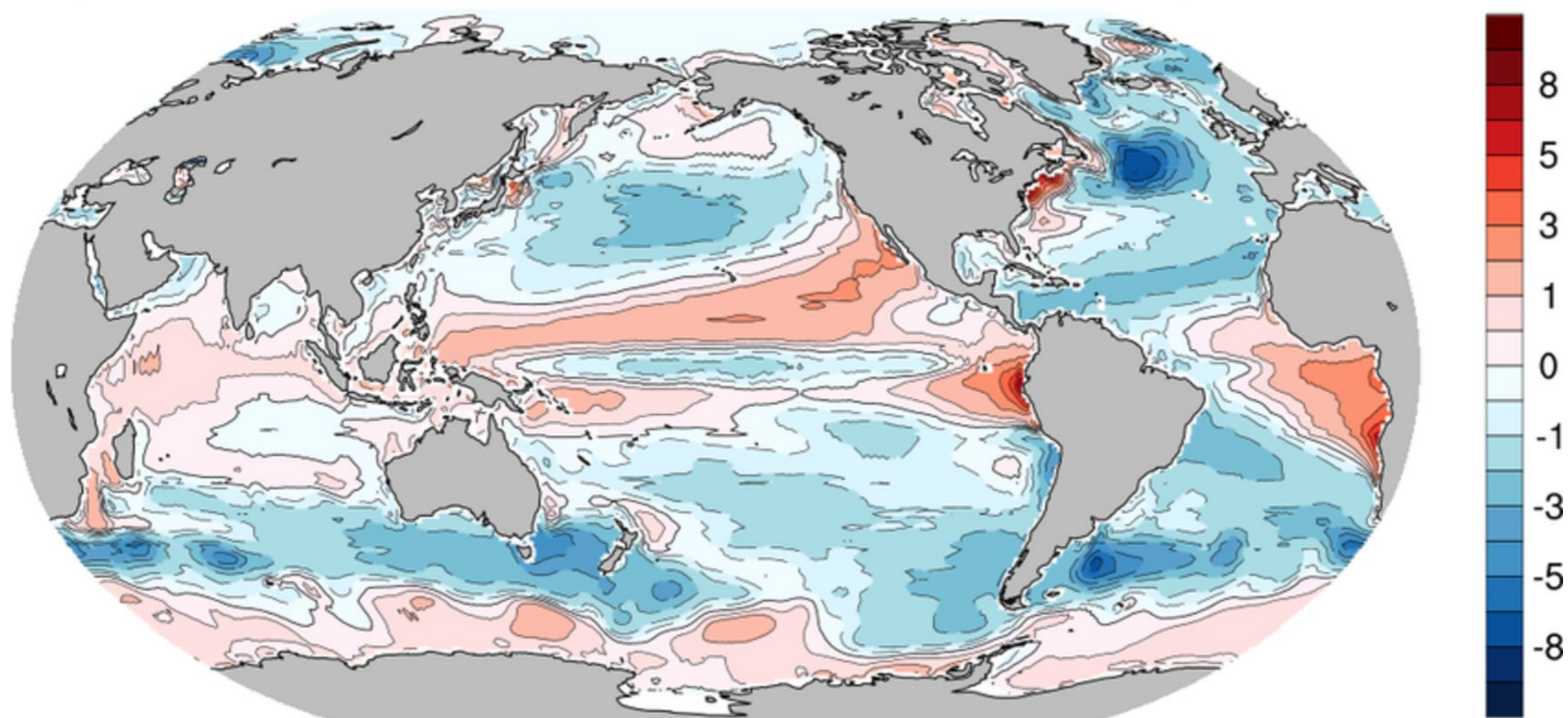
bias=-1.01 ; rmse=1.74 ; corr=0.984



IPSL-CM5A-MR r1i1p1 (vs WOA13-v2) 1980-2005

tos, ANM

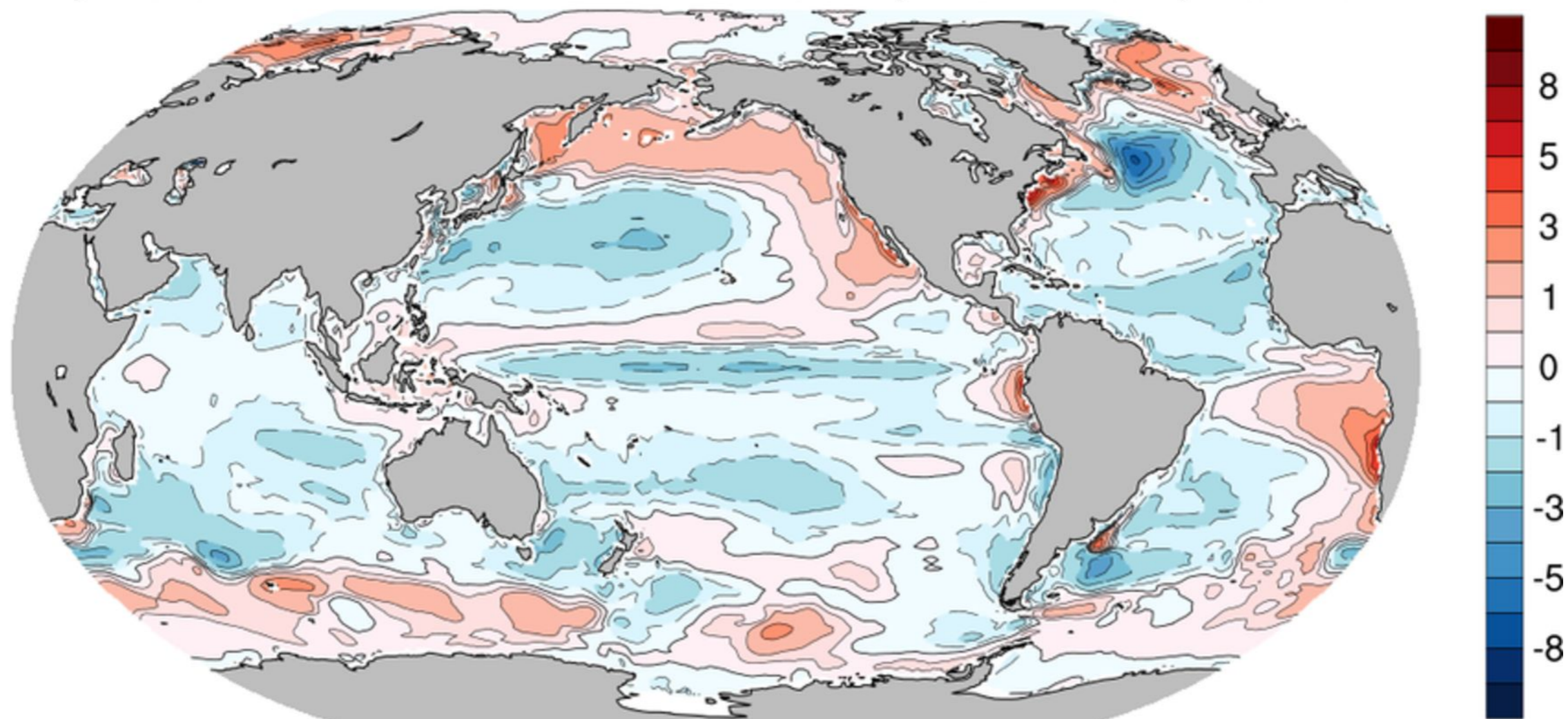
bias=-0.464 ; rmse=1.4 ; corr=0.986



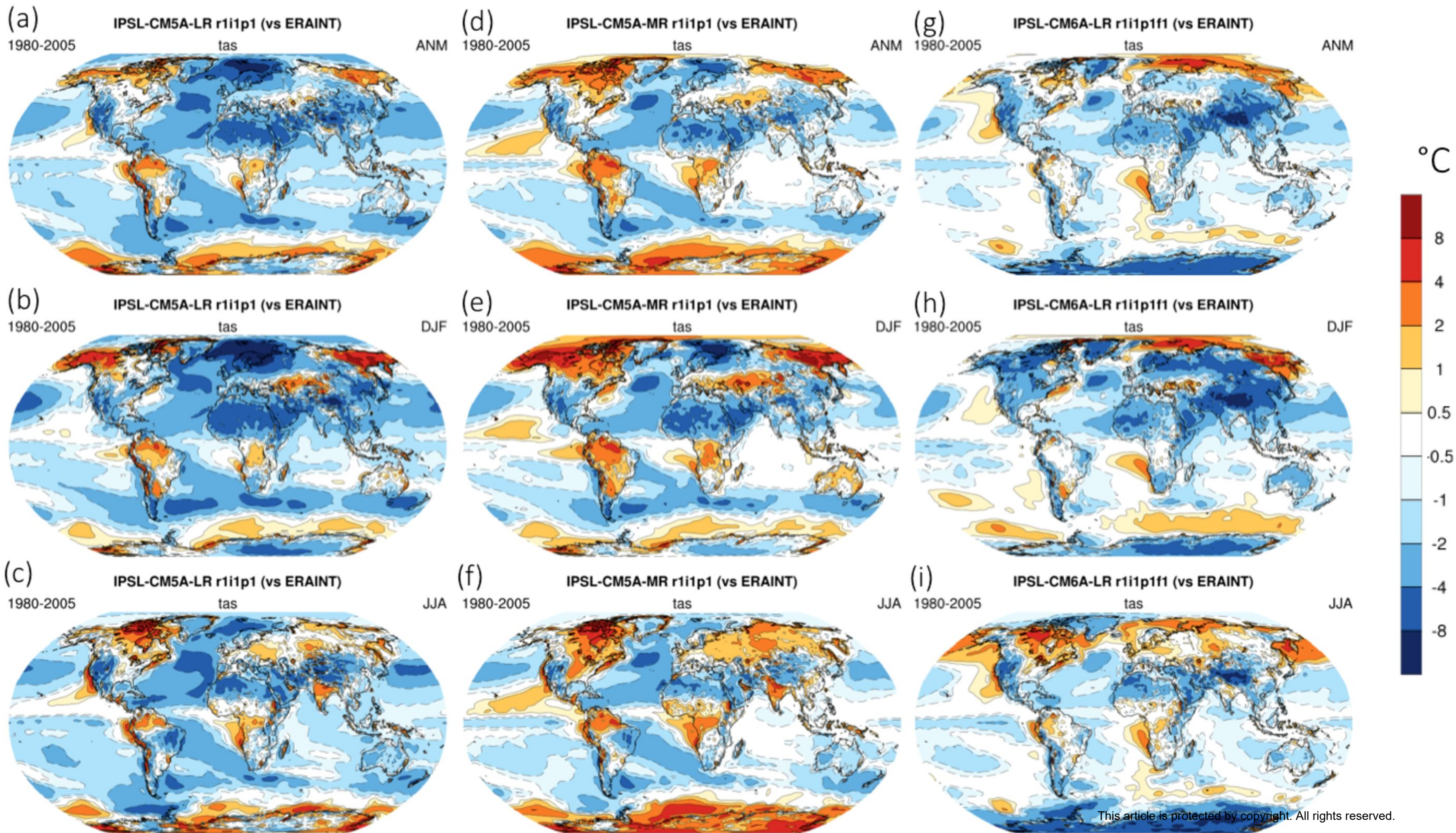
IPSL-CM6A-LR r1i1p1f1 (vs WOA13-v2) 1980-2005

tos, ANM

bias=-0.252 ; rmse=0.975 ; corr=0.988

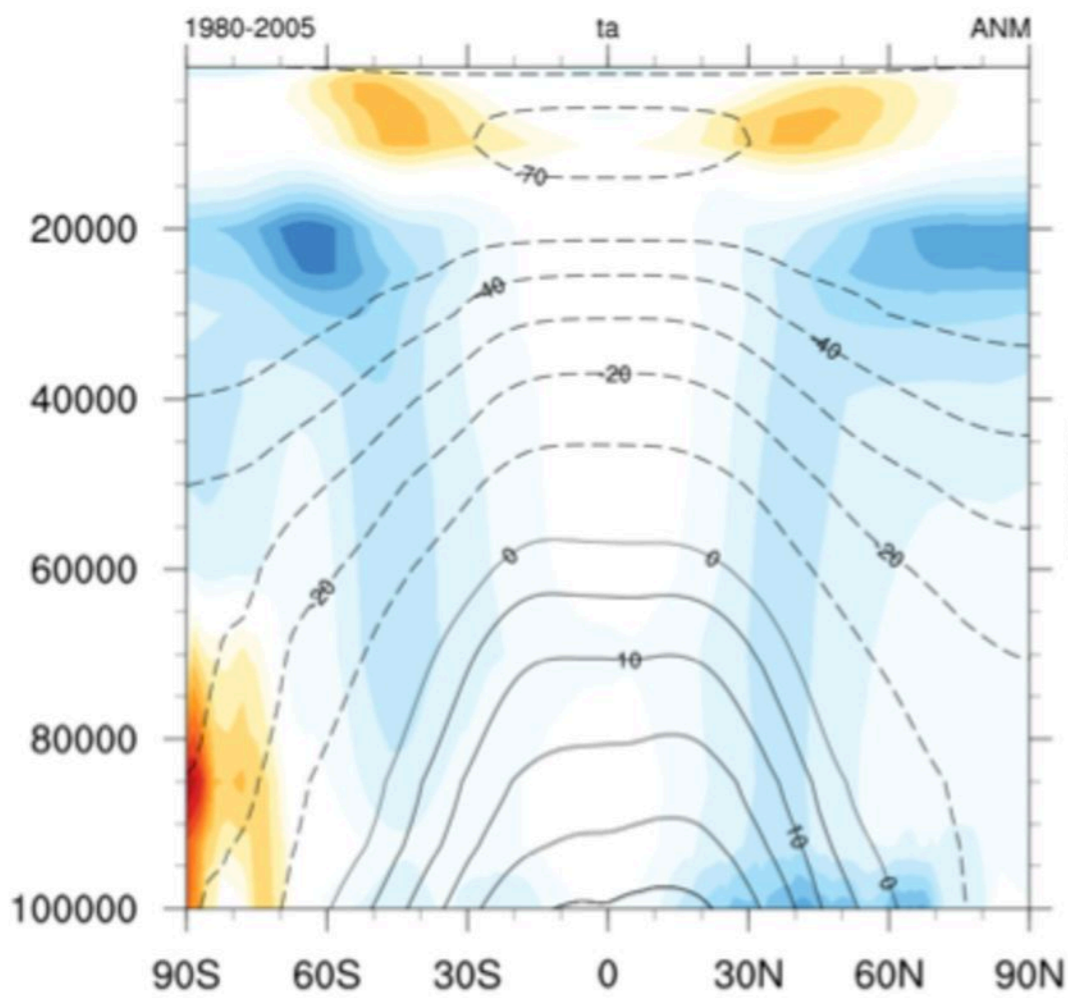


Accepted Article

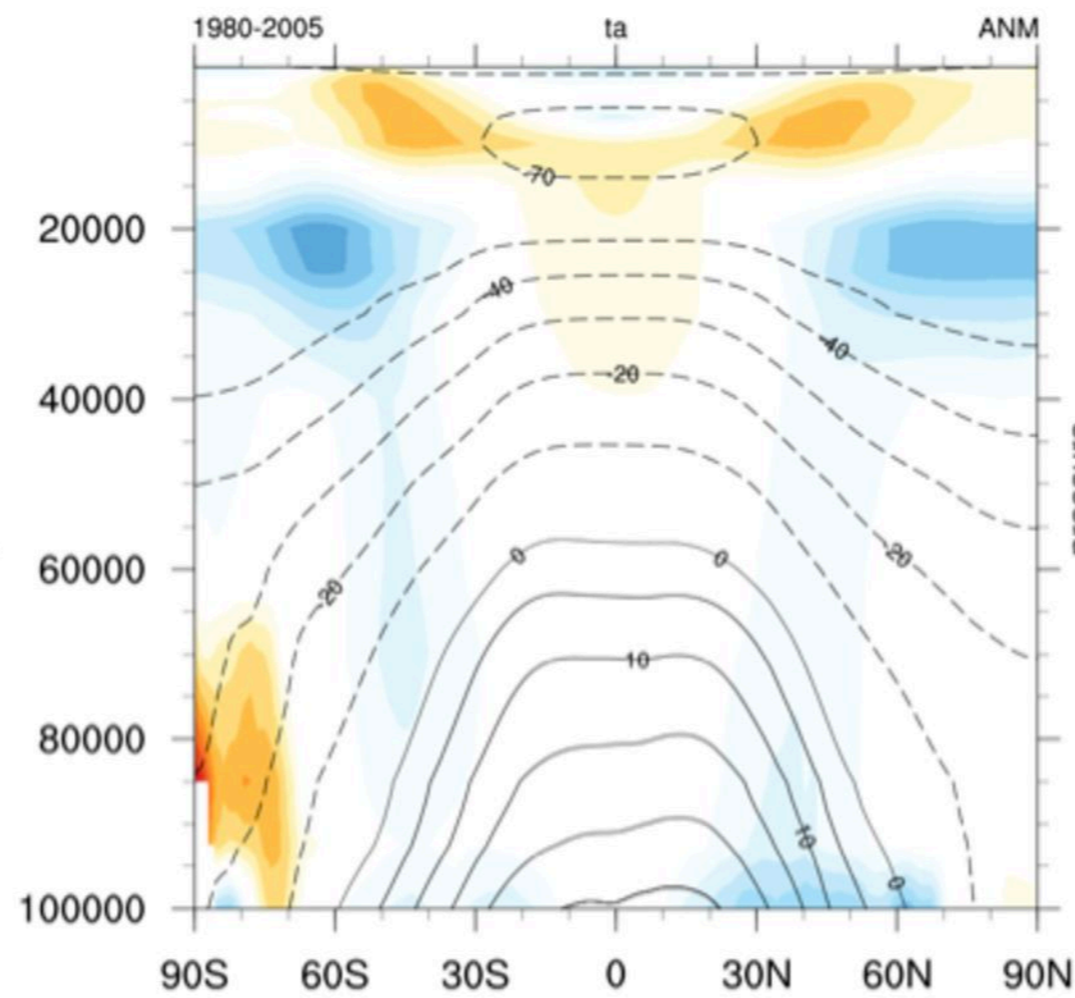


Accepted Article

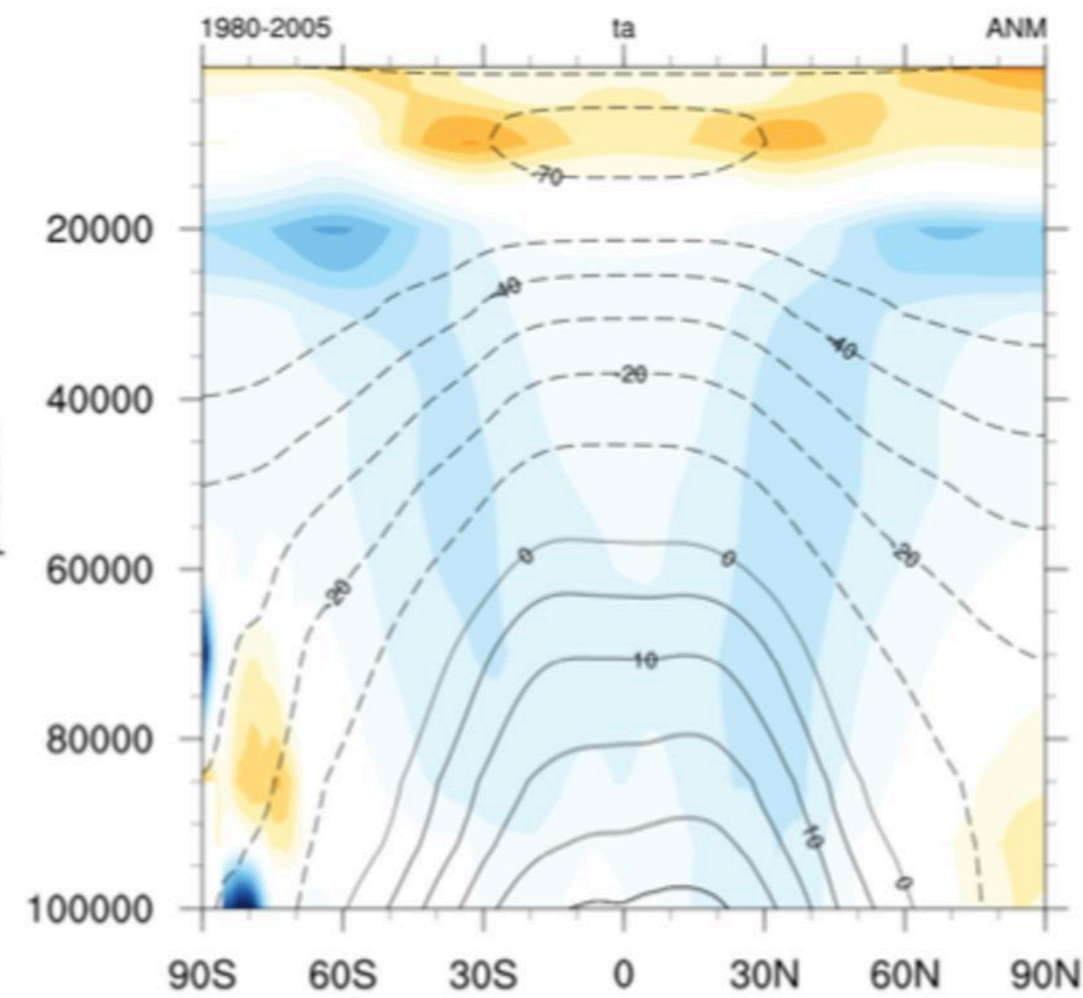
IPSL-CM5A-LR r1i1p1



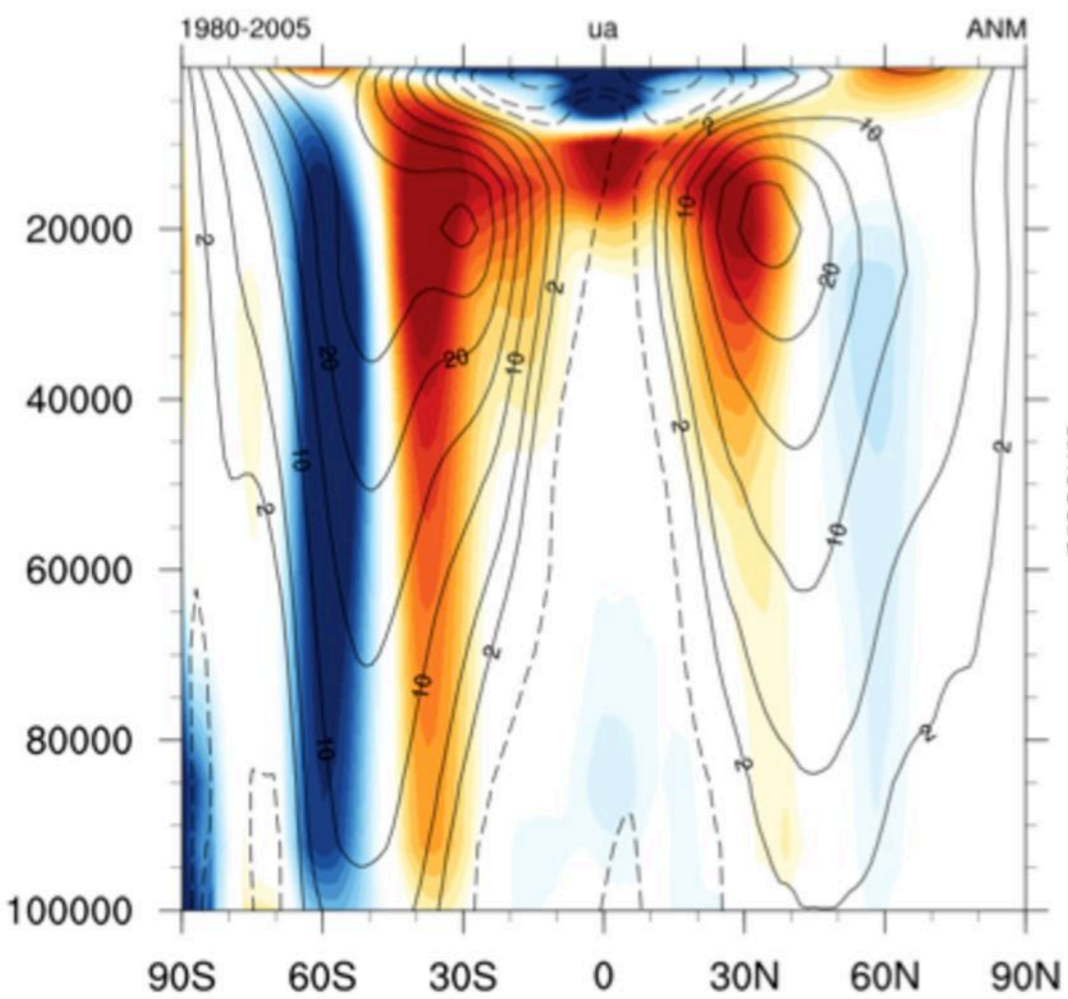
IPSL-CM5A-MR r1i1p1



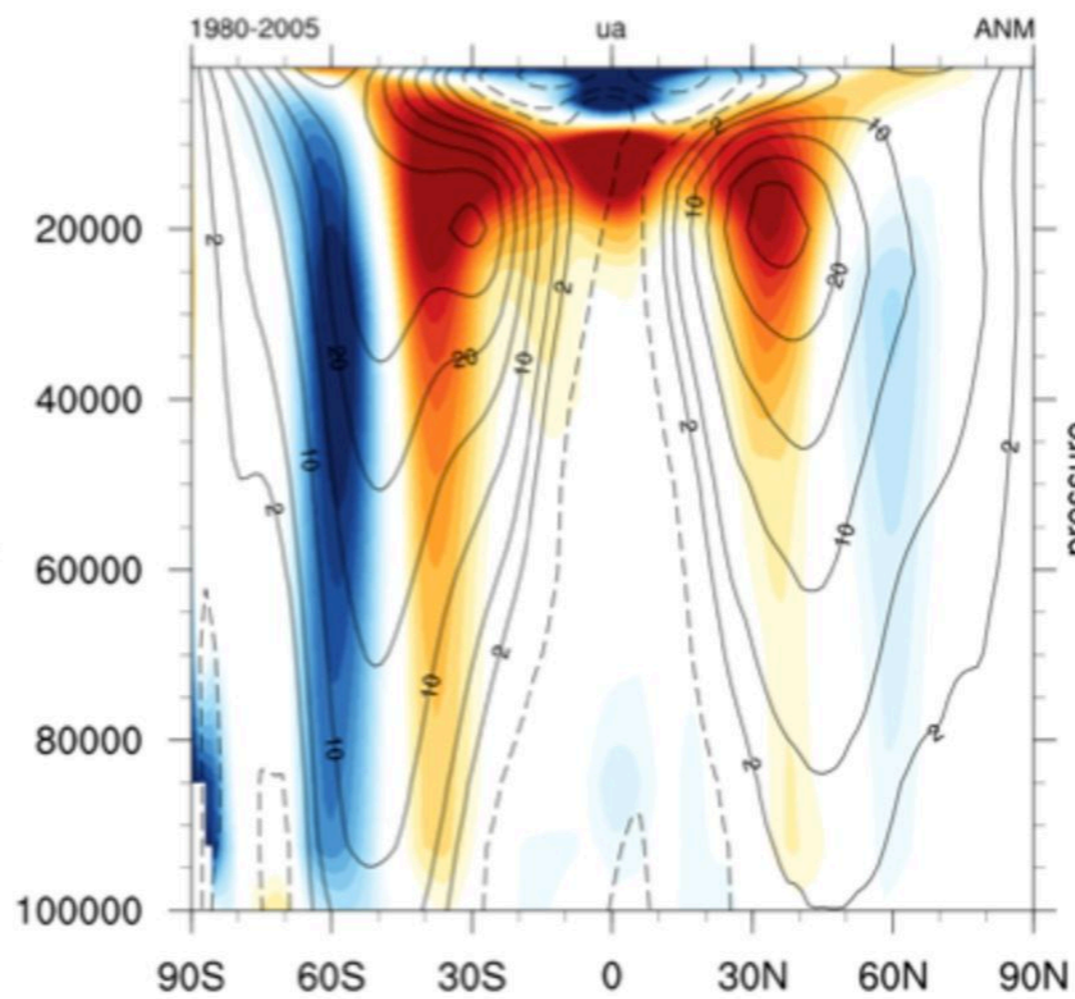
IPSL-CM6A-LR r1i1p1f1



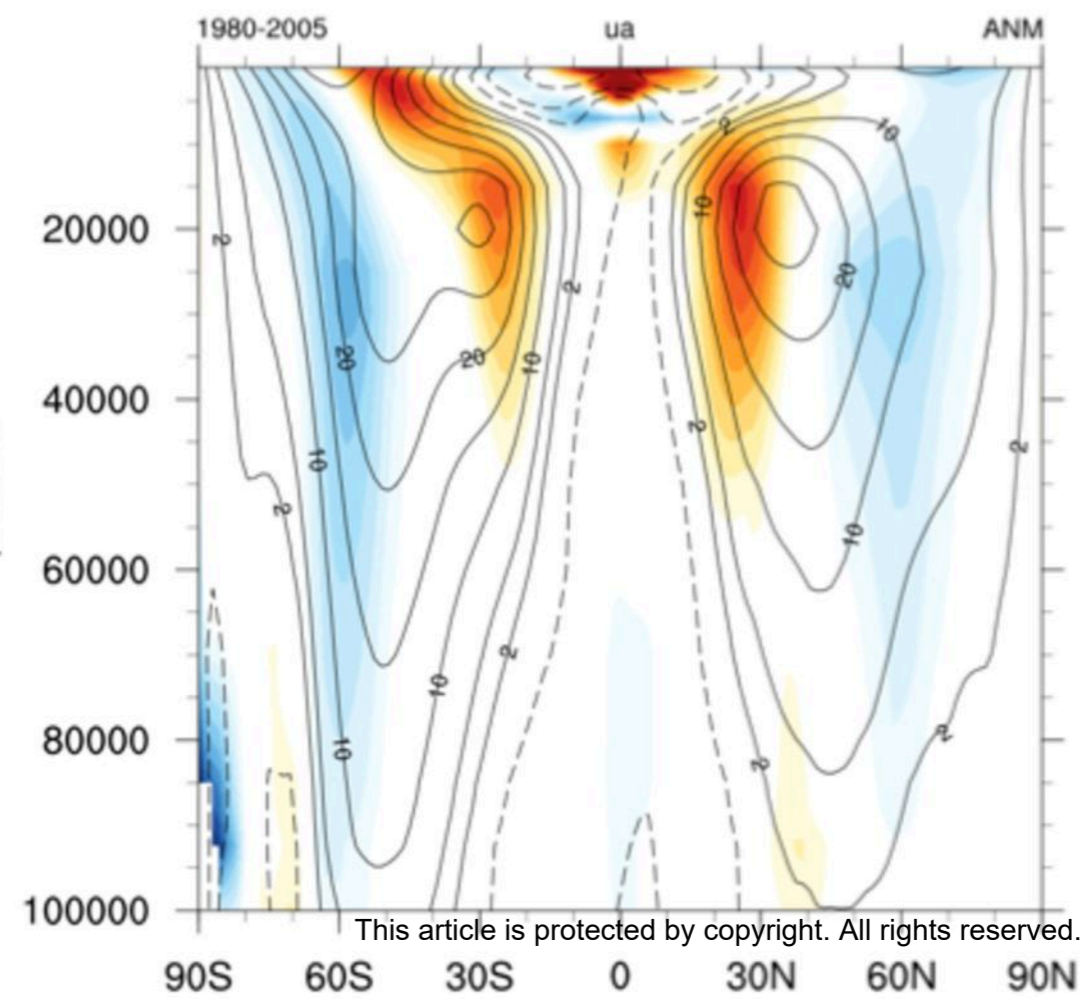
IPSL-CM5A-LR r1i1p1



IPSL-CM5A-MR r1i1p1

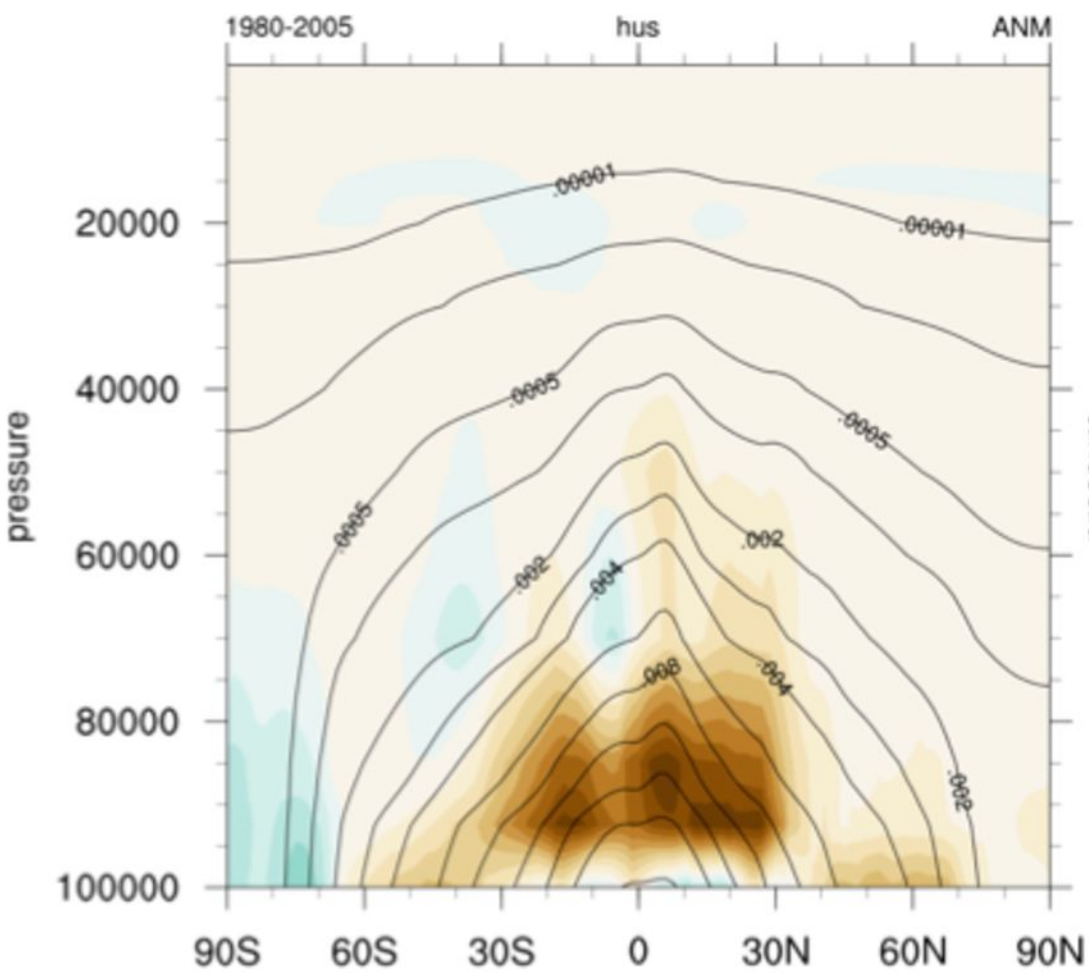


IPSL-CM6A-LR r1i1p1f1

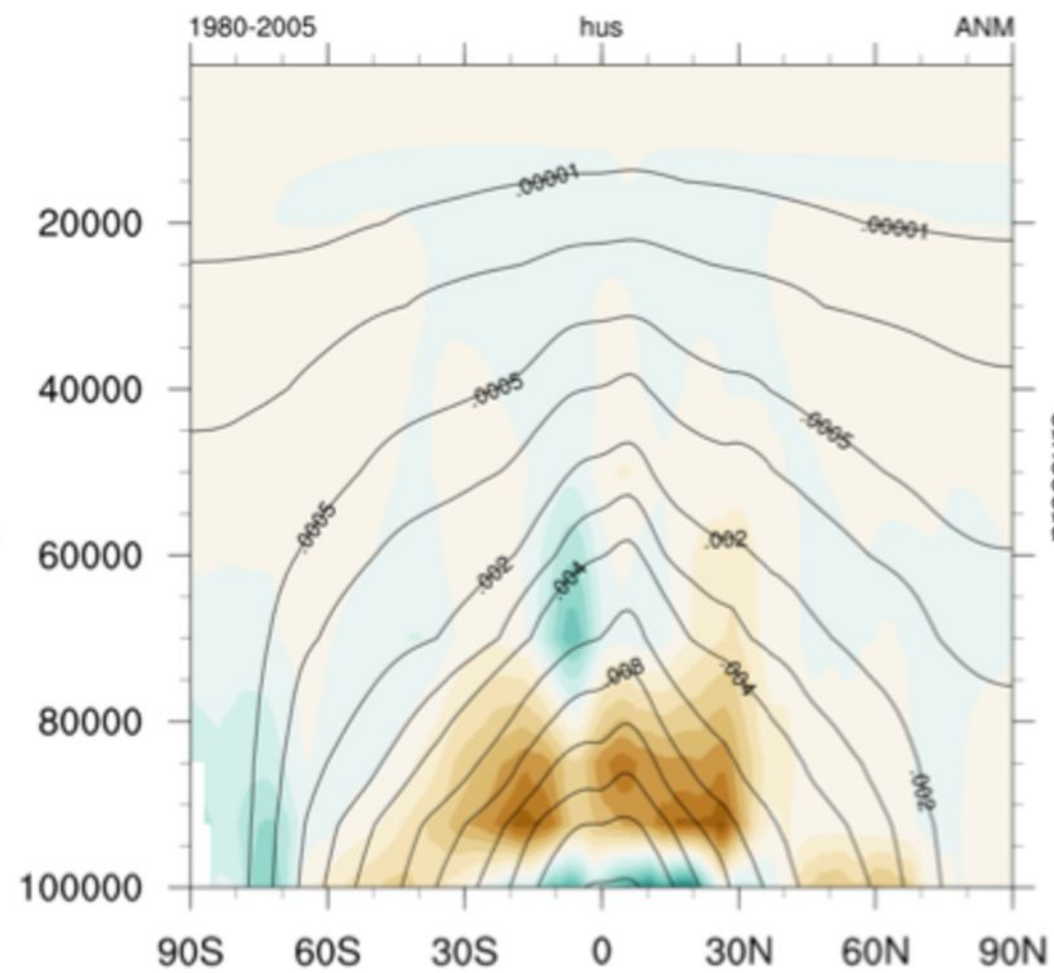


Accepted Article

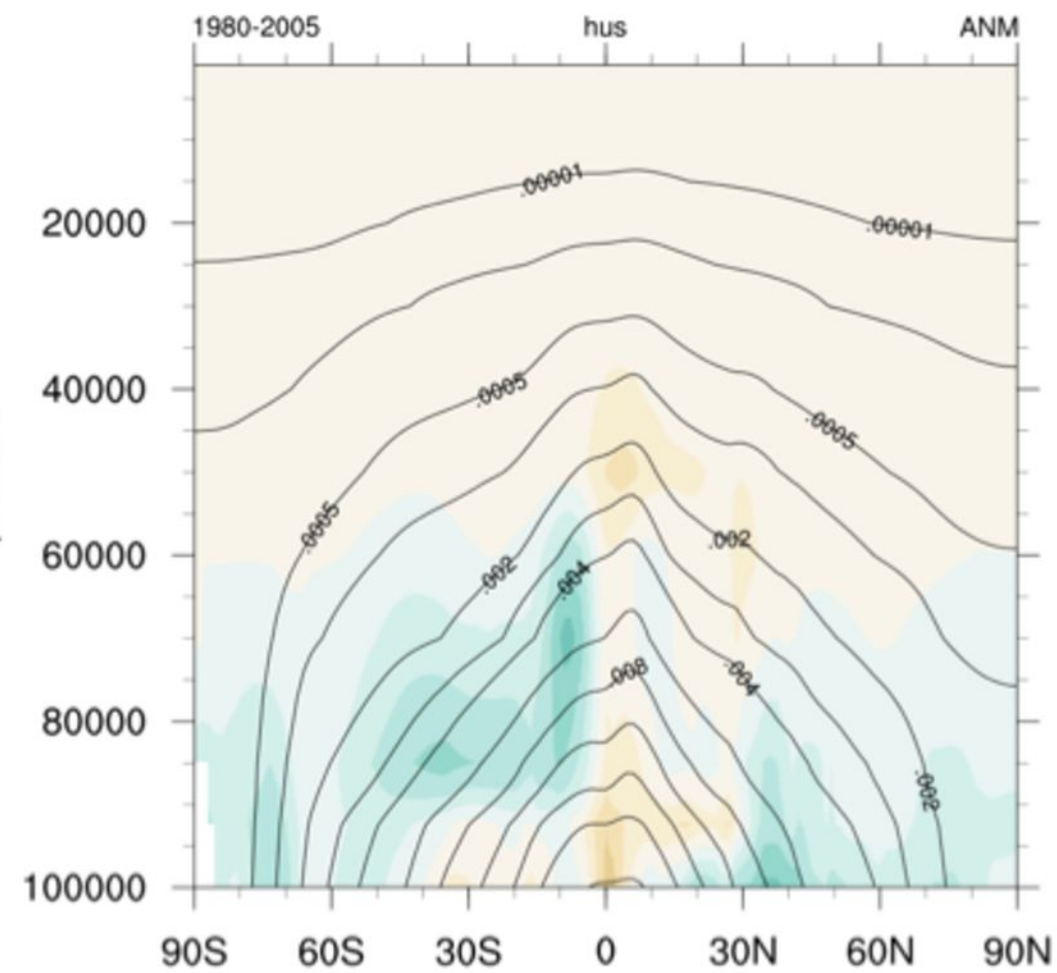
IPSL-CM5A-LR r1i1p1



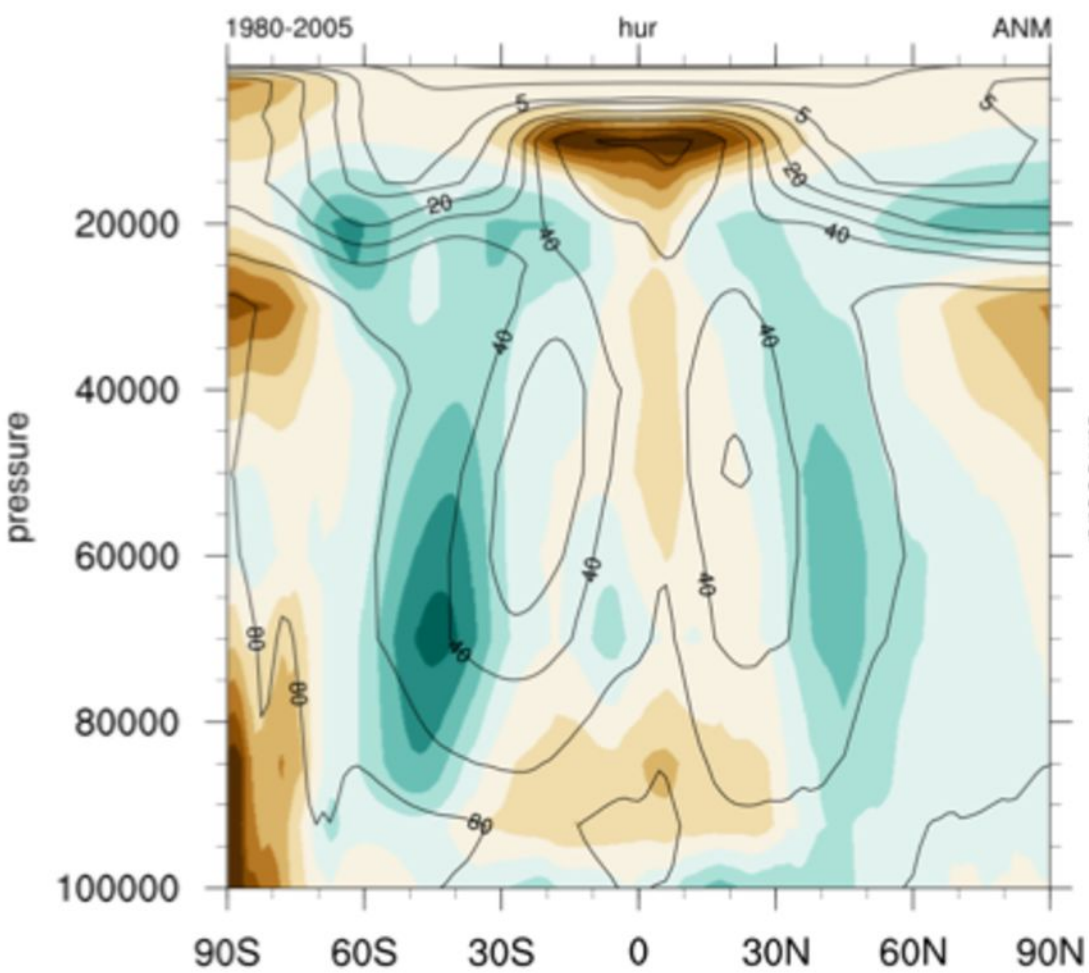
IPSL-CM5A-MR r1i1p1



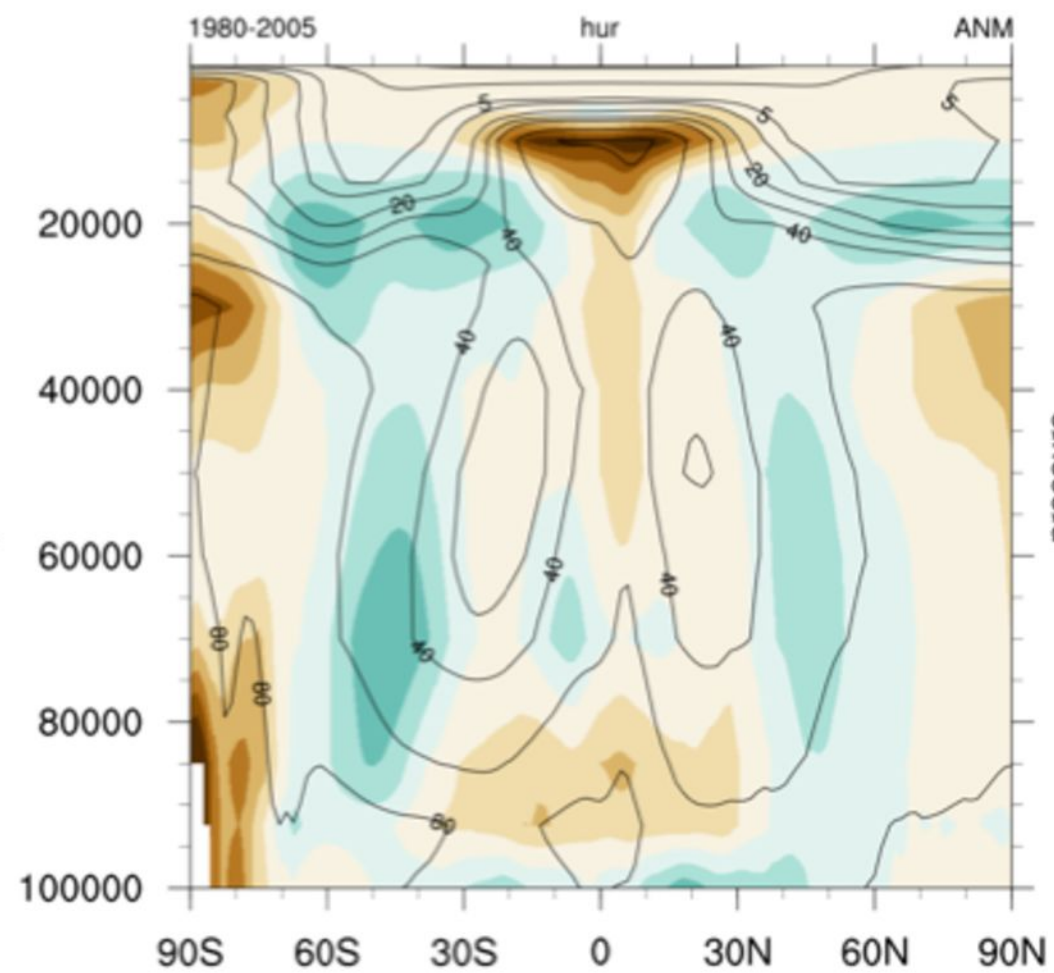
IPSL-CM6A-LR r1i1p1f1



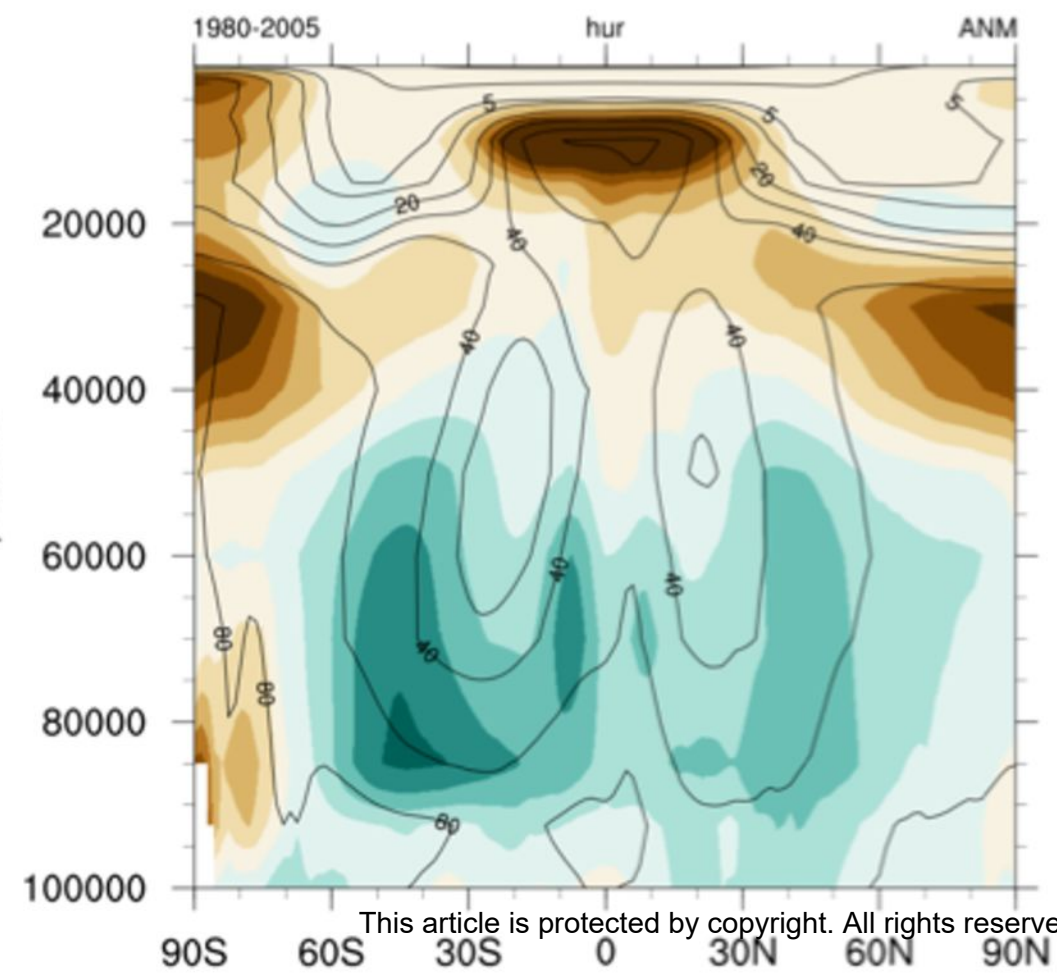
IPSL-CM5A-LR r1i1p1



IPSL-CM5A-MR r1i1p1



IPSL-CM6A-LR r1i1p1f1

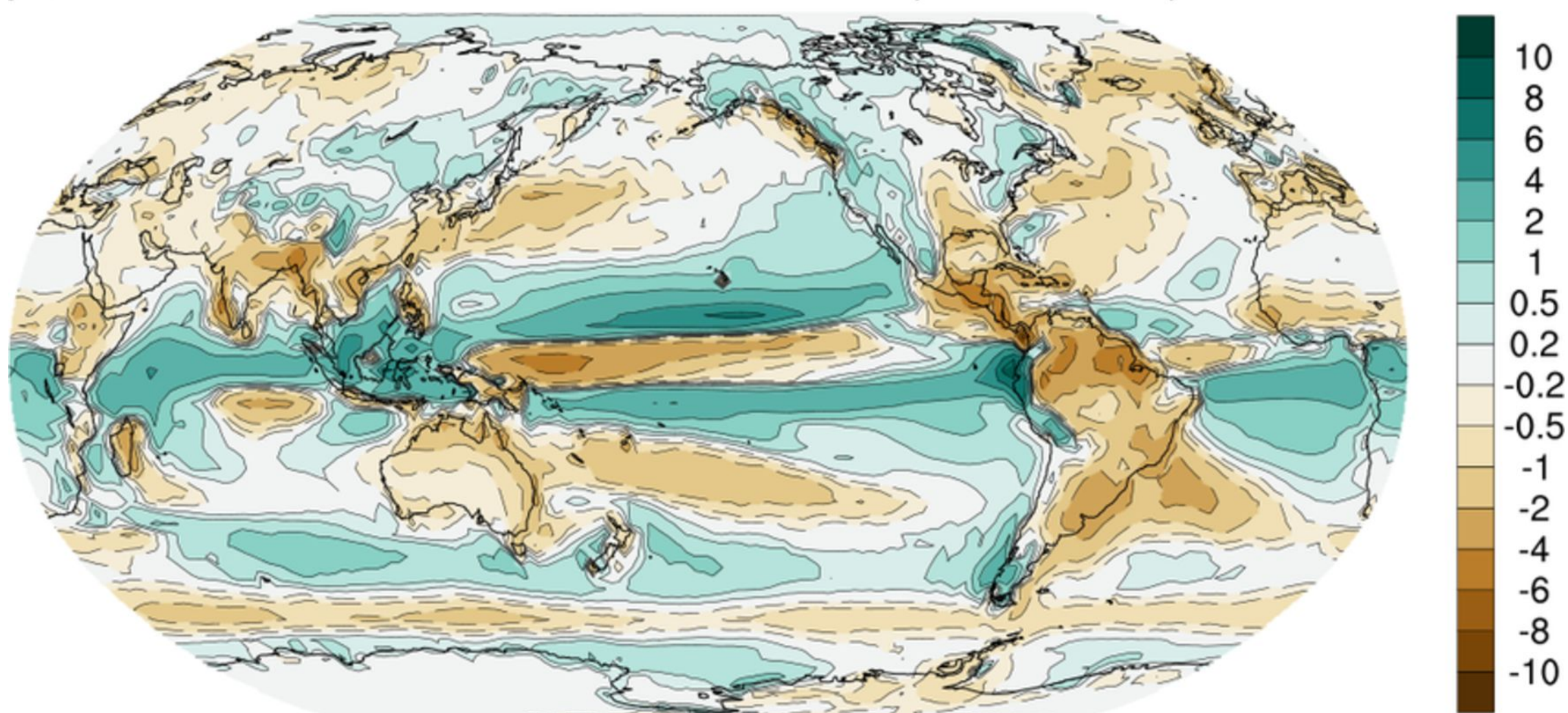


Accepted Article

IPSL-CM5A-LR r1i1p1 (vs GPCP) 1980-2005

pr, ANM

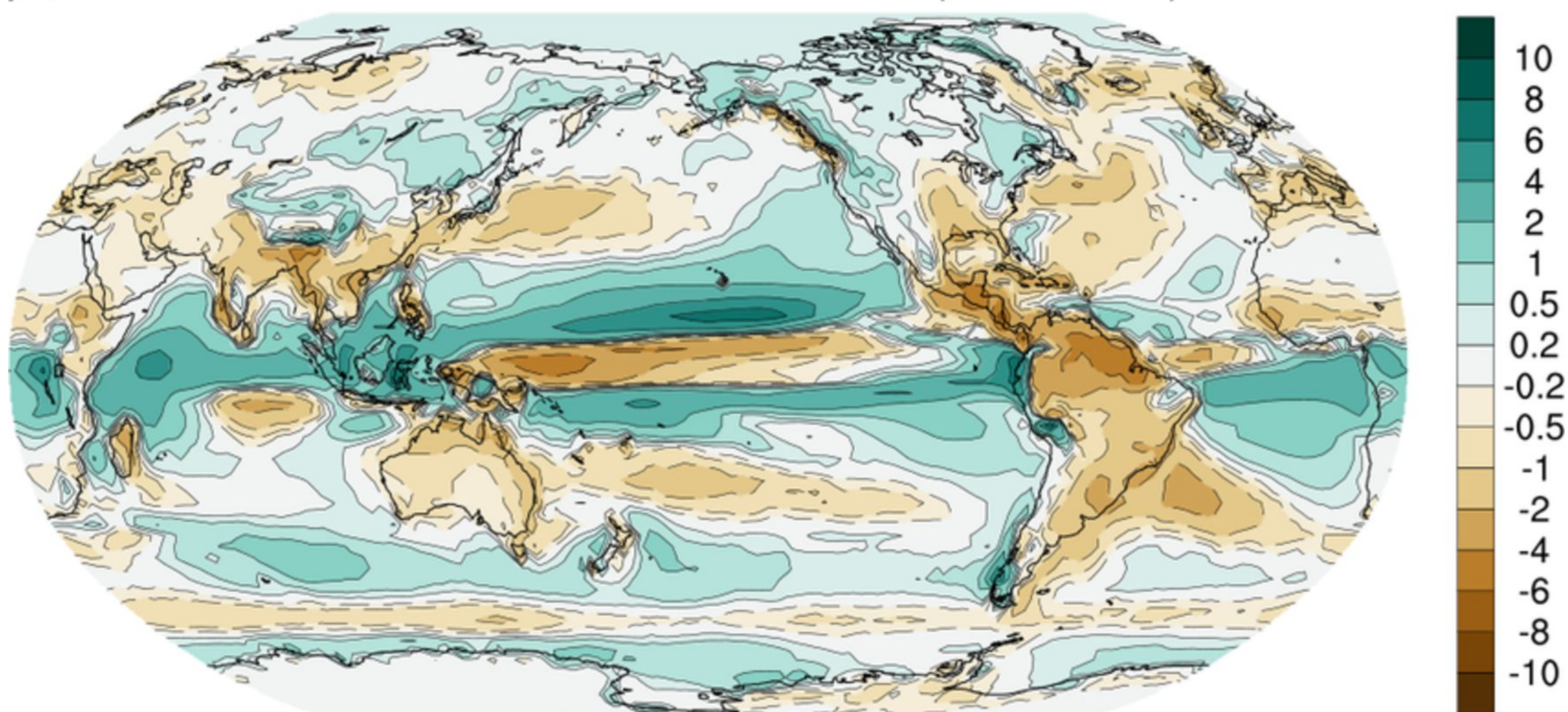
bias=0.0384 ; rmse=1.36 ; corr=0.772



IPSL-CM5A-MR r1i1p1 (vs GPCP) 1980-2005

pr, ANM

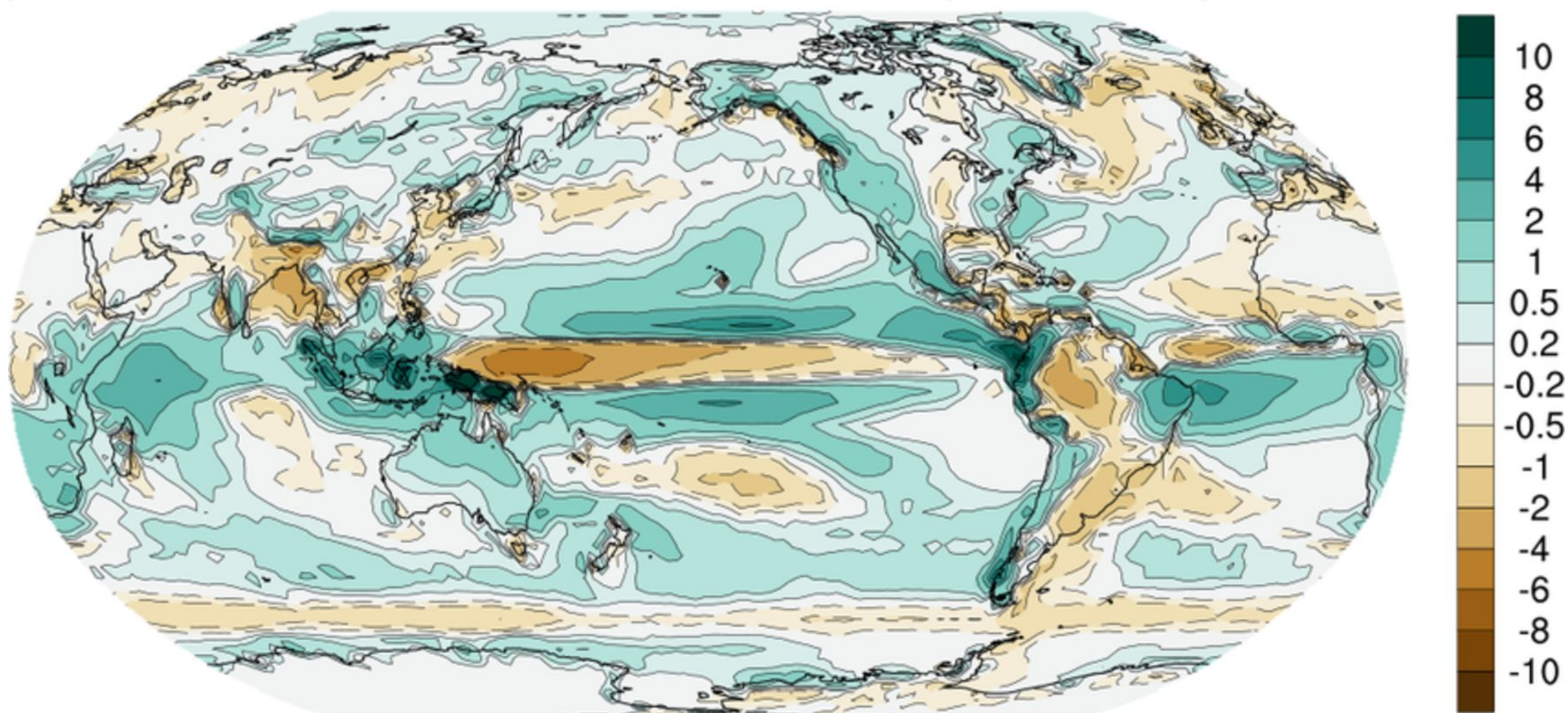
bias=0.109 ; rmse=1.4 ; corr=0.769



IPSL-CM6A-LR r1i1p1f1 (vs GPCP) 1980-2005

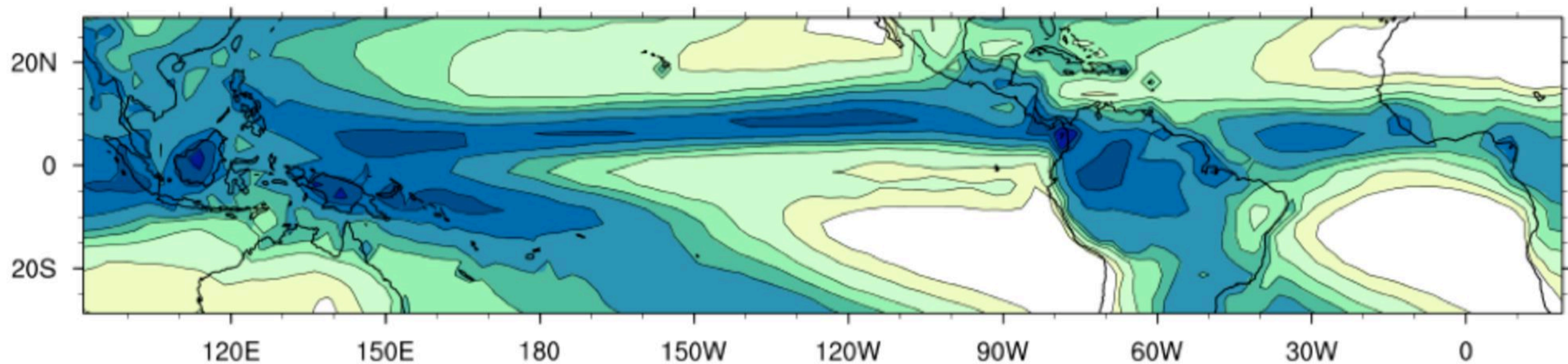
pr, ANM

bias=0.342 ; rmse=1.45 ; corr=0.81

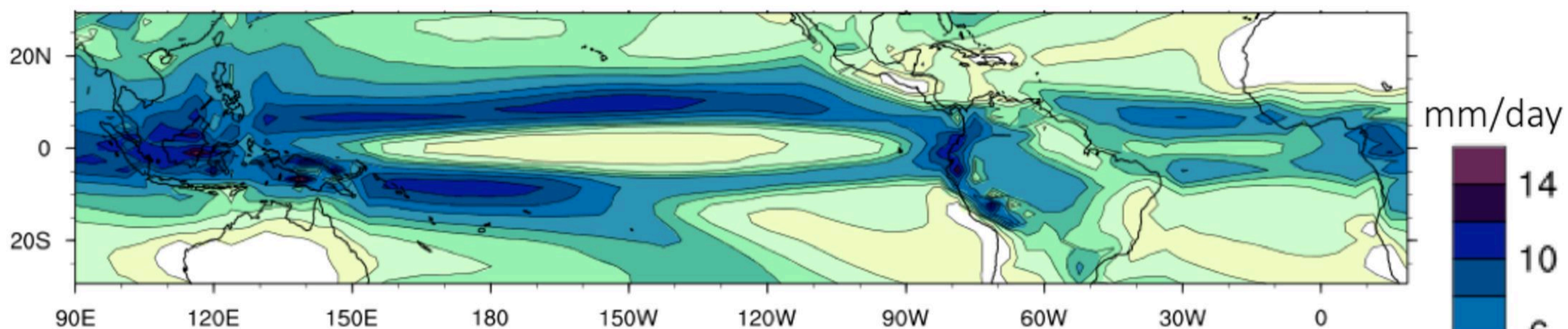


Accepted Article

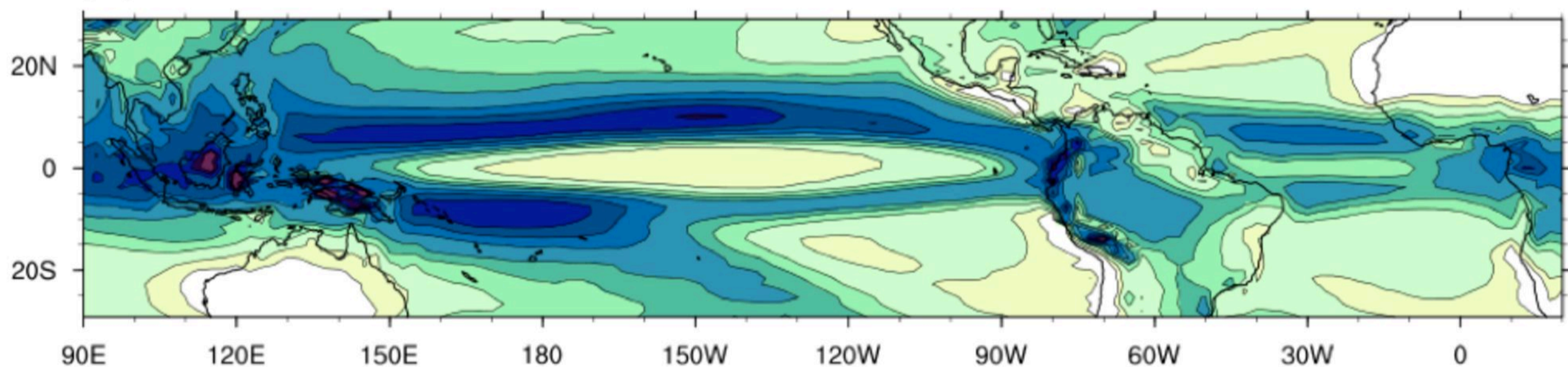
(a) GPCP



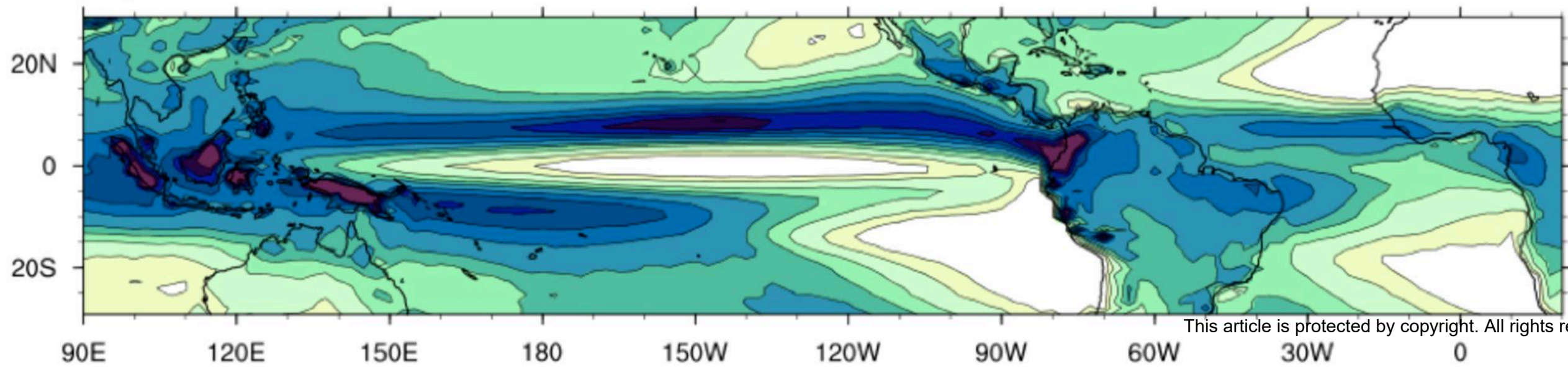
(b) IPSL-CM5A-LR



(c) IPSL-CM5A-MR

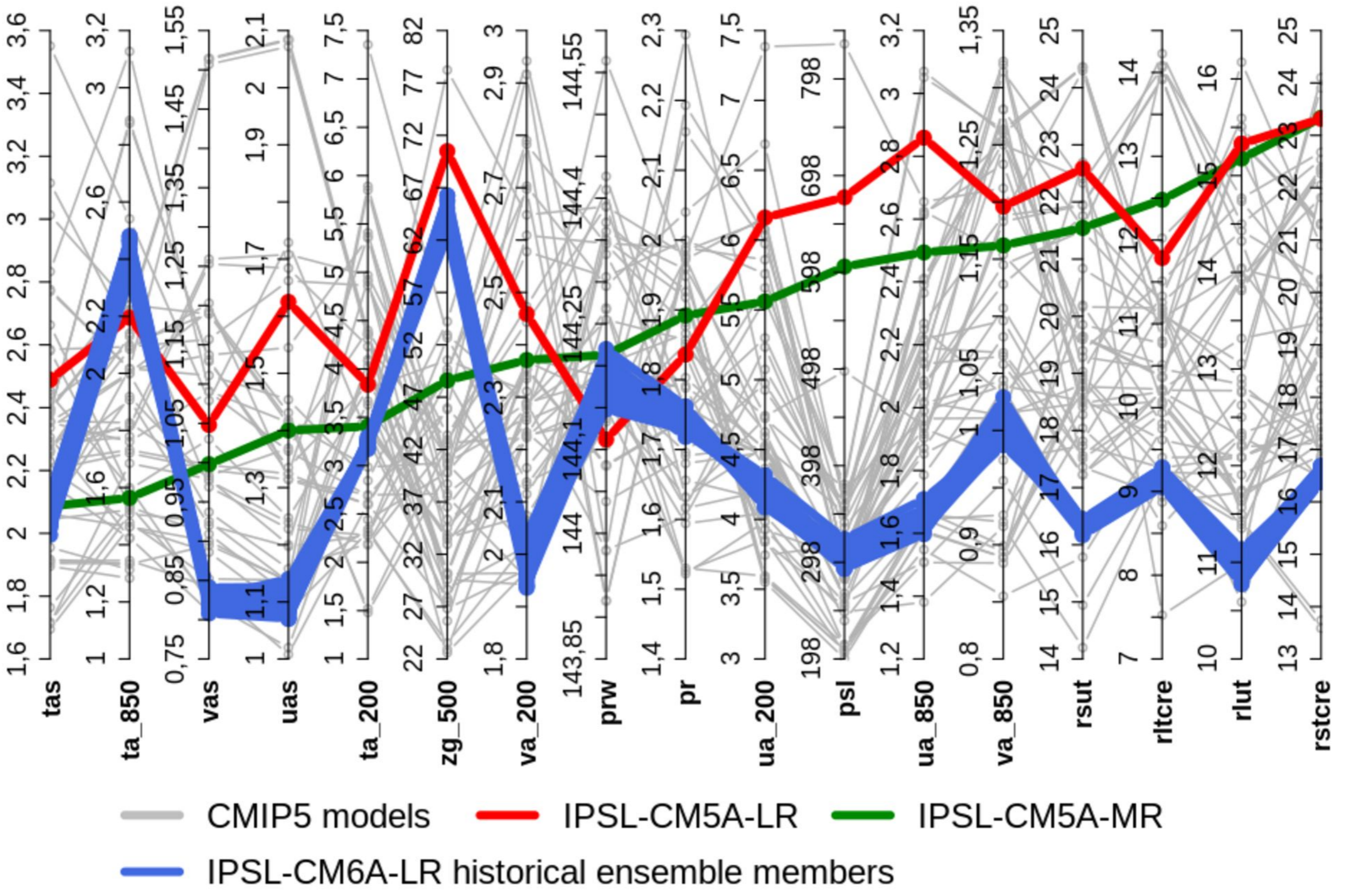


(d) IPSL-CM6A-LR

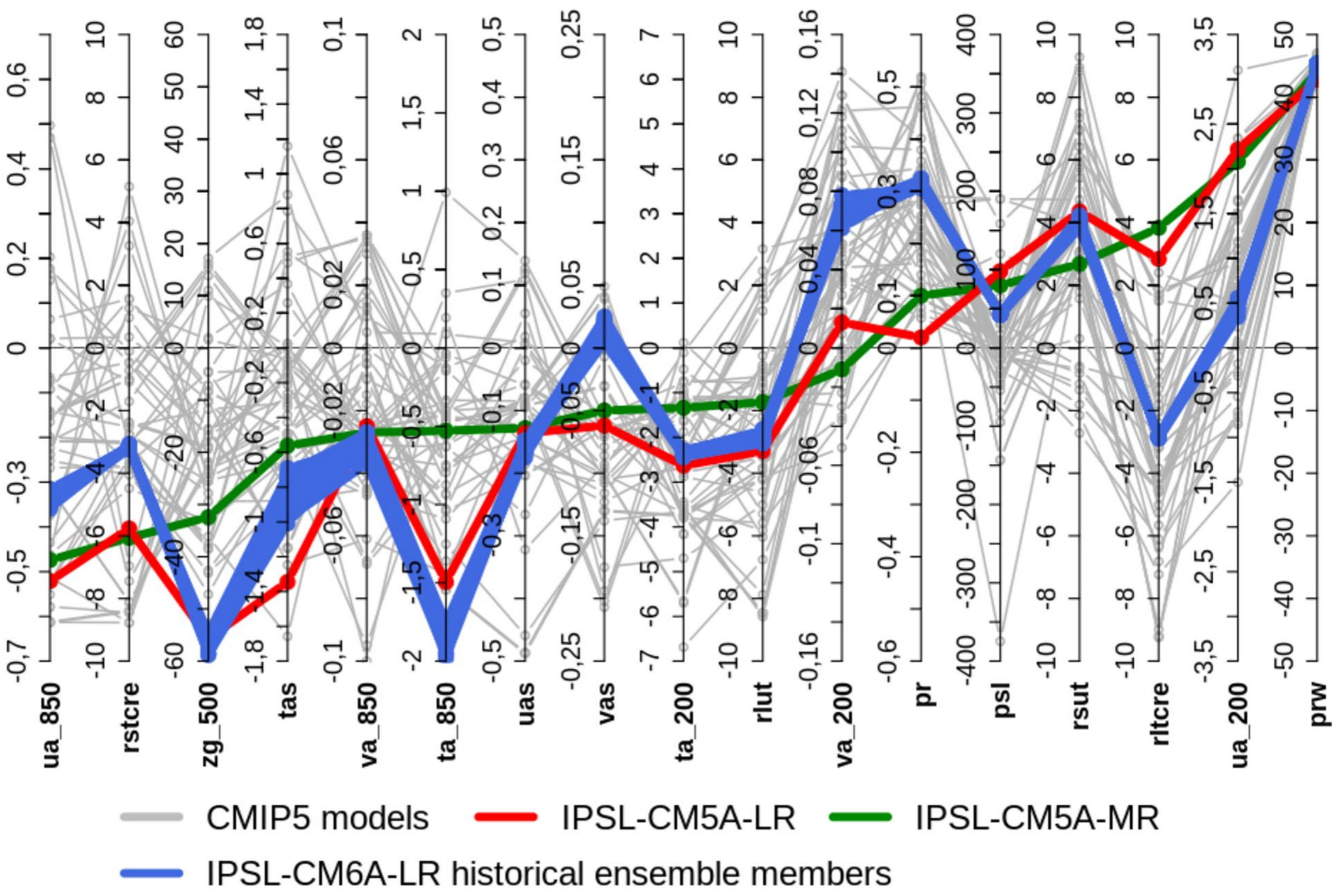


Accepted Article

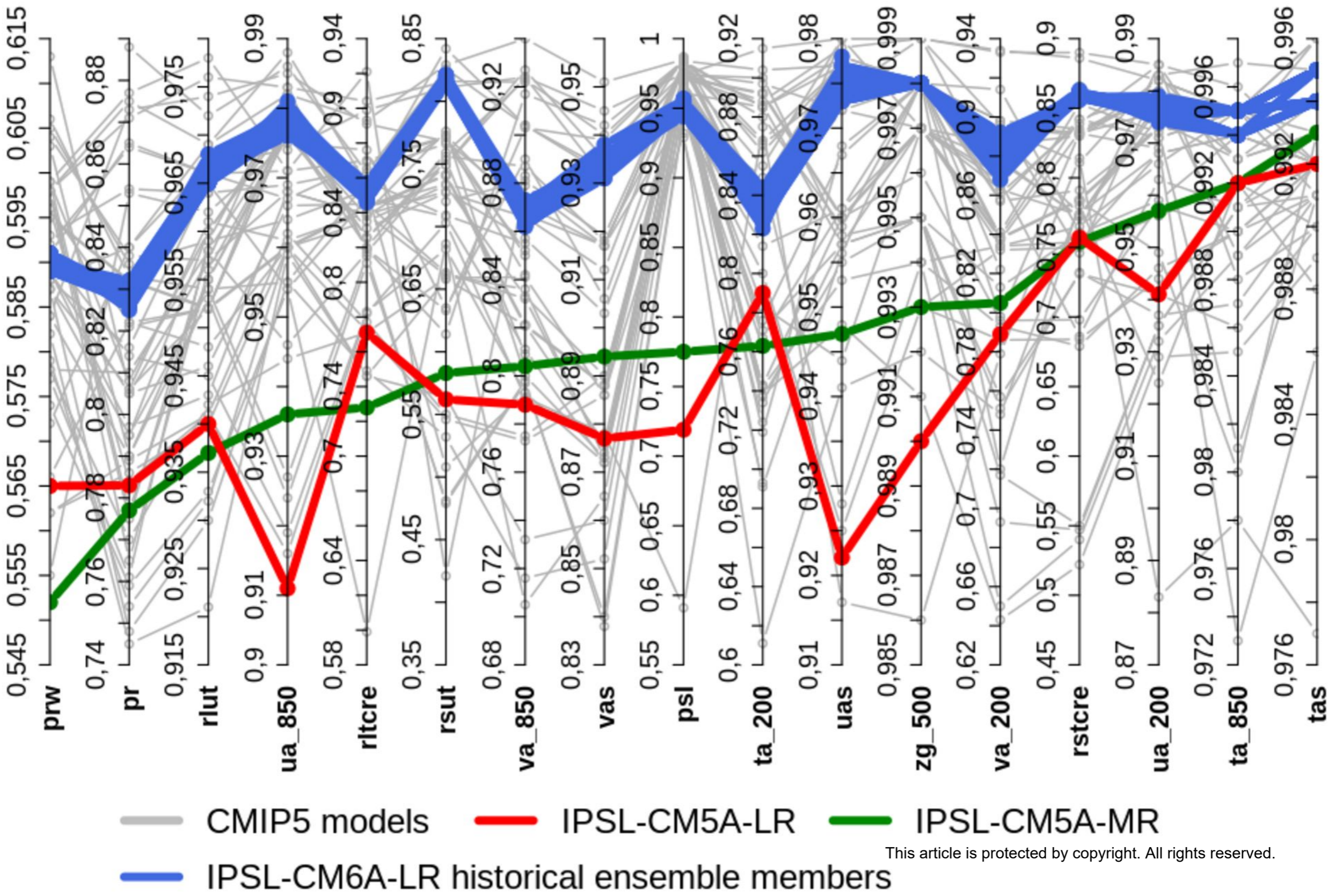
PMP - Spatio-temporal RMS on global annual cycle



PMP - Global annual mean bias



PMP - Spatial correlation on global annual mean

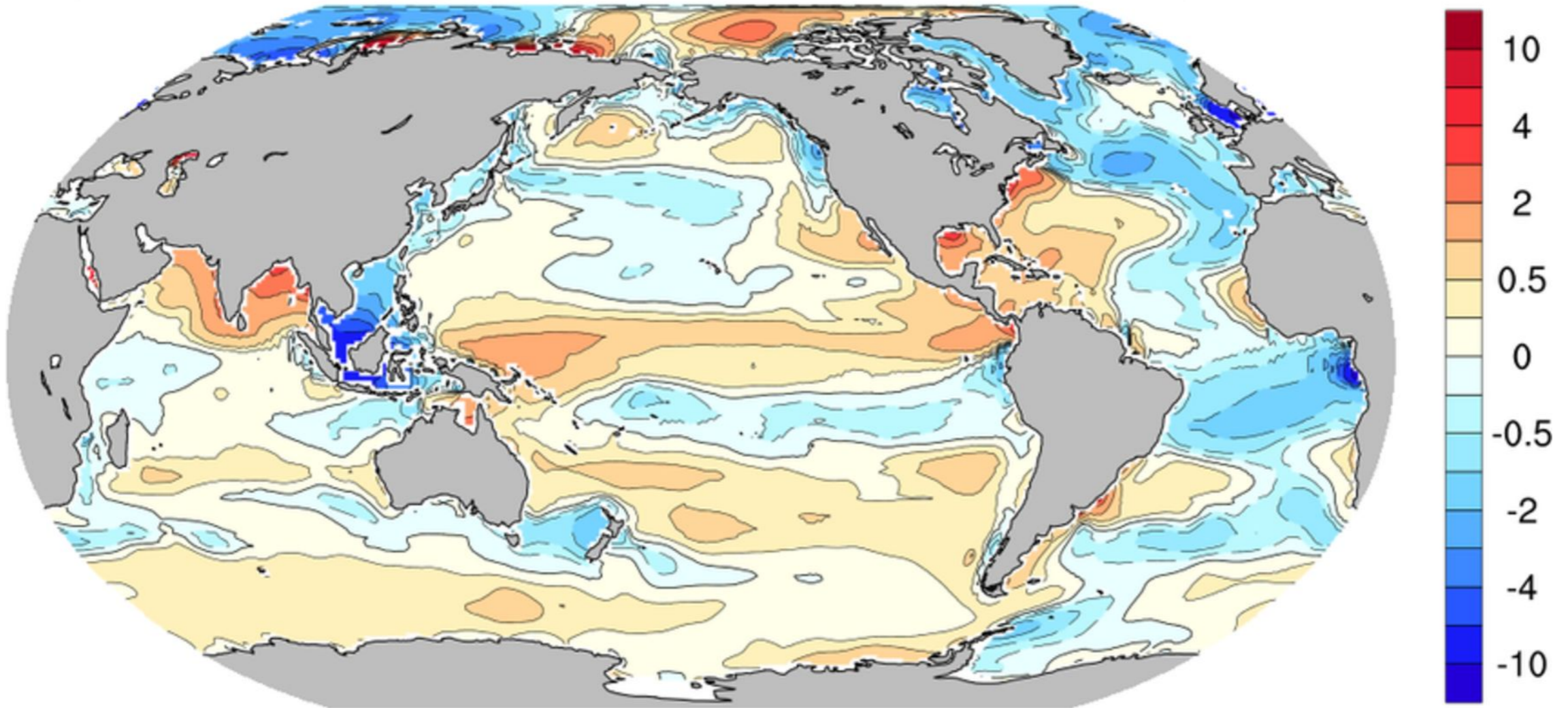


Accepted Article

IPSL-CM5A-LR r1i1p1 (vs WOA13-v2) 1980-2005

sos, ANM

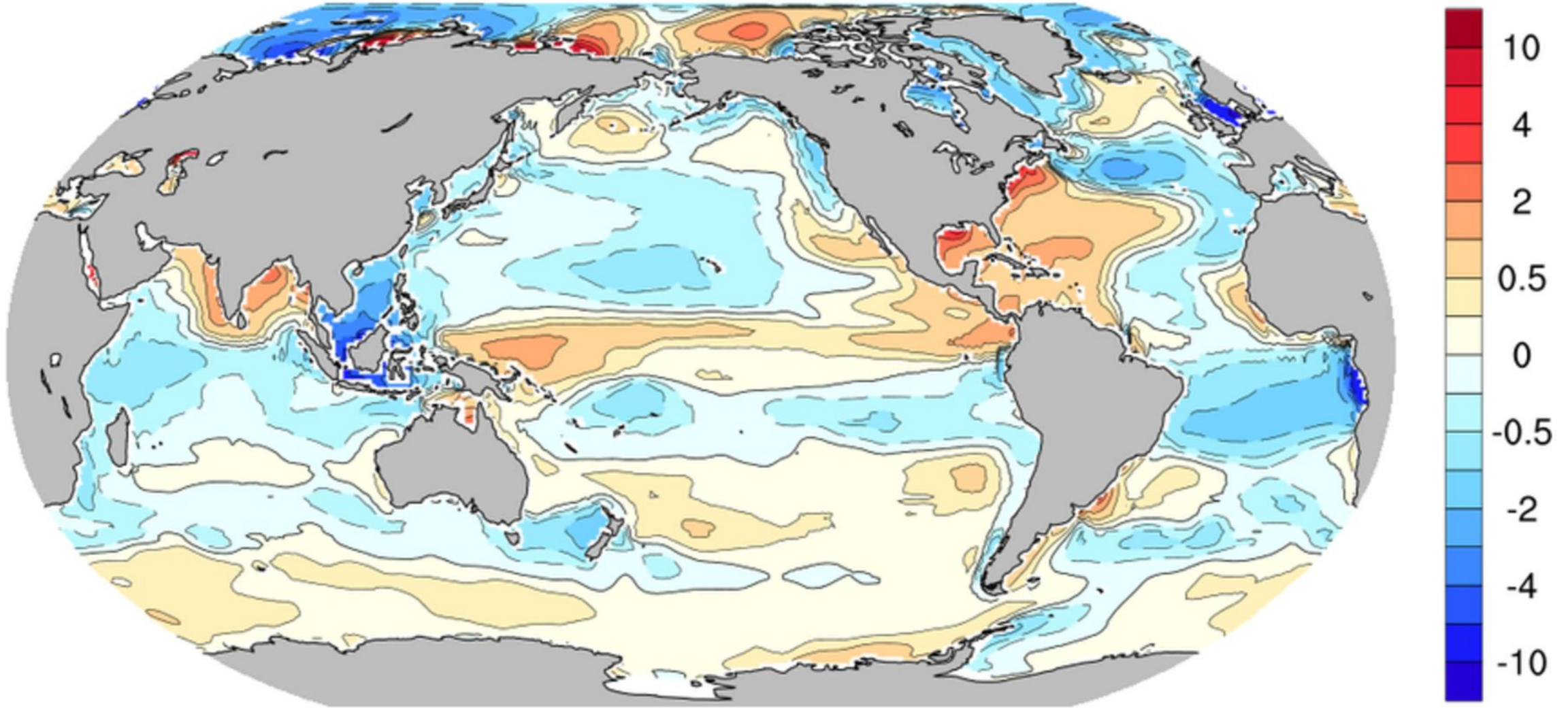
bias=0.00391 ; rmse=0.924 ; corr=0.63



IPSL-CM5A-MR r1i1p1 (vs WOA13-v2) 1980-2005

sos, ANM

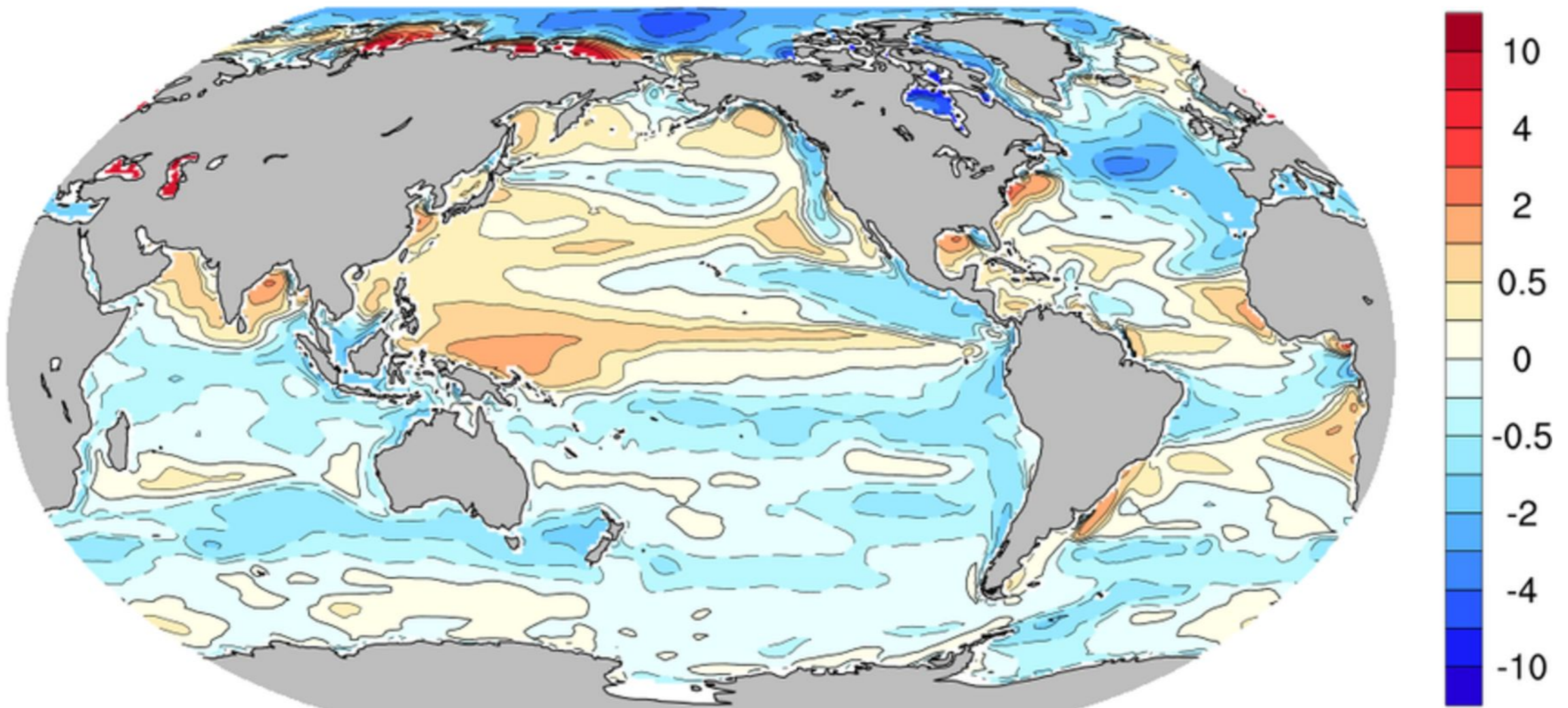
bias=-0.0964 ; rmse=0.864 ; corr=0.634



IPSL-CM6A-LR r1i1p1f1 (vs WOA13-v2) 1980-2005

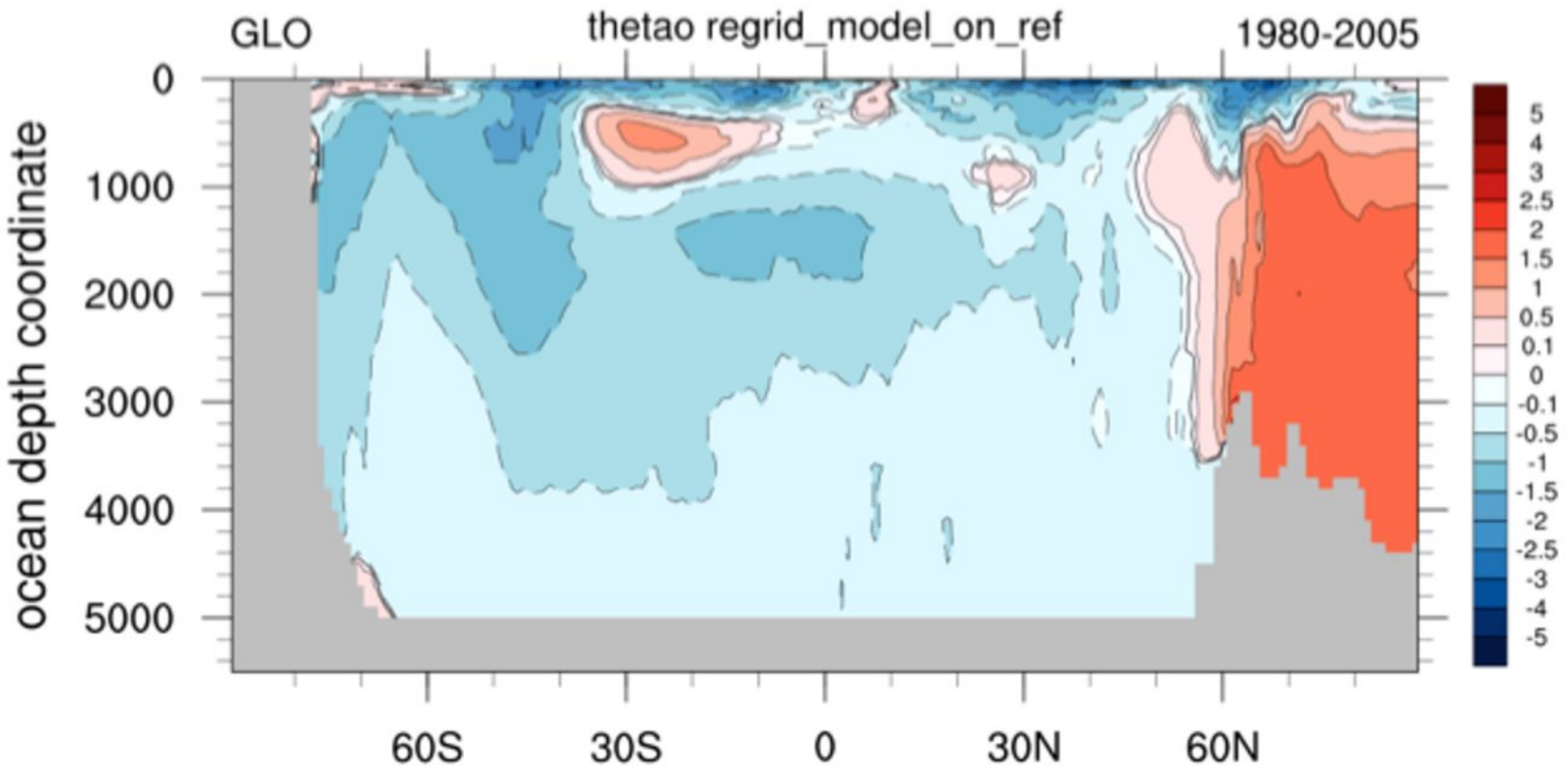
sos, ANM

bias=-0.156 ; rmse=0.886 ; corr=0.721

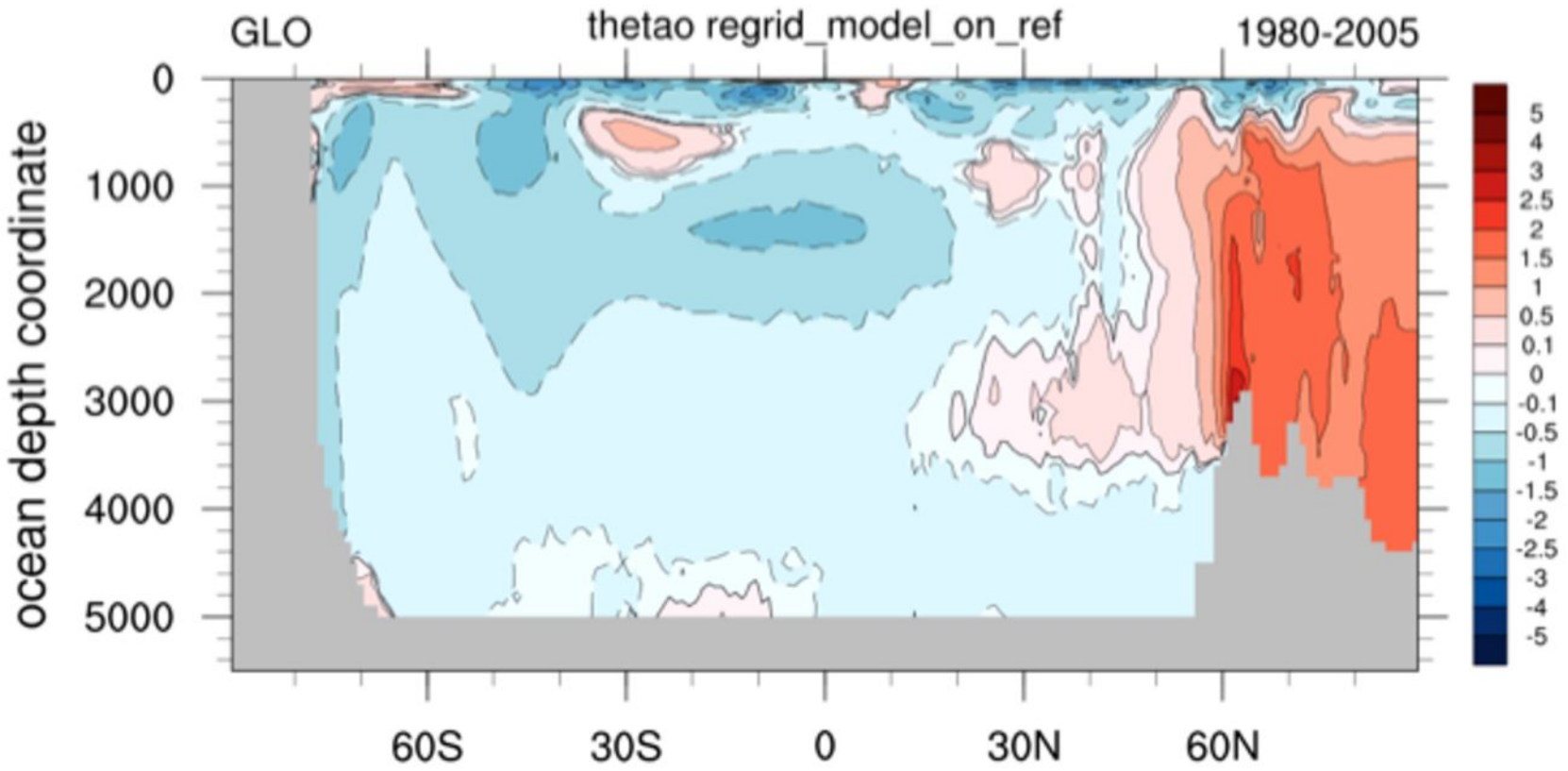


Accepted Article

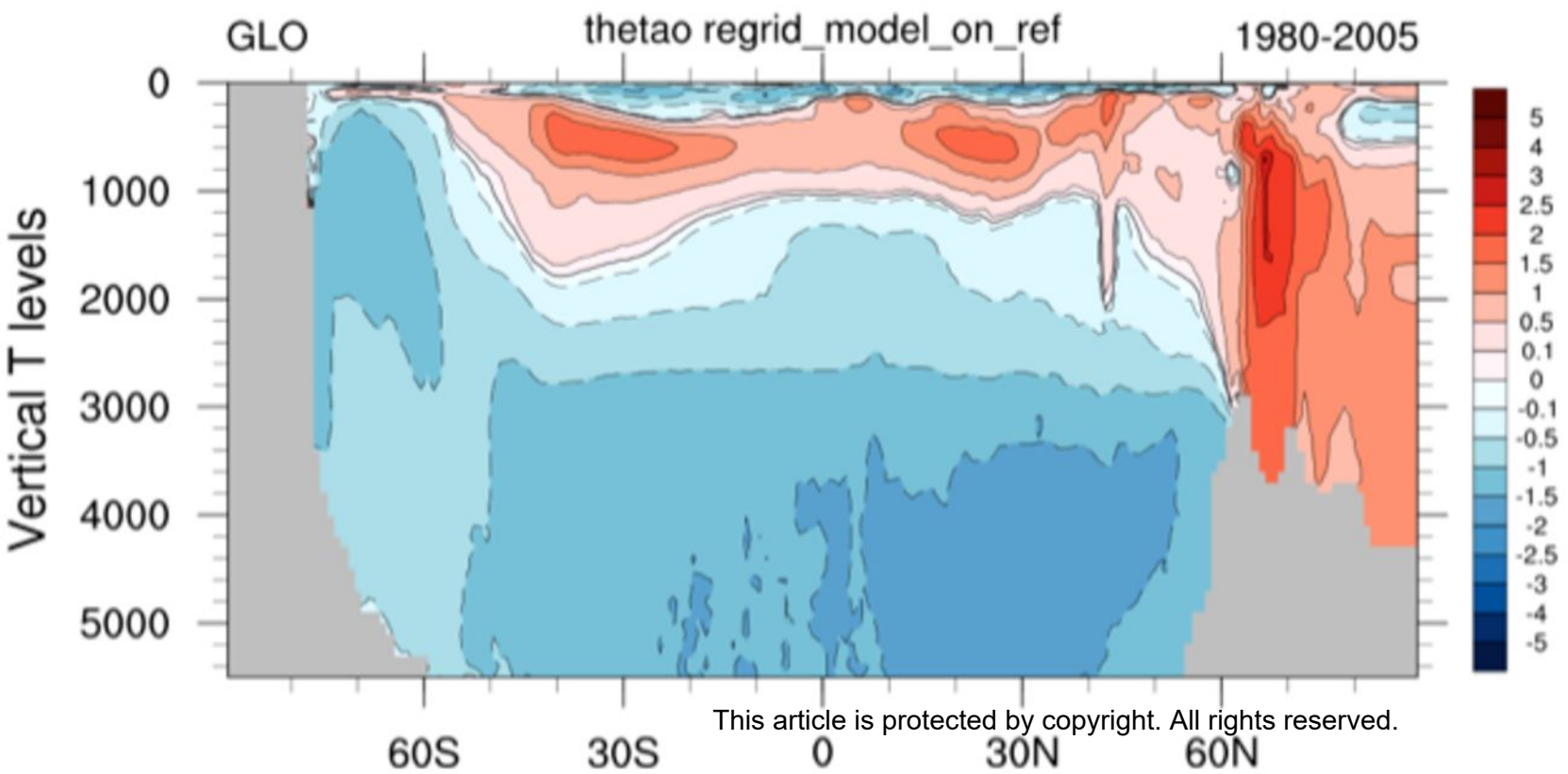
CMIP5 IPSL-CM5A-LR



CMIP5 IPSL-CM5A-MR

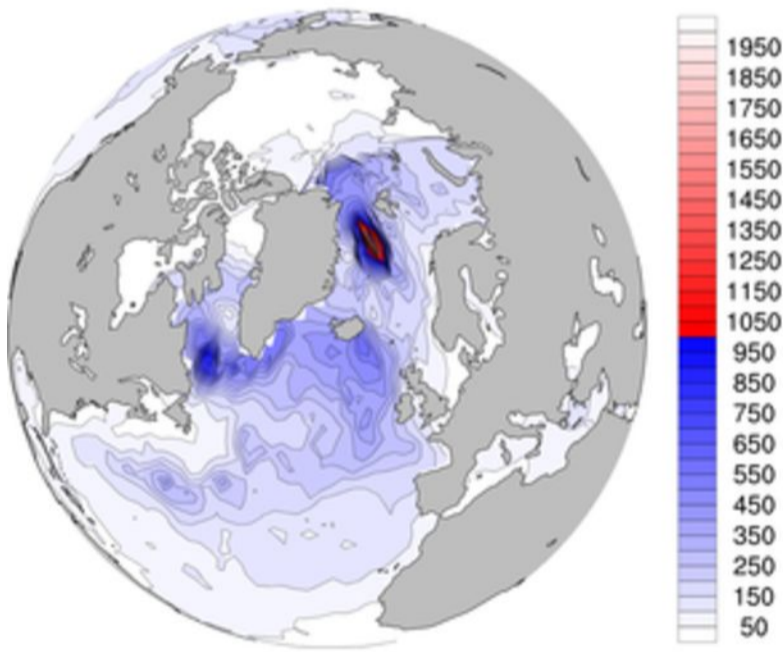


r1i1p1f1

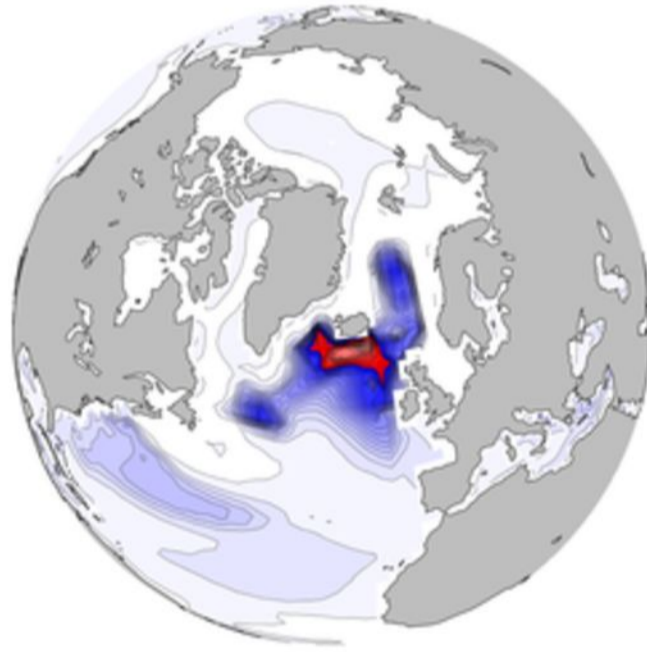


Accepted Article

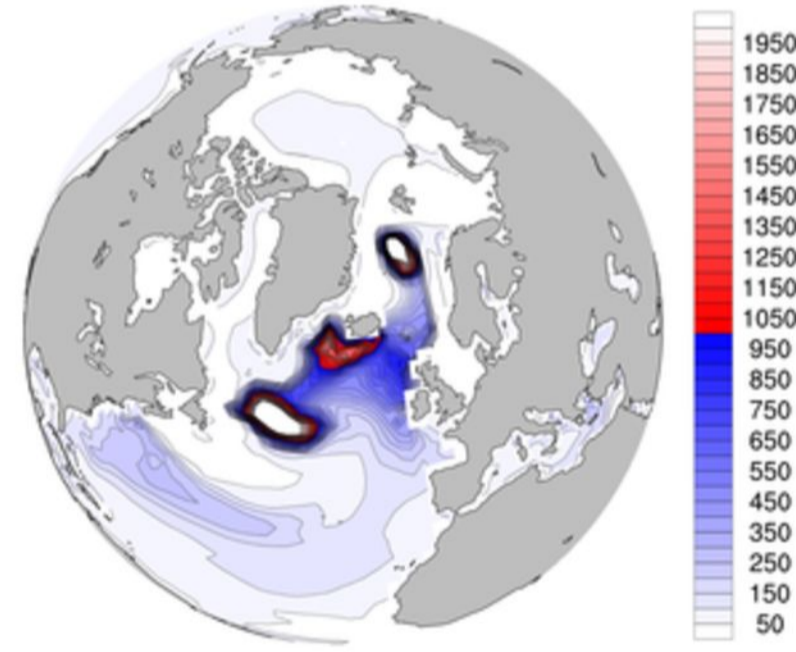
De Boyer Montegut et al. 2004



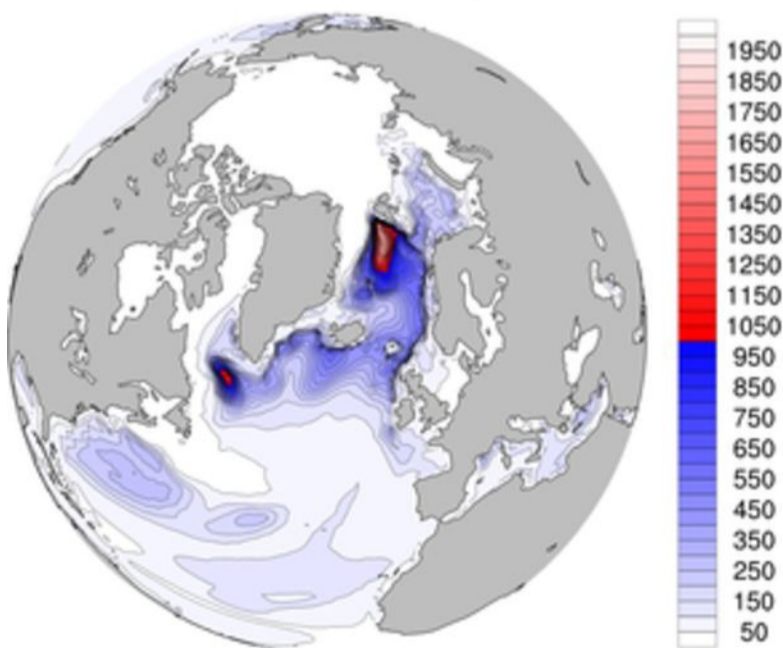
IPSL-CM5A-LR



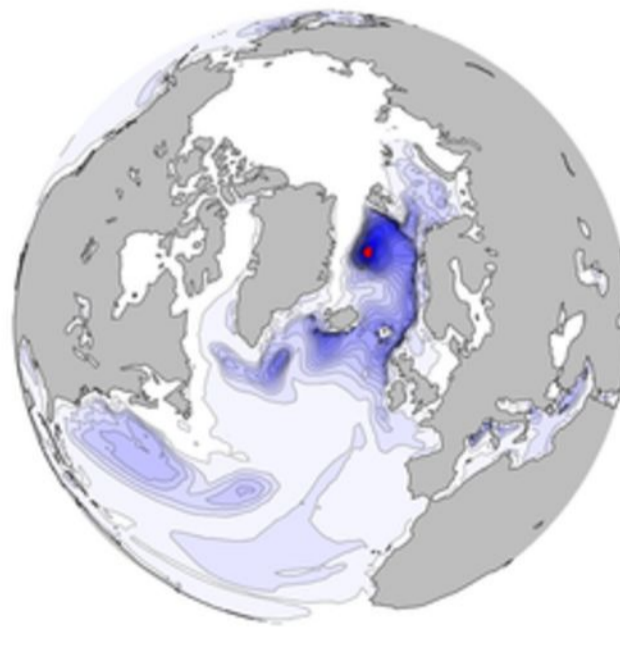
IPSL-CM5A-MR



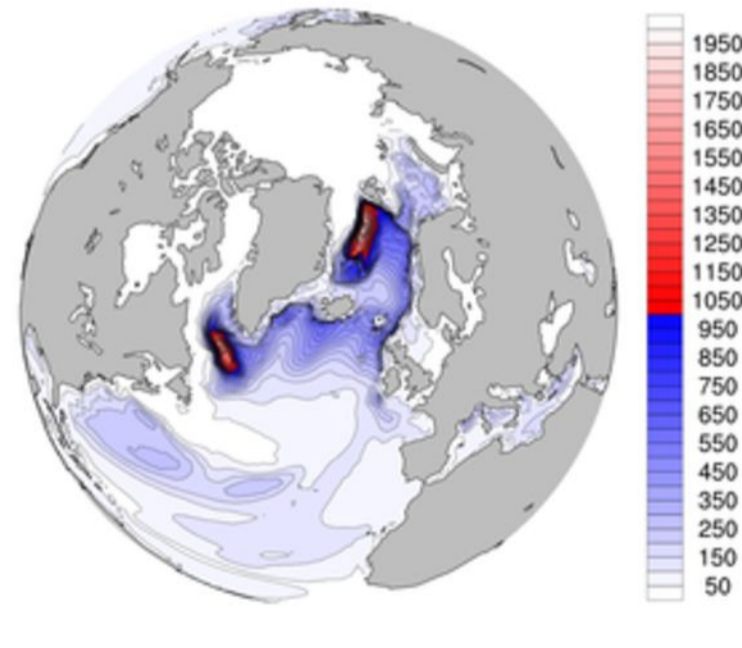
IPSL-CM6A-LR r1i1p1f1



IPSL-CM6A-LR low MLD member (r8)

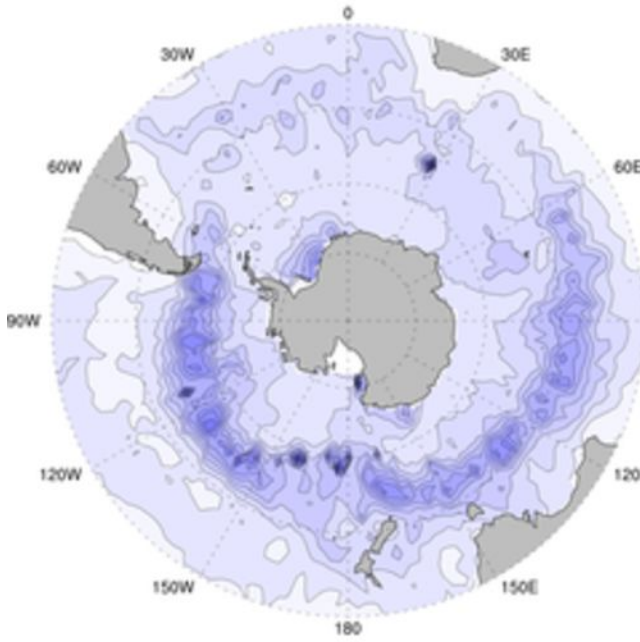


IPSL-CM6A-LR deep MLD member (r12)

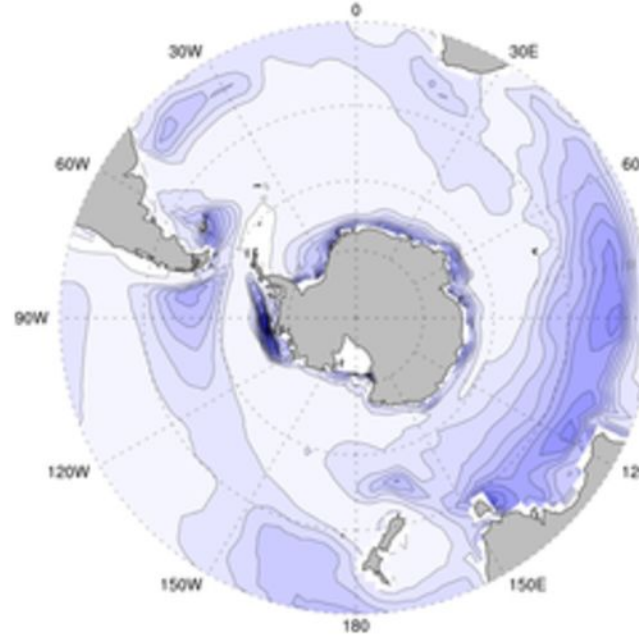


Accepted Article

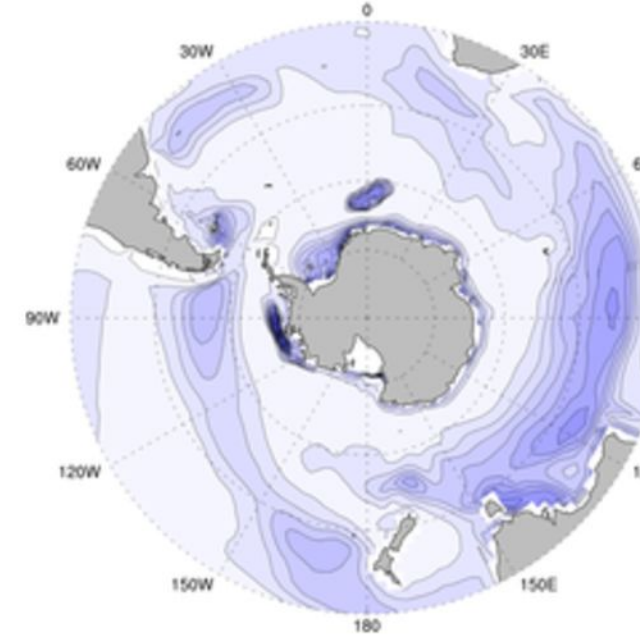
De Boyer Montegut et al. 2004



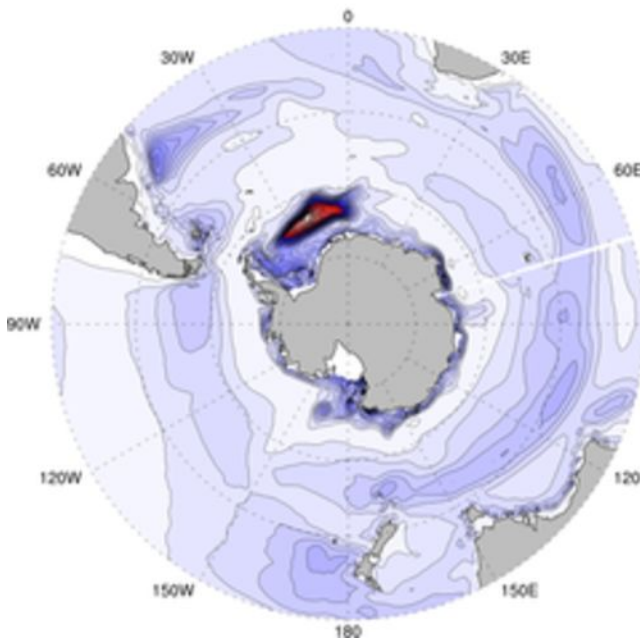
IPSL-CM5A-LR



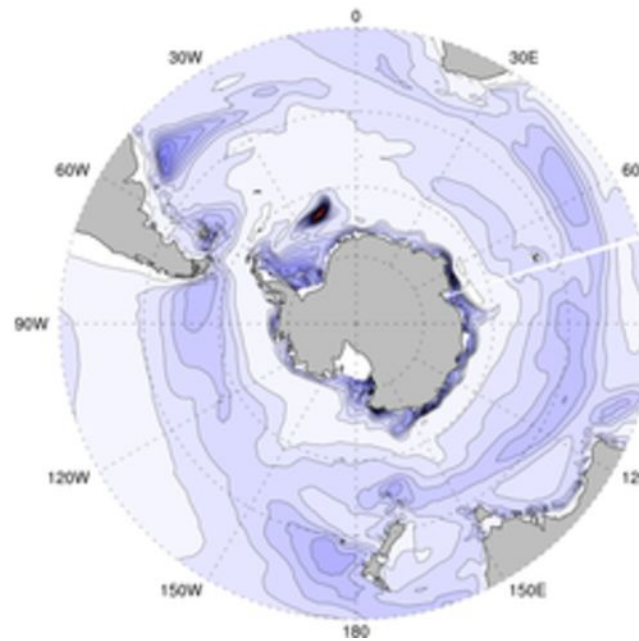
IPSL-CM5A-MR



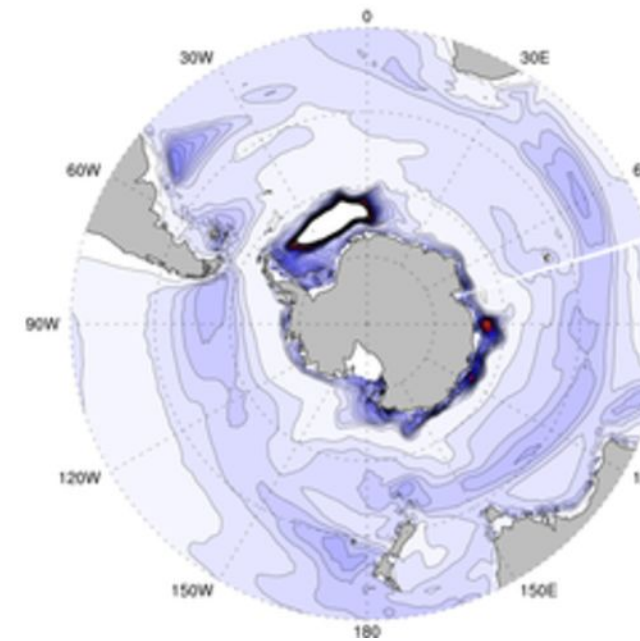
IPSL-CM6A-LR r1i1p1f1



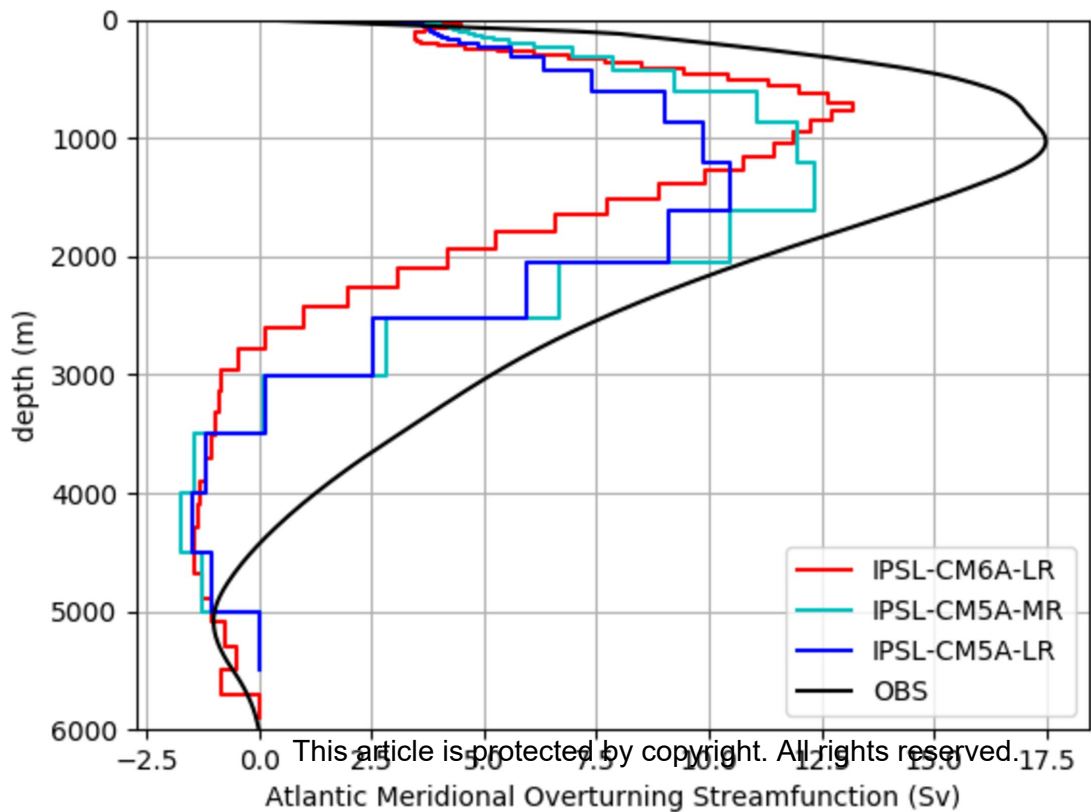
IPSL-CM6A-LR low MLD member (r3)



IPSL-CM6A-LR deep MLD member (r17)

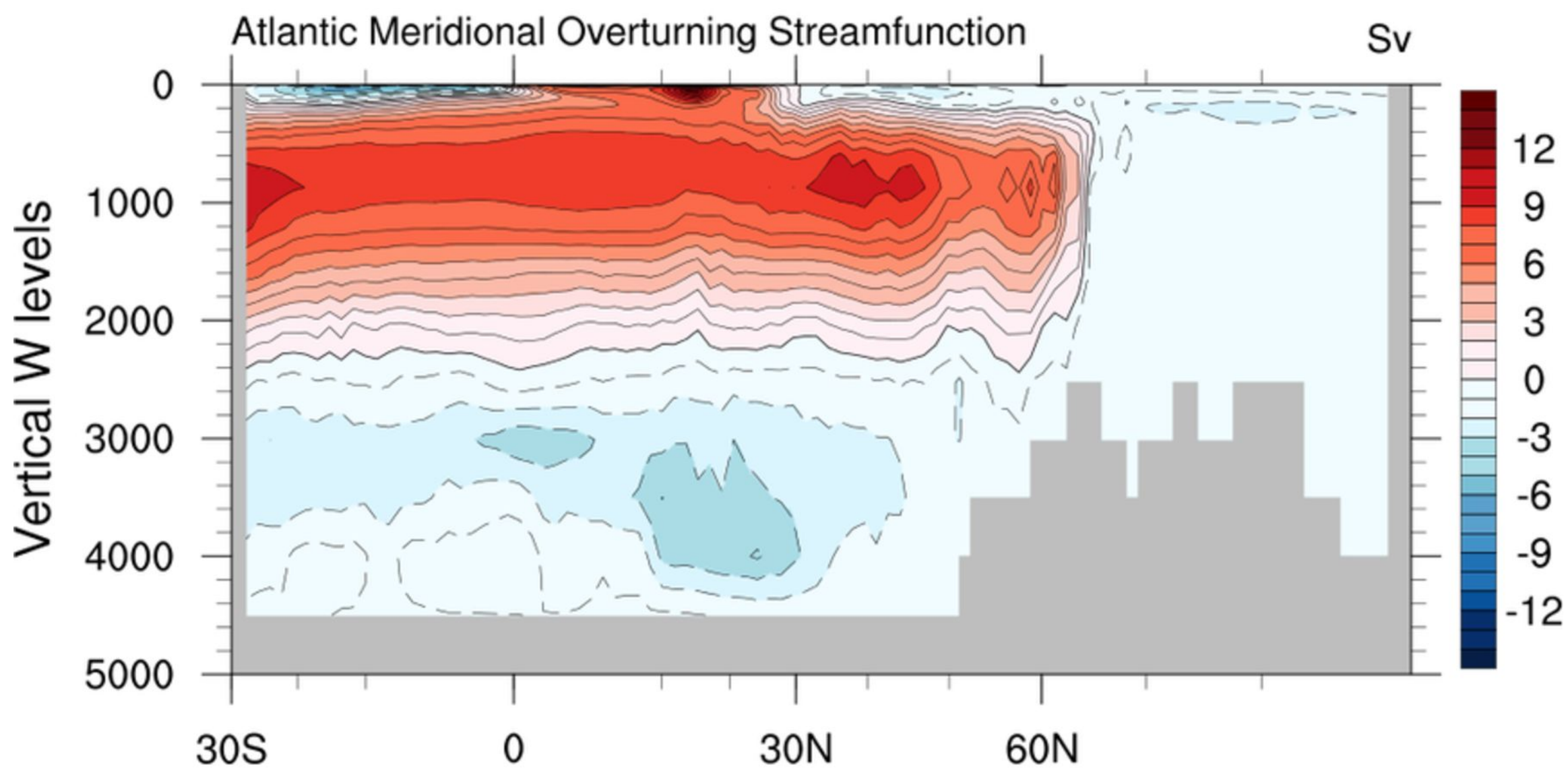


Accepted Article

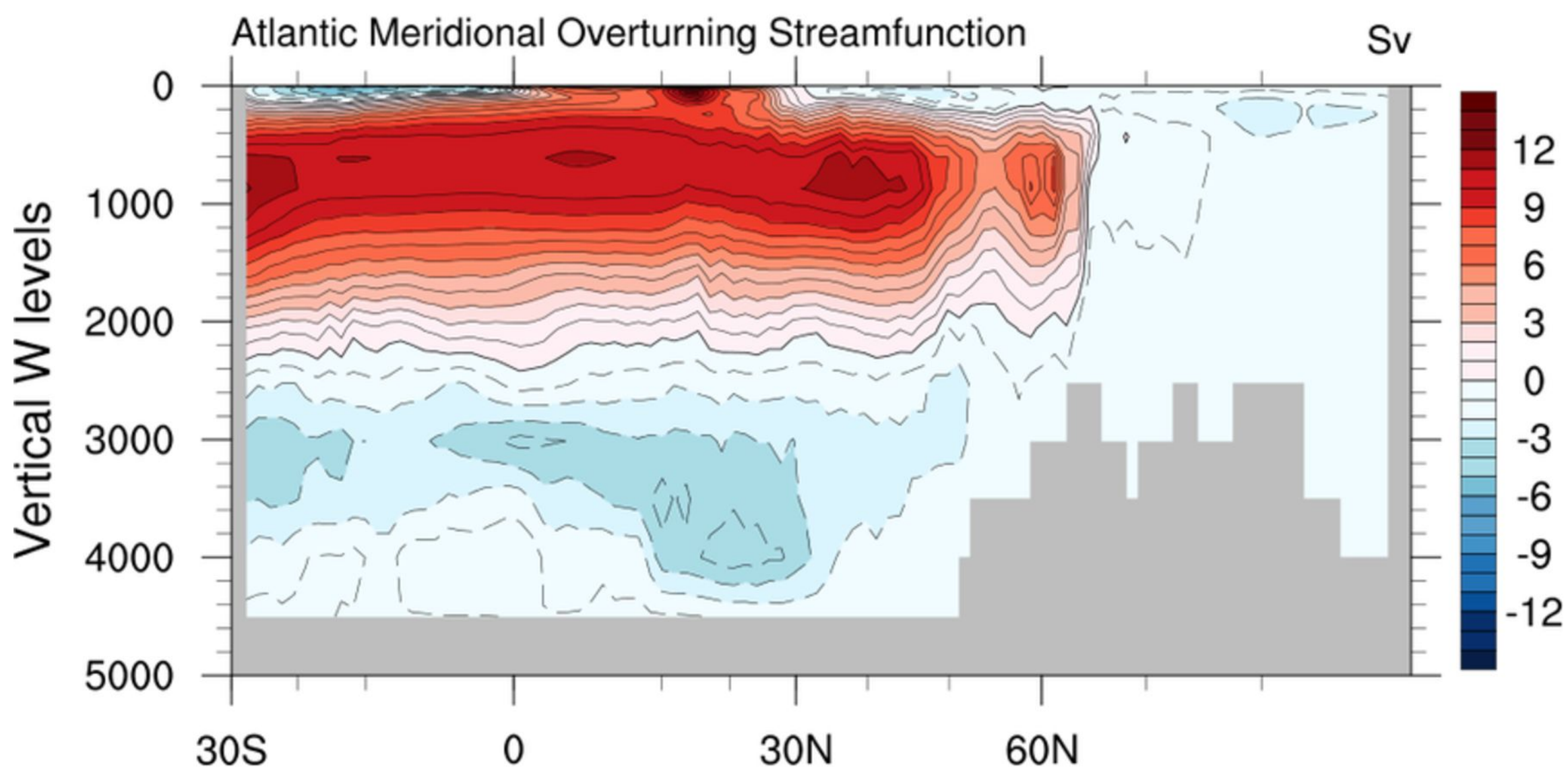


Accepted Article

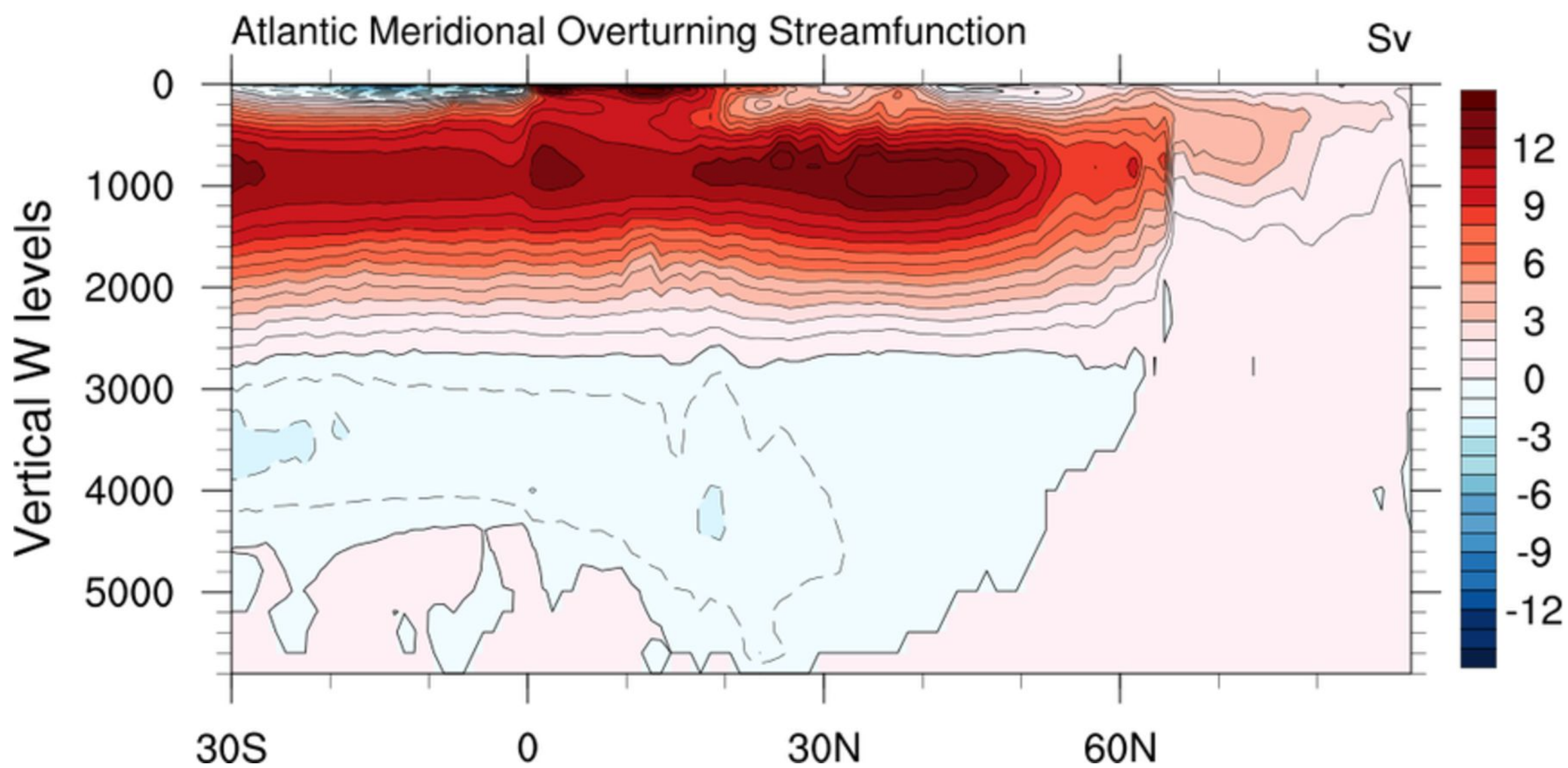
IPSL-CM5A-LR



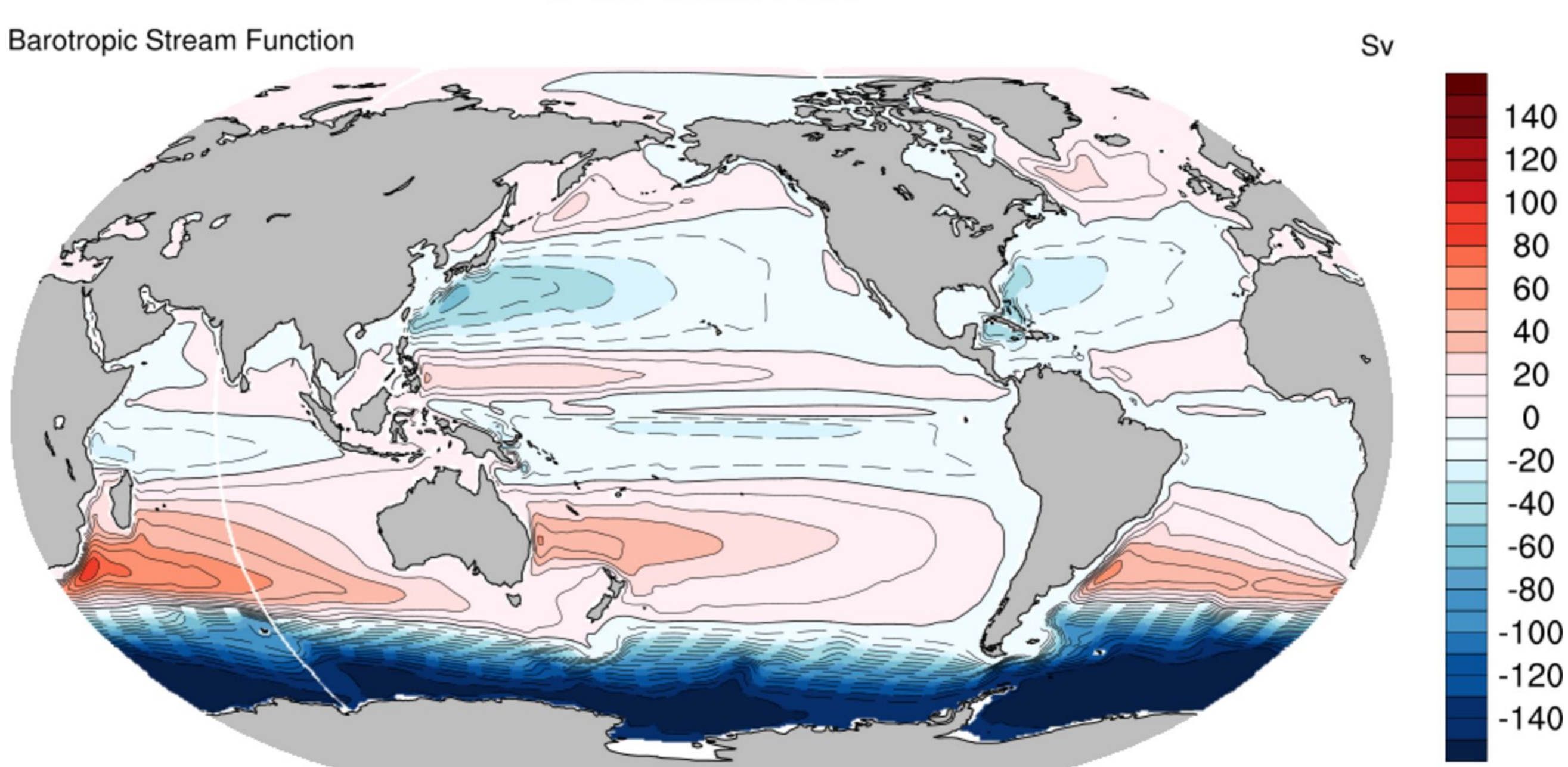
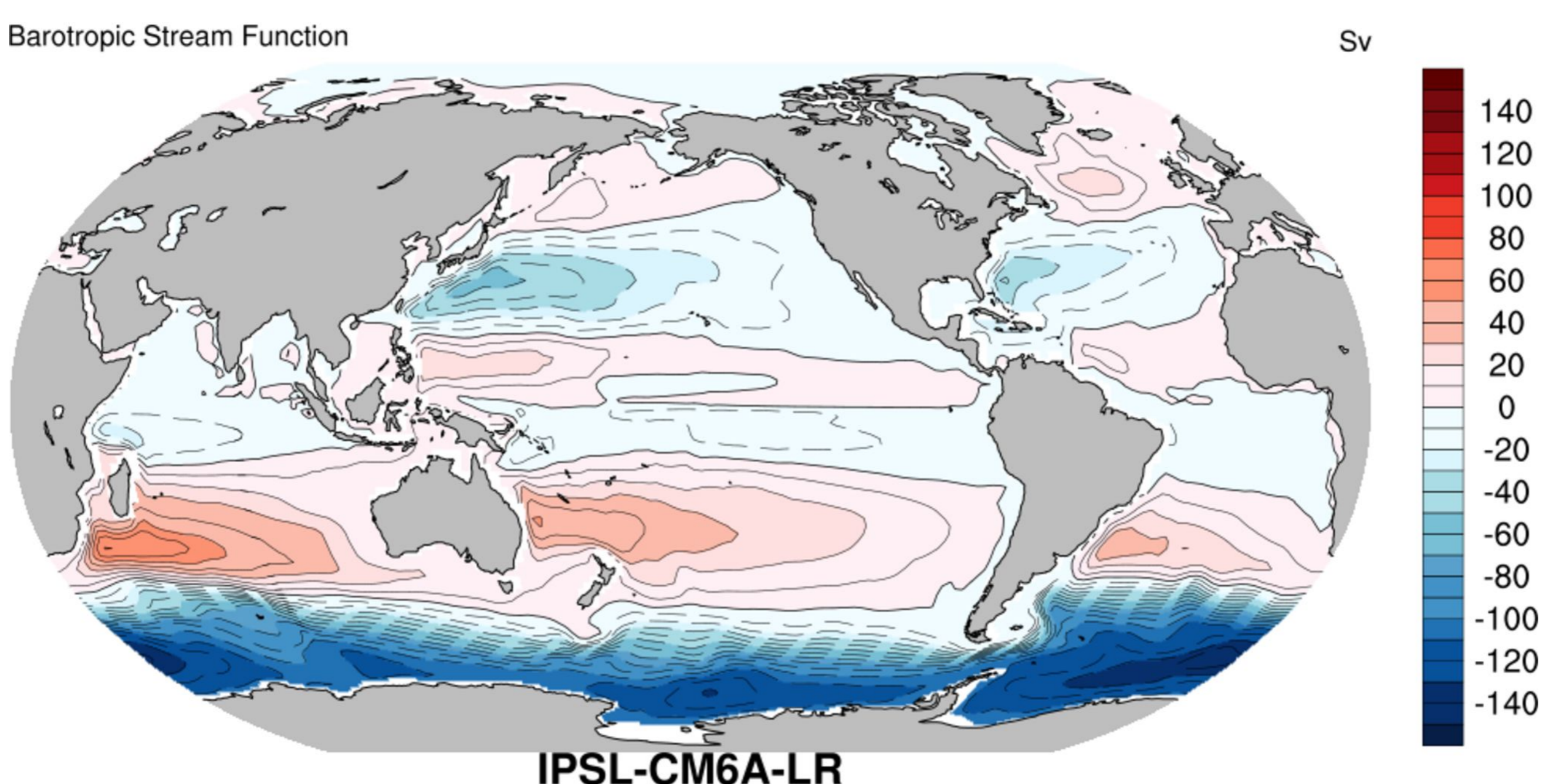
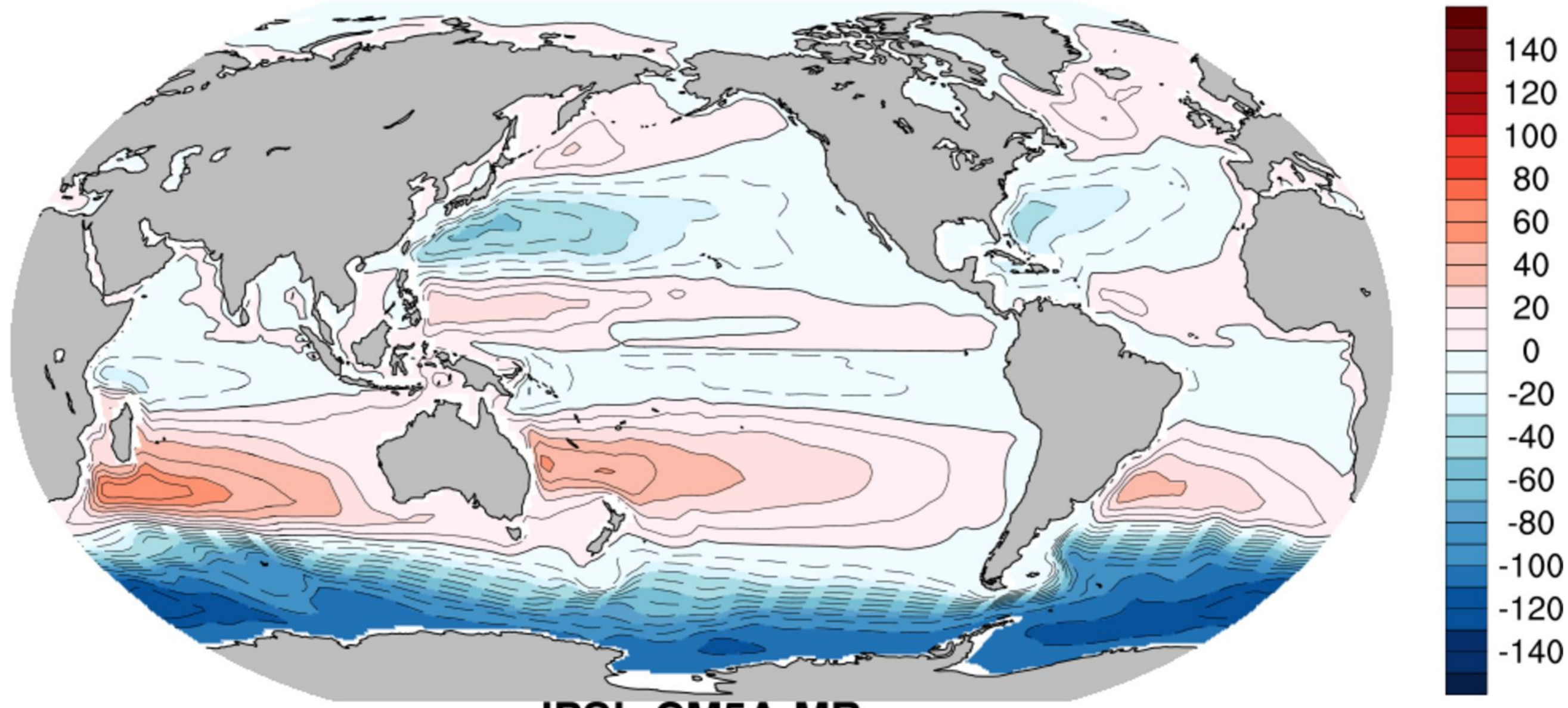
IPSL-CM5A-MR



IPSL-CM6A-LR

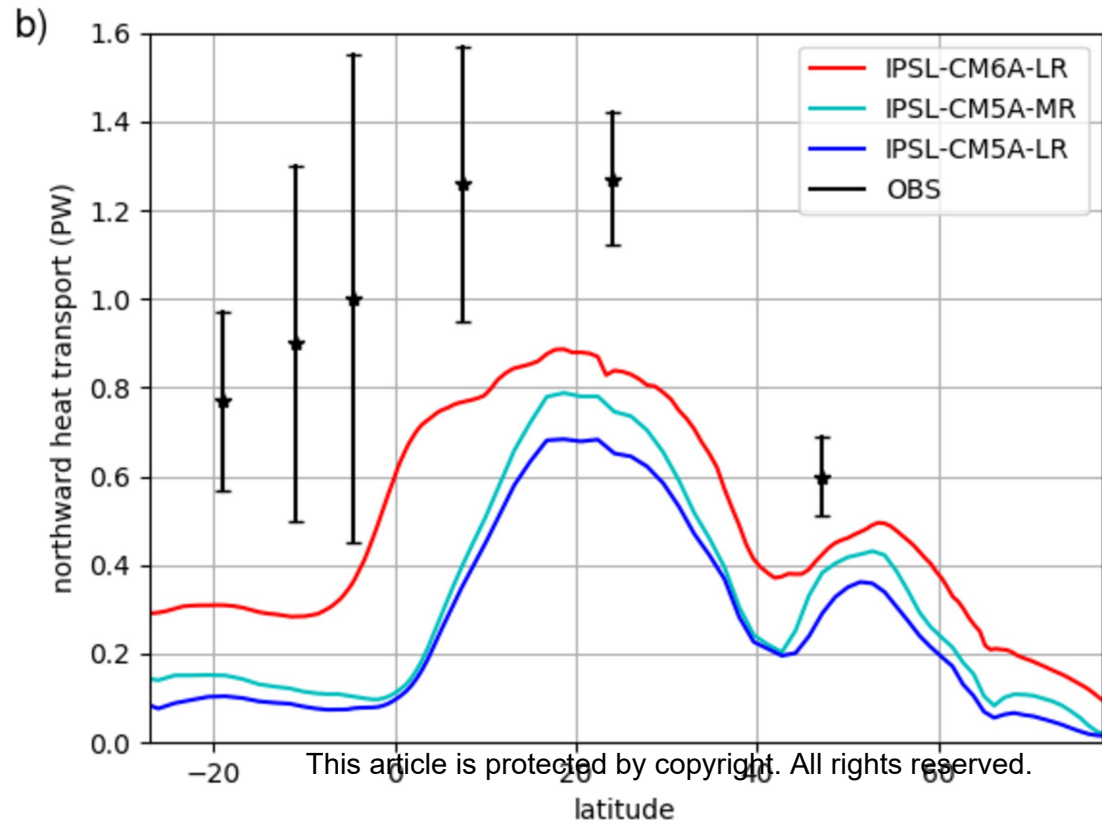
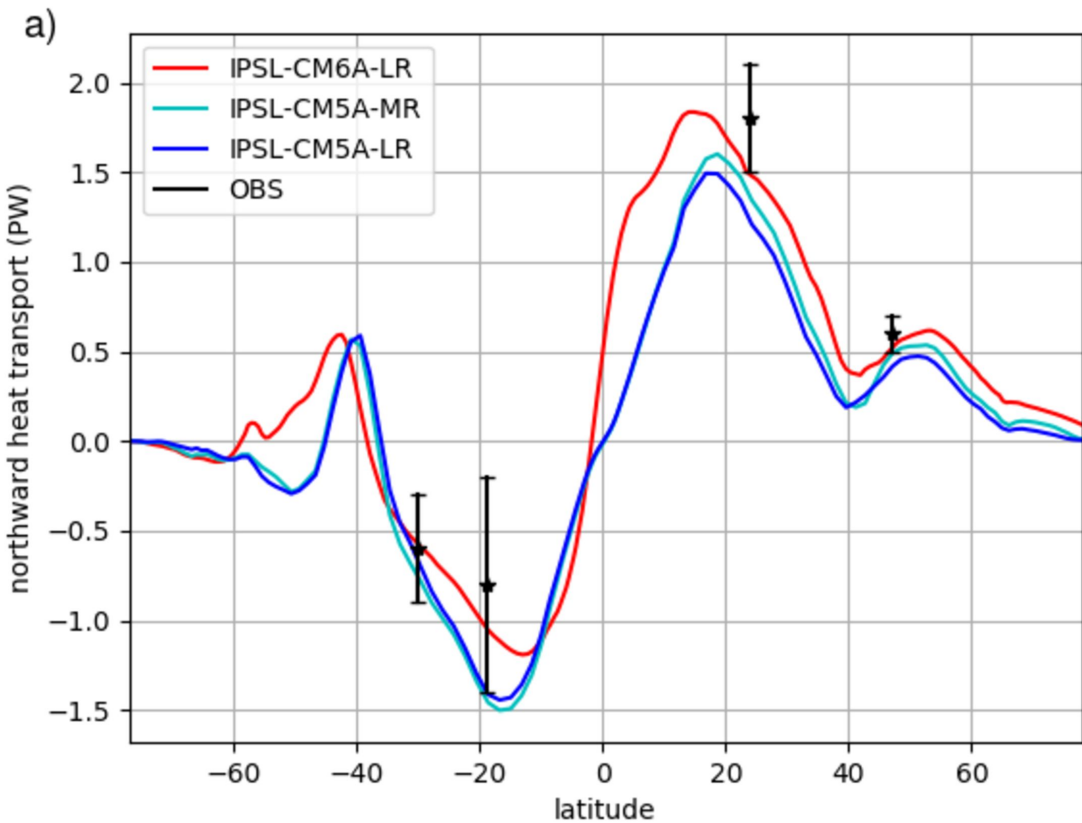


Accepted Article



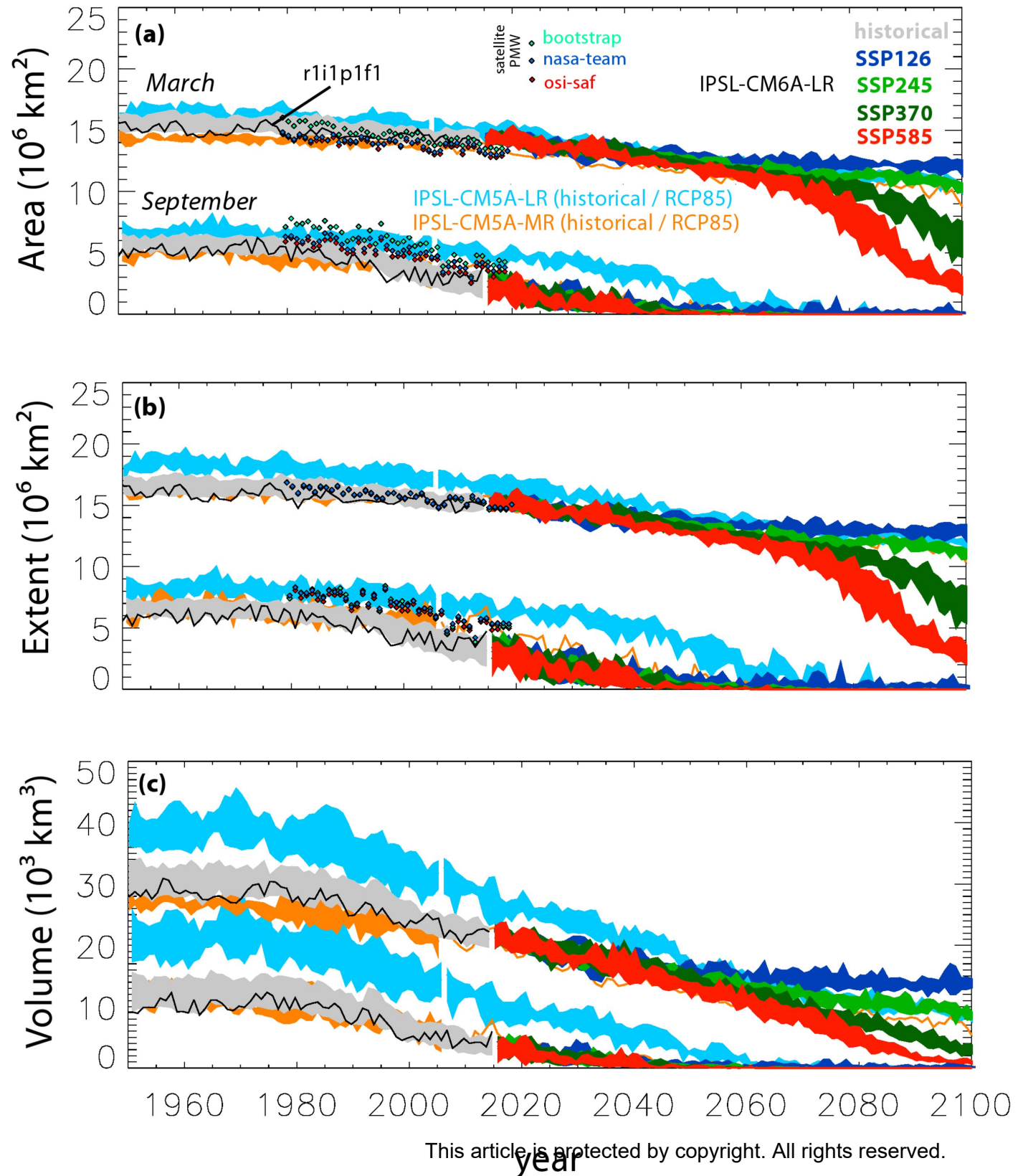
Accepted Article

Accepted Article



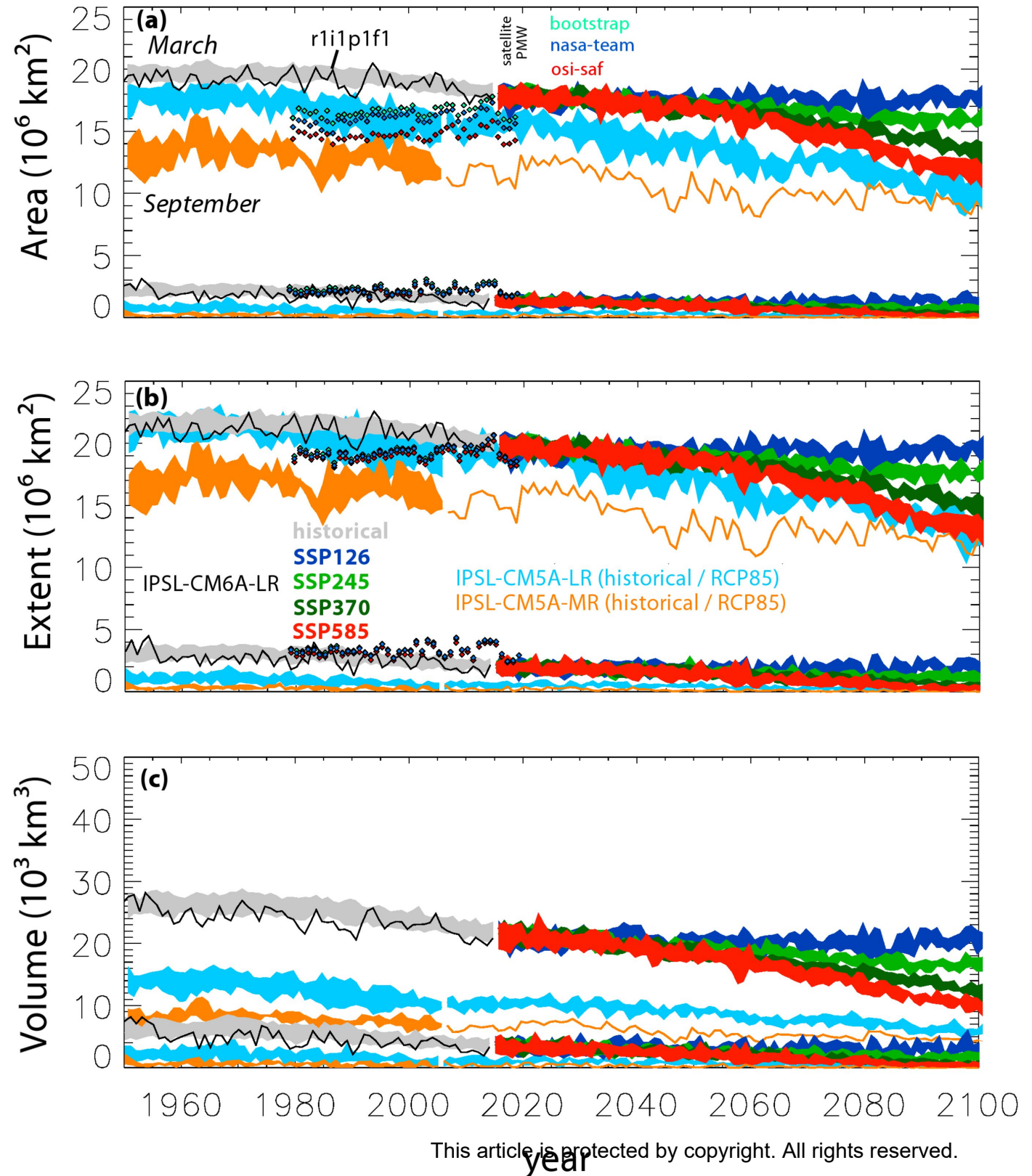
Accepted Article

Sea ice in IPSL-CM (Northern Hemisphere)

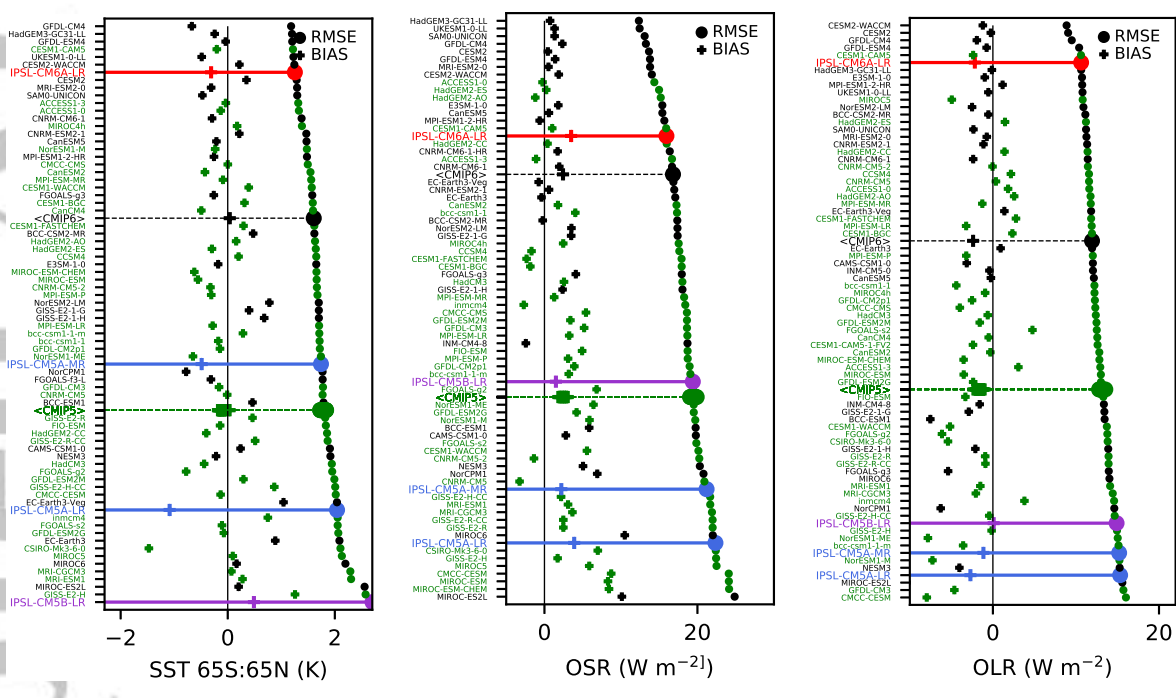


Accepted Article

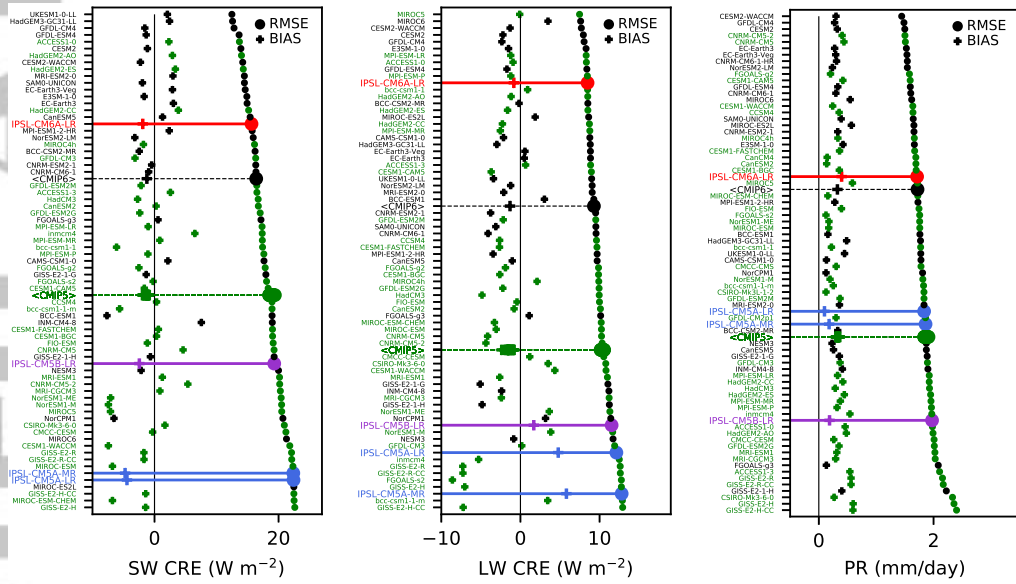
Sea ice in IPSL-CM (Southern Hemisphere)



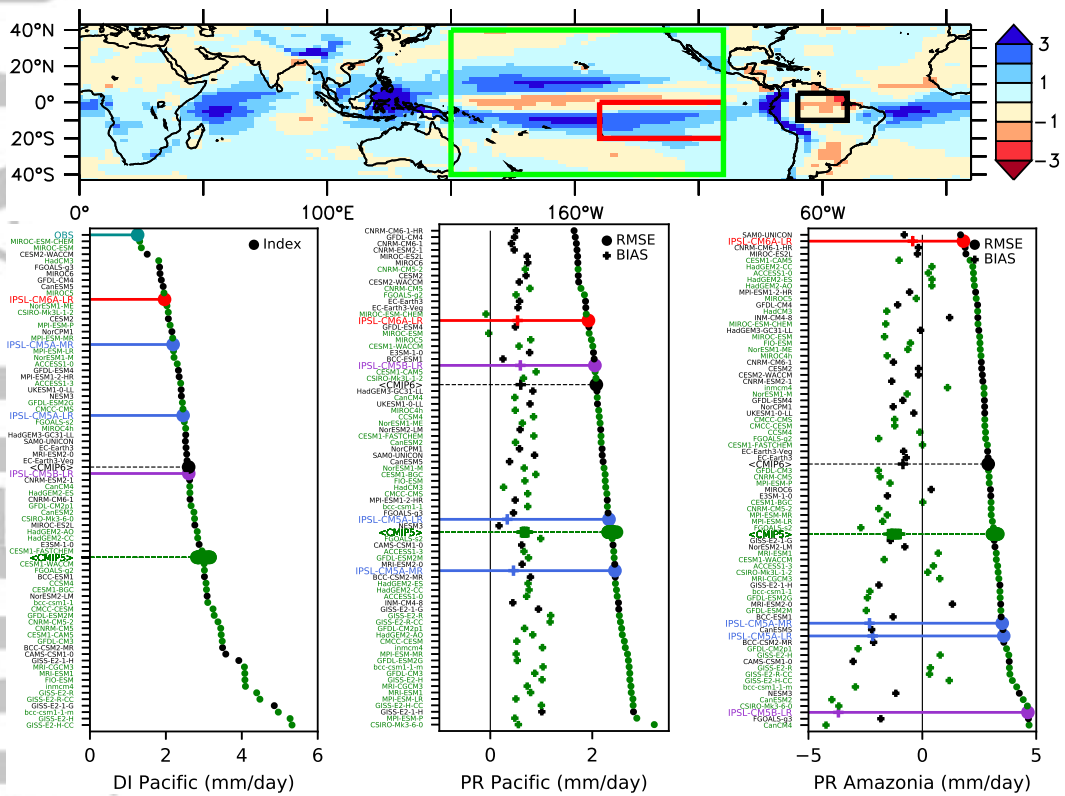
Accepted Article



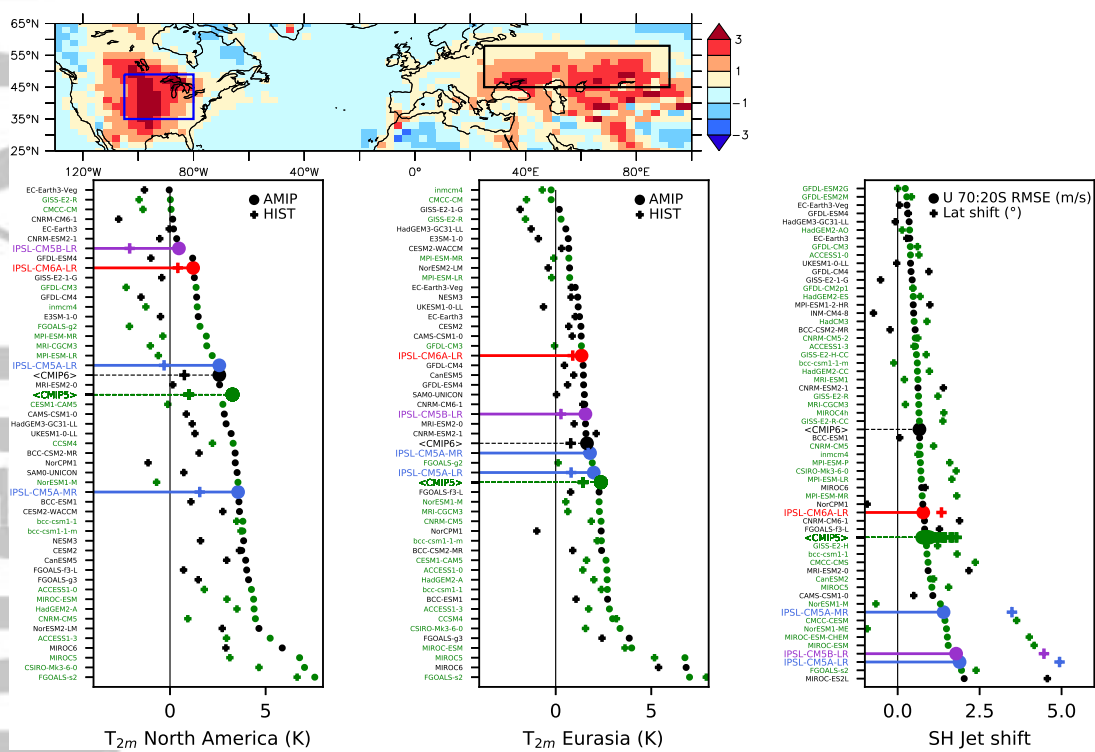
Accepted Article



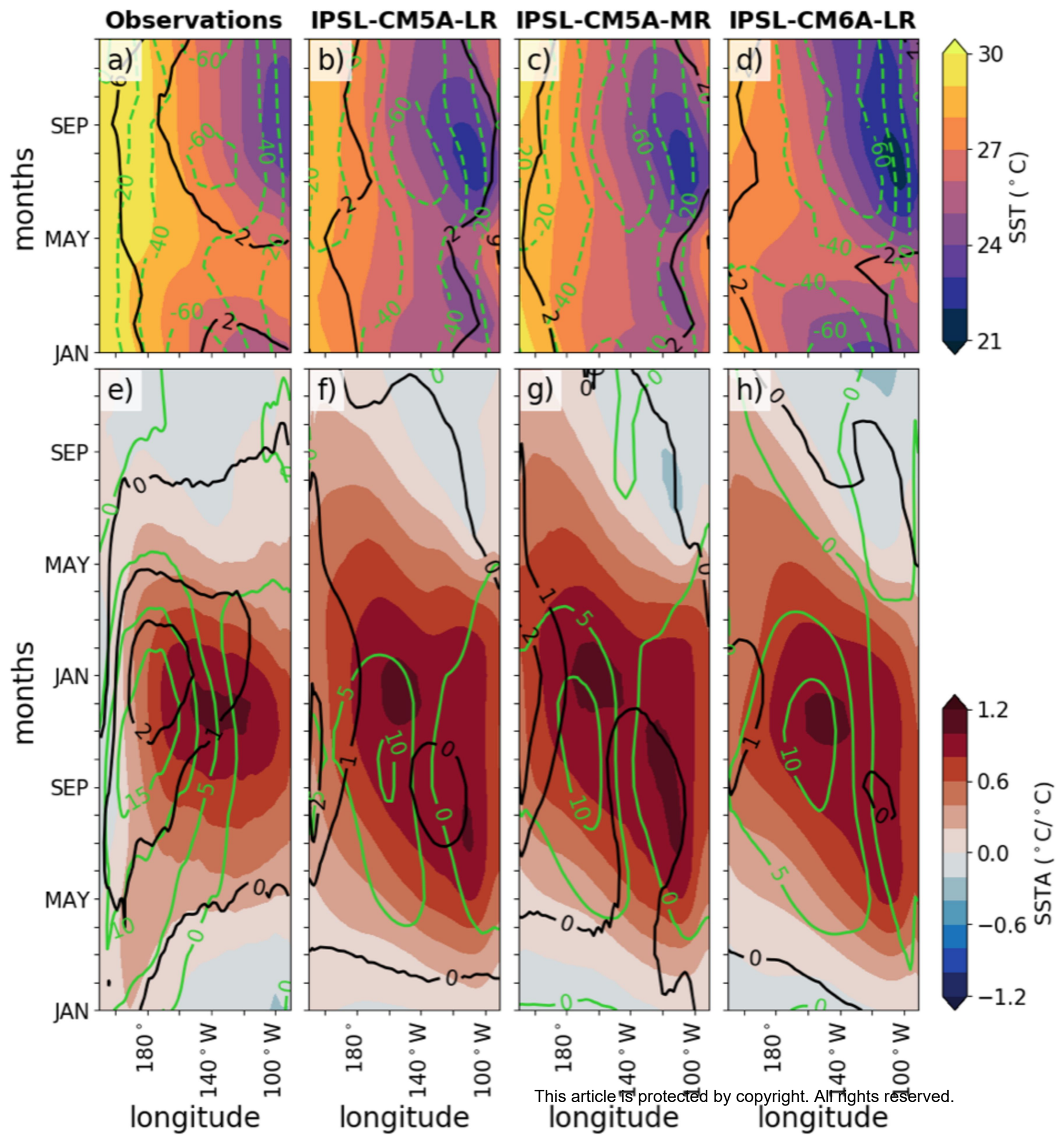
Accepted Article



Accepted Article

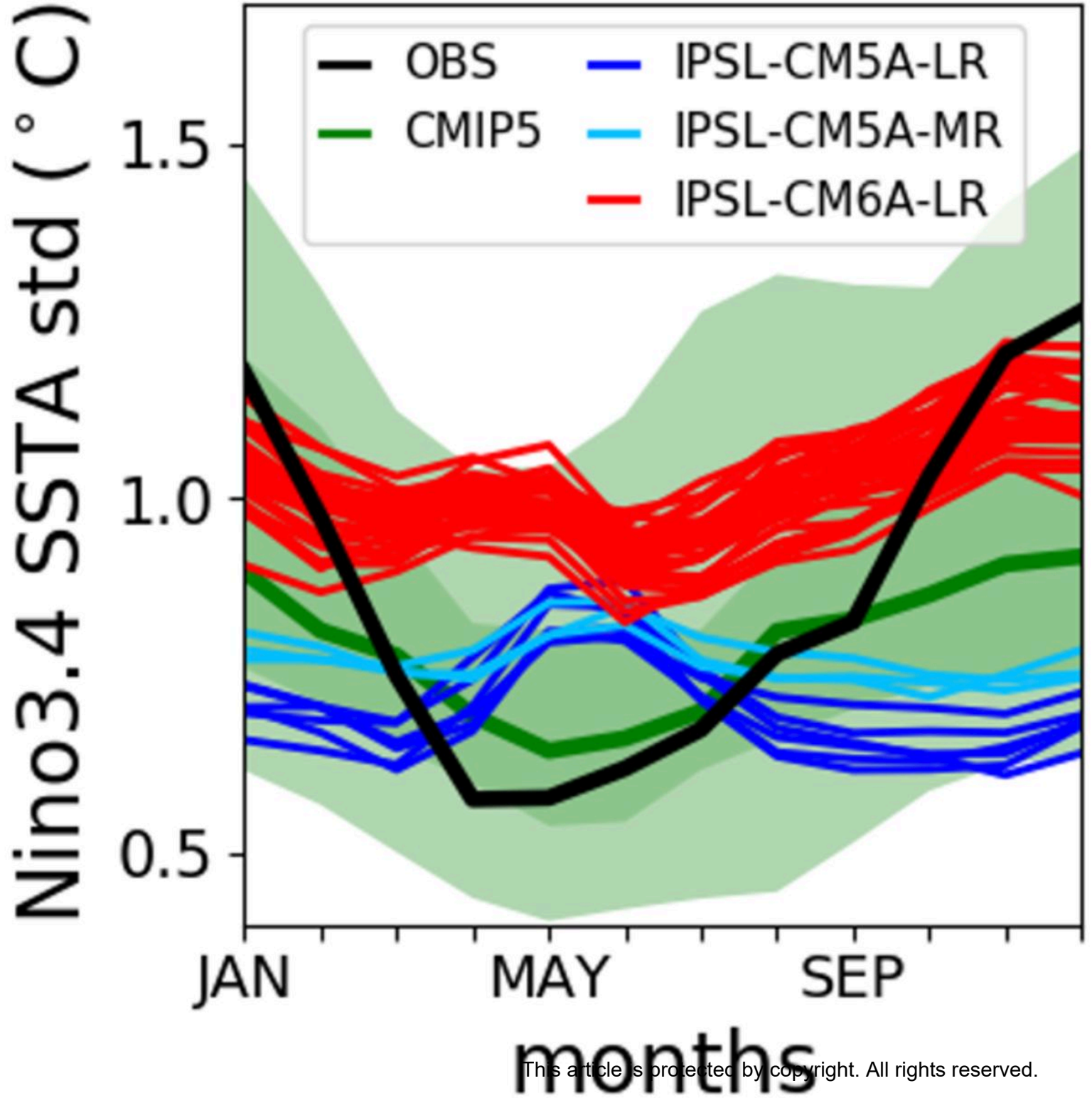


Accepted Article

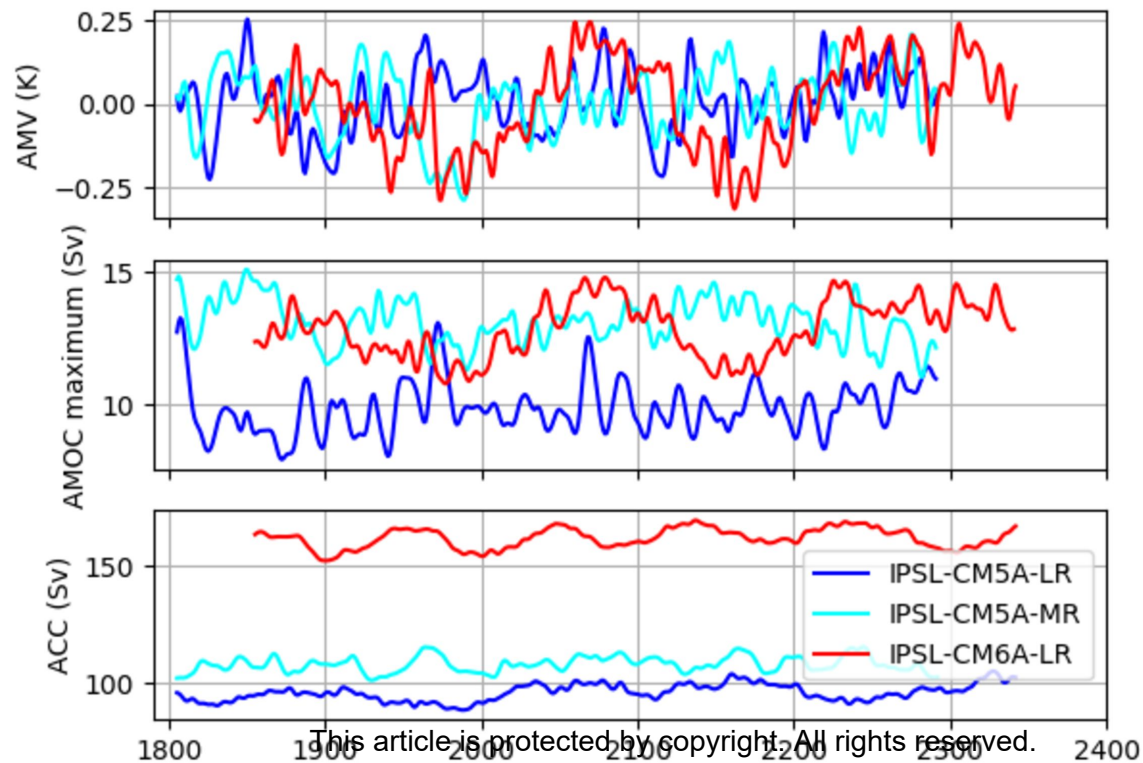


Accepted Article

ENSO seasonality



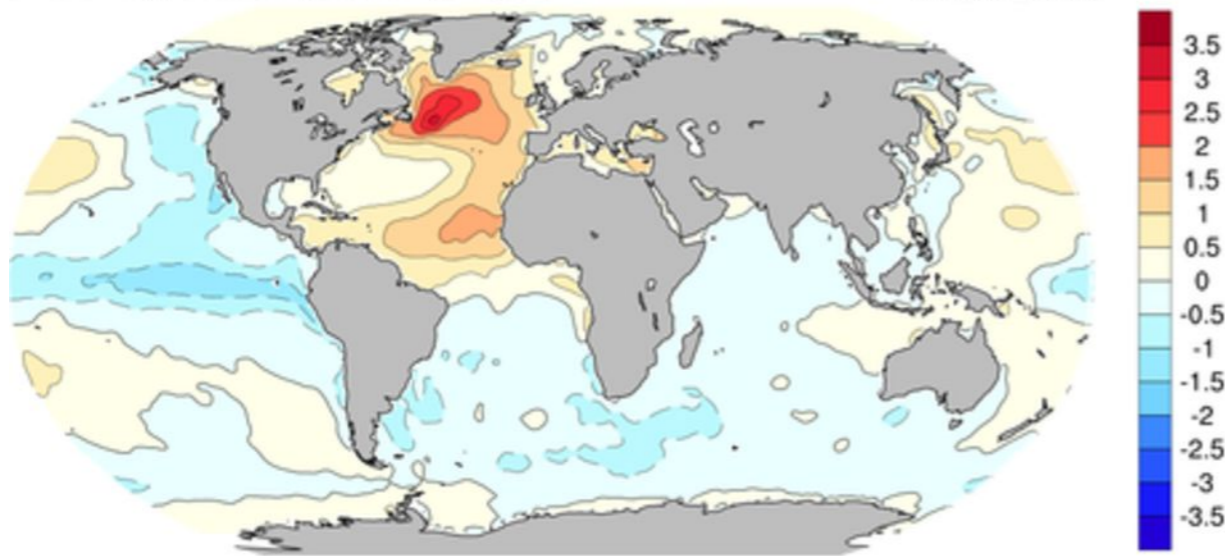
Accepted Article



Accepted Article

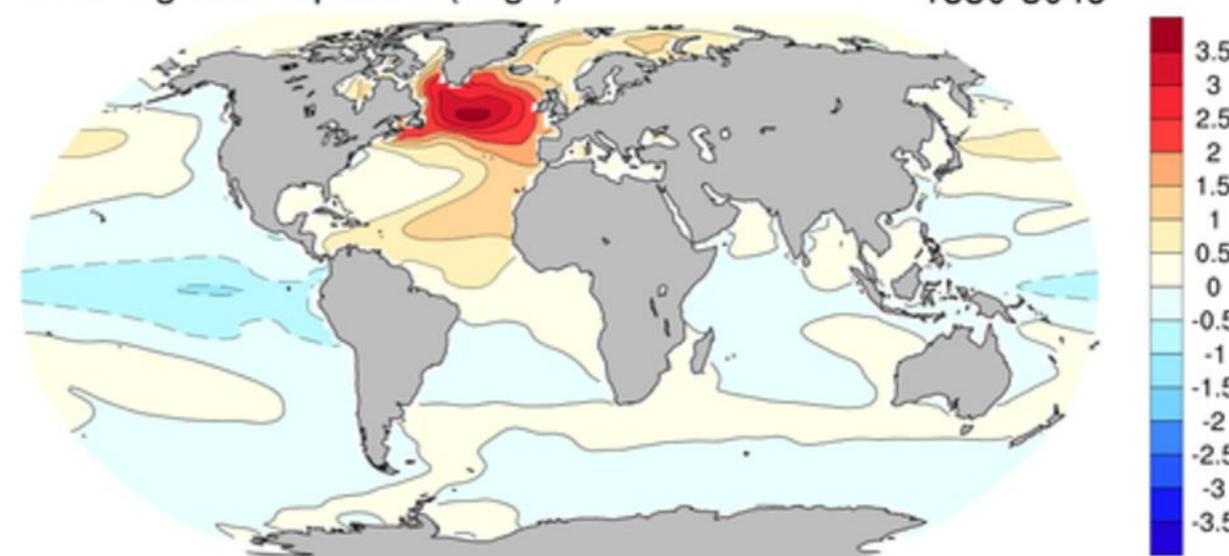
HadISST

AMO regression pattern (degC) 1920-2016



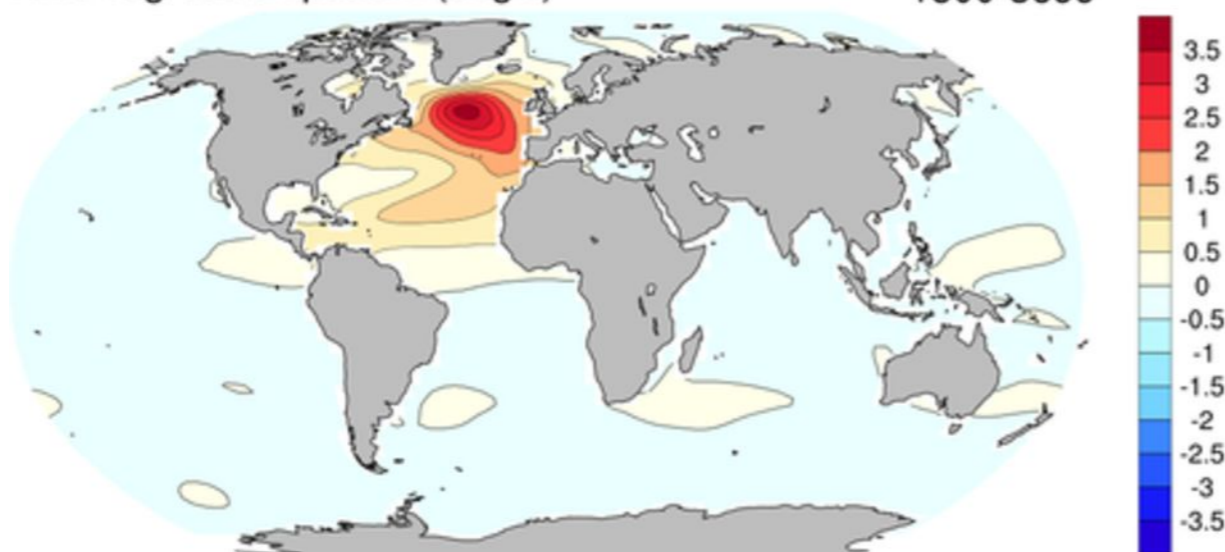
IPSL-CM6A-LR piControl

AMO regression pattern (degC) 1850-3049



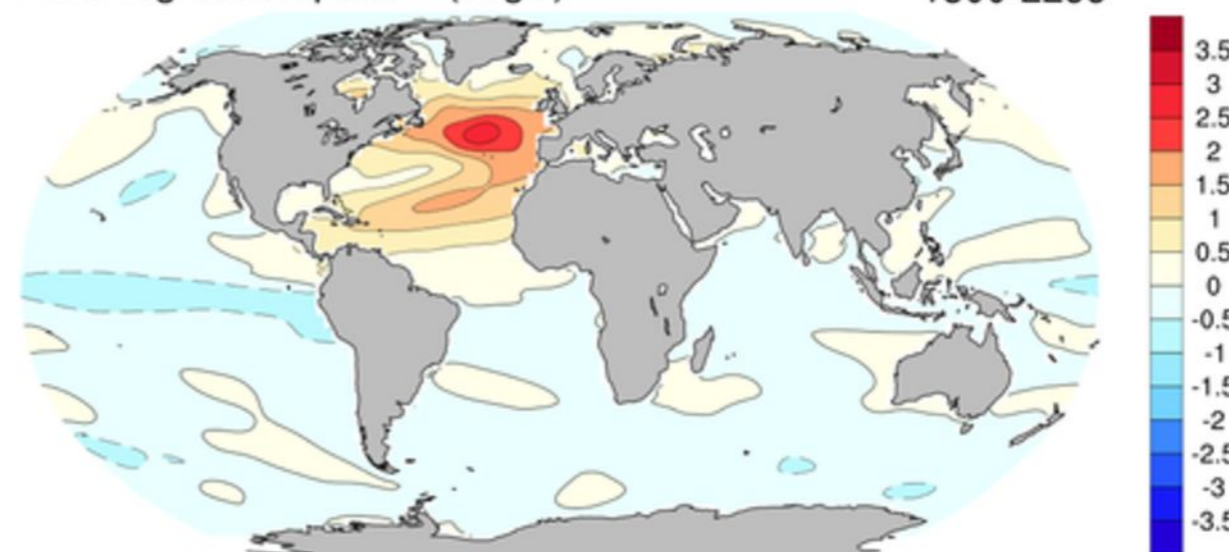
IPSL-CM5A-LR piControl

AMO regression pattern (degC) 1800-3699



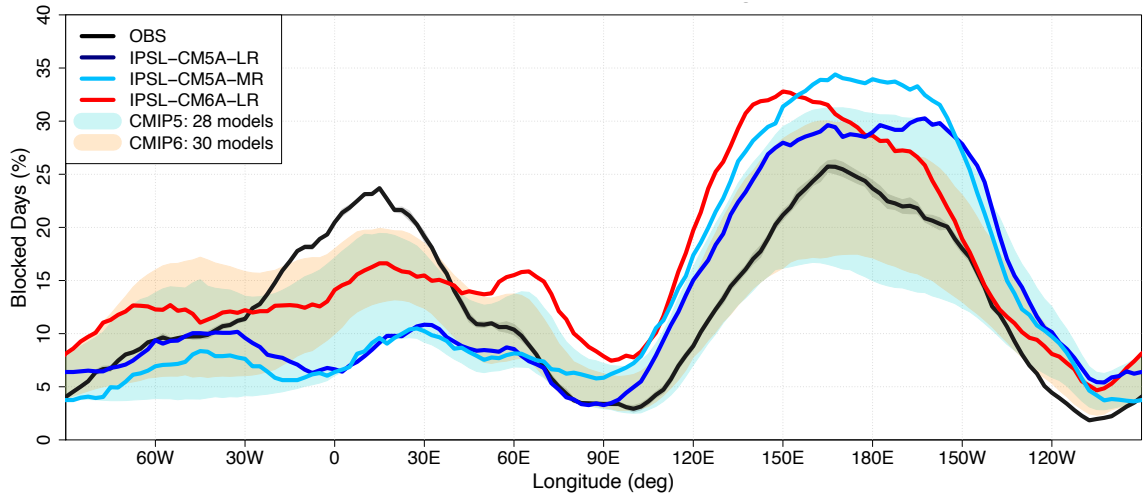
IPSL-CM5A-MR piControl

AMO regression pattern (degC) 1800-2299

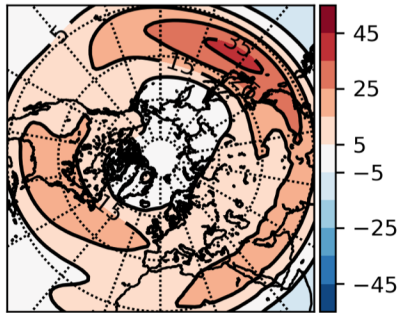


Accepted Article

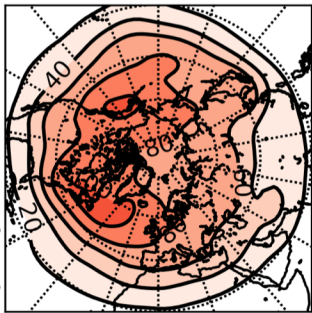
a) Northern Hemisphere blocking frequency DJFM 1980-2005



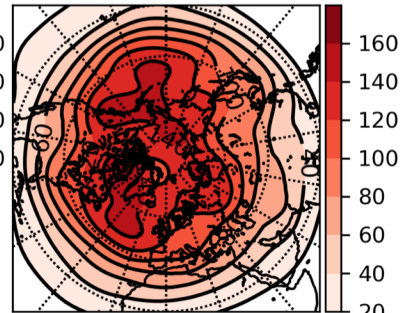
b) \bar{U} IPSL-CM6



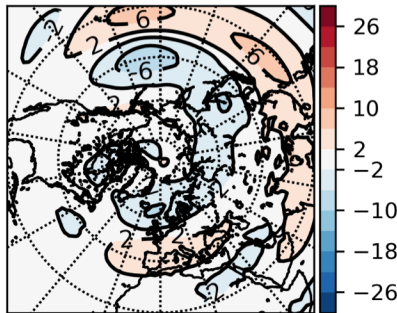
c) high-Freq STD



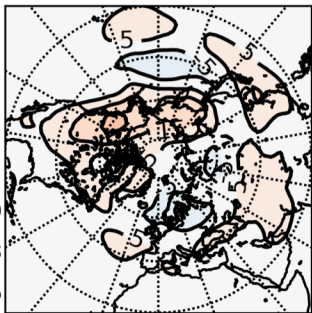
d) Low-Freq STD



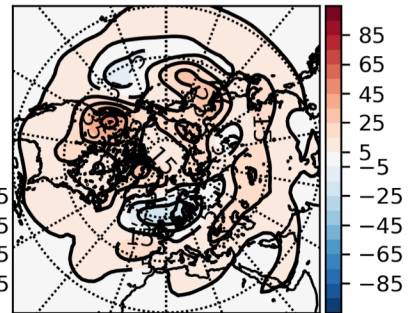
e) CM6 - ERAi



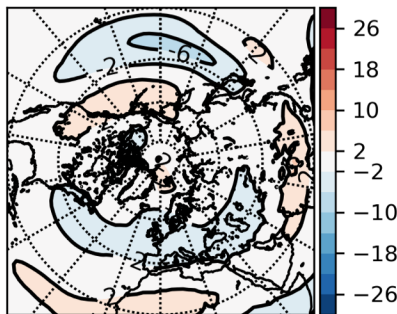
f) CM6 - ERAi



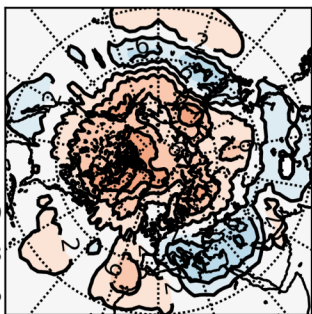
g) CM6 - ERAi



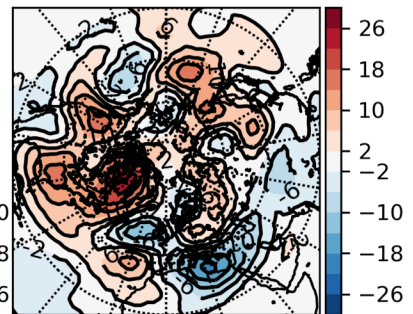
h) CM6 - CM5



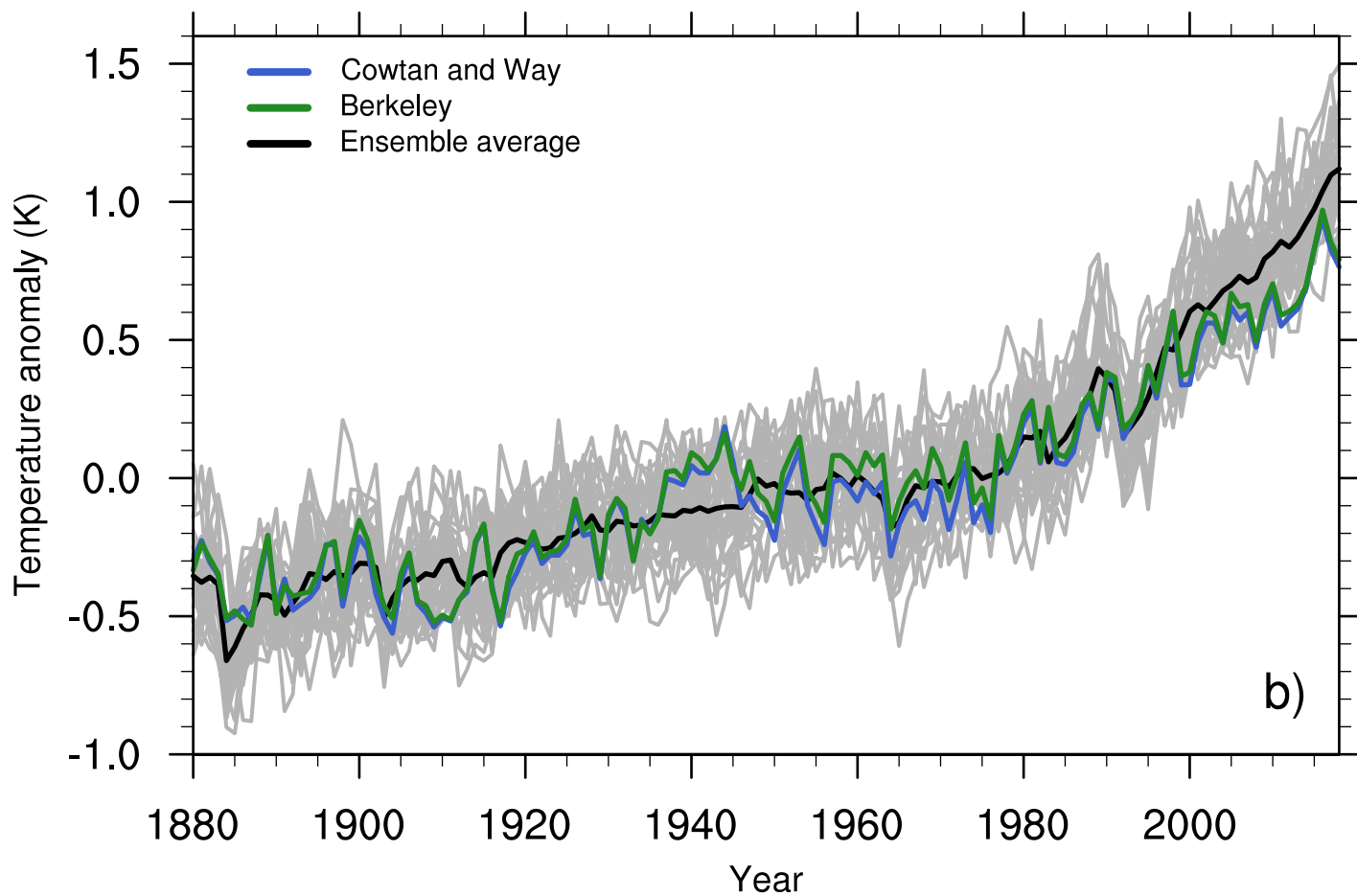
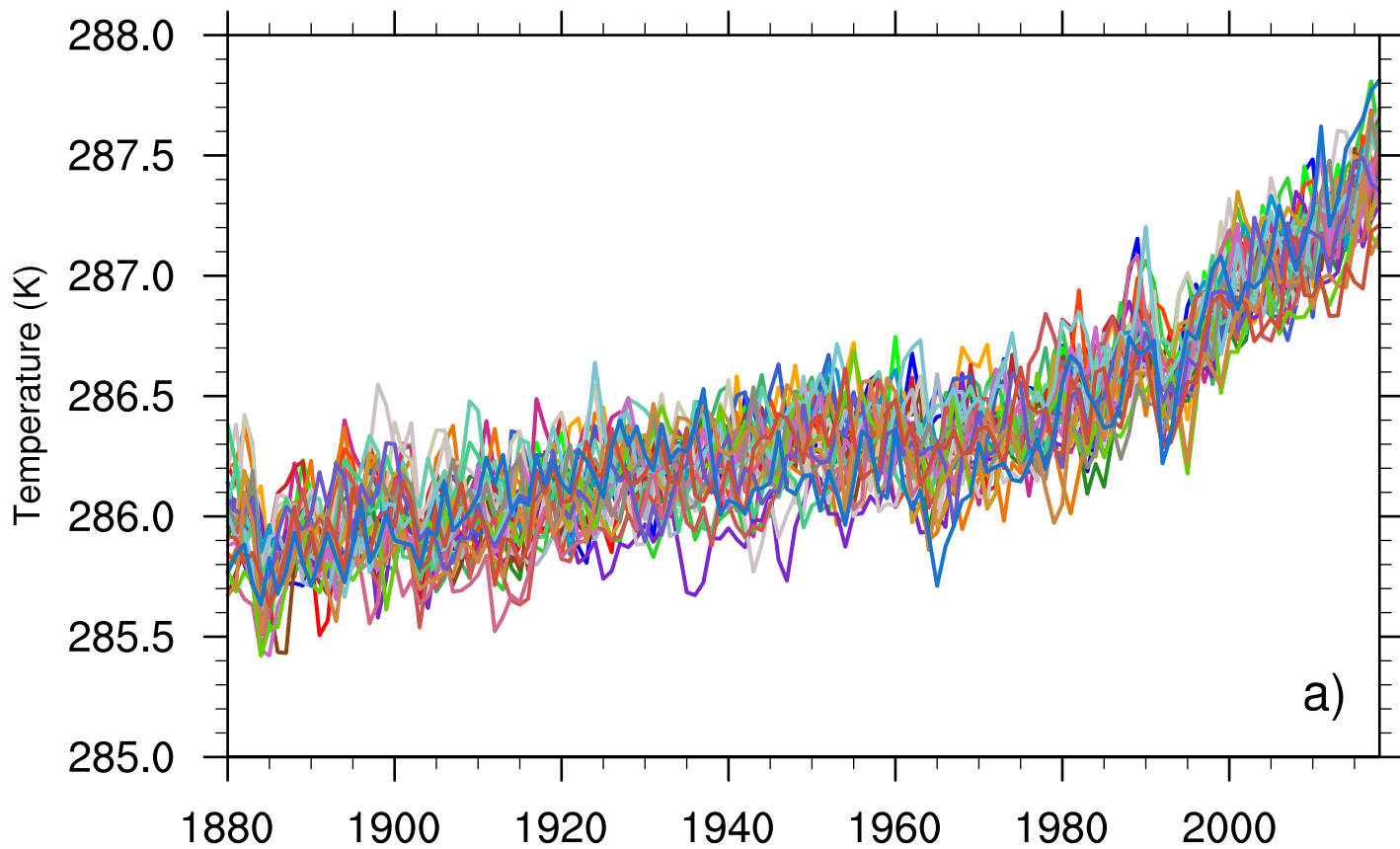
i) CM6 - CM5



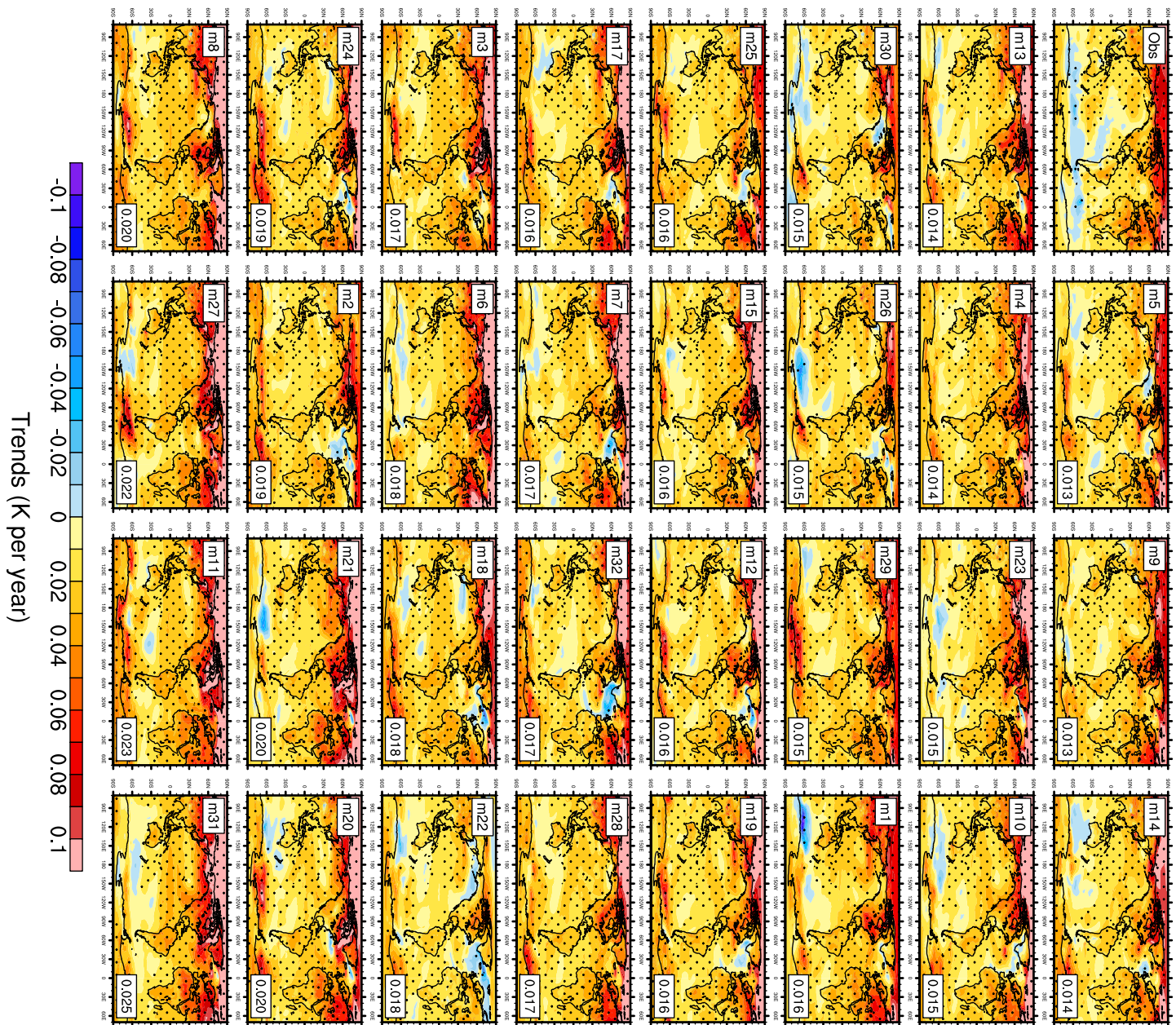
j) CM6 - CM5



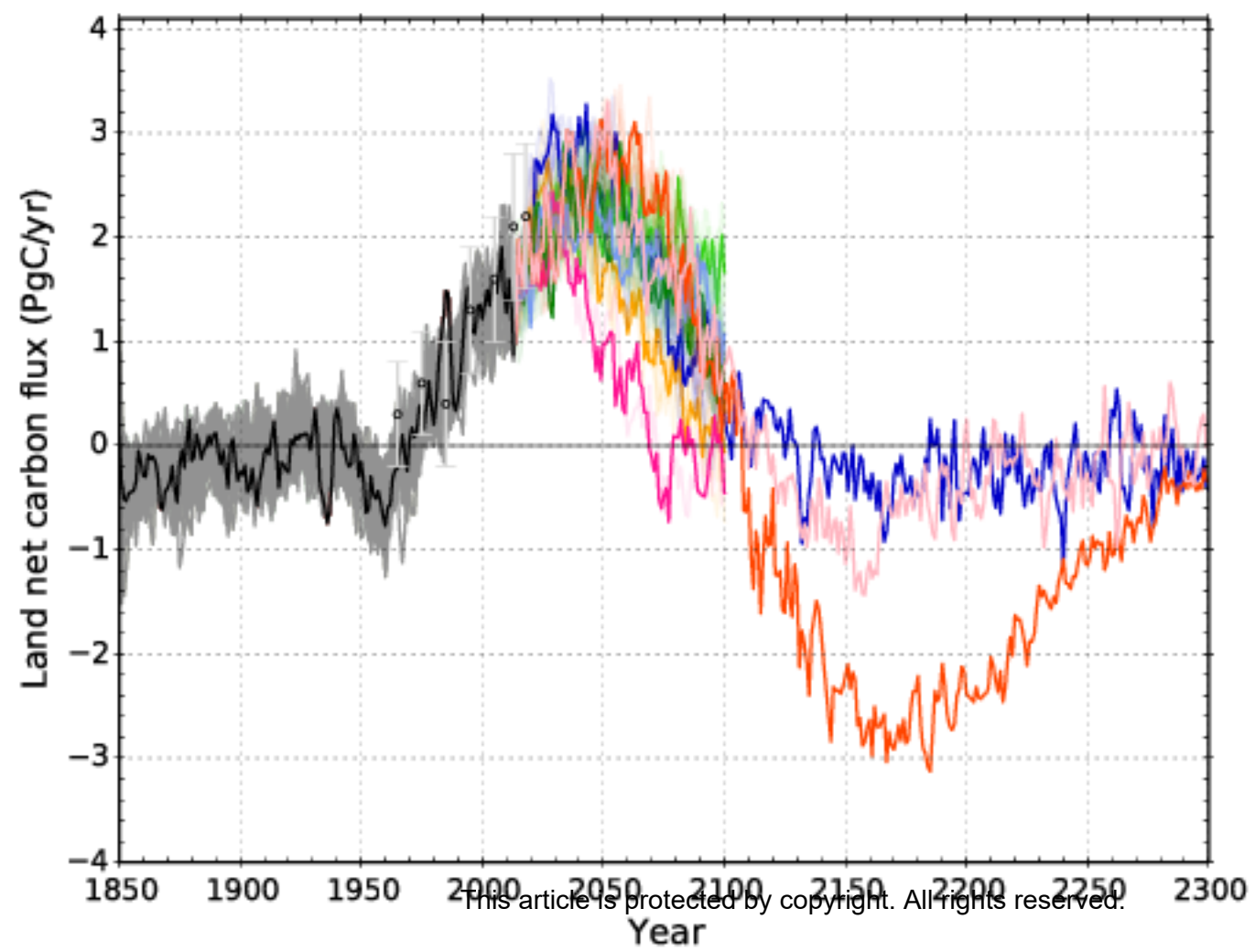
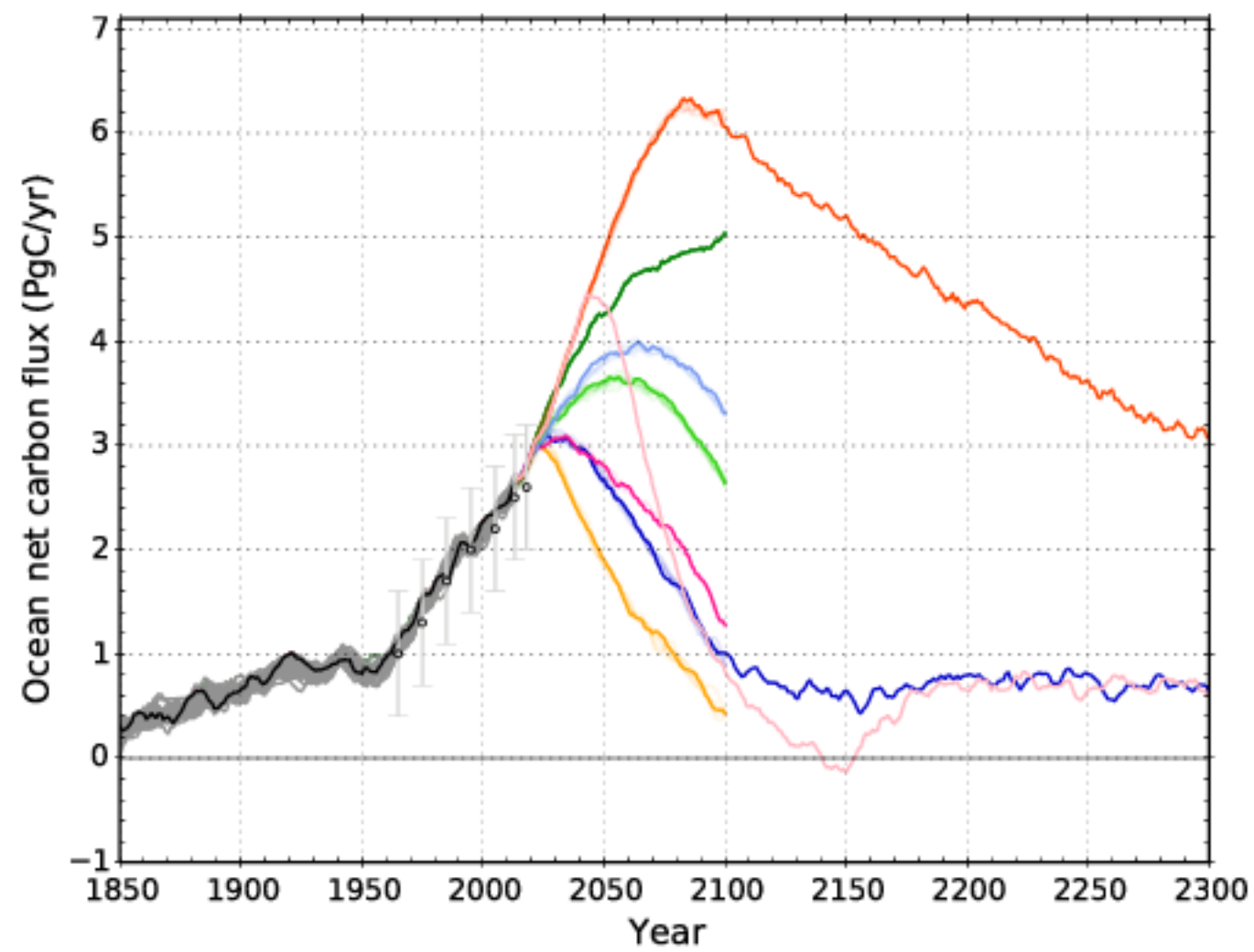
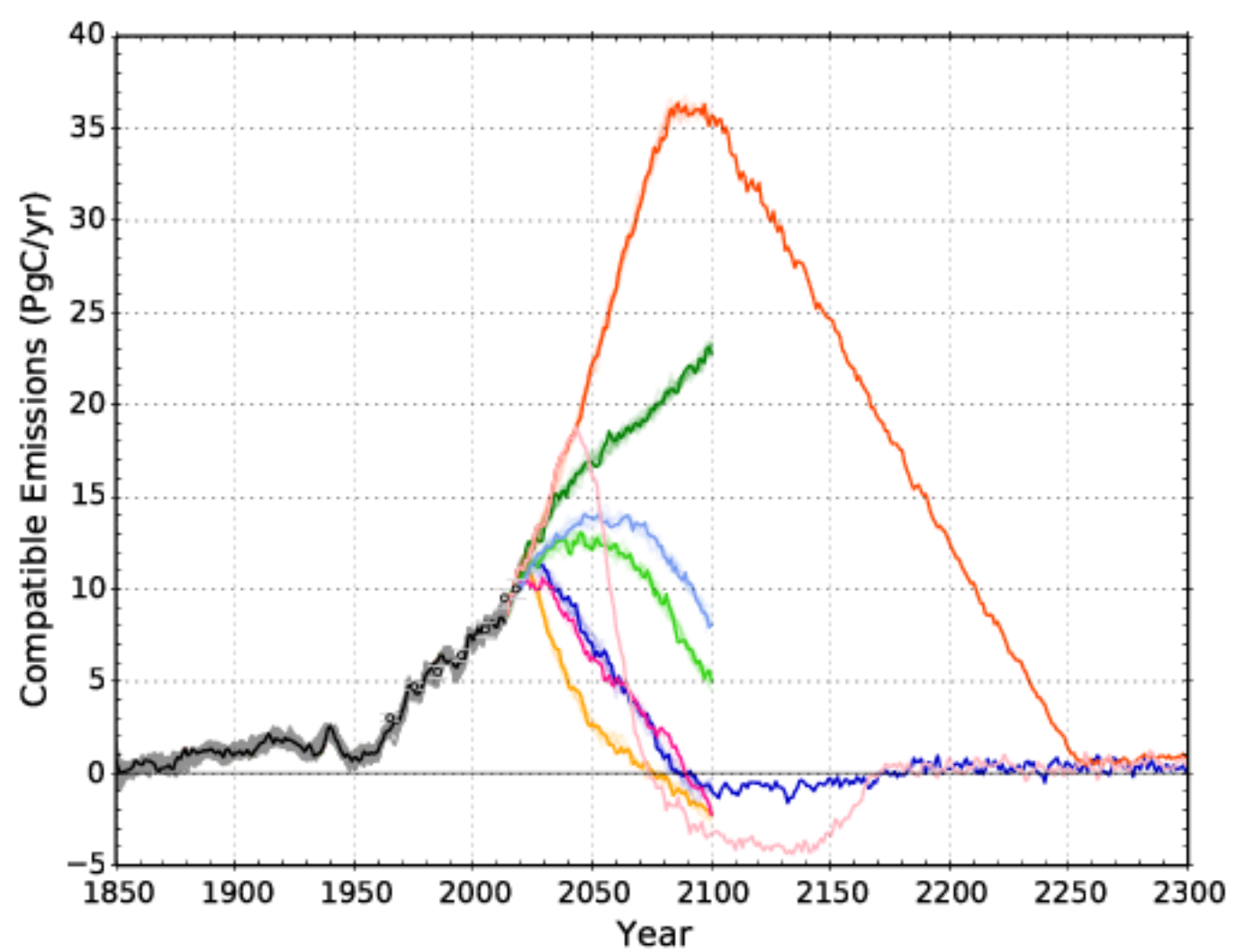
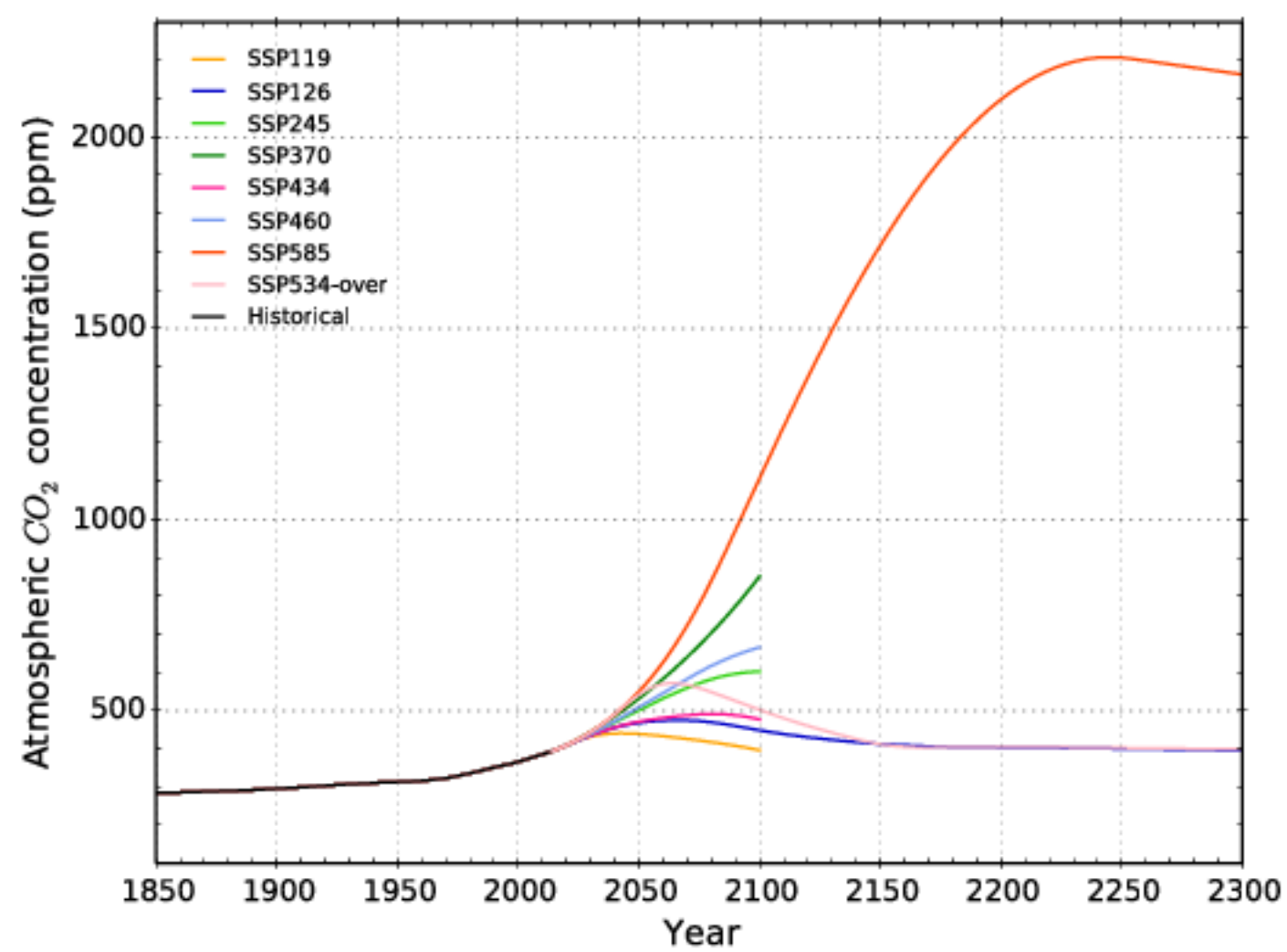
Accepted Article



Accepted Article

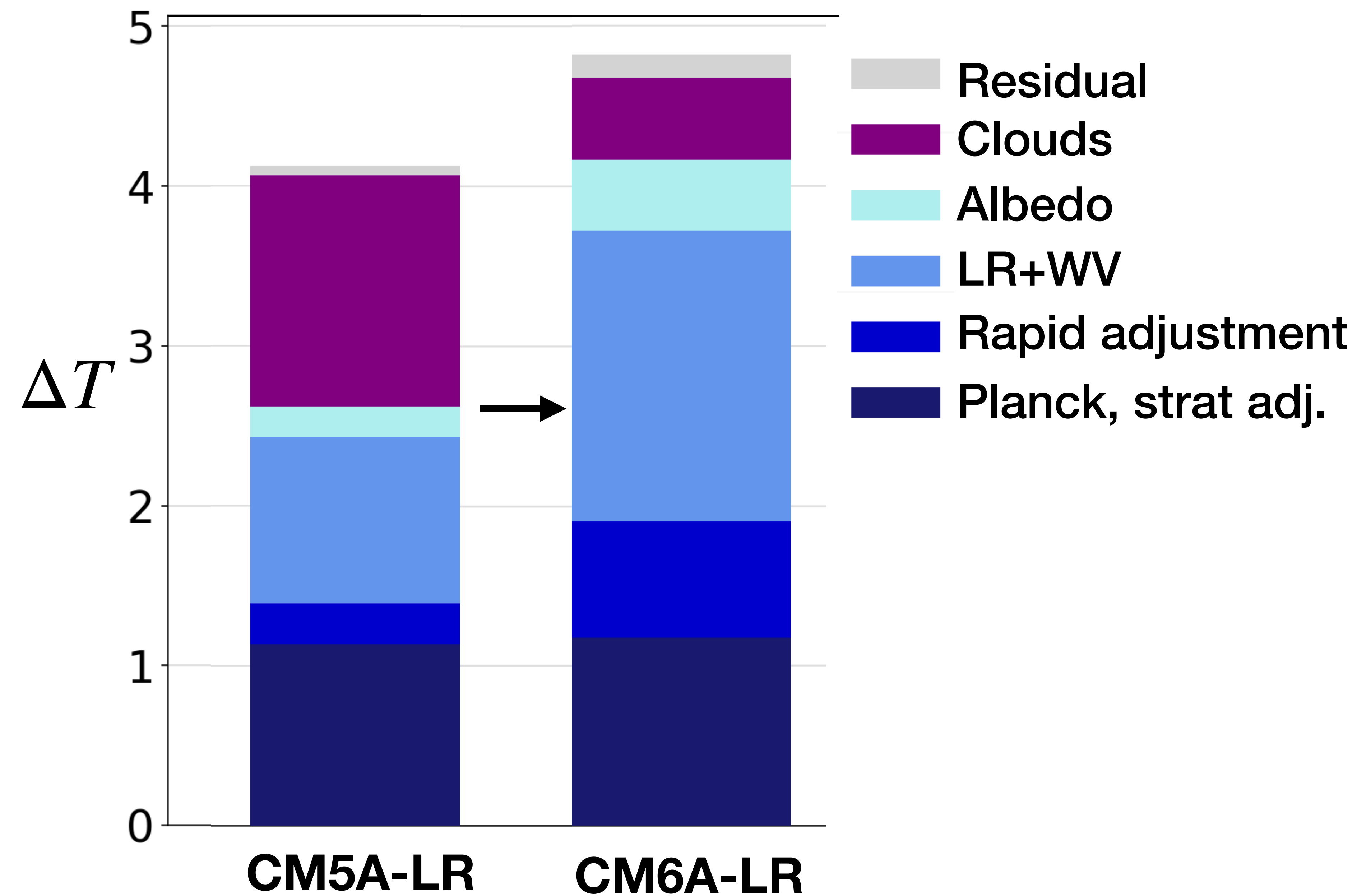


Accepted Article

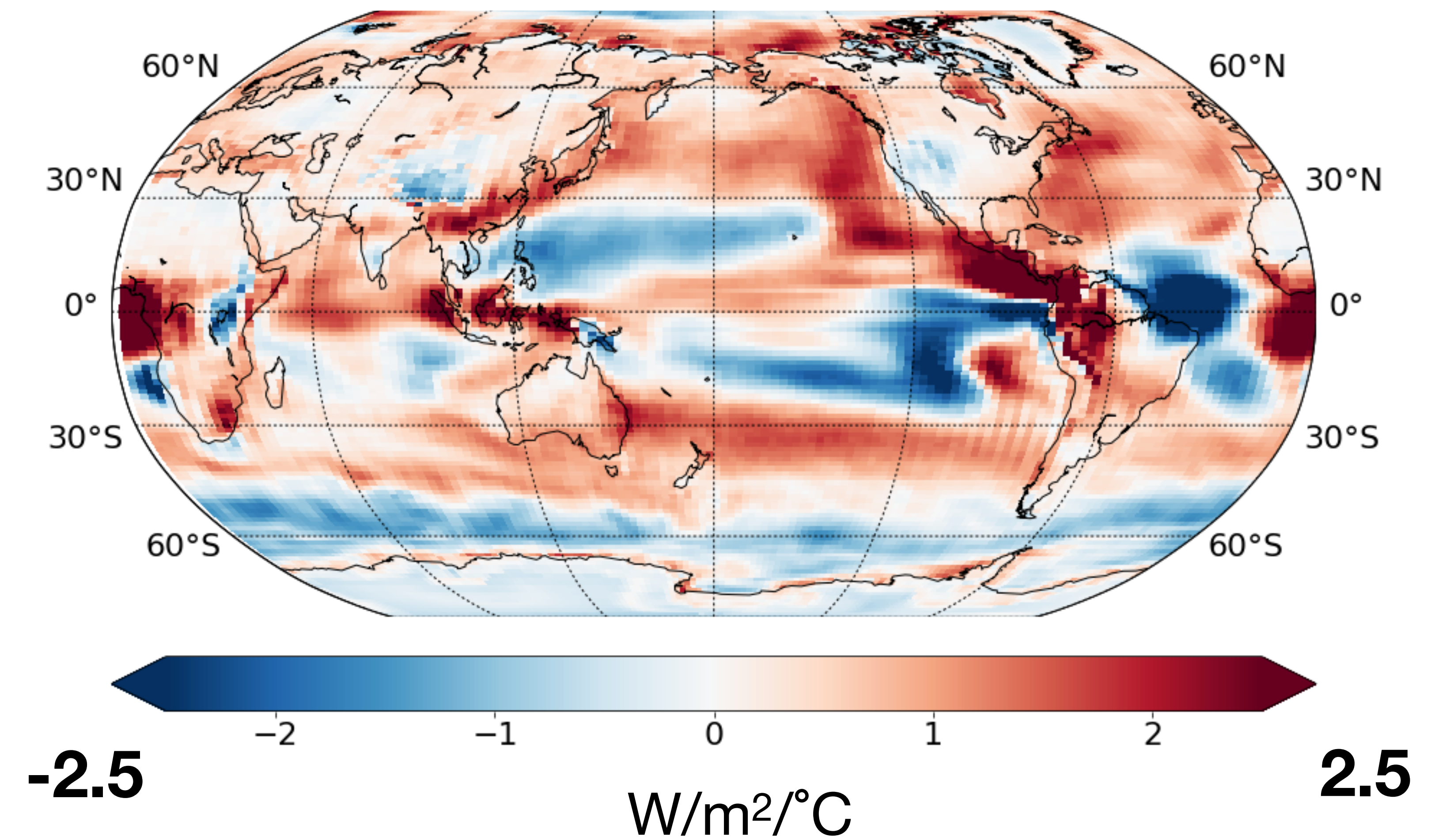


Accepted Article

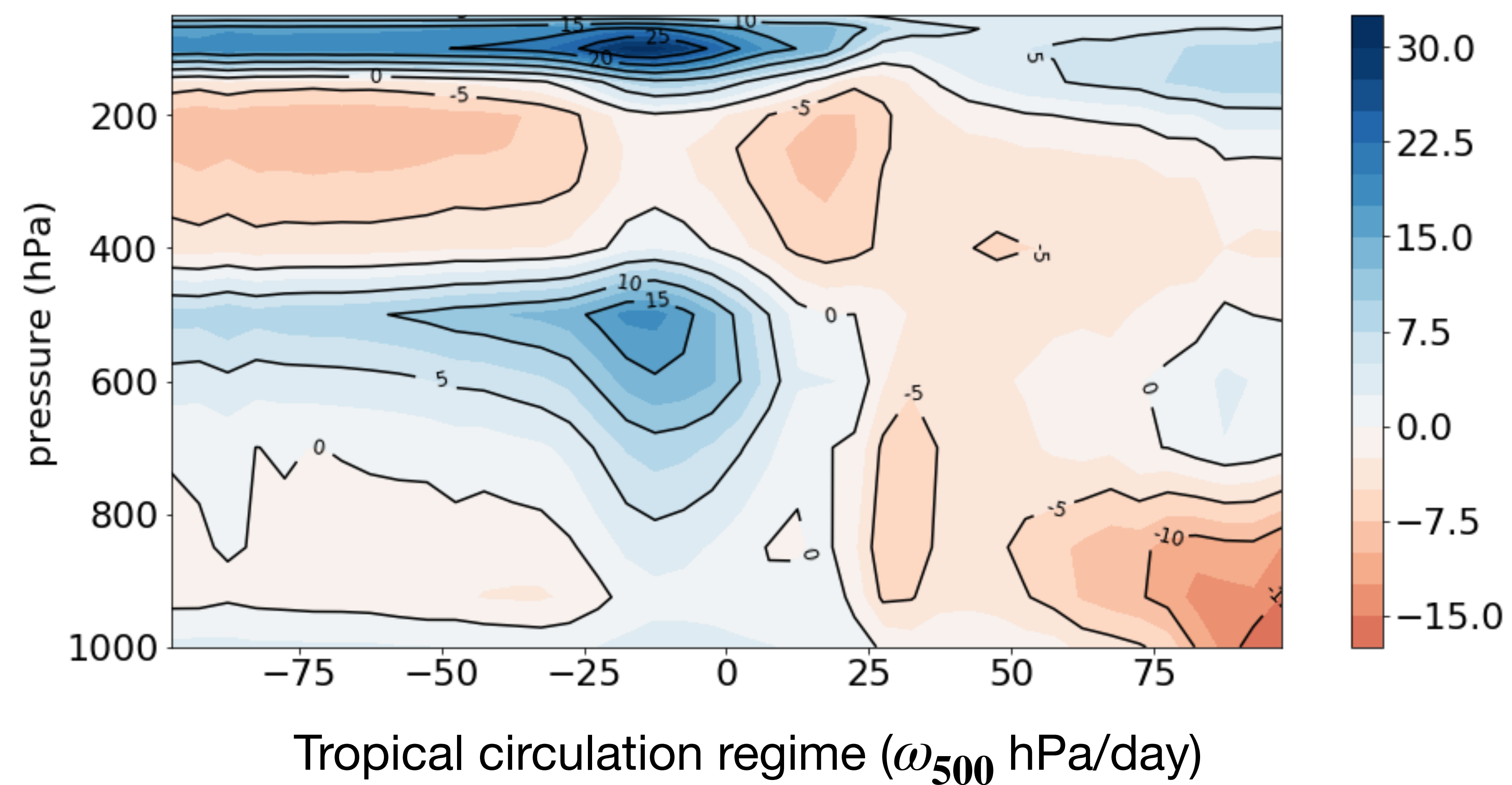
a) Contributions to ECS



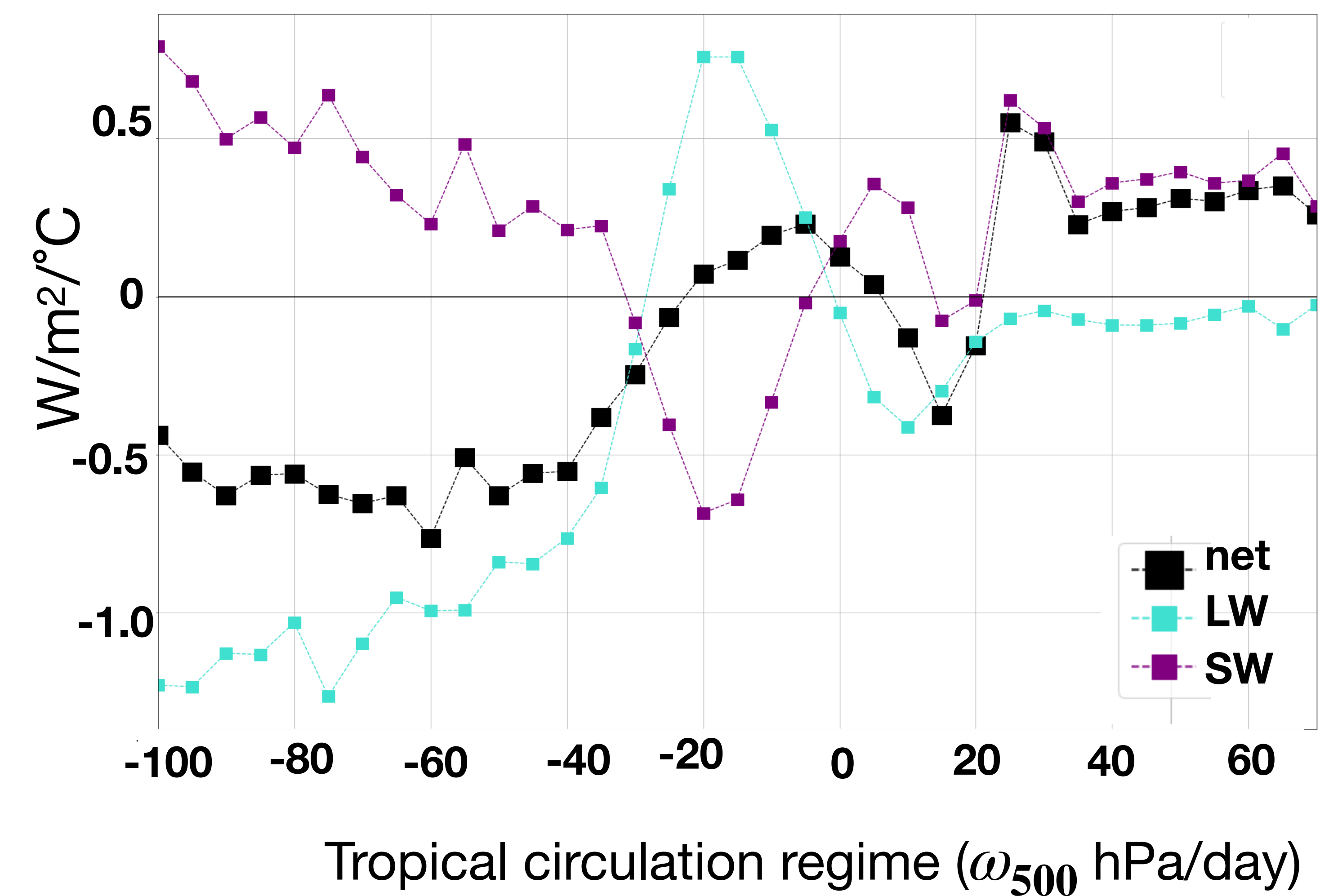
b) Net cloud feedback



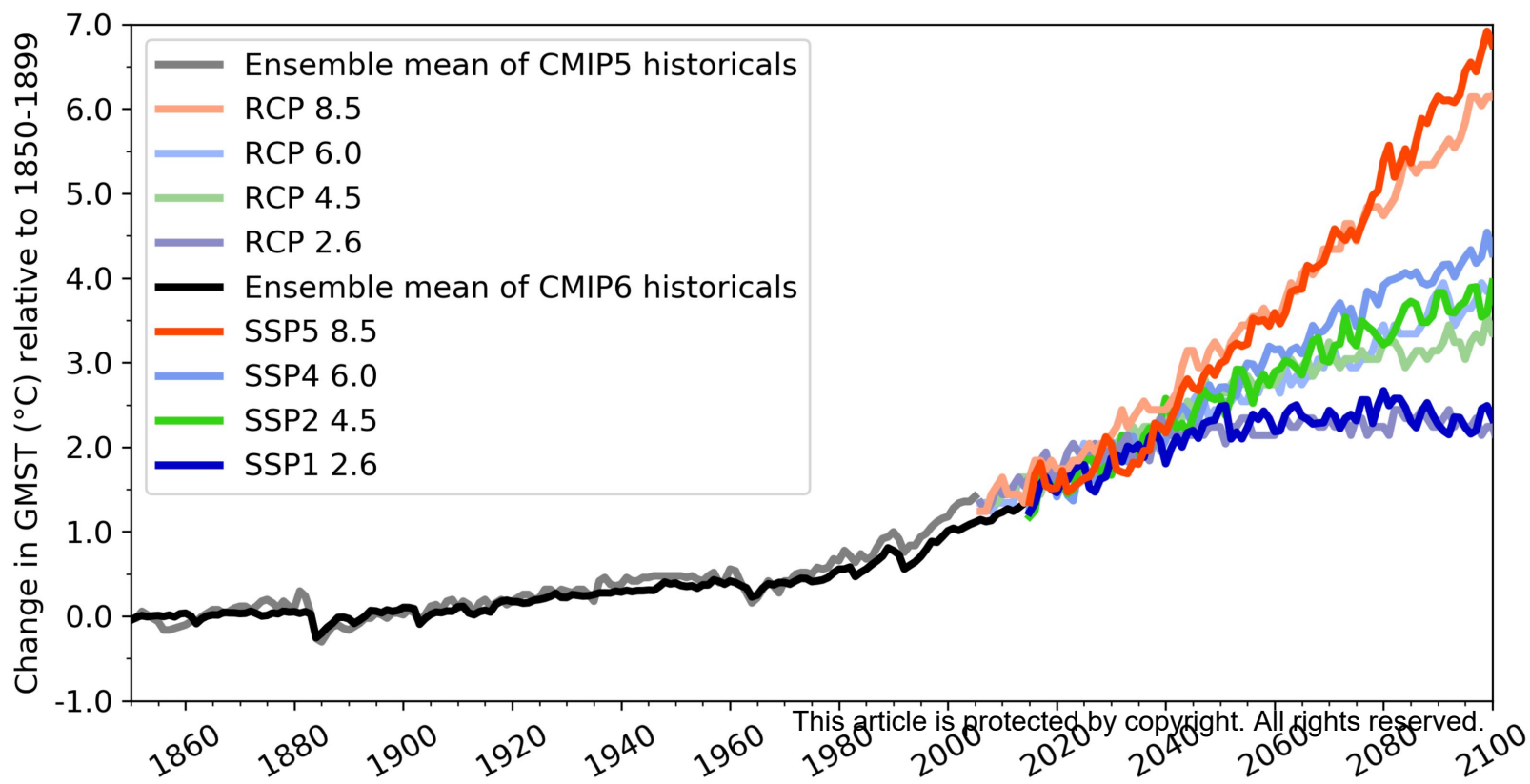
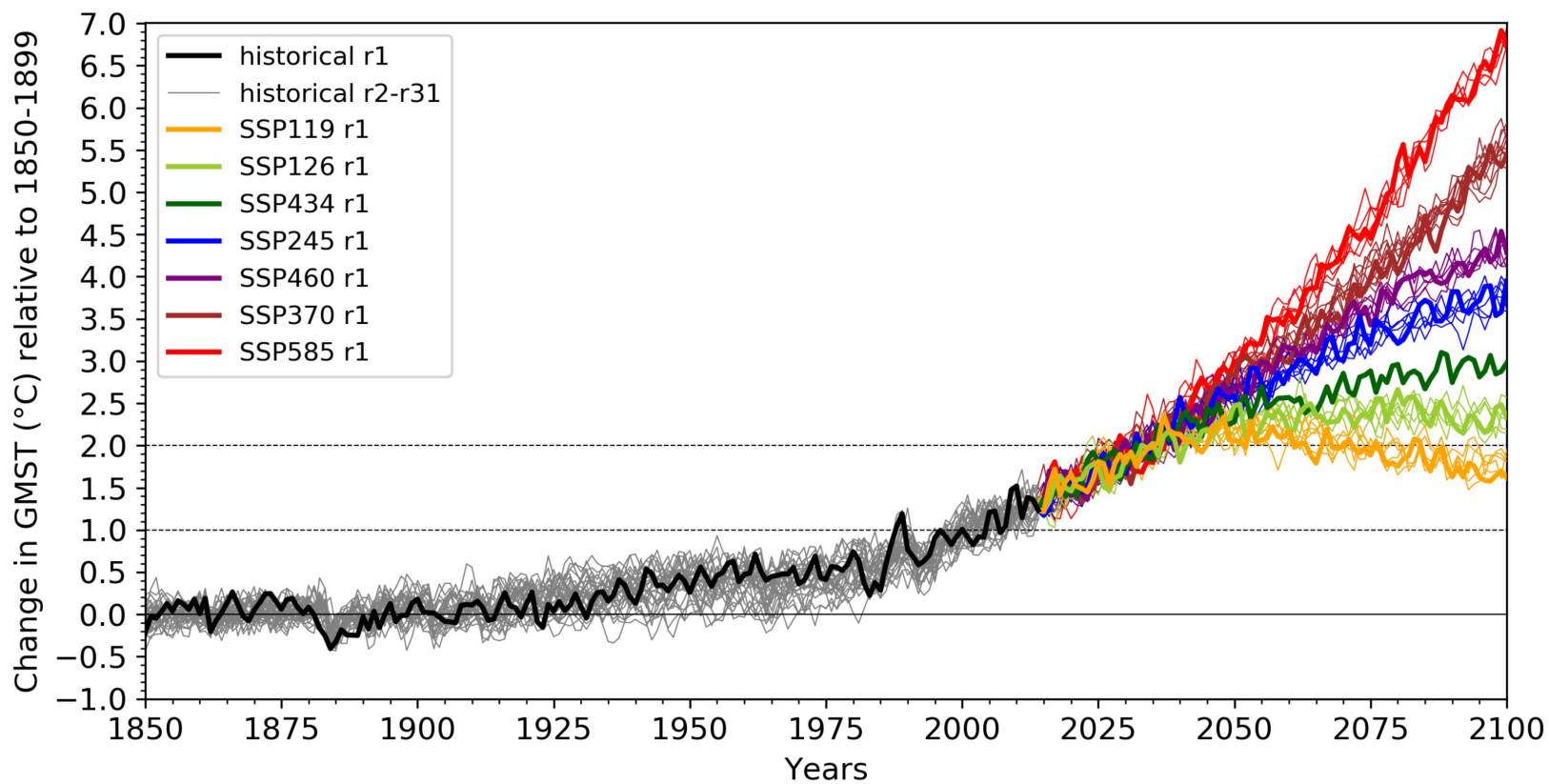
c) Tropical relative humidity anomalies %



d) Tropical cloud feedback

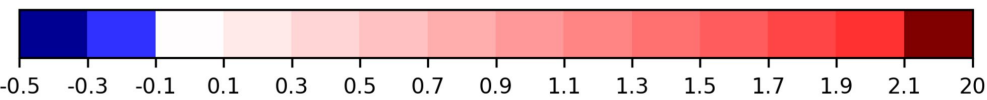
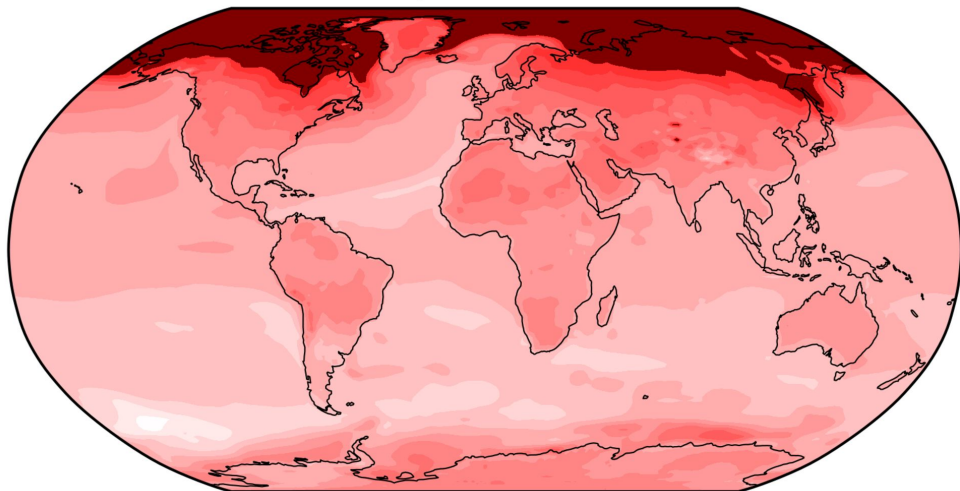


Accepted Article

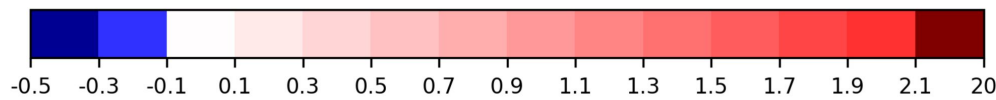
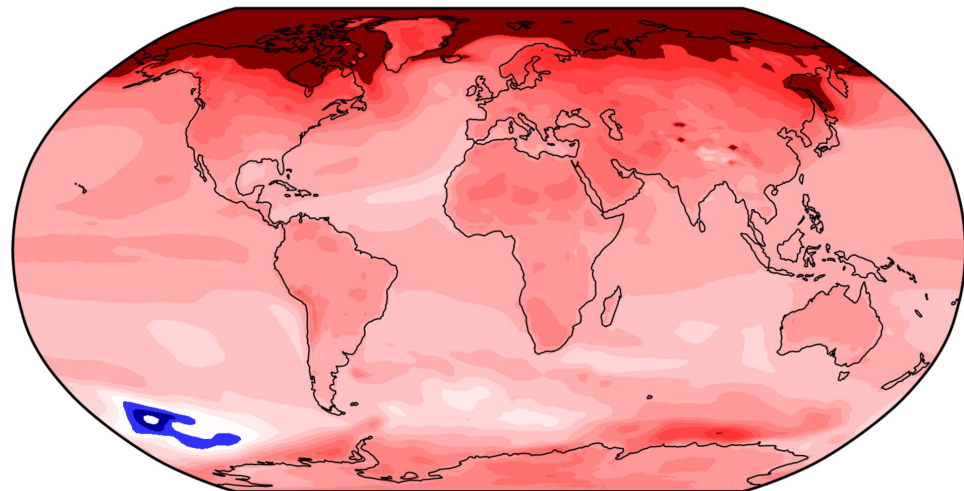


Accepted Article

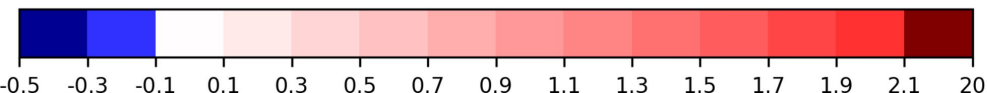
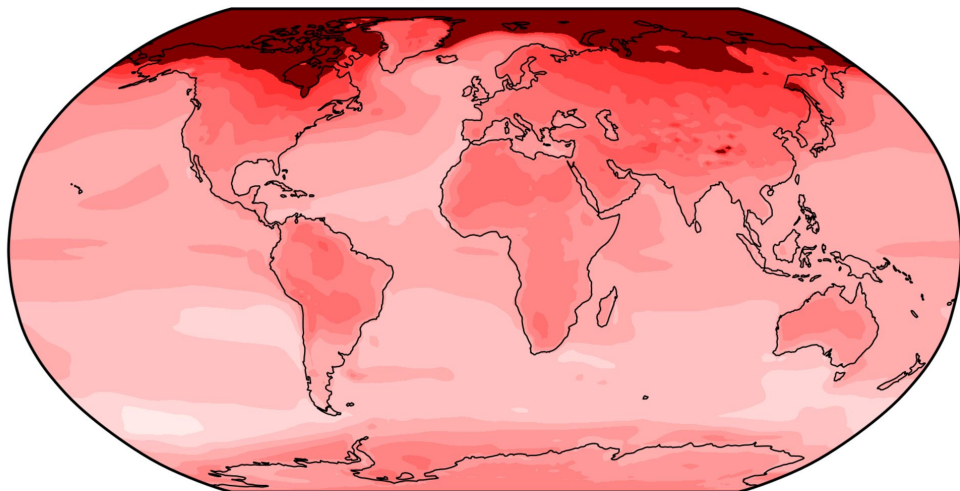
ssp126 2100



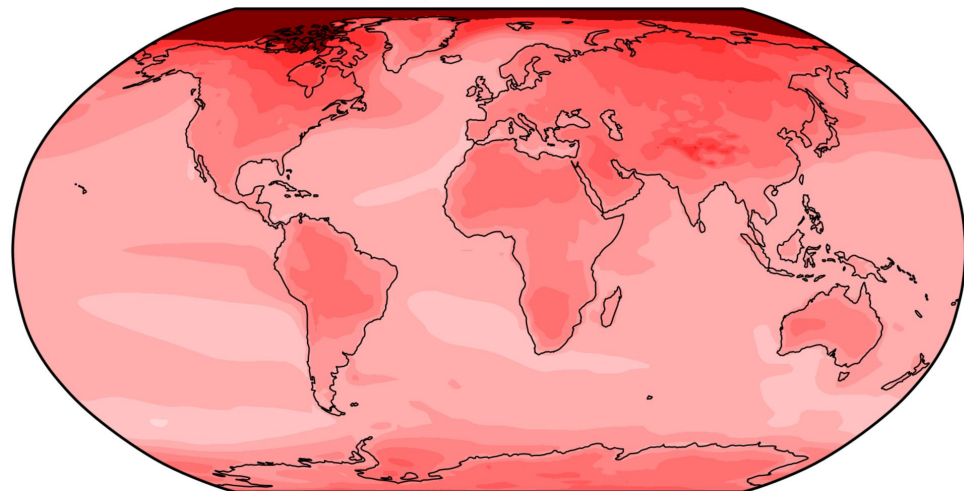
ssp126 2300



ssp585 2100



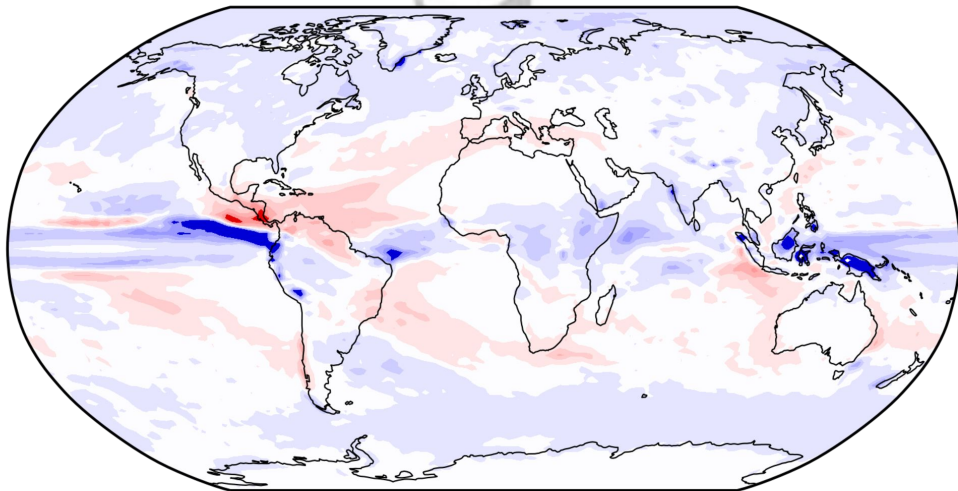
ssp585 2300



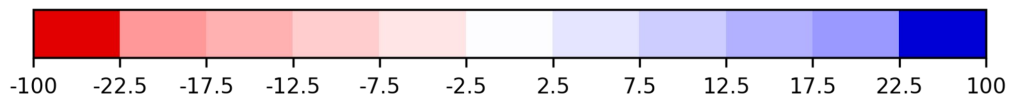
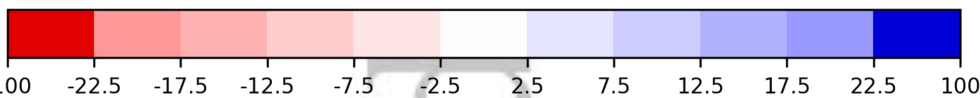
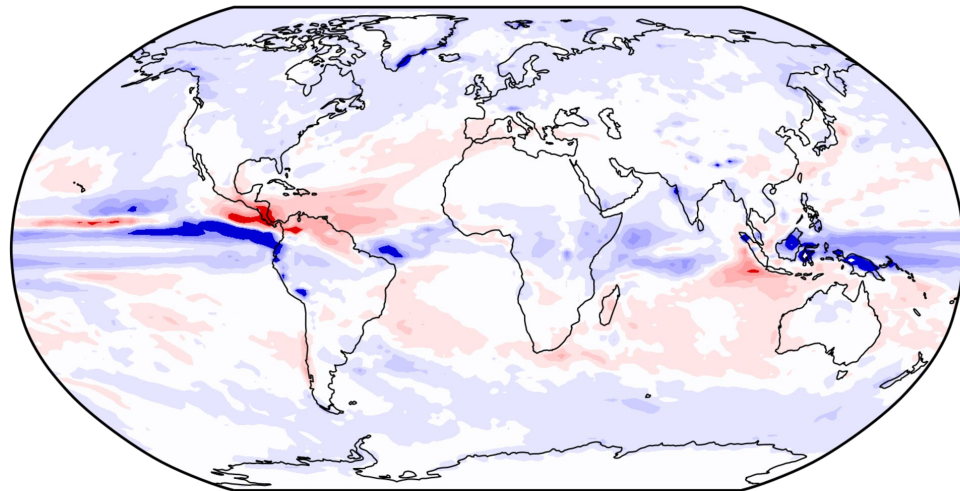
This article is protected by copyright. All rights reserved.

Accepted Article

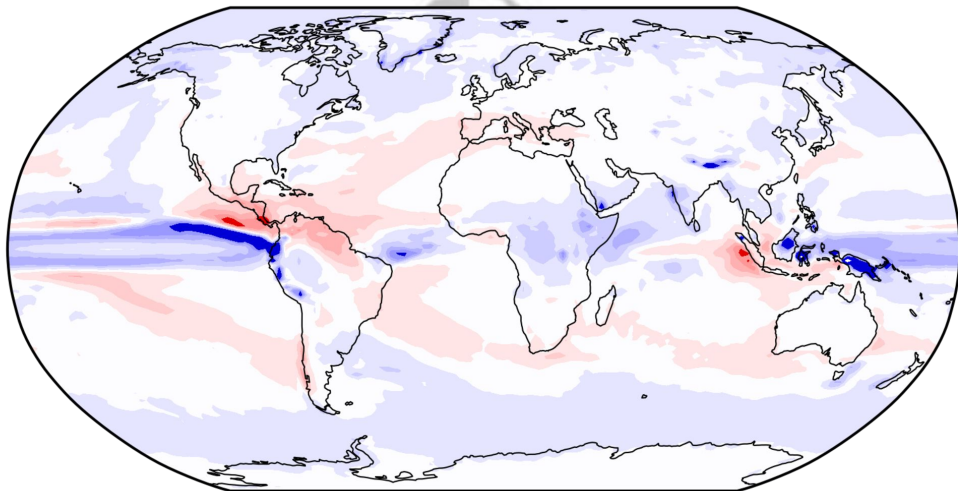
ssp126 2100



ssp126 2300



ssp585 2100



ssp585 2300

